

The Pennsylvania State University

The Graduate School

**Exploration of Internal Cooling Schemes
Enabled Through Additive Manufacturing**

A Dissertation in
Mechanical Engineering

By

Thomas M. Corbett

© 2024 Thomas M. Corbett

Submitted in partial fulfillment
of the requirements
for the degree of

Doctor of Philosophy

May 2024

The dissertation of Thomas M. Corbett was reviewed and approved by the following:

Karen A. Thole
Distinguished Professor of Mechanical Engineering
Dissertation Advisor
Chair of Committee

Timothy Simpson
Paul Morrow Professor in Engineering Design and Manufacturing

Stephen P. Lynch
Associate Professor of Mechanical Engineering

Allison M. Beese
Professor of Materials Science and Engineering and Mechanical Engineering

Robert F. Kunz
Associate Department Head for Graduate Programs of Mechanical Engineering
Professor of Mechanical Engineering

ABSTRACT

The additive manufacturing (AM) process opens up many opportunities for engineers to explore novel cooling designs that historically may have been costly or even impossible to manufacture. To leverage AM for cooling schemes effectively, engineers must first understand the impact of AM surface roughness on the performance of a variety of internal geometries. The goal of this dissertation was to assess a suite of cooling technologies that were made using AM by comparing the fluid dynamic and heat transfer performance as well as the ability to construct the designs. Specifically, the cooling schemes investigated included wavy channels, pin fin arrays, lattice structures, broken wavy ribs, and diamond pyramid surface features. All of these features were evaluated over a wide range of Reynolds numbers in the turbulent flow regime.

The cooling schemes evaluated covered a range of friction factor augmentations from 2 to 500, and heat transfer augmentations between 1.2 and 6 relative to smooth cylindrical channels with no features. The heat transfer and pressure drop of wavy channels was found to be largely a function of the secondary flows with the augmentation scaling as a function of the relative waviness of the channel. Wavy channels were also identified to perform best, in terms of heat transfer, at low Reynolds numbers. Pin fin geometries induced greater heat transfer and pressure loss augmentations than the wavy channels as result of the enhanced surface area and turbulent mixing. Pin shape and spacings were the variables that dictated the pressure loss and heat transfer, though the addition of surface roughness enhanced both flow characteristics. Small surface protrusions such as diamond pyramid turbulators and broken wavy ribs had small performance augmentations relative to the pin fin and wavy channel designs, but these augmentations were found to be insensitive to Reynolds number. The surface features induced substantial near wall mixing with increases in both heat transfer and pressure loss but was further increased as the relative endwall surface roughness increased. Lattice structures had the most significant pressure penalty of all geometries that were considered despite offering only similar heat transfer enhancement to that of the pin fin arrays.

Throughout these studies, variations in materials and machines used for the additive manufacturing were identified and related to the performance of internal cooling and pressure loss. These variations led to varying degrees of roughness and a range of surface morphologies. Highly rough wavy channels, for example, significantly increased pressure drop but did not produce an equivalent increase to heat transfer. While arithmetic mean roughness was the primary driver of cooling performance, the surface skewness and kurtosis were found to be key secondary variables.

The work presented in this dissertation identified the key flow characteristics and impacts of surface roughness on a variety of internal cooling designs. The data and analyses presented

bridge the gap in understanding the performance implications of a range of additively manufactured cooling features empowering designers to integrate new cooling technologies into practical applications.

TABLE OF CONTENTS

List of Figures.....	x
List of Tables	xvii
Nomenclature.....	xviii
Acknowledgements.....	xxi
Preface	xxiii
1. Introduction.....	1
1.1. Internal Cooling Technologies.....	2
1.2. Laser Powder Bed Fusion.....	4
1.3. Impact of surface roughness on cooling design performance.....	6
1.4. Research Objectives.....	7
1.5. Outline of Dissertation.....	8
2. Amplitude and wavelength effects for wavy channels	10
2.1. Abstract.....	10
2.2. Introduction.....	10
2.3. Literature Review	11
2.4. Description of Test Coupons	13
2.5. Channel Characterization.....	15
2.6. Experimental Methods.....	15
2.7. Measurement Uncertainty.....	17
2.8. Computational Methods.....	18
2.9. Effect of Channel Wavelength.....	19
2.10. Effect of Channel Amplitude.....	25
2.11. Overall Channel Performance.....	28
2.12. Conclusions.....	32
3. Impacts of pin fin shape and spacing on heat transfer and pressure losses.....	34
3.1. Abstract.....	34
3.2. Introduction.....	34
3.3. Literature Review	35

3.4. Description of Test Coupons	37
3.5. Coupon Characterization	39
3.6. Experimental Methods	41
3.7. Measurement Uncertainties	43
3.8. Pin Shape Effects	43
3.9. Streamwise Pin Spacing Effects	45
3.10. Overall Array Performance	47
3.11. Correlating roughness with performance	48
3.12. Conclusions	53
4. Large Eddy Simulations of Kagome and Body Centered Cubic Lattice Cells	54
4.1. Introduction	54
4.2. Computational Setup	56
4.2.1. Modeling Domain and Methods	56
4.2.2. Mesh Generation and Validation	58
4.2.3. Benchmarking with Experimental Simulations	60
4.2.4. Data Reduction	61
4.3. Results and Discussion	63
4.3.1. Local Pressure Drop and Heat Transfer	63
3.3 Flow and Thermal Developing Region	65
4.3.2. Turbulence and Unsteady Flows	71
4.4. Conclusion	76
5. Scaling Heat Transfer and Pressure losses of Novel Additively Manufactured Rib Designs....	77
5.1. Abstract	77
5.2. Introduction	77
5.3. Literature Review	78
5.4. Geometric Description	80
5.5. Geometric Characterization	82
5.6. Experimental Setup	85

5.7. Uncertainty Quantification	86
5.8. Computational Setup	86
5.9. 1x Wavy Rib Performance.....	88
5.10. Overall Performance	93
5.11. Scaled Testing.....	94
5.12. Conclusions.....	97
5.13. Acknowledgements.....	98
6. Thermohydraulic Performance and Flow Structures of Diamond Pyramid Arrays.....	99
6.1. Abstract.....	99
6.2. Introduction.....	99
6.3. Literature Review	100
6.4. Geometric Description.....	102
6.5. Geometric Characterization	103
6.6. Experimental Setup.....	106
6.7. Computational Setup	109
6.8. Uncertainty Quantification	110
6.9. Surface Temperature Measurements	110
6.10. Developing and Developed Flow	111
6.11. Flow Structures and Thermal Fields	118
6.12. Overall Performance	122
6.13. Conclusions.....	124
6.14. Acknowledgement	125
7. Expanding material selections for Additively manufactured cooling designs.....	126
7.1. Abstract.....	126
7.2. Introduction.....	126
7.3. Literature Review	127
7.4. Test Matrix Description.....	129
7.5. Geometric Characterization	133

7.6. Thermal Conductivity	138
7.7. Experimental Methods	139
7.8. Measurement Uncertainty	141
7.9. Wavy Channel Cooling Performance	142
7.10. Pin Fin Array Cooling Performance	145
7.11. Efficiency Index of Tested Designs	147
7.12. Conclusions.....	149
7.13. Notice Of Copyright	149
7.14. Acknowledgements.....	150
8. Impacts of Materials and Machine on the Variation of Additively Manufactured Cooling Channels.....	151
8.1. Abstract.....	151
8.2. Introduction.....	151
8.3. Literature Review	152
8.4. Description Of Test Matrix.....	154
8.5. Surface Roughness Characterization	157
8.6. Geometric Accuracy Characterization.....	163
8.7. Experimental Methods.....	165
8.8. Measurement Uncertainty.....	166
8.9. Thermal Performance of Wavy Channels.....	166
8.10. Thermal Performance of Pin Fins.....	170
8.11. Conclusions.....	173
8.12. Acknowledgements.....	175
9. Conclusions.....	176
9.1. Comparisons Of Internal Cooling Designs.....	176
9.2. Machine and Material Considerations in the DMLS Process.....	179
9.3. Recommendations for Future Work	180
References.....	182

A.	Preliminary Lattice Structure Scaling Results	199
B.	Comparisons To Prior Literature	203
C.	Uncertainty Calculations.....	206

LIST OF FIGURES

Figure 1-1. Burned through high pressure turbine blade. Image from [4].....	1
Figure 1-2. (a) Electronic heat sink that utilizes internal microchannels [11] and (b) Internal cooling of gas turbine blade [12].....	3
Figure 1-3. A diagram of the additive manufacturing process [25].....	5
Figure 1-4. Diagram of the L-PBF influence parameters [28].....	6
Figure 2-1. Dimensioned test coupon used to determine the friction factor and bulk Nusselt number of the wavy channels with internal geometry exposed.....	13
Figure 2-2. Test matrix description and amplitude and wavelength definitions for wavy channels.	14
Figure 2-3. Cross section of test rig used to evaluate coupon heat transfer and friction factor performance.....	16
Figure 2-4. Example of domain used in computational study.	18
Figure 2-5. Friction factor testing results for channels of varying wavelength and constant amplitude as a function of channel Reynolds number.....	20
Figure 2-6. (a) Friction factor augmentation and (b) Nusselt number augmentations as compared to the nominal case for channels of varying wavelength and constant amplitude.....	21
Figure 2-7. Nusselt number as a function of Reynolds number for coupons of varying wavelength and constant amplitude in the turbulent regime.	22
Figure 2-8. (a-e) Thermal contours for the tested channels normalized by the inlet and wall temperatures.	23
Figure 2-9. Normalized maximum velocity and secondary flows at three planar locations along a given wavelength for the reduced amplitude (a-c), reduced wavelength (e-f), nominal (g-i), increased wavelength (j-l), and increased amplitude (m-o) cases.	25
Figure 2-10. Friction factor as a function of Reynolds number for channels of varying amplitude and constant wavelength.	26
Figure 2-11. (a) Friction factor and (b) Nusselt number augmentations from the nominal case for channels of varying amplitude and constant wavelength.	27
Figure 2-12. Nusselt number for channels of varying amplitude and constant wavelength as a function of channel Reynolds number.....	28
Figure 2-13. (a) Friction factor augmentation, (b) Nusselt number augmentation, and (c) efficiency index as a function of channel relative waviness.	30
Figure 2-14. Nusselt number augmentation as a function of the friction factor augmentation for all channels.....	32

Figure 3-1. Test coupon diagram with exposed internal geometry and relevant coupon dimensions.	38
Figure 3-2. Accuracy of as-measured pin to design intent for diamond shaped pins.	40
Figure 3-3. Internal surfaces of the coupons containing (a) triangle pins (b) cylindrical pins, and (c) diamond pins recreated from CT scans.	41
Figure 3-4. Diagram of test section.....	41
Figure 3-5. Friction factor data for coupons of varying pin shape at a streamwise spacing of $X/D = 3$	44
Figure 3-6. Nusselt number values for pins of varying shapes at a streamwise spacing of $X/D = 3$	45
Figure 3-7. Friction factor values for pins of varying shape and streamwise spacings at $Re = 10,000$ and $18,000$	46
Figure 3-8. Nusselt number values for pins of varying shape and streamwise spacings at $Re = 10,000$ and $20,000$	47
Figure 3-9. Efficiency index performance of coupons tested in the current study compared to a traditionally manufactured pin fin array of the same spacing.	48
Figure 3-10. Nusselt number for various cylindrical pins of similar spacing found in literature compared to data from current study.....	49
Figure 3-11. Prediction accuracy of developed correlation against data in literature.....	51
Figure 3-12. Developed Nusselt number correlation compared to data and correlations found in literature.	52
Figure 4-1. (a) Kagome and (b) body centered cubic lattice definitions.	56
Figure 4-2. Computational domain used for simulations.....	57
Figure 4-3. (a) Kagome and (b) body centered cubic mesh at the midplane of the domain and (c) the spectral power density of the three velocity components as a function of frequency at a point downstream of the first row of Kagome lattice.	58
Figure 4-4. Single unit cell from CT scan of metal (a) Kagome and (b) BCC lattice test coupons.	60
Figure 4-5. (a) Friction factor and (b) Nusselt number as a function of X	63
Figure 4-6. Normalized time-averaged (a-e) velocity and (f-j) thermal contours at five streamwise planes for the Kagome lattice.....	66
Figure 4-7. Normalized time-averaged vorticity in three streamwise planes for the first five rows of the Kagome lattice (a-c).....	67

Figure 4-8. Normalized time-averaged (a-e) velocity and (f-j) thermal contours at five streamwise planes for the BCC lattice.	68
Figure 4-9. Normalized time-averaged thermal contours with streamlines in the (a) horizontal and (b) vertical midplane of the Kagome lattice with highlighted regions of interest (c-f).	70
Figure 4-10. Normalized time-averaged thermal contours with streamlines in the (a) horizontal and (b) vertical midplane of the BCC lattice with highlighted regions of interest (c,d).	70
Figure 4-11. Turbulence intensity at two planar locations for the (a-b) Kagome and (c-d) BCC lattice.	72
Figure 4-12. Instantaneous (a) vortices and (b) thermal profiles around the Kagome lattice at four time intervals.	73
Figure 4-13. Instantaneous (a) vortices and (b) thermal profile around the BCC lattice at four time intervals.	73
Figure 4-14. Local Strouhal number in the wake region of the (a) Kagome and (b) BCC lattice.	74
Figure 4-15.	74
Figure 5-1. (a) Pitch and broken spacing for all rib geometries, and (b-f) diagrams of rib location in the coupon duct and rib design.	81
Figure 5-2. Profile of the nominal rib design intent (a) compared against the five printed variants (b-f).	82
Figure 5-3. Relative rib height determined from the CT scans for the nine test coupons featuring ribs.	84
Figure 5-4. The (a) top and (b) side profiles of the computational domain, (c) zoomed out and (d) zoomed in view of the computational mesh, and (e) mesh independence study for the nominal case.	88
Figure 5-5. Measured (a) friction factor and (b) Nusselt number as a function of Reynolds number for the varying rib designs for 1x scale.	88
Figure 5-6. Friction Factor and Nusselt number augmentation at a Reynolds number of 20,000.	89
Figure 5-7. Contours of Theta for the five different wavy rib designs at three streamwise planes.	90
Figure 5-8. Contours of the near wall normalized y-component of vorticity for the nominal case.	91
Figure 5-9. Local Nusselt number augmentation for the (a) 0.5λ , (b) 1.5λ , (c) Nominal, (d) Nominal Aligned, and (e) Nominal Offset rib geometries.	92
Figure 5-10. Efficiency index versus Reynolds number of the wavy rib geometries against other advanced rib designs.	93

Figure 5-11. Augmentation plot of the wavy rib designs investigated in this study compared against designs from literature.....	94
Figure 5-12. Friction factor and Nusselt number augmentation for the nominal design at several scales.	95
Figure 5-13(a) Friction factor and (b) Nusselt number as a function of relative roughness at three Reynolds numbers for the scaled test coupons.....	96
Figure 6-1. Example of test coupon with dimensioned pyramid, and side profiles of the different pyramid arrangements.	102
Figure 6-2. Measurements of pyramid height, spanwise width, and streamwise length from optical profilometry scans.	105
Figure 6-3. Cross section of rig used to take IR images of coupon surface.....	108
Figure 6-4. (a) Domain used for computations, (b) mesh used for computations, (c) mesh convergence study.	109
Figure 6-5. Temperature distribution on the surface of the large pyramids case.....	111
Figure 6-6. (a) Friction factor and (b) Nusselt number as a function of Reynolds number for the various diamond pyramid configurations.	112
Figure 6-7. Friction factor augmentation from a (a) smooth duct and the (b) empty duct cases at a Reynolds number of 20,000.	113
Figure 6-8. Nusselt number augmentation from a (a) smooth duct and the (b) empty duct cases at a Reynolds number of 20,000.	115
Figure 6-9. (a) Friction factor and (b) Nusselt number augmentation for three variations to the aligned pyramids on both sides case.	116
Figure 6-10. Development of local (a) Friction factor and (b) Nusselt number as a function length along the duct with locations of minimum flow area highlighted for the large, both sides aligned case.	117
Figure 6-11. Contours of normalized temperature for the (a) small, (b) medium, (c) large, (d) large both sides aligned, and (e) large both sides offset for a streamwise oriented plane in the entry region.....	119
Figure 6-12. Thermal contours with streamlines for the third row of the (a) round edge and (b) sharp edge aligned pyramids on both sides case.	120
Figure 6-13. Contours of normalized temperature for the (a) small, (b) medium, (c) large, (d) large both sides aligned, and (e) large both sides offset for planes normal to the streamwise direction.	121

Figure 6-14. Contours of the endwall Nusselt number augmentation for the (a) small, (b) medium, (c) large, (d) large both sides offset bottom wall, (e) large both sides offset top wall, and (f) large both sides aligned cases, with a zoomed in view of the (g) upstream and (h) downstream region of the small pyramids case.	122
Figure 6-15. Augmentation plot comparing investigated designs to prior data.	123
Figure 7-1. General shape of all test coupons used as part of this study.	130
Figure 7-2. Channel hydraulic diameter and internal channel geometry for the (a) nominal width, (b) 1.5 width, and (c) 2.0 width wavy channels, in addition to the pin geometry and spacing for the pin fin design.	130
Figure 7-3. (a) Vertical and horizontal print orientations and (b) schematic of different zones in a layer during a L-PBF build that may use different process parameters.	132
Figure 7-4. Pictures of several as-built test coupons.	133
Figure 7-5. Deviation from design intent for the twenty test coupons that underwent experimental testing.	134
Figure 7-6. (a-c, e-g) Wavy channel and (d,h) diamond pin fin profiles at two discrete locations.	135
Figure 7-7. Measured Ra for the wavy channel designs.	137
Figure 7-8. Surface morphology for the (a) 2.0X width wavy channels and the (b) upskin pin fin surfaces.	138
Figure 7-9. Thermal conductivity of newly developed superalloys compared against standard IN718.	139
Figure 7-10. Test section of test rig used in this study.	140
Figure 7-11. (a-c) Friction factor augmentation and (d-f) Nusselt number augmentation for the three wavy channel designs.	143
Figure 7-12. Friction factor augmentation of the wavy channel coupons at Reynolds number of 10,000 and 30,000.	144
Figure 7-13. Nusselt number augmentation of the wavy channel coupons at Reynolds numbers of 10,000 and 30,000.	145
Figure 7-14. (a) Friction factor augmentation and (b) Nusselt number augmentation for the pin fin designs.	146
Figure 7-15. Efficiency index for the (a-c) wavy channel and (d) pin fin array coupons as a function or Reynolds number.	148
Figure 8-1. The general coupon shape used in this study and regions of the test coupons imaged using a laser microscope.	155

Figure 8-2. Images captured with a laser microscope of pin fin channel walls (a,c,e,g,i,k,m,o) and wavy channel walls (b,d,f,h,j,l,n,p) in the respective regions indicated in Figure 8-1.	158
Figure 8-3. Images captured with a laser microscope of upskin surfaces of the diamond pins (a,c,e,g,i,k,m,o), and downskin surfaces of the diamond pins (b,d,f,h,j,l,n,p) in the respected regions shown in Figure 8-1.	159
Figure 8-4. Roughness statistics for the imaged surfaces of the test coupons, including arithmetic mean roughness (a), mean roughness depth (b), skewness (c), and kurtosis (d).	160
Figure 8-5. Illustration showing potential differences in measured and actual roughness profile.	161
Figure 8-6. Height variation in the z-direction for the channel walls taken along a given length in the x-direction.	163
Figure 8-7. Analysis of the shape of the diamond pins for EOS machines (a) and IN718 material (b).	164
Figure 8-8. Wavy channel friction factor (a,c) and Nusselt number (b,d) augmentation as a function of Reynolds number.	167
Figure 8-9. Augmentation plot of the wavy channel design from the nine different build conditions.	170
Figure 8-10. Pin fin friction factor (a,c) and Nusselt number (b,d) augmentation as a function of Reynolds number.	171
Figure 8-11. Augmentation plot of the pin fin design from the eight different build conditions.	173
Figure 9-1. Augmentation plot of all designs tested in this dissertation.	177
Figure A-1. Friction factor data from the current study compared against literature.	199
Figure A-2. (a) The three scales of test coupons used for characterizing the performance of the lattice structures, with a view of the internals with the (b) top surface and (c) side wall removed.	200
Figure A-3. Scaling the friction factor of the lattice designs using (a) channel definitions and (b) proposed lattice definitions.	201
Figure B-1. Augmentation plot of pin fin data from the current study compared against data from literature.	203
Figure B-2. Augmentation plot of surface feature data from the current study compared against data from literature.	204
Figure B-3. Augmentation plot of lattice structure data from the current study compared against data from literature.	204

Figure B-4. Augmentation plot of microchannel data from the current study compared against data from literature..... 205

LIST OF TABLES

Table 2-1. Coupon Geometric Characteristics.....	13
Table 3-1. Coupon Specifications and Roughness.....	38
Table 3-2. Geometric Characteristics of Test Coupons	50
Table 3-3. Correlation Constants	51
Table 3-4. Correlations for Pin Fin Array Heat Transfer.....	52
Table 4-1. Geometric Properties and Experimental Results of Simulated and Tested Lattice	57
Table 5-1. Coupon Designs Investigated in the Current Study.....	81
Table 5-2. Roughness Measurements from the Open AM Channels.....	84
Table 5-3. Geometric Characteristics of Designs Investigated In Prior Studies.....	93
Table 6-1. Coupon Geometric Descriptions	103
Table 6-2. Geometric Summary of the Current and Prior Investigations on Surface Features....	123
Table 7-1. Test Set Build Conditions.....	131
Table 8-1. Test Coupon Manufacturing.....	155
Table C-1. Uncertainty Contributions For Reynolds Number at a Reynolds Number of 5,000..	209
Table C-2. Uncertainty Contributions For Reynolds Number at a Reynolds Number of 15,000	209
Table C-3. Uncertainty Contributions For Friction Factor at a Reynolds Number of 5,000	210
Table C-4. Uncertainty Contributions For Friction Factor at a Reynolds Number of 15,000	210
Table C-5. Uncertainty Contributions For Coupon Surface Temperature at a Reynolds Number of 10,000.....	212
Table C-6. Uncertainty Contributions For Coupon Surface Temperature at a Reynolds Number of 30,000.....	213
Table C-7. Uncertainty Contributions for Nusselt Number at a Reynolds Number of 10,000....	214
Table C-8. Uncertainty Contributions for Nusselt Number at a Reynolds Number of 30,000....	214

NOMENCLATURE

A	channel amplitude
A _c	cross-sectional flow area
A _s	surface area
D _h	hydraulic diameter, $D_h = 4 \frac{A_c}{p}$
D	pin diameter
e	surface feature height
f	Darcy friction factor, $f = \Delta P \frac{D_h}{L} \frac{2}{\rho u^2}$
f _f	Fanning friction factor, $f_f = \frac{\Delta P}{2 \rho u_{\max}^2} \frac{1}{N_{\text{row}}}$
h	convective heat transfer coefficient, $h = \frac{Q_{\text{in}} - \Sigma Q_{\text{loss}}}{A_s \cdot \Delta T_{\text{LM}}}$
H	channel height
k	thermal conductivity
k _s	equivalent sand grain surface roughness
L	channel length
L _{center}	width of a unit cell at the midplane location
L _x	diamond pyramid streamwise length
N _{row}	number of streamwise rows of pins
N _{span}	number of pins in the spanwise direction
Nu	Nusselt number, $Nu = h \frac{D_h}{k_{\text{air}}}$
Nu _D	pin Nusselt number, $Nu = h \frac{D}{k_{\text{air}}}$
p	channel perimeter
P	surface feature pitch
P _s	static pressure
ΔP	static pressure drop

Pr	Prandtl number
Q	heat transfer rate
Ra	arithmetic mean surface roughness, $R_a = \frac{1}{n} \sum_{i=1}^n z_{\text{surf}} - z_{\text{ref}} $
Re	hydraulic diameter Reynolds number, $Re = \frac{uD_h}{\nu}$
Re _D	pin diameter Reynolds number, $Re_D = \frac{uD}{\nu}$
S	spanwise distance
S _a	arithmetic mean roughness, $S_a = \frac{1}{n} \sum_{i=1}^n z_{\text{surf}} - z_{\text{ref}} $
S _q	root mean square roughness, $S_q = \sqrt{\frac{1}{n} \sum_{i=1}^n (z_{\text{surf}} - z_{\text{ref}})^2}$
S _{ku}	kurtosis, $S_{ku} = \frac{1}{nS_q^4} \sum_{i=1}^n (z_{\text{surf}} - z_{\text{ref}})^4$
S _{sk}	skewness, $S_{sk} = \frac{1}{nS_q^3} \sum_{i=1}^n (z_{\text{surf}} - z_{\text{ref}})^3$
S _z	mean roughness depth, $S_z = \frac{1}{5} \sum_{i=1}^5 (z_{\text{max}} - z_{\text{min}})_i$
T	temperature
TI	turbulence Intensity, $TI = \frac{\sqrt{\frac{1}{3}((u')^2 + (v')^2 + (w')^2)}}{u_{m,in}}$
TLM	log-mean temperature, $\Delta T_{LM} = \frac{T_{in} - T_{out}}{\ln\left(\frac{T_s - T_{in}}{T_s - T_{out}}\right)}$
u	mass average velocity
UC	unit cell size
W	coupon duct width
X	normalized streamwise distance, x/D_h , x/D , x/UC
Y	normalized spanwise coordinate, y/D_h , y/UC
y ⁺	dimensionless wall coordinate
z _{ref}	reference surface height
z _{surf}	roughness height

z vertical position
 Z normalized z coordinate, z/D_h , z/UC

Greek

$+\Delta x$ dimensionless grid spacing, $+\Delta x = \frac{\Delta x}{\nu \cdot \sqrt{\rho/|\tau_w|}}$

$+\Delta y$ dimensionless grid spacing, $+\Delta y = \frac{\Delta y}{\nu \cdot \sqrt{\rho/|\tau_w|}}$

$+\Delta z$ dimensionless grid spacing, $+\Delta z = \frac{\Delta z}{\nu \cdot \sqrt{\rho/|\tau_w|}}$

ε lattice porosity

η efficiency index, $\eta = \left(\frac{Nu}{Nu_0}\right) \cdot \left(\frac{f}{f_0}\right)^{-\frac{1}{3}}$

λ wavelength

ν kinematic viscosity

ρ fluid density

Θ Non-dimensional temperature, $\theta = \frac{T(x,y,z) - T_{in}}{T_{wall} - T_{in}}$

τ_w wall shear stress

ω in-plane vorticity

Subscripts

d as-design condition

in inlet condition

n nominal case

max maximum condition

out outlet condition

s surface condition

w wall condition

∞ freestream condition

0 smooth condition

ACKNOWLEDGEMENTS

My graduate school journey would not have been possible without the tireless support of so many people. I would like to start by thanking my advisor, Dr. Karen Thole, for her years of advice and guidance. I would also like to express my gratitude to my dissertation committee, Dr. Steven Lynch, Dr. Tim Simpson, and Dr. Alisson Beese for their technical expertise and perspective on my work, ensuring it was of high quality. I would like to thank Solar turbines and the US Department of Energy¹, who provided the funding for my time at Penn State and grounded my research in real problems that engineers face today.

I would also like to say thank you to the entirety of the START staff, including Mike, Reid, Jerimiah, Scott, Becca, and Justin, for repeated assistance in ensuring I had every available resource I could want to complete my research. Thank you to all of the current and past START students who I have had the pleasure of working with (forgive me for not naming all 24 of you). I will always appreciate the mentorship I received from those who came before me, and for opportunity to impart any amount of knowledge I might have on those who came after. A special thanks goes out to Alexander, Emma, Maria and Abbie who were there when I needed support both in and outside of the lab. I will forever cherish the countless hours we spent rambling on about research, cooking, Youtube videos, life after graduate school, and everything in between. I would also like to express a special thank you to Peter and Emily, who accepted me as their graduate mentor, teaching me just as much as I hope I taught you. Furthermore, I want to thank Dr. Federico Sciammarella and Dr. Nicholas Pohlman for encouraging me to pursue graduate studies, and who have continued to offer me advice in the years after finishing my bachelors.

A special thanks also goes out to the many friends away from Penn State, including Tim, Adam, Josh, Chris, Ryan, Mason, Kyle, Matt, Josh, Lauren, and more who helped keep me going through the many nights we spent playing games and making jokes together.

Of course, none of this would have been possible without the direct support of my family. I would like to thank both of my parents, who have pushed me to always pursue every opportunity and emphasized the importance of education. I want to thank my sisters Carinna and Abigail and my brother Alex for their many phone calls and words of encouragement over these past four and

¹ This research was sponsored by the US Department of Energy, Office of Energy Efficiency and Renewable Energy (EERE), Advanced Materials & Manufacturing Technologies Office (AMMTO), under Contract DE-AC05-00OR22725 with UT-Battelle LLC. This work was performed in part at the Oak Ridge National Laboratory's Manufacturing Demonstration Facility, an Office of Energy Efficiency and Renewable Energy user facility.

a half years. I want to thank my grandparents, aunts, and uncles as well, and promise that I'll have more to talk about at family gatherings than college going forward.

Lastly, I would like to express my endless gratitude to Kelsey, who has been a shining light making even the hardest moments over the past few years not as grim. You have been there for me in more ways than I can number, and make me truly excited for our future together. I love you.

PREFACE

Chapter 8 is composed of a paper where I was not the first author. This chapter was co-written by myself and the first author over the course of several months. The conception, test coupon preparation, initial experimental testing, and the analysis of all flow results was completed by myself, and the surface roughness characterization and analysis were completed by my co-author. Both authors contributed significantly to the actual written content of the paper. Chapter 8 is included in this dissertation because it expands on the results discussed in Chapter 7, and allows for more specific conclusions about the relative impacts of materials and machines on the performance of additively manufactured parts.

1. INTRODUCTION

The effective application of heat transfer theory enables many of the luxuries of modern life—from the densely integrated cooling solutions used in high performance compute clusters that power an abundance of cloud services, to the internal cooling passages of a modern turbine blade which enable mass transit worldwide. To continue to enhance the performance across a broad range of applications, internal cooling schemes will need to be tailored and tuned to their specific usages, and understanding a broad spectrum of how different internal cooling designs can be applied will be of great importance.

One example of an application that takes advantage of advanced cooling schemes are the aforementioned gas turbine blades. The turbine section of a gas turbine operates in temperatures in excess of 1400°C [1], which exceeds the metal softening temperature of the typically Ni-based alloys that compose the components [2]. To ensure that the blades can survive these temperatures, ceramic coatings are applied to part surfaces and complex internal and external cooling features are integrated throughout the components. There are a broad range of internal features used, including microchannels, pin fin arrays, surface turbulators, and impingement holes [3]. Significant blade damage can occur if the design of these internal features fails to effectively cool the blade, leading to decreased engine efficiency, and in the worst case, engine failure. An example of a turbine blade that has been fully burned through can be seen in Figure 1-1.



Figure 1-1. Burned through high pressure turbine blade. Image from [4]

A turbine engine operates on an ideal Brayton cycle, which ultimately means that the efficiency of the engine is dependent on the temperature difference between the inlet of the engine and the turbine rotor inlet temperature (TRIT). Over the past several decades, TRITs have increased dramatically to improve overall efficiency [1], leading to amplified interest into the development of increasingly effective cooling schemes to ensure part durability. While computational methods can be used in the development of these schemes, given the significant complexity of the flows present in the turbine section and the significant cost associated with part failures, experimental validation of these schemes is always required. The timeline for casting development parts can be on the order of years, limiting the speed at which engine components can be improved. One promising method of investigating potential cooling schemes faster and cheaper is by leveraging additive manufacturing (AM). To use AM as a tool for development or even production, one must first understand what the implications for doing so are.

AM does not come without its own faults. This includes increased surface roughness, an overabundance of process conditions that impact part quality, high residual stresses in manufactured parts, and reduced mechanical properties relative to traditional single crystal cast parts. These downsides lead to the conclusion that while AM can be leveraged for the development of blades, the reduced creep strength limits the viability of end use AM rotational turbine hardware. However, stationary hardware like tip shrouds [5,6], injector nozzles[7,8], and vanes [9,10] are under significantly less thermal and mechanical stress, and have the potential to be produced through AM as final components.

The primary focus of this work is to identify the performance of a suite of additively manufactured internal cooling features that could be leveraged in any number of internal cooling schemes. By mapping out the potential design space and understanding the impact of the surface roughness intrinsic to AM on a variety of internal features, designers can more effectively develop a scheme for a given application. The secondary focus is to understand how variations to the material and additive machine impact the surface topography of different additive cooling designs, and ultimately how that impacts the performance of design.

1.1. Internal Cooling Technologies

Many types of internal micro-scale cooling technologies can be used to augment heat transfer. The focus of this work is specifically on the performance of microchannels, pin fin arrays, surface features, and lattice structures, examples of which can be seen in Figure 1-2.

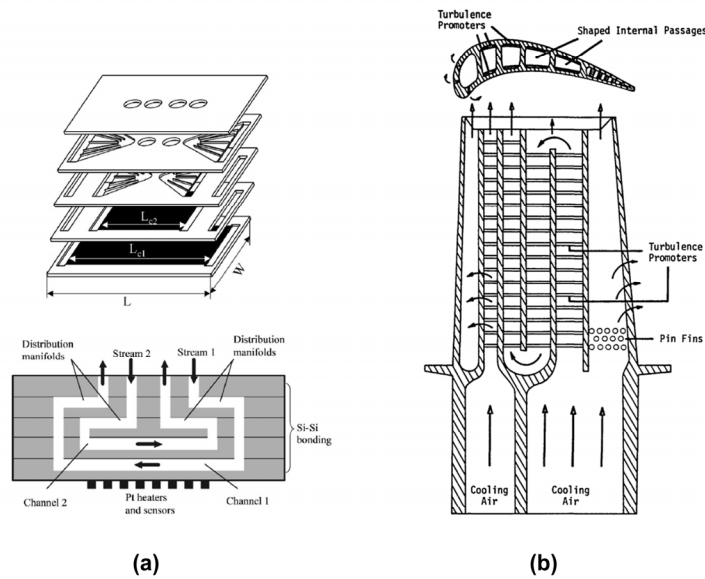


Figure 1-2. (a) Electronic heat sink that utilizes internal microchannels [11] and (b) Internal cooling of gas turbine blade [12].

Microchannels or mini-channels are a form of cooling technology that has been in use for many years for a variety of applications, particularly within the fields of gas turbine cooling [13,14] and electronics cooling [15–18]. As the name suggests, these channels have diameters on the order of a millimeter to a few micrometers, enabling high heat transfer at the cost of high-pressure loss, especially in the case of increased surface roughness [19]. While these channels have traditionally been implemented as simple straight passages, they can also be integrated in more complex ways, such as following a sinusoidal centerline to form a wavy channel [20]. By making the channel wavy in shape, beneficial secondary flows are formed which enhance heat transfer beyond that of a typical channel at an increased pressure cost.

Pin fins arrays are another common cooling technology that have been studied for several decades in many varieties of heat transfer applications. A pin fin array is typically composed of a series of bluff bodies (pins) arranged into a grid inside of a channel, where the spacing between pins is a function of the pin diameter. The primary function of pin fins is to induce turbulent mixing and increase the surface area within a typically small volume. The heat transfer and pressure loss of these designs has been seen in the past to scale with the pin diameter and pin spacing [21], as opposed to the channel hydraulic diameter as was used for microchannels. This is the result of the flow disturbance caused by the fins dominating both the heat transfer and pressure drop of design, rather than the diameter of the channel that the pins exist in. The pin shape also plays a role in the performance of the design, as the shape can change the magnitude and structure of the wake

formations resulting in different distributions of heat transfer between the endwall and pin surfaces [22].

Another family of cooling geometries that are of pertinence to this body of work are turbulence promoters, such as ribs. Ribs typically take the form of patterned short protrusions from the wall into the flow. Ribs enable increases in heat transfer through encouraging detachment of the boundary layer from the wall, as well as by increasing the overall surface area of the design. This detachment can cause substantial pressure loss relative to microchannels depending on the height of the rib, as it requires the flow to regularly reattach to the wall. In addition to ribs, surface features can also take the form of small dimples or extruded shapes from the surface of the design, which also serve to detach boundary layers and increase effective surface area [23]. Ribs and surface features are of extreme prominence to gas turbine cooling, and are commonly used in internal cooling channels of blades and vanes [3].

The last variety of geometries investigated as part of this dissertation are lattice structures. Lattice structures geometries fall into one of two major categories, those being triply periodic minimal surfaces (TPMS) and strut-based lattices. TPMS lattice are typically defined using a 3D mathematical equation, where strut-based lattices are usually composed of a series of struts that are distributed in a known pattern within a set volume, called a unit cell. Strut based lattice share many similar features with pin fins; however, their complex shapes can induce flow structures that have not been seen with traditional pin fin designs. These complex flow interactions are usually associated with significant enhancements to the design heat transfer and pressure loss. That being said, it should be noted that at the time of writing there is no agreed-upon standard for the appropriate method of scaling the heat transfer and pressure loss of lattice structures. There has been limited public research on the heat transfer and fluid dynamics induced by traditionally manufactured lattice structures [24], however by leveraging AM, several researchers have begun investigating their potential as a new heat transfer technology.

1.2. Laser Powder Bed Fusion

While there are many forms of additive technology, the form of AM this work will focus on is the laser powder bed fusion (L-PBF) process. For the remainder of this document, the term AM is used to refer to the L-PBF process. A diagram of the AM process can be seen in Figure 1-3.

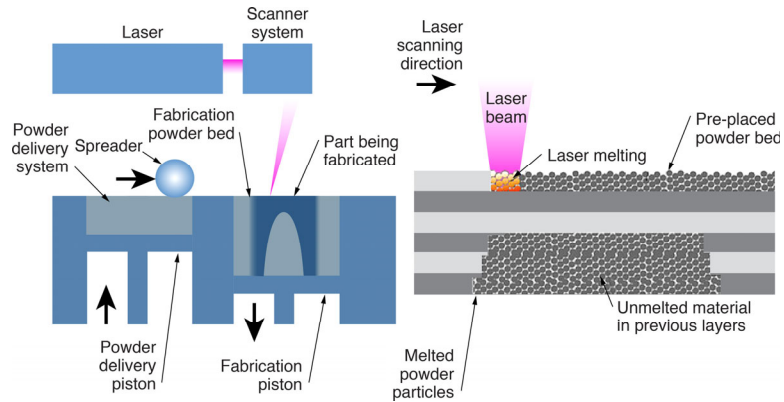


Figure 1-3. A diagram of the additive manufacturing process [25].

The AM process works by first depositing a thin, typically 20 to 80 microns, layer of powder on the surface of a substrate. A high-powered laser is then used to either sinter or melt the powder together as well as fuse it to the substrate. The build plate is then lowered by the height of one layer of powder, and a new layer of powder is deposited on top by a re-coater blade or roller. The process is then repeated several hundred or thousand times over until a full part is realized. This layer-by-layer process enables the construction of complex shapes that would have been difficult to traditionally machine, as well as allows for internal designs that would have required some form of advanced casting in the past.

There are a multitude of different properties that influence the quality and repeatability of an additive part, with a summary of these parameters categorized into key groups is shown in Figure 1-4. The properties of the L-PBF process that are of relevance to the studies discussed in this paper are primarily in the process and material categories. Within the process category this included layer thickness, laser power, hatch distance, and scan speed, which were largely summarized using a volumetric energy density (VED) parameter. It should be noted that while VED is a common parameter used within literature, surface roughness historically has been found to not scale well with volumetric energy density alone, and that typically a greater understanding of the underlying weld physics are required [26]. Within the material category, the parameters of interest, particle shape and the particle size distribution, were kept as similar as possible for all of the used materials. Modification to these parameters can be used to specifically curate differences in surface morphologies [27], though for the vast majority of this body of work the parameters were maintained at the vendor or manufacturer recommended values.

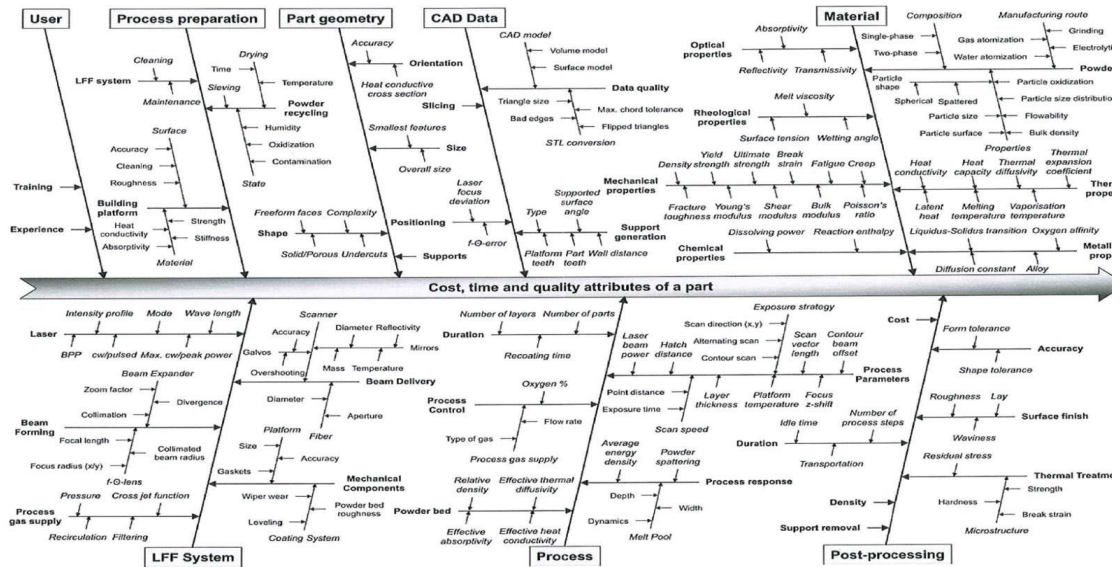


Figure 1-4. Diagram of the L-PBF influence parameters [28].

1.3. Impact of surface roughness on cooling design performance

One of the most significant implications of manufacturing components additionally is the surface roughness. The surface roughness present on parts created through the AM process is quite large with respect to other kinds of manufacturing, with typical reported values ranging from 5 to 50 μm [29]. External surface roughness may be removed through traditional post processing methods, but intricate internal cooling schemes may be impossible to reach using traditional tooling, and abrasive slurry methods may destroy remove smaller heat transfer enhancing features. It is difficult to predict the impact that roughness of this scale and distribution will have on the cooling performance using traditional correlations and CFD modeling tools [30], so experimental testing and validation is necessary to characterize the impact of roughness.

While the general rule of surface roughness increasing heat transfer and pressure drop generally holds true, the amount that it impacts the performance of a given cooling feature varies significantly. This is the result of how the specific cooling feature drives heat transfer and pressure loss. For example, the pressure loss and heat transfer in an internal channel is driven by the velocity and thermal gradients in the boundary layer. AM roughness elements can extend significantly from a channel wall, particularly for microchannels whose diameter can approach the scale of the size of the roughness element, disrupting these boundary layers and causing near wall mixing. This mixing can bring cooler fluid from the center of the channel back near the wall resulting in significant heat transfer enhancement. The drag induced by these elements and their resulting wakes also incurs additional pressure drop. In the case of a pin fin geometry, the majority of the pressure drop and heat transfer is a function of the wakes and mixing resulting from flow detaching from the pins

themselves. While there may be increased pressure loss and heat transfer as a result of the flow interacting with the rough endwall surfaces, the overall performance index is similar to prior investigations as will be shown in Chapter 3. While there are several studies that investigated both wavy channels [31,32] and pin fin arrays [33,34] that featured additive roughness, there is fairly limited work investigating the impact the surface roughness has on surface features, like ribs and turbulators [35,36]. As such a significant portion of the body of this work will explore the impacts of surface roughness on the performance of surface features, and broaden the scale and variety of surface roughness present on additive wavy channel and pin geometries.

1.4. Research Objectives

The first objective of this dissertation is to map out a design space of advanced internal cooling designs featuring additive roughness which can be leveraged for a variety of applications. To map out the design space, a series of parametric design studies were completed, all of which leveraged metal AM to produce cooling features at a micro-scale, ensuring that the scale of internal surface roughness was comparable to what would be found in true components. While several of the types of designs investigated in this analysis have been previously studied, the studies discussed in this dissertation specifically explore how these designs can be modified to understand the potential range of performance. By experimentally capturing the heat transfer and pressure loss of these internal cooling designs, the relative impact that surface roughness has on the performance of advanced cooling structures was identified. It is the author's intention that the design space that was mapped out from these studies can then be used as a starting point for a cooling scheme optimization, which could leverage any host of computational methods to specifically curate a design for a given application. Since beginning the work used to develop this dissertation, a patent leveraging the investigated cooling designs has been published [5] establishing some level of commercial viability.

The second objective of this dissertation is to better understand how the L-PBF machine and material used impacts the surface quality and resulting heat transfer and pressure loss performance. There is limited published literature covering a single design printed on many machines, which obfuscates the implications of printing on one machine over another. Throughout the work of this dissertation, more than 10 different additive builds were completed on a variety of machines and out of a variety of materials, with many of the builds sharing similar designs between them. This selection of metal AM coupons was then used to specifically identify how changes to material and machine impacted the as-printed quality of a design. Variations to the surface roughness topography and accuracy to design intent were then directly related to experimental flow results.

1.5. Outline of Dissertation

This dissertation is composed of seven chapters that are either published peer reviewed research papers, or are currently under review to become a peer reviewed research paper. Chapters 2, 3 and 7 have been accepted into the *ASME Journal of Turbomachinery*, Chapter 4 was accepted into the *International Journal of Heat and Mass Transfer*, and Chapters 5, 6, and 8 have all been submitted to and are under review for *ASME Turbo Expo 2024*. This dissertation is broken into two parts, where Chapters 2-6 discuss the thermohydraulic performance of a variety of internal cooling geometries that were additively manufactured. The second part which is composed of Chapters 7 and 8 explored the impacts of differing materials and machines on the printability and quality of additively manufactured cooling designs.

Chapter 2 covers the thermohydraulic performance of a range of additively manufacturing wavy microchannels, primarily identifying the secondary flows that enhance the performance of wavy channels over their straight counterpart. Chapter 3 explores the performance of additively manufactured pin fin arrays and how additive surface roughness can be directly related to the array heat transfer. These two chapters were first presented at *ASME Turbo Expo 2021* in Rotterdam, Netherlands. Chapter 4 leverages high fidelity large eddy simulations (LES) to identify the performance of two differing internal lattice structures, diving into both the time-averaged and unsteady flow structures that lead to enhanced heat transfer and pressure loss. Chapter 4 was accepted into the *International Journal of Heat and Mass Transfer* in October 2023, and will be published in January 2024. Chapter 5 is comprised of a parametric evaluation of broken wavy surface ribs, which leveraged both computational and experimental methods. Covered in Chapter 5 is also the impact of scale on the performance of additive surface features, and identifies experimentally how decreasing the relative surface roughness from the coupon designs impacted bulk flow characteristics. Chapter 6 was a similar parametric investigation into the performance of diamond turbulator features, using computational methods to understand the underlying flow structures which resulted in experimentally measured heat transfer and pressure loss results. Also covered in chapter six are the impact of surface fillets intrinsic to both cast and AM on the bulk heat transfer and pressure loss performance. Both Chapters 5 and 6 have been submitted to *ASME Turbo Expo 2024* and are currently under peer review. Chapter 7 investigates how printing a variety of internal cooling designs, including both wavy channels and pin fin arrays, out of different materials and on different printers impacted the surface quality and resulting flow performance. Chapter 7 was presented in Boston, MA, USA, at *ASME Turbo Expo 2022*. Chapter 8 builds off of the work presented in Chapter 7, expanding the test matrix to include more materials and machines,

specifically looking to delineate the impacts from the additive machine from the material used. Chapter 8 has been submitted to *ASME Turbo Expo 2024*, and is currently under review.

Chapter 9, which is the last chapter in this dissertation, summarizes the key finding from all of the studies which comprise this dissertation. Comparisons between the performance of the internal cooling schemes are discussed, as well as recommended future work needed to be able to leverage additive manufacturing for internal cooling schemes.

2. AMPLITUDE AND WAVELENGTH EFFECTS FOR WAVY CHANNELS²

2.1. Abstract

To improve the efficiency and durability of gas turbine components, advancements are needed in cooling technologies. To accomplish this task, some manufacturers are turning to additive manufacturing (AM), as it offers the ability to both rapidly iterate on component design, as well as incorporate unique internal cooling structures directly into parts. As one example, wavy microchannels can be readily integrated into turbine components. This study investigates wavy channels of varying channel amplitude and wavelength through experimental measurements of heat transfer and pressure loss. In addition to experimental testing, CFD predictions were made to identify internal flow features that impacted performance.

Five channel geometries were integrated into test coupons that were additively manufactured out of Hastelloy-X using direct metal laser sintering. True coupon geometric characteristics and wall roughness values were captured non-destructively using computed tomography (CT) scans. Geometric analyses indicated that coupons were reproduced accurately with minimal deviation from design intent. Experimental results indicated that decreasing the channel wavelength and increasing the channel amplitude resulted in substantial increases in both bulk friction factor and Nusselt number with respect to the nominal case and were scaled using a relative waviness parameter. CFD simulations predicted significant mixing of flow in the cases with the smallest wavelength and greatest amplitude.

2.2. Introduction

The efficiency of gas turbine engines is important for many reasons, especially given the impacts on the economy and environment. Airlines use approximately 20% of all revenue on fuel alone (depending upon the market) [37] and the burning of CO₂ producing fossil fuels is directly related to the increasing rate of climate change. To address these issues, it is common practice to improve the engine efficiency by raising the operating temperature of the turbine. This process requires increasingly innovative methods to cool both rotating and static turbine components while minimizing the use of cooling air. Traditionally, many types of cooling technologies, such as

² Corbett, T. M., Thole, K. A., and Bollapragada, S., 2022, “Amplitude and Wavelength Effects for Wavy Channels,” *J Turbomach*, **145**(3), pp. 031011.

microchannels, pin fins, ribs, and more have been integrated into turbine components, and each have been explored at length [3].

One such internal cooling technology, wavy channels, is of particular interest. It is possible for wavy channels to be integrated into many static turbine parts, such as the blade outer air seal or shrouds, in combustor liners, or in turbine airfoils as a potential concept in considering double-wall cooling designs that are often used. Turbine manufacturers have already demonstrated the use of this concept in actual turbine components [38]. Wavy microchannels have been explored for several decades in many low Reynolds number studies; however, their implementation and use in conjunction with additive manufacturing (AM) have only recently begun to be studied for turbine applications.

To facilitate these developments and construct complex parts, some manufacturers are turning to additive manufacturing. AM offers many benefits over traditional methods, such as increased part complexity without significant increase in cost, the ability to imbed novel internal features that would have been otherwise impossible, and the capacity to quickly iterate on designs. One of the primary AM methods of pertinence for gas turbines is direct metal laser sintering (DMLS) due to its ability to produce fine details and growing material selection. While there are elements of AM design that are unique to the process and require further consideration, such as build angle and process parameters, understanding and taking advantage of these barriers can make AM a highly effective tool for developing components with advanced cooling schemes.

This study expands on prior wavy channels studies by investigating how the amplitude and wavelength independently impact the pressure loss and heat transfer of AM wavy microchannels. To characterize these effects, five AM test coupons were printed using DMLS and then tested to capture their heat transfer and pressure loss performance. These results were explored further through CFD analysis which identified the internal flow features that facilitate or hamper performance.

2.3. Literature Review

Wavy channels are beneficial to cooling performance due to their ability to generate unique flow structures not present in straight channels. Many early investigations explored wavy channels through two-dimensional computational modeling of laminar flow [39–43]. These groups identified that the flow along the wall, even while in the low Reynolds number regime, would detach and develop a vortex in the cavity between waves. Nishimura et al. [42] investigated this phenomenon in a converging-diverging wavy channel and found that the size of the recirculation zones were a function of Reynolds number. These zones increase in size with increases in Reynolds number for laminar flows, but after the flow transitions to turbulence these recirculation zones

reduce in size to a limiting value with continued increases in Reynolds number. Snyder et al. [44] expanded on these findings, identifying that this detachment and recirculation resulted in local heat transfer augmentations with levels being periodic along a wavelength. The location of highest heat transfer enhancements coincided with the lowest wall shear stress, which occurred just downstream of the flow detachment.

As studies of these channels grew more sophisticated, three-dimensional computational domains were used more often to understand the unique flow features. Comini et al. [45] explored how the aspect ratio of a wavy channel impacted performance, finding that in the laminar regime Dean vortices developed whose magnitude was a function of channel aspect ratio. These Dean vortices enhanced local heat transfer by moving fluid from the wall into the channel center. These findings were later validated by Sui et al. [20], who conducted a study with channels of varying relative waviness, and showed the development of Dean vortices. Siu et al. also noted that this enhancement was accomplished with minimal increases to pressure drop, making wavy channels a potential cooling technology.

Recent studies have continued to investigate geometric variations of wavy channels [46] still focusing on the performance in the laminar regime. Several studies were conducted by Harikrishnan et al. [47,48] investigating the performance of 3D wavy channels who found secondary flows enhanced heat transfer in the valleys of a wave, but the greatest heat transfer occurred at the crest of a wave due to re-attachment. Lin et al. [49] found that by modulating the amplitude and wavelength of a wavy channel along the flow length, it was possible to increase the magnitude of the Dean vortices and improve heat transfer. Further investigations of amplitude and wavelength were completed by Zhou et al. [50], who showed how channels with high amplitudes or low wavelengths induced strong vortices in the pits of the wave, enhancing heat transfer at a high pressure cost.

Additive manufacturing (AM) offers the ability to integrate novel cooling designs, such as wavy channels, into gas turbine components easier than ever before, as shown by Wimmer et al. [6]. Integration, however, presents new complications that are not present in traditional manufacturing. An initial study from Kirsch and Thole [31] investigated both the feasibility of constructing AM wavy microchannels, as well as heat transfer and pressure loss performance. Much like previous AM microchannel studies [51,52], they found that the channel surfaces had a high roughness relative to their hydraulic diameter and, due to their size, were difficult to post process. Convective heat transfer was enhanced significantly by the roughness especially at high Reynolds numbers.

Previous studies highlighted the impact that additive roughness has on the performance of wavy microchannels, and the unique flow features that develop as a function of channel geometry, but questions still remain. This study aims to address one such question by methodically investigating how the amplitude and wavelength of AM wavy microchannels impacts performance over a range of Reynolds numbers.

2.4. Description of Test Coupons

Five flat test coupons were additively manufactured for this study, as shown in Figure 2-1, that were similar in construction to test coupons used in prior studies by one of the co-authors [53]. The specific dimensions and characteristics of each the coupons can be seen in Table 2-1. Each coupon was designed to be 50.8 mm long, 25.4 mm wide, and have a total thickness of 3.05 mm. Channel lengths were defined along the centerline of the channel and were over 40 hydraulic diameters long to minimize entrance effects, and varied in total length due to changes in the channel amplitude or wavelength. Between seven and nine wavy channels were packaged into each coupon depending upon the geometry. Each channel had an aspect ratio of 1:2 with a height of 1.91 mm. These dimensions resulted in a channel hydraulic diameter of 1.27 mm.

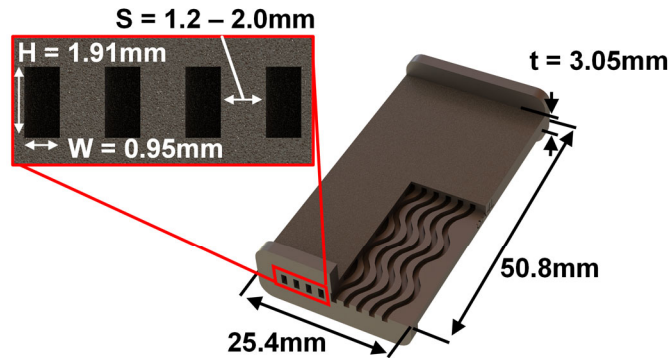


Figure 2-1. Dimensioned test coupon used to determine the friction factor and bulk Nusselt number of the wavy channels with internal geometry exposed.

Table 2-1. Coupon Geometric Characteristics

Coupon Name	Amplitude (mm)	Wavelength (mm)	Measured Dh (mm)	Channel Length (mm)	Number of Channels	Design Surface Area (m ²)	Measured Surface Area (m ²)	Ra (μm)	Ra/Dh
0.5A	1.0	10.2	1.20	52.1	8	0.00238	0.00240	14.3	0.0120
0.5λ	2.0	5.1	1.21	69.9	7	0.00280	0.00272	20.7	0.0171
0.5λ-Mod	2.0	5.1	1.21	34.7	7	0.00139	0.00135	20.7	0.0171
Nominal	2.0	10.2	1.23	56.8	9	0.00292	0.00287	15.9	0.0130
1.5λ	2.0	15.2	1.27	53.2	8	0.00243	0.00230	16.2	0.0128
1.5A	3.0	10.2	1.21	62.2	8	0.00284	0.00276	15.4	0.0127

A nominal wavy channel was defined with a given amplitude and wavelength, with the cross section of the channel being kept constant along the flow direction as shown by the blue line in Figure 2-2. In addition to this nominal case, four more designs were developed by varying the amplitude or wavelength of the channel resulting in the test matrix seen in Figure 2-2. The colors illustrating these designs are consistent throughout the entirety of the paper when reporting the data in later sections.

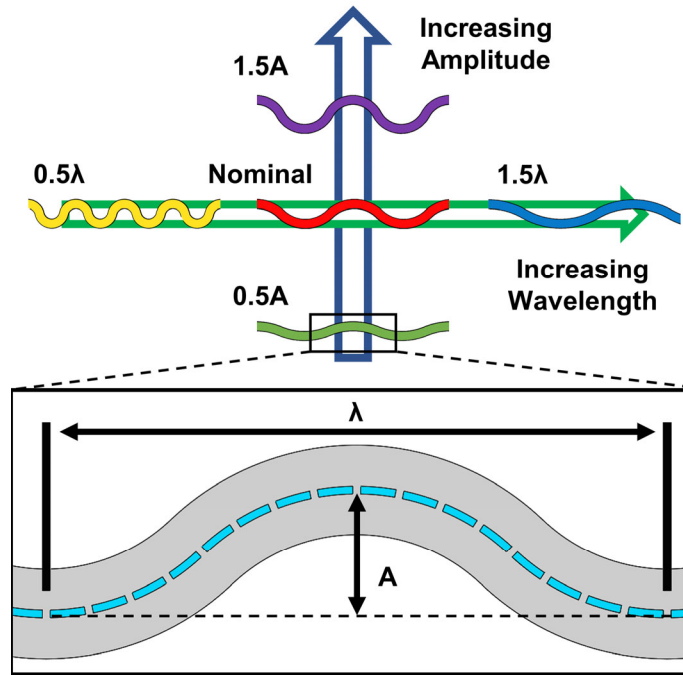


Figure 2-2. Test matrix description and amplitude and wavelength definitions for wavy channels.

The five coupons were manufactured using direct metal laser sintering (DMLS) using an EOS M280 printer. The coupons were manufactured out of Hastelloy X, using the process parameters recommended by the manufacturer. This material was selected based on its prevalence to gas turbine components so as to accurately capture inherent roughness effects.

The coupons were manufactured in a vertical orientation, where the build direction was along the length of the coupon. Supports were used for the top flange and to anchor the parts to the build plate. Following the build, the parts were cleared of powder, heat treated to relieve thermal stresses, and machined by EDM to remove supports and extract the parts from the build plate. Computed tomography (CT) scans showed the powder was removed from the channels.

During coupon testing, it was discovered that for the shortest wavelength coupon (0.5λ), the heat transfer was so high that the flow temperature thermally saturated resulting in high uncertainties. To avoid saturation, the test coupon was shortened for the 0.5λ wavelength coupon. Comparisons of pressure loss data taken with both the shorter and longer coupon for this geometry

compared well. The shorter coupon is shown in Table 2-1 as 0.5 λ -Mod, and was used for all heat transfer tests.

2.5. Channel Characterization

To accurately capture the geometric characteristics inside the channels non-destructively, as well as to quantify the roughness on the interior coupon surfaces, each of the coupons underwent CT scans. The scans were completed using a voxel size of 35 microns, which was then further resolved using a commercial software, enabling the determination of the surface of the coupon to one tenth the voxel size, or 3.5 microns [54].

Arithmetic mean roughness (R_a) measurements were calculated using a method similar to that described by Stimpson et al. [51], wherein the roughness is representative of the average deviation of a surface from a reference. The values from several measurements were combined using a surface-area-average for each coupon, and is reported in Table 2-1.

The roughness for the internal channel surfaces ranged between $14 < R_a < 21$ microns, which matched similar levels of surface roughness for a vertical build orientation as seen by Wildgoose et al. [53]. Notably, the shortest wavelength coupon had the highest measured R_a , which was likely a result of the increased number of downskin surfaces.

To capture the hydraulic diameter (D_h) of each of the channels, the coupon surfaces were exported from the CT software and analyzed using an in-house code. This code sectioned the channels into over 900 slices along their flow direction from which an average channel perimeter and cross-sectional area for each slice was calculated. These values were then averaged over all slices for a given coupon to find the average hydraulic diameter for the coupon, which is reported in Table 2-1. The measured hydraulic diameter was consistently close to the design with a maximum deviation of 5%.

2.6. Experimental Methods

A test rig was constructed to experimentally evaluate the performance of the coupons over a range of Reynolds numbers. The test rig used was similar in construction to that used by Stimpson et al. [51] as illustrated in Figure 2-3.

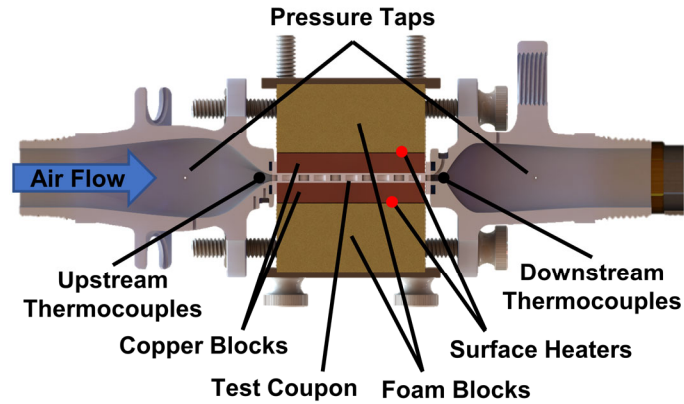


Figure 2-3. Cross section of test rig used to evaluate coupon heat transfer and friction factor performance.

Each coupon was installed between two plenums to ensure that the flow entering and leaving the coupon was uniform. Air entering the test section was metered using a mass flow controller located upstream and pressure in the test section was regulated through a needle valve located downstream allowing for independent control of the Reynolds number and Mach number. Each plenum was fitted with a pressure tap to capture the pressure drop across the coupon using a differential pressure transducer with swappable diaphragms to capture different pressure ranges. An additional gauge pressure sensor was fitted to the upstream pressure tap to capture the operating pressure.

For the heat transfer tests, a heating assembly was placed on both sides of the test coupons. Each assembly consisted of a custom-built heater installed between a foam block and a copper block. Each heater was connected to its own power supply, allowing for independent control of the heat applied to each side of the coupon. The copper blocks interfaced with the test coupon, with a thin layer of thermal paste applied between the two components to minimize conductive resistance. The heat lost to components surrounding the coupon was determined by calculating 1D losses from thermocouple measurements in the foam blocks and plenums. These losses were typically at or less than 1% of the total heat input into the system for all heat transfer tests. The copper blocks were fitted with several precisely placed thermocouples to determine the surface temperature of the coupon using a 1D conduction analysis as described by Simpson et al. [51]. The thermal conductivity of the Hastelloy-X test coupons was measured to be 10.0 W/m-K.

The temperature of the air upstream and downstream of the coupon was captured with additional thermocouples placed into the flow just upstream and downstream of the test coupon. The system was required to reach steady state while testing, which was determined by monitoring a time resolved plot of temperatures. An iterative calculation assuming 1D isentropic flow was used to accurately determine the temperature, pressure, velocity, and density of the air at the inlet and

exit of the test coupon. The coupon surfaces were assumed to be isothermal based on calculated high fin efficiencies. The bulk convective coefficient and Nusselt number were calculated using the coupon surface temperature, as seen in Equation 2-1.

$$h = \frac{Q_{in} - \sum Q_{loss}}{A_s \cdot \Delta T_{lm}} \quad (2 - 1)$$

To ensure all the energy in the system was captured an energy balance was conducted by comparing the total heat input minus losses to that measured using a first law analysis. The energy balance for low Reynolds number tests were within 5% with some of the tests at high Reynolds numbers having a balance within 8%.

As an additional measure, the test procedures and facility were benchmarked against known correlations using a smooth-walled coupon featuring straight circular channels. Friction factor measurements during benchmarking were compared to the Colebrook correlation in the fully turbulent regime seen as Equation 2-2 [55].

$$\frac{1}{\sqrt{f}} = -2 \log_{10} \left(\frac{k_s}{3.7D_h} + \frac{2.51}{Re \sqrt{f}} \right) \quad (2 - 2)$$

Note that it was expected that the benchmarking machined coupon's surface roughness, k_s , was zero. By iteratively solving the Colebrook equation with this assumption, the friction factor for a smooth channel was then defined as f_0 , which was used for the augmentation factors.

Heat transfer measurements were similarly taken using the same benchmarking coupon and compared against the Gnielinski correlation, which is shown in Equation 2-3 [56].

$$Nu = \frac{\frac{f}{8} (Re - 1000) Pr}{1 + 12.7 \sqrt{\frac{f}{8}} \left(Pr^{\frac{2}{3}} - 1 \right)} \quad (2 - 3)$$

The smooth channel Nusselt number, Nu_0 , was then found by solving the Gnielinski correlation with f_0 over a range of Reynolds numbers, which was also used for the augmentation.

2.7. Measurement Uncertainty

Measurement uncertainty was determined using the methods as described by Dunn [57]. Friction factor measurements were found to have a high uncertainty in the low Reynolds regime, at just over 20% of measured value with the main contributors being the differential pressure measurement and the mass flow rate. After a Reynolds number of 5,000 all measurements were within a 5% uncertainty. During testing, several friction factor data points were collected multiple

times for each coupon using different differential pressure sensor diaphragms and identified that pressure drop results were repeatable to within 3% of the full-scale value.

Nusselt number uncertainty was similarly calculated, and it was found the relative uncertainty of Nusselt number was less than 8% with the main contributors being thermocouple measurements at the exit of the test coupon and the temperature measured in the copper blocks. Additional heat transfer measurements were made to evaluate repeatability, and found the measured Nusselt number was repeatable within 2%.

2.8. Computational Methods

A computational fluid dynamics (CFD) simulation was conducted for each of the five channel geometries previously discussed. The objective of this analysis was to identify any driving flow features that impacted the heat transfer and friction factor performance of the channels within the study. The CFD domain shown in Figure 2-4 was modeled for these comparisons. It was assumed that the coupon wall temperature was constant due to a high fin efficiency. A symmetric boundary condition was applied to the top wall and the channel lengths were increased by a factor of 2.5 to better understand the thermal saturation. Modeling AM roughness computationally has been shown previously to be difficult [30]. As such, the channel walls were assumed to be smooth, as the CFD was intended to provide a relative comparison rather than be fully representative of the as-built channel performance.

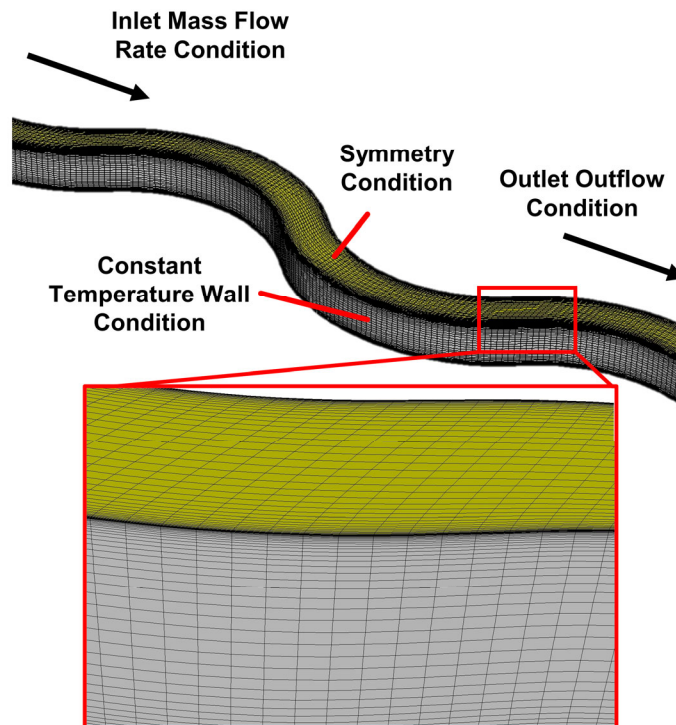


Figure 2-4. Example of domain used in computational study.

A mass flow inlet was imposed on the entrance of each of the channels, with a flow rate set to achieve a Reynolds number of approximately 10,000. An outflow boundary condition was imposed at the channel exit. For the CFD simulations, the inlet velocity profile was considered uniform given the plenum used in the experiment accelerated the flow and flattened the profile.

The density of the air was assumed to be constant based on a testing relevant pressure and temperature. The simulations were solved by approximating the solution to the Reynolds Averaged Navier-Stokes (RANS) equations using a commercial CFD solver [58]. The pressure-density coupling scheme was SIMPLE, and all spatial equations were resolved to 2nd order. Turbulence was modeled using the realizable k- ϵ model, and heat transfer at the wall was modeled using enhanced wall treatment. Prior studies by one of the co-authors [31,32] have shown that while secondary flows may be moderately underpredicted using the realizable k- ϵ model, the relative performance between channels is captured.

The grids used to model the channels were created using a commercial grid generation software [59]. Structured grids were generated with a value of $y^+ \sim 1$ in the near wall regions. The grid size between the computational cases varied, but the total number of cells for each case was near 3.5 million elements. A mesh-sensitivity study was conducted using increasing mesh sizes from 1.5 million to well over 8 million elements. Increasing the cell count from 3.5 million to 8 million yielded a change in friction factor and Nusselt number results of less than 1%.

The simulation was considered converged when the outlet temperature remained constant over 200 iterations and all normalized residuals were below 10^{-6} .

2.9. Effect of Channel Wavelength

The measured pressure losses in terms of friction factors for coupons of varying wavelengths at a constant amplitude are seen in Figure 2-5. Also shown in Figure 2-5 is the data from a coupon used for benchmarking the test rig and data for a straight AM channel with a similar hydraulic diameter and relative roughness ($D_h = 1.25\text{mm}$ and $Ra = 12$ microns) [53]. These results indicate that all wavy channels have a much higher friction factor than both the smooth and additively manufactured straight channels. The results also indicate that decreased wavelength results in substantially increased friction factors. As the wavelength decreases, the increased friction factor is caused by increased flow detachment and reattachment as the flow passes over increasingly steep convex walls. The data in Figure 2-5 also indicates that the friction factor for the wavy channels becomes independent of Reynolds number as early as $Re \sim 2,000$, as compared with $Re \sim 10,000$ for the rough straight channels. This independence is typically associated with highly turbulent flows indicating impacts of roughness and turbulence.

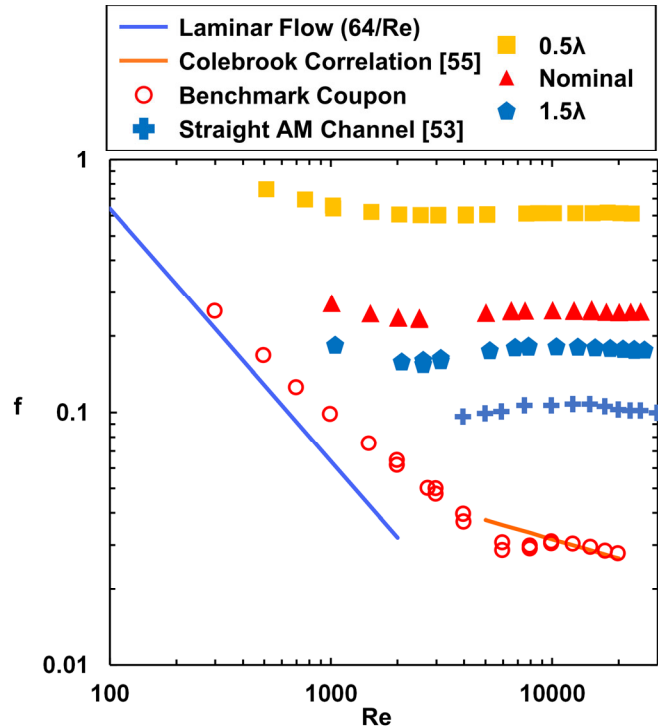


Figure 2-5. Friction factor testing results for channels of varying wavelength and constant amplitude as a function of channel Reynolds number.

To understand the impact that the channel geometry has on performance, the predicted local friction factor and Nusselt number were calculated from the simulations as shown in Figure 2-6. Note that these results are presented as augmentations from the nominal case, whereby f_n and Nu_n are the average of the values predicted for the nominal case after 10 wavelengths for the computational results and the experimental value of the nominal case for the experimental results. Using this normalization, the nominal case in Figure 6 oscillates about unity as would be expected. The x-axis in Figure 2-6 is the global x-coordinate, \bar{X} , normalized by the channel wavelength, λ . Using this coordinate system aligns the wave of each channel making it possible to compare performance along a wavelength.

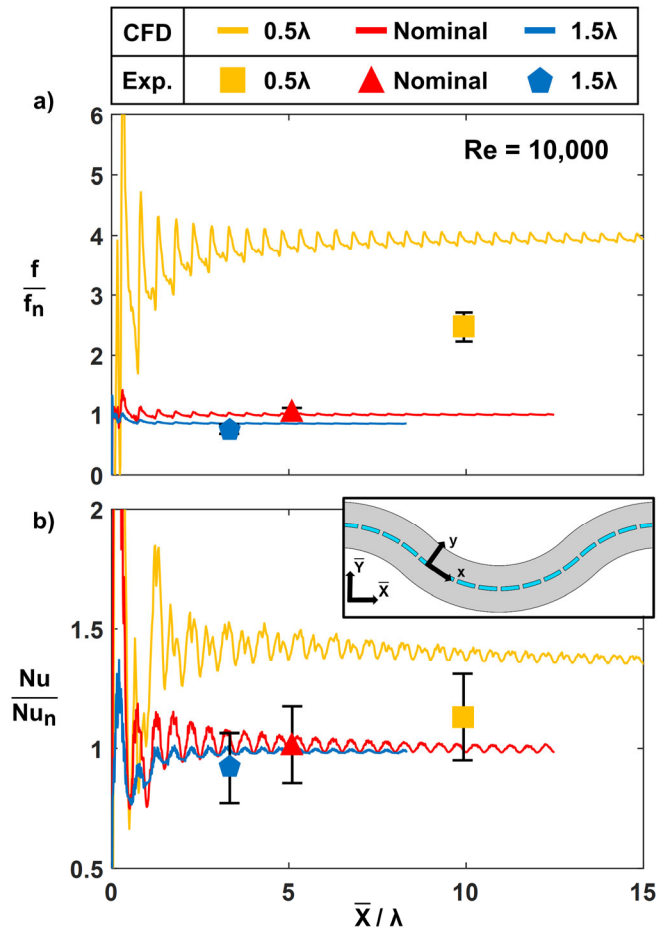


Figure 2-6. (a) Friction factor augmentation and (b) Nusselt number augmentations as compared to the nominal case for channels of varying wavelength and constant amplitude.

In Figure 2-6(a), there is a periodic nature to the friction factor results due to the channel wave. The peaks were co-located near the flow attachment, whereas the valleys are co-located near the flow detachment. The peaks are most pronounced for the low wavelength case (0.5λ), given that the channel requires the most aggressive changes to flow direction. The periodic behavior occurs through the developing region of the flow with the oscillations damping to nearly constant peak and valley values after approximately $L/D_h \sim 30$ (or 7.5λ) for the low wavelength case (0.5λ). In the highest wavelength case (1.5λ), the oscillations dampen after only $L/D_h \sim 20$ (1.25λ). While Figure 2-6(a) illustrates that the CFD significantly overpredicted the relative increase in friction factor for the low wavelength case (0.5λ), the predictions for both the nominal and 1.5λ cases are relatively good. It is likely that this disagreement between the computational and experimental data is due to the realizable $k-\epsilon$ model inaccurately capturing the near-wall behavior as was seen in the shortest wavelength case. However, the same trends were found between measured and predicted data.

Experimentally obtained heat transfer data from coupons of varying wavelength at a constant amplitude is shown in Figure 2-7. Also shown is the benchmark data for smooth channels and heat transfer measurements for the same straight AM channel presented in Figure 2-5. A similar trend was seen to that of the friction factor results, where the decreased wavelength resulted in increased Nusselt numbers. Particularly, the Nusselt number for the nominal and increased wavelength (1.5λ) were nearly the same at high Reynolds number. Also shown in Figure 2-7 is the notable increase in heat transfer over the straight AM channel, demonstrating how even moderately wavy channels can induce significantly increased heat transfer.

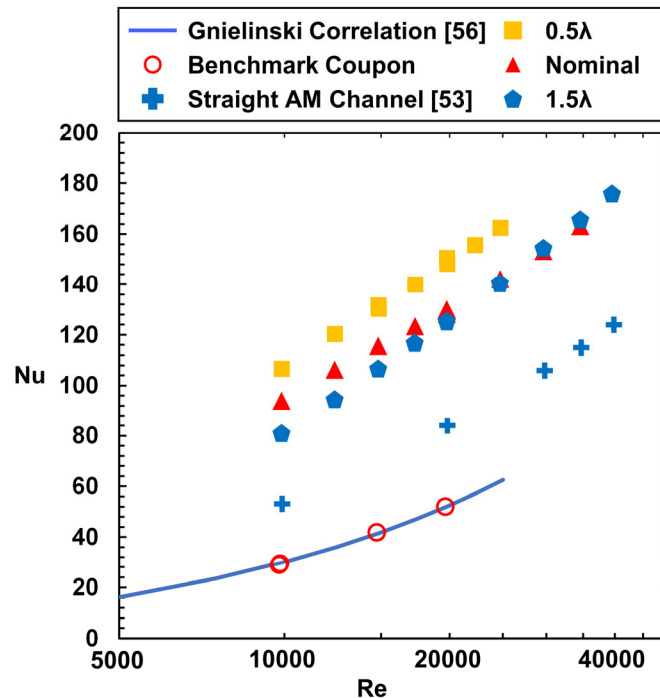


Figure 2-7. Nusselt number as a function of Reynolds number for coupons of varying wavelength and constant amplitude in the turbulent regime.

Evaluating the local Nusselt number in Figure 2-6(b) reveals a similar oscillatory structure in the heat transfer, as was seen with the friction factor, where the detachment and reattachment of the fluid on the crests of a wave resulted in high heat transfer regions. The peak and valley behavior of heat transfer occurs because the heated flow along the wall mixes into the cooler channel flow towards the center as it detaches from the wave with cooler fluid replacing it from the central flow region upon reattachment. Similar to the friction factor data, the CFD overpredicted the heat transfer for the low wavelength (0.5λ) channel, but gave reasonable predictions for the others.

The predicted thermal profiles across the entire channel can be seen in Figure 2-8 (a-e), with Figures 2-8(b), 2-8(c), and 2-8(d) representing the low (0.5λ), nominal, and high (1.5λ) wavelength cases for the same amplitude. The predictions show decreasing the wavelength of the

channel results in higher heat transfer to the working fluid, which is consistent with the experimental Nusselt number data. These results show that the shortest wavelength coupon, Figure 2-8(b), becomes thermally saturated at the full coupon length, also matching experimental results. The predicted heat transfer trends between channels also matches the results shown in Figure 2-7, in that the nominal and high wavelength cases, shown as figures 2-8(c) and 2-8(d) respectively, had very similar thermal pickup.

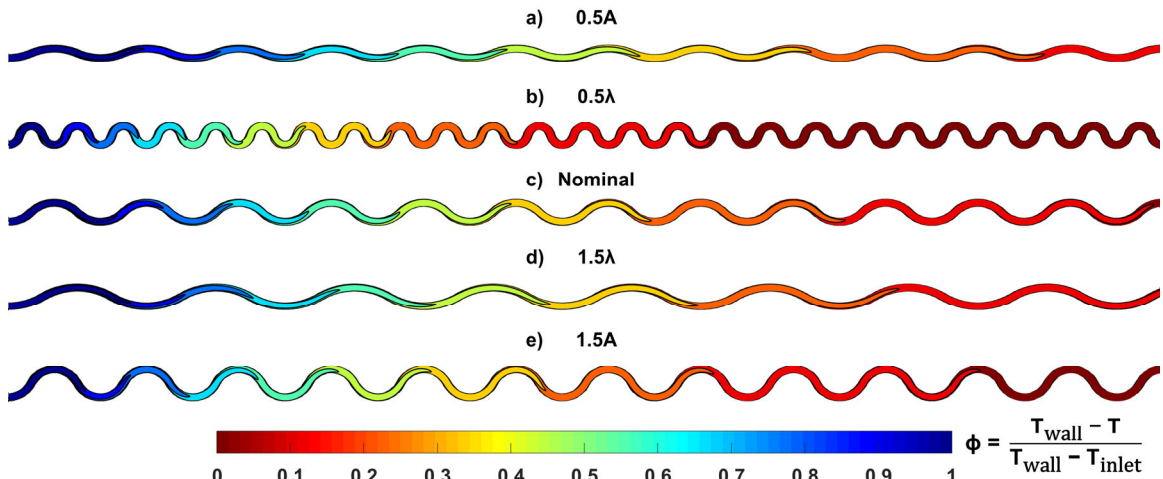


Figure 2-8. (a-e) Thermal contours for the tested channels normalized by the inlet and wall temperatures.

To further investigate this periodic structure, the velocity fields predicted by the CFD were captured at three different planar locations for each of the five wavelengths as presented in Figures 2-9(a-o). The concave and convex sides of the channel are annotated for the first channel in a row, but are true for the remaining channels in the row. The low (0.5λ), nominal, and high (1.5λ) wavelength cases are presented in Figures 2-9(d-f), 2-9(g-i), and 2-9(j-l) for the same amplitude. The velocity contours show that the distribution of the flow shifts towards the convex side of the channel as wavelength decreases. This change in the flow distribution results from the pressure gradients that form along the steep convex walls of the channel similar to large ribs.

Figures 2-9(d), 2-9(g), and 2-9(j) show distribution of secondary flows at the first planar location for the three channels in the order of increasing wavelength. The secondary velocities indicate the magnitude increases with decreasing wavelength. The secondary flow structures change as a function of wavelength as shown in Figures 2-9(g) and 2-9(j), which indicate the development of two pairs of Dean vortices along the concave wall and in the corners of the convex wall of the wave. One pair of the Dean vortices are not present in the low wavelength case (0.5λ) as shown in Figure 2-9(d). For the low wavelength case in Figure 2-9(d) the secondary flows develop into two large cells that occupy the top and bottom of the channel. In the second planar location mid-way between the peak and valley, Figures 2-9(e), 2-9(h), and 2-9(k), indicate that

there are almost no vortices as the flow shifts from one curved wall to the other. The planar location at the valley of the curve, shown as Figures 2-9(f), 2-9(i), and 2-9(l) for the low (0.5λ), nominal, and high (1.5λ) wavelength cases also indicates that the flow is completely mirrored between the first and last planar locations. The secondary flows exhibited in the channels of varying wavelength, Figures 2-9(d-l), improved heat transfer in the channels computationally; however, it is expected that the surface roughness will have a more significant impact on the heat transfer of the channel, as seen by prior researchers [31].

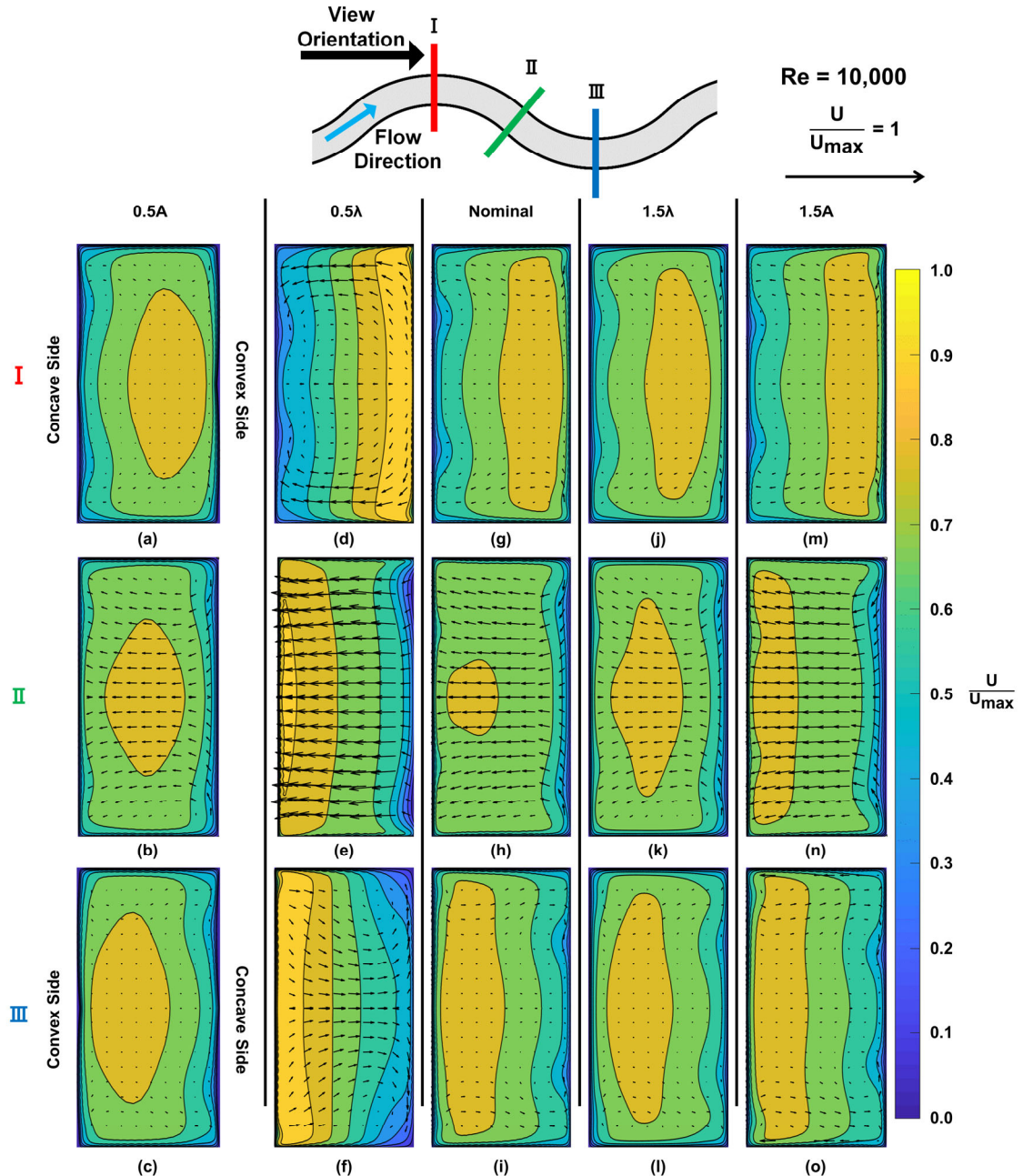


Figure 2-9. Normalized maximum velocity and secondary flows at three planar locations along a given wavelength for the reduced amplitude (a-c), reduced wavelength (e-f), nominal (g-i), increased wavelength (j-l), and increased amplitude (m-o) cases.

2.10. Effect of Channel Amplitude

The friction factor results from coupons of varying amplitude at a constant wavelength can be seen in Figure 2-10. The influence of amplitude was found to be the inverse of wavelength with higher amplitudes resulting in increased friction factors. Given that increased pressure loss is largely a function of the flow detaching and attaching from the inside walls of the channels, it is expected that increasing amplitudes resulted in higher friction factors. Similar to Figure 2-5 for

different wavelengths, Figure 2-10 also indicates that the friction factor of the wavy channels becomes independent of Reynolds number at low values ($Re \sim 4,000$) relative to that of the smooth coupon.

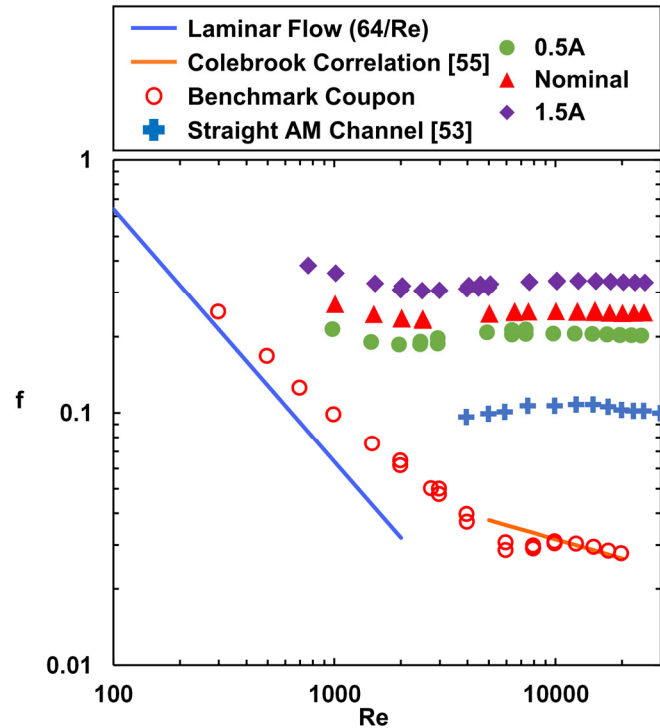


Figure 2-10. Friction factor as a function of Reynolds number for channels of varying amplitude and constant wavelength.

Predictions of the development of the local friction factor and Nusselt number augmentation relative to the nominal case along the channel length are shown in Figure 2-11. Two conclusions can be drawn from Figure 2-11(a): the amplitude of the oscillations present in the friction factor results is dependent on the wave amplitude; and the CFD predictions were correct in trend but slightly off in comparing the average bulk values. Increasing channel amplitude results in increases to the amplitude of the periodic behavior in friction factor, as well as streamwise length required for the periodic behavior to reduce to the fully developed value. These results for the changing amplitude differ from the modifications to wavelengths over which we studied, where changes in friction factor from the nominal case was found to be significantly higher when wavelength was changed.

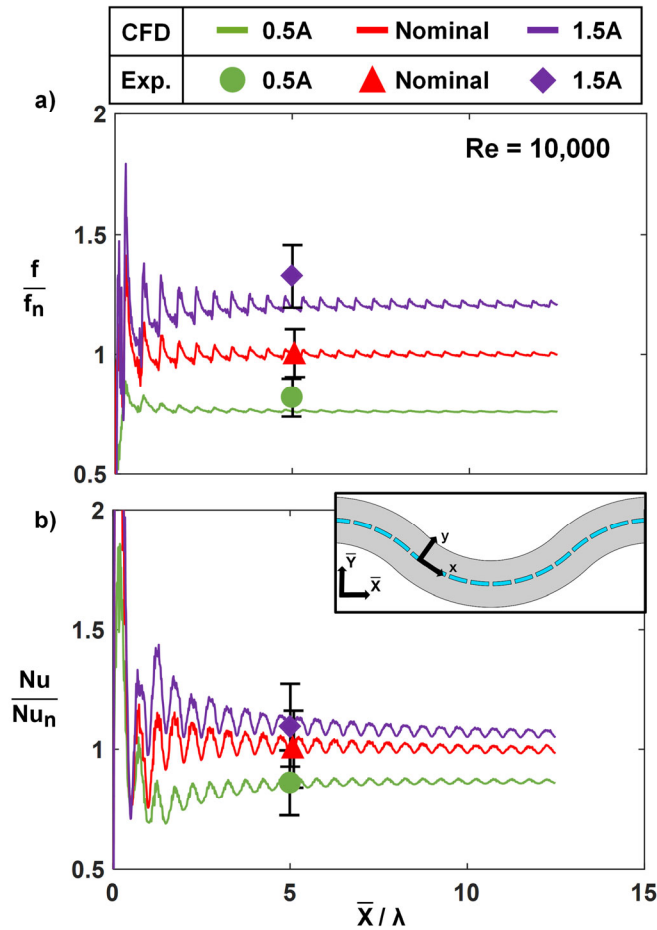


Figure 2-11. (a) Friction factor and (b) Nusselt number augmentations from the nominal case for channels of varying amplitude and constant wavelength.

Figure 2-11(b) shows the local development of Nusselt number, where it can be seen the CFD predictions were close to the measured average heat transfer. Similar to the friction factor predictions, the amplitude of the oscillations in heat transfer are smaller for the decreased amplitude case (0.5A) as compared to the increased amplitude case (1.5A). Based on the predictions, the influence of the wave amplitude on the oscillations is lower than that of the wavelength for the ranges studied.

The experimentally obtained Nusselt number for the coupons of varying amplitude over the entire Reynolds number range are shown in Figure 2-12. The highest amplitude channel (1.5A) achieved the highest Nusselt numbers throughout the test range. The heat transfer performance of the channels approached similar values at the highest Reynolds number tested for the highest amplitude case (0.5A) and the nominal case. These results align well with the assumption that the increased protrusion of the convex walls into the main channel flow results in increased flow mixing and subsequent heat transfer, as seen in the channels of varying wavelength. The impact of

this change can be seen in Figures 2-8(a), 2-8(c), and 2-8(e), where the thermal contours for the decreased (0.5A), nominal, and increased (1.5A) amplitude cases can be seen. Opposite to the channels of varying wavelength, there is a clear trend of increased fluid temperatures as the channel amplitude increases, matching experiments.

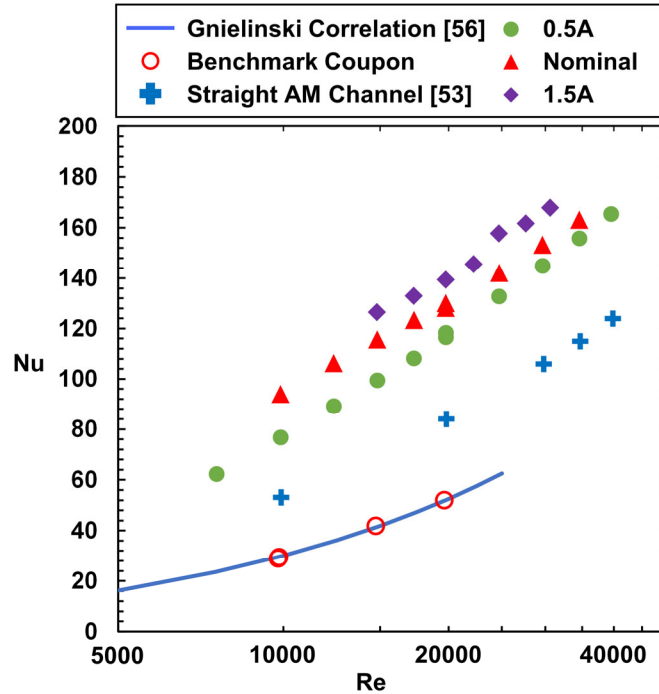


Figure 2-12. Nusselt number for channels of varying amplitude and constant wavelength as a function of channel Reynolds number.

The velocity contours presented in Figure 2-9 with the channels of varying amplitude are displayed in Figures 2-9(a-c), 2-9(g-i), and 2-9(m-o). Similar to changing wavelength, the peak velocities shift between the convex walls as the fluid passes through the channel, which is also apparent for the smallest amplitude case (0.5A) represented in Figure 9(a-c). This shift becomes more pronounced with increasing amplitude, shown in Figure 2-9(m-o), where the flow is largely hugging the convex channel wall regardless of streamwise location resulting from the cross-channel pressure gradient. There is a less pronounced impact on the development of the secondary flows as compared to changing wavelength over the ranges studied with very similar formations of Dean vortices for all the amplitudes as shown by Figures 2-9(a), 2-9(g) and 2-9(m). Similar to decreasing wavelength, increasing channel amplitude increased the magnitude of the secondary flows, as seen in Figures 2-9(c), 2-9(i), and 2-9(o).

2.11. Overall Channel Performance

To scale the relative performance of all the wavy channels, a parameter previously recommended by Sui et al. [20] was evaluated. Sui et al. suggested the use of a *relative waviness*

parameter, defined as the channel amplitude divided by the channel wavelength. Figures 2-13(a) and 2-13(b) show the performance augmentation with respect to a smooth coupon for both friction factor and Nusselt number augmentations as function of relative waviness for three Reynolds numbers. The dashed lines in both Figures 2-13(a) and 2-13(b) are intended to represent the general performance trend and is not representative of any correlation. Straight AM channel data is also plotted in Figure 2-13(a) and 2-13(b) ($A/\lambda = 0$) for reference. At a Reynolds number of $Re = 30,000$ the friction factor augmentation shows a strong functional increase as A/λ increases, which results from the increased obstruction of the convex wall into the flow path resulting in increasing pressure losses. These trends in friction factor are the same as Reynolds number is decreased, though the magnitude of the friction factor augmentation decreases.

Re	0.5A	0.5λ	Nominal	1.5λ	1.5A	Straight Channel [53]	Trendline
10k	○	□	△	◇		+	- · - · -
20k	●	■	▲	◆	◇	+	- - - - -
30k	⊕		▲	◆	◇	+	· · · · ·

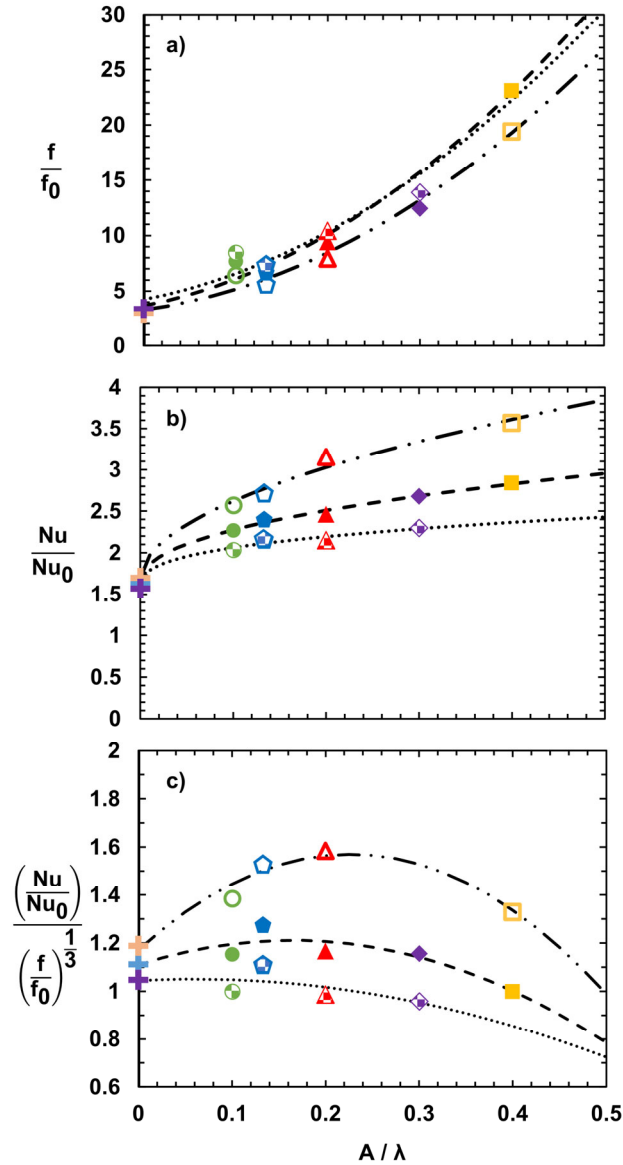


Figure 2-13. (a) Friction factor augmentation, (b) Nusselt number augmentation, and (c) efficiency index as a function of channel relative waviness.

The augmentations to heat transfer in Figure 2-13(b) at a Reynolds number of $Re = 30,000$ show only a slight increase with A/λ , nearly flattening as A/λ approaches 0.5. As Reynolds number is decreased however, there is an apparent trend of increased heat transfer as relative waviness is increased. This alligns with what was seen previously in Figures 2-7 and 2-12, as all tested channels

approached similar Nusselt number values as the Reynolds number was increased. These results imply that for some cases there is a diminishing impact for turbine cooling relative to pressure loss.

To capture these cases of diminished cooling, two methods were used to compare the overall performance of the channels. The first used the efficiency index, as described by Equation 2-4.

$$I = \frac{\left(\frac{Nu}{Nu_0}\right)}{\left(\frac{f}{f_0}\right)^{\frac{1}{3}}} \quad (2 - 4)$$

The efficiency index is an indicator of the heat transfer performance enhancement relative to the required increase in pumping power and was adapted from previous studies [60]. The efficiency index is plotted as a function of the relative waviness in Figure 2-13(c). It is clear from this figure that the efficiency index for channels of a relative waviness of less than $A/\lambda = 0.3$ were similar for Reynolds number of 20,000 and 30,000. This is not true for the coupons tested at a Reynolds number of 10,000, where the increases in heat transfer seen in Figure 2-13 (b) outweighed the frictional losses shown in Figure 2-13(a), particularly for the relative waviness range of $0.1 < A/\lambda < 0.3$. There was a decrease in performance across all Reynolds numbers after a waviness of $A/\lambda > 0.3$, as the increased frictional losses were met with only minor increases in heat transfer as was seen in Figure 2-13(b). As the Reynolds number was increased it should also be noted that the efficiency index continued to decrease, and almost all wavy channels at a Reynolds number of $Re = 30,000$ had a smaller efficiency index than a straight microchannel, indicating that wavy channels would be most effective in a Reynolds number range of $5,000 < Re < 10,000$.

The second method to compare the overall performance of the channels was to compare the Nusselt augmentation for a given friction factor augmentation across the tested designs. The augmentations with respect to a smooth coupon are presented in Figure 2-14 for all Reynolds numbers. These results showcase the wide range of performance available from channels of varying amplitude and wavelength. Notably, channels that had a small amplitude ($0.5A$) and high wavelength (1.5λ) saw similar performance throughout the testing range whereas high amplitudes ($1.5A$) and low wavelengths (0.5λ) saw substantial increases in friction factor for notable increases in Nusselt augmentation. The performance of wavy channels relative to a straight AM channel is also presented on this plot where it can be seen that any level of channel waviness was found to substantially increase both friction factor and Nusselt number. Note that the straight AM channel is still affected by the channel roughness, which is why the augmentations are above one.

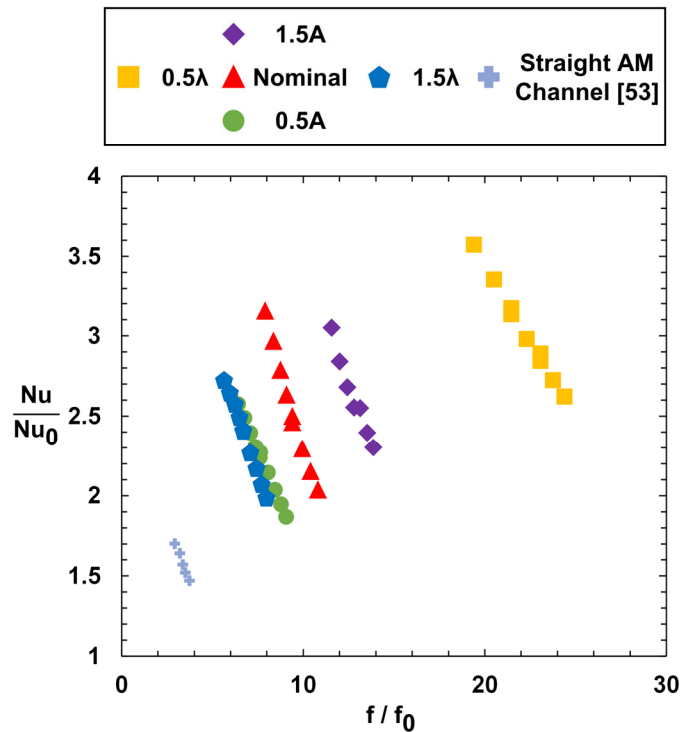


Figure 2-14. Nusselt number augmentation as a function of the friction factor augmentation for all channels.

2.12. Conclusions

This study investigated how the amplitude and wavelength of additively manufactured wavy channels impacts heat transfer and pressure loss using experimental testing and CFD predictions. Test coupons were additively manufactured using direct metal laser sintering and were then analyzed using CT scans to determine the accuracy to the design intent and investigate internal surface roughness.

Coupon characterization showed that when built vertically the channel shape and diameter were manufactured with only slight variations relative to the design intent. The roughness was found to be similar across all coupons, except for the shortest wavelength case, which saw a notable increase because of the increased number of downskin surfaces.

The experimental and predicted data indicated that either decreasing channel wavelength or increasing the channel amplitude resulted in increases to both heat transfer and pressure losses. For the friction factor, the data indicated nearly a constant value throughout the range of Reynolds numbers starting as low as $Re \sim 2,000$ indicating a fully turbulent flow.

The friction factor and heat transfer predictions exhibited an oscillatory behavior with decreasing amplitudes of the oscillations when becoming fully developed. The predictions indicated flow detaching and reattaching from the channel surfaces leading to streamwise

oscillations in the local friction factors and heat transfer coefficients, which were dependent on both channel amplitude and wavelength. The CFD predictions also elucidated the secondary flows changed considerably with decreasing wavelength while changing increasing the wave amplitudes resulted in the same secondary flow pattern only stronger vortices.

Scaling the friction factor and Nusselt number data by the relative waviness parameter (A/λ) showed clear trends in both pressure loss and heat transfer. This scaling indicated that friction factor greatly increased with increasing relative waviness, whereas the heat transfer increased moderately with increasing relative waviness. Due to the high increases in friction factor as compared to the modest increase in heat transfer, the efficiency index was similar for all coupons of low relative waviness, but decreased slightly for the coupon of highest relative waviness. Continued increases in relative waviness would only result in worse efficiency index performance, and the ideal range of relative waviness to maximize heat transfer for a given pumping power is between $0.1 < A/\lambda < 0.3$.

This paper uniquely characterized the performance of additively manufactured channels of varying amplitude and wavelength. The data presented in this paper can be used by the gas turbine community to select the best wavy channel configuration for turbine components that require small cooling features, such as blades, vanes, or shrouds. Improved component design can lead to a reduction in required cooling flow, thus resulting in improved overall engine performance.

3. IMPACTS OF PIN FIN SHAPE AND SPACING ON HEAT TRANSFER AND PRESSURE LOSSES³

3.1. Abstract

Additive manufacturing (AM) provides designers with the freedom to implement many designs that previously would have been costly or difficult to traditionally manufacture. This experimental study leverages this freedom and evaluates several different pin shapes integrated into pin fin arrays of a variety of spacings. Test coupons were manufactured out of Hastelloy-X using direct metal laser sintering (DMLS) and manufacturer recommended process parameters. After manufacturing, internal surface roughness and as-built accuracy were quantified using Computed Tomography (CT) scans. Results indicated that pin fins were all moderately undersized, and that there was significant surface roughness on all interior surfaces. Experimental data indicated that diamond shaped pins were found to have the highest heat transfer of the tested shapes, but triangle shaped pins pointed into the flow incurred the smallest pressure drop. Modifications to the streamwise spacing of the pins had little impact on the friction factor, but did increase heat transfer with increasing pin density. Prior Nusselt number correlations found in literature underestimated heat transfer and pressure loss relative to what was measured resulting from the AM roughness. A new correlation was developed accounting for AM roughness on pin fin arrays.

3.2. Introduction

The continued improvement of gas turbine efficiencies is critical with consistent year-to-year growth in commercial air travel expected for the foreseeable future [46] and anticipated increases in demand for electricity generation globally [61]. Developments toward more effective cooling schemes are of particular interest, as they can be integrated into a variety of components to extend life and reduce usage of limited cooling air. There have been many technologies that historically have been used in turbine cooling, notably ribs, channels, impingement and, the focal point of this study, pin fins [62]. Pin fins for use in turbine cooling, which are well suited for small internal cooling passages, have been studied for decades [63].

Gas turbine components that are exposed to the highest temperatures are typically cast using advanced single crystal techniques [2,64,65]. Within these cast parts are intricate internal

³ Corbett, T. M., Thole, K. A., and Bollapragada, S., 2023, "Impacts of Pin Fin Shape and Spacing on Heat Transfer and Pressure Losses," *J Turbomach*, **145**(5). pp.051014.

cooling features that are often left “as is” without a post-smoothing. The casting can result in increased roughness levels not accounted for in prior studies.

Similar to cast components, additively manufactured (AM) parts also exhibit rough surfaces. AM offers additional advantages, however, being both cheaper and faster than traditional casting when developing one-off parts, as well as providing considerable design freedom. There is interest in how AM roughness impacts on the performance of pin fin arrays as well as how these impacts relate back to the performance expected of cast components. Several prior researchers have explored AM produced pin fin arrays for gas turbine applications [33,34]; though a correlation that can be used to predict the performance of rough walled arrays has not yet been reported.

This study investigates pin fin arrays featuring a variety of practical streamwise spacings and pin shapes that were produced using AM. After being printed test coupons were evaluated using computed tomography (CT) scans to capture the as-built geometry and roughness and then tested to measure the heat transfer and pressure performance. A new correlation was developed based on the data obtained in this study, as well as from literature, that can be used to predict heat transfer on the basis of pin spacing, Reynolds number, and a new term added to account for roughness in the array.

3.3. Literature Review

Early investigations on the performance of pin fin arrays identified the independent impacts that the pins and endwall surfaces had on the total heat transfer. Zukauskas [66] summarized the results from several early pin fin studies that featured long tubes in staggered and in-line formations. Their work identified that the mean heat transfer of such pins could be predicted without considering the endwalls, indicating that the majority of the heat transfer resulted from the pin surfaces. This difference in heat transfer between the pins and endwalls was further explored by Sparrow et al. [67], who found that the heat transfer near the endwalls was significantly lower than that around the circumference of the pin.

The relative magnitudes of heat transfer from the endwalls and pin surfaces was later found to be a function of the pin height-to-diameter ratio (H/D). A study from VanFossen et al. [68] found that by shrinking the pin H/D to a size relevant to turbine airfoil cooling ($0.5 < H/D < 2$), a greater fraction of the total heat transfer occurred on the endwalls relative to what was seen previously with arrays featuring long pins. They also found that the array-averaged Nusselt number for the low aspect ratio pin fins was smaller than what had previously been reported for longer pins. Brigham et al. [69] continued investigating the effects of the H/D ratio and found that the heat transfer performance of an array is similar when the pin height-to-diameter ratio is between $0.5 < H/D < 2$. Aligning well with these findings, Chyu et al. [70] later determined that the heat transfer

coefficient on the endwall surfaces became significantly higher as the pin aspect ratio decreased from $H/D = 4$ to 2. Later work from Kirsch and Thole [33] investigated additively manufactured low aspect ratio pin fins ($H/D = 1$), featuring rough wetted surfaces. Their work revealed that this roughness increased heat transfer considerably relative to similar geometries with smooth surfaces.

Many studies have focused on investigating the impacts of the spacing of low aspect ratio pin fins in arrays. Multiple studies led by Metzger et al. [21,71] evaluated low aspect ratio pins at several streamwise spacings ($1.5 \leq X/D \leq 5$). It was found that the heat transfer increased notably with decreases in streamwise spacings within this test range. Both Lawson et al. [72] and Ostanek [73] continued evaluating the changes in performance as a result of pin spacing for low aspect ratio pin fins. Their investigations identified similar patterns of array performance based on their tested streamwise spacing ($1.73 \leq X/D \leq 3.46$), but additionally found that the spanwise spacing did not have a significant impact on heat transfer within their test range ($2 \leq S/D \leq 4$) relative to the streamwise spacing. In addition to heat transfer, Lawson et al. and Ostanek captured the array friction factor and found it to be almost entirely a function of spanwise spacing, counter to what was seen for heat transfer. Decreases in spanwise spacing resulted in increases to friction factor within the test range given the greater flow obstruction.

The pin shape also plays a role in heat transfer and pressure loss of the array. Metzger et al. [74] investigated how oblong pins oriented at different directions impacted performance. They found some pin orientations resulted in decreased heat transfer and significant pressure penalties as compared to standard cylindrical pins. Chyu et al. [75] investigated diamond and square shaped pins finding that both shapes had higher heat transfer than circular pins. The diamond pins were found to incur a higher pressure penalty relative to the square shapes. A later analysis performed by Chyu et al. [22] expanded on these results and found that the diamond and square shaped pins had a similar or lower heat transfer coefficients on the pin as compared to the circular pins. They also found that the two pin shapes induced unique and complex flow fields that improved convective heat transfer on endwalls in the wake region. Note that these studies used smooth surfaces.

Ferster et al. [34] investigated additively manufactured pin fin arrays featuring several different pin shapes at different spacings. They found that certain pin shapes, such as a star and dimpled sphere, imposed a greater pressure penalty than heat transfer benefit as compared to cylindrical pins. Other shapes however, such as triangle shaped, sustained minimal pressure loss while maintaining heat transfer to that of circular pins.

Several investigators in the past have strived to correlate the heat transfer performance of pin fin arrays using equations of varying complexity. Metzger et al. [21] developed a widely

accepted correlation based on the streamwise spacing and pin Reynolds number to determine the array averaged Nusselt number. This correlation was quickly followed by VanFossen et al. [68], who developed their own correlation using a modified length scale to predict the array average performance. VanFossen's correlation was followed later by groups like Chyu et al. [70], who developed a series of correlations based on the pin aspect ratio. The correlations developed by Chyu et al. were solely a function of the pin Reynolds number and aspect ratio, and were therefore independent of the pin spacing. This exclusion was found to result in moderately less accurate prediction of array performance as compared to correlations proposed earlier, but did capture the impact of aspect ratio that had not yet been described. Lawson [76] developed a more intricate correlation that used pin spacing as a basis for all equation constants, which was found to improve agreement with experimental data as compared to earlier proposals. Ostanek [73] also developed a correlation that was a function of Reynolds number, streamwise and spanwise spacings, which showed improved agreement to data collected from several studies.

Previous published papers have identified the impacts of geometric characteristics of pins and spacing of pins with smooth surfaces. In contrast, the study reported in our paper uniquely evaluates the impact of AM roughness by evaluating eight different pin shapes and spacings. Coupons were characterized to capture true dimensions and surface roughness, and then experimentally tested to find the friction factor and heat transfer performance. Using these results, a correlation was developed to predict the performance of several geometries.

3.4. Description of Test Coupons

All pin fin arrays used in this study were packaged into tests coupons that were similar in construction to those used in prior studies by one of the co-authors [33,53], as shown in Figure 3-1. These test coupons were designed to be 50 mm long, with an internal duct width of 19 mm and height of 1.9 mm. These duct dimensions resulted in a duct hydraulic diameter (D_h) of 3.46 mm. The thickness of the endwalls was minimized to allow for accurate predictions of heat transfer during experimental testing.

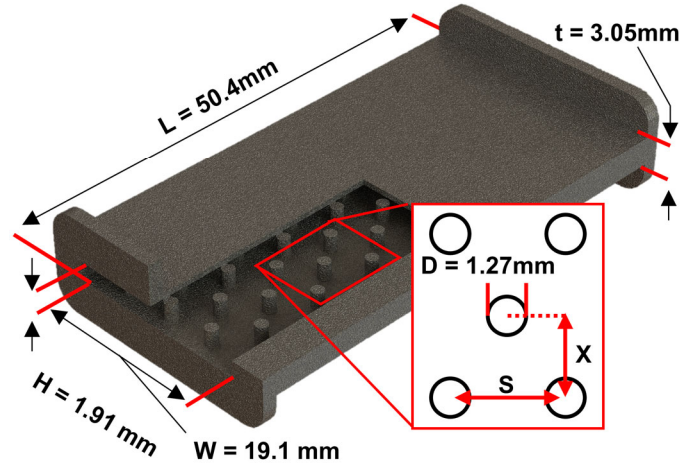


Figure 3-1. Test coupon diagram with exposed internal geometry and relevant coupon dimensions.

Cylindrical, diamond, and triangle pins were chosen to be investigated for this study. The triangle pins were oriented both with the “point” directed into the flow and in the downstream direction, which are referred to as the point and face orientations respectively. These shapes were decided based on a previous work by Ferster et al. [34] who analyzed similar pin shapes. The diameter (D) for each of the pin geometries was taken to be the thickness at the point of maximum flow obstruction and was set to be a constant $D = 1.27$ mm across all tested shapes. This definition meant that the pins had a height to diameter ratio of $H/D = 1.5$, which is representative of the pin size in engine components. The streamwise spacing of the diamond and triangle shaped pins was varied between $2 \leq X/D \leq 4$, while the spanwise spacing was kept constant at $S/D = 3$. These coupons were intended to be used to explore both the impacts of streamwise spacing and shape. The coupon featuring cylindrical pins was designed to match the spacings from a prior study where $X/D = 2.6$ and $S/D = 4$ [33]. A summary of the pin shape and spacings of the coupons used in this study including roughness can be seen in Table 1.

Table 3-1. Coupon Specifications and Roughness

Pin Shape	X/D	S/D	Endwall R_a/D_h	Pin R_a/D_h
Cylinder	2.6	4	0.0120	0.0100
Triangle Point	2	3	0.0119	0.0048
Triangle Point	3	3	0.0129	0.0050
Triangle Point	4	3	0.0110	0.0028
Triangle Face	2	3	0.0119	0.0048
Triangle Face	3	3	0.0129	0.0050
Triangle Face	4	3	0.0110	0.0028
Diamond	2	3	0.0106	0.0019
Diamond	3	3	0.0133	0.0030
Diamond	4	3	0.0154	0.0018

Coupons were manufactured using an EOS M280 machine out of Hastelloy-X. The coupons were built in the vertical build orientation such that the pins were unsupported inside the ducts. Support structures were used to bind the coupons to the build plate and support the top flanges. The coupons containing triangular pins were constructed such that the point of the triangle pin pointed downward to allow the pin to be self-supporting. Coupons were manufactured using the process parameters recommended by the manufacturer.

After being printed, coupons were cleared of powder and heat treated to relieve residual stresses from the build. Parts were removed from the build plate, support structures were cut away, and interface surfaces were cut to size using wire EDM.

3.5. Coupon Characterization

Coupon geometries were characterized using non-destructive computed tomography (CT) scans. Scans were completed using a voxel size of 35 microns. Using commercial software, these scans were resolved to 1/10th the voxel size, determining the wall features down to 3.5 microns [54].

Using these scans, the as built dimensions of the test coupons were captured in a multistep process. The first step was to reconstruct the coupon surfaces from the CT scan using commercial software, followed by exporting these surfaces for analysis using an inhouse code. The inhouse code analyzed the duct diameter by splitting the reconstructed surfaces of the coupon along the flow direction into over 800 slices to determine the perimeter and cross-sectional area for each slice. These measurements were then averaged across all slices to define the measured duct hydraulic diameter. The pin diameters were captured separately by using the scans parsed into over 100 slices along the height of the channel where the perimeter, maximum flow obstruction, and cross-sectional area were captured for each pin in the coupon independently. Once captured, these values were averaged across all pins in a coupon. The pin cross-sectional perimeter and area determined from this analysis were used to calculate the total wetted surface area inside the coupon.

Figure 3-2 showcases the midsection of one of the diamond shaped pins captured from the CT scans along with the design intent. The unsupported melt pool at the base of the pin permeated lower than intended thereby lengthening the pin along the build direction. This phenomenon is particularly noticeable at the two spanwise corners, where they become rounded from lack of support functionally reducing the pins maximum diameter. As a result of this rounding, pin diameters were consistently undersized. The triangle shaped pins had the most significant deviations while the diamond shaped pins were printed more accurately.

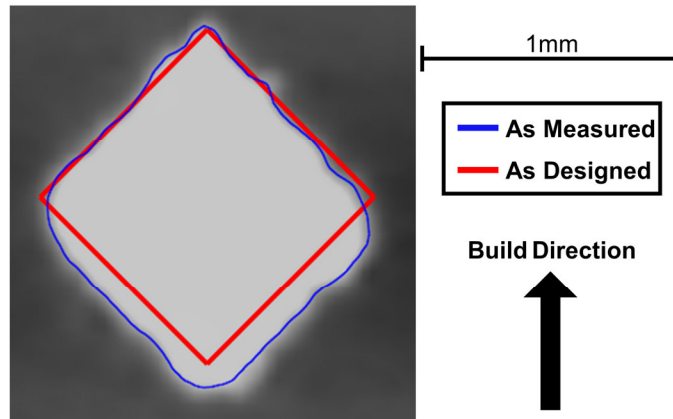


Figure 3-2. Accuracy of as-measured pin to design intent for diamond shaped pins.

The interior surfaces of the coupons, as shown in Figure 3-3 and indicated in Table 3-1, were rough for all the geometries built. The endwalls, in particular, had high roughness. The roughness on these surfaces were determined quantitatively using the methods described by Snyder et al. [52]. In short, a plane was fit to the coupon surface, and then the surface deviation from this plane was measured. These deviations were then averaged to define arithmetic mean roughness (R_a) for a given location. A minimum of four planes were used for each endwall surface in a coupon, with each being approximately one square millimeter in area. The roughness of the pin surfaces and the endwall surfaces were captured independently, and the area averaged values for both as normalized by the hydraulic diameter are reported in Table 3-1. Unlike what has been previously reported in literature [33], the area-averaged roughness of these channels was largely the same regardless of pin spacing. This difference is likely a due to the coupon geometry being considerably larger than that which was reported previously, in addition to improved process parameters. It can also be seen in Table 3-1 that the pin roughness is between 50-90% lower than the roughness on the endwalls. This is likely due to the decreased conduction resistance of the pin surfaces as compared to the thin endwalls which impacted surface morphology during the build.

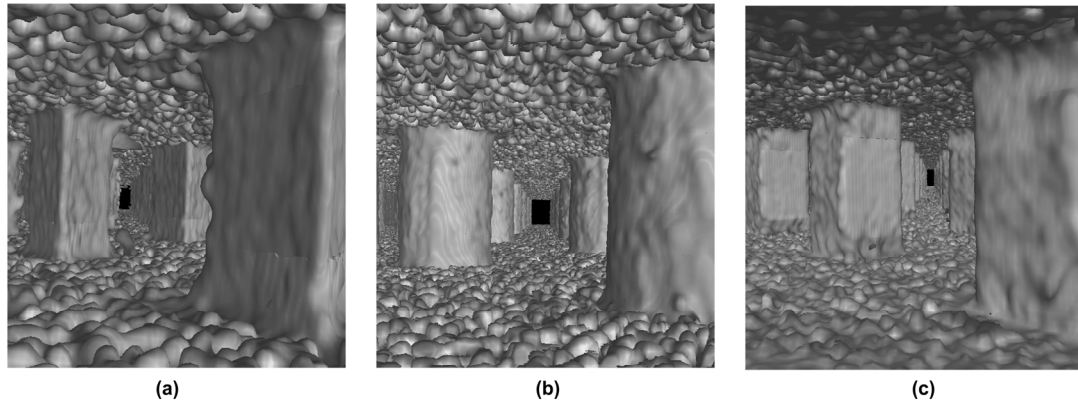


Figure 3-3. Internal surfaces of the coupons containing (a) triangle pins (b) cylindrical pins, and (c) diamond pins recreated from CT scans.

3.6. Experimental Methods

The experimental test facility is similar to that used in previous AM test coupon studies as shown in Figure 3-4 [33,51]. During experimental testing a coupon was installed between two plenums, which conditioned the flow to be uniform as it entered and exhausted from the test coupon. The air flow through the test section was controlled by a mass flow controller located upstream of the test section. To control the flow pressure in the coupon, a needle valve was used downstream of the test section. Fluid temperatures were captured upstream and downstream of the coupon using several E-type thermocouples. Pressure in the system was captured using an upstream gauge pressure sensor, and pressure drop across the coupon was measured using a differential pressure transducer featuring removable diaphragms to allow for accurate capture of a wide range of pressure drops. Pressure in the test section varied from 15-100 psia depending on the Reynolds number being tested.

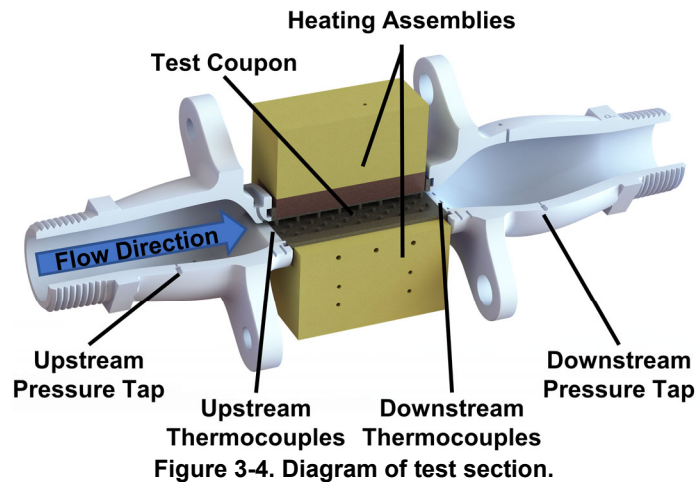


Figure 3-4. Diagram of test section.

For the pin fin studies, the Reynolds number and friction factor were calculated using the minimum flow area through the coupon, which was a function of the spanwise pin spacing, as seen below in Equation 3-1.

$$U_{\max} = U_{\text{mean}} \left(\frac{W}{W - N_{\text{span}} * D} \right) \quad (3 - 1)$$

Where N_{span} is the number of spanwise pins, W is channel width, and D is pin diameter. It should be noted that the Fanning friction factor was used for these studies.

Heat transfer measurements were captured using a constant surface temperature boundary condition with the use of heated copper blocks as shown in Figure 4. Coupon wall temperatures were constant for a given test, and ranged from 60-70°C between tests. Thermal losses were quantified through thermocouples placed throughout the foam blocks and plenums. The heat transfer into the coupon was determined using a one-dimensional conduction analysis based on precisely positioned thermocouples in the copper blocks. This analysis is described in greater detail by Stimpson et al. [51]. The total heat input into the coupon was determined by subtracting the heat that was lost to the surrounding components from the heater power. To ensure that the heat transfer into the system was accurately captured throughout tests, the total heat introduced into the test coupon was compared to the heat calculated using the first law of thermodynamics. This energy balance was found to be within 5% for all tests throughout the range evaluated providing confidence in the measured convective heat transfer.

All sensor data was post processed using an inhouse code to calculate the temperature, pressure, density, and flow speed at the coupon entrance and exit using 1D isentropic flow assumptions. The convective coefficient was calculated based on an isothermal wall assumption, which was validated by the high fin efficiency of the array. The convective coefficient is defined in Equation 3-2.

$$h = \frac{\sum Q_{\text{in}} - \sum Q_{\text{out}}}{A_s \Delta T_{\text{lm}}} \quad (3 - 2)$$

where A_s is the entire wetted surface area of the coupon. The definition of the wetted area is the surface area where the working fluid is touching and, as such, the pin footprint is removed.

To validate the performance of the test rig, it was first benchmarked by collecting data from a smooth traditionally manufactured open channel coupon and comparing the results to known correlations. Friction factor results were validated by comparing against the laminar flow relation and the Colebrook equation seen as Equation 3-3 [55].

$$\frac{1}{\sqrt{f}} = -2 \log_{10} \left(\frac{k_s}{3.7D_h} + \frac{2.51}{\text{Re}_{D_h} \sqrt{f}} \right) \quad (3 - 3)$$

Because the test coupon was smooth, the Colebrook equation was solved assuming $k_s = 0$ for comparisons against the collected data. It is common practice in pin fin studies to use the Fanning friction factor, which is one fourth the value for channel flows. As such, all smooth friction factor values determined from the Colebrook equation reported in later sections are divided by four.

Heat transfer measurements were similarly taken using this smooth coupon and were compared against the Gnielinski Correlation as seen as Equation 3-4 [56].

$$\text{Nu} = \frac{\frac{f}{8} (\text{Re}_{\text{Dh}} - 1000) \text{Pr}}{1 + 12.7 \sqrt{\frac{f}{8}} (\text{Pr}^{\frac{2}{3}} - 1)} \quad (3 - 4)$$

The results presented using this correlation were determined using the friction factor for a smooth coupon.

3.7. Measurement Uncertainties

Measurement uncertainty was calculated using the method of propagation of error [57]. The largest sources of error in calculating the friction factor were the differential pressure measurements and the measured mass flow rate. The combined uncertainty was approximately 7% for $\text{Re}_{\text{D}} < 5,000$, and was 5% or lower for $\text{Re}_{\text{D}} > 5,000$. During testing several data points were repeated in an overlapping region of pressure diaphragms to ensure measured results were consistent. Repeatability of the friction factor measurements were within 2-4%.

The uncertainty with heat transfer was also quantified with the primary driver being the thermocouples located at the exit of the coupon and the copper blocks, with uncertainties under 7% for the entire test range and results being repeatable within 2%.

3.8. Pin Shape Effects

The change in pin geometry had several distinct impacts on overall performance of the arrays. Figure 3-5 shows the friction factor as a function of Reynolds number for coupons of differing pin shape. Based on the results presented in Figure 3-5, it is evident that the flows were fully turbulent throughout the entire test range, as indicated by friction factor being independent of Reynolds number. This rapid transition to a turbulent flow is the result of the turbulence induced by the flow interacting with the pins and the rough walls. The triangle pins in the point orientation have the lowest friction factor of the tested shapes, being 36% less than the diamond shaped pins and 45% less than the triangle pins in the face orientation. This decreased pressure losses for the point orientation are due to two complimentary effects. Firstly, the flow impinging on the pin frontal area is anticipated to play a significant role in the overall pressure losses and this expectation is substantiated by the triangles in the face orientation inducing the highest friction factor. The diamond shaped pins had the next highest pressure loss, which aligns well with this hypothesis

given that the flow through the array had a steeper angle of impact on the diamond pins than on the triangle pins in the point orientation. The second effect is the interactions of the wake regions that occur behind the pins, which has been shown to change depending on pin shape in past literature [22]. While the effects of the wake region have previously been reported to minimally impact friction factor for smooth arrays [72], it is anticipated that due to the increased endwall roughness for these wake regions are contributing significantly to overall pressure loss.

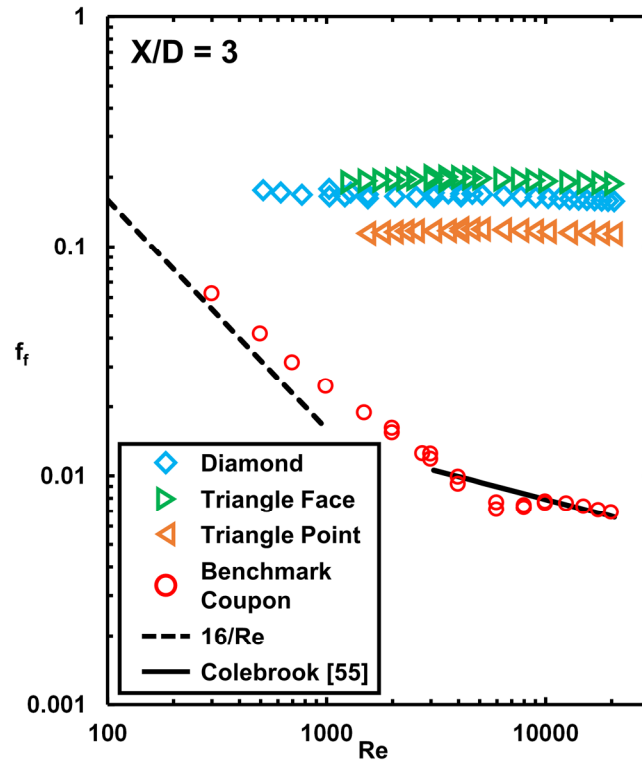


Figure 3-5. Friction factor data for coupons of varying pin shape at a streamwise spacing of $X/D = 3$.

Figure 3-6 shows the heat transfer results for the same test coupons that were shown in Figure 3-5. As the Reynolds number increases, the difference in performance between the different pin shapes also increases, but the percent difference between the shapes remains largely constant with the diamond shaped pins performing between 15% and 18% better than the triangles in the point orientation. Aligning with previous research [22], the diamond shaped pins achieved the highest heat transfer of the tested shapes. This enhancement is augmented further by the increased endwall surface roughness resulting in significantly greater heat transfer than would be expected from smooth pin fin arrays. All pins had similar levels of roughness on the endwall surfaces as seen in Table 3-1, so the relative differences in heat transfer between these arrays is primarily a function of pin shape.

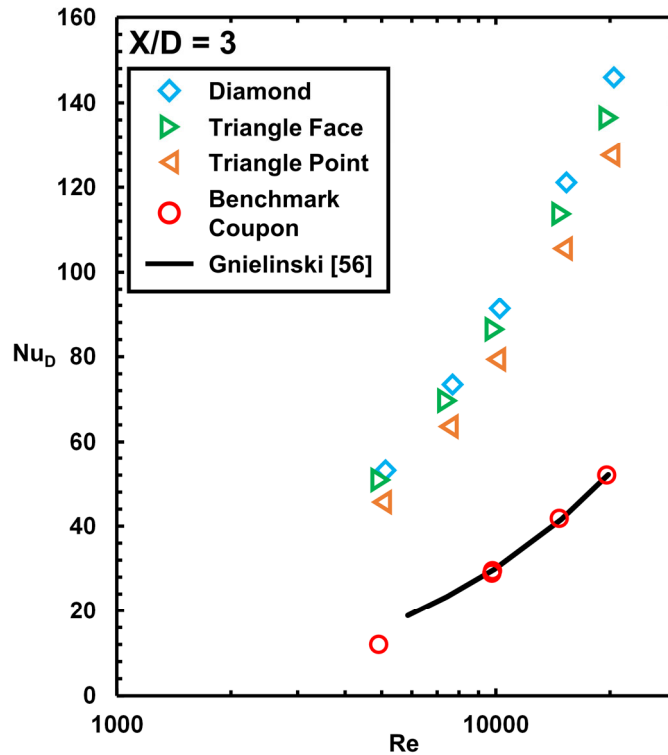


Figure 3-6. Nusselt number values for pins of varying shapes at a streamwise spacing of $X/D = 3$.

3.9. Streamwise Pin Spacing Effects

The friction factors of the coupons at two Reynolds numbers for three different streamwise spacings are shown in Figure 3-7, where it can be seen there was minimal variation in friction factor between streamwise spacings. The streamwise spacing effects in this Reynolds regime ($1,000 < Re_D < 20,000$) have been shown previously to have little impact on the friction factors for smooth pins as the wake interactions between rows is significantly less influential on pressure drop than the increased flow blockage from decreases in spanwise spacing [72,73]. Conversely, previous AM pin fins have shown that any increase in pin density, either through decreased spanwise or streamwise spacing, resulted in higher friction factors [33]. These heightened friction factors were linked to the increased AM surface roughness, which was also found to increase with tighter spaced arrays. As seen in Table 3-1, roughness on both the array endwalls and on the pin surfaces were largely the same among the different array geometries. This difference in surface morphology between the current and prior study is likely a function of the increased coupon size, where the current study used a hydraulic duct diameter of 3.5 mm and the prior used test coupons that had a duct diameter of 2.1 mm. Additionally, improvements to the additive process parameters likely played a role in improving these surfaces.

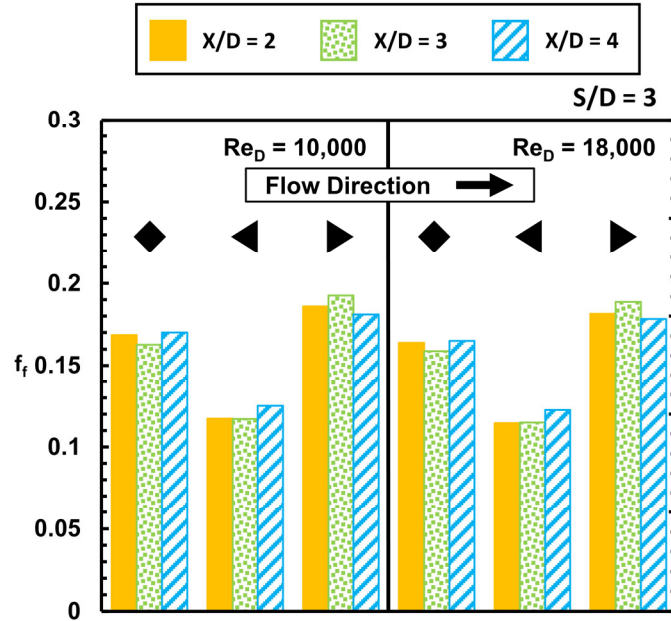


Figure 3-7. Friction factor values for pins of varying shape and streamwise spacings at $Re = 10,000$ and $18,000$.

Figure 3-7 shows that the pin shape and orientation had a much more significant impact on the array performance as compared to streamwise spacing, with the friction factor changing by no more than 6% between spacings for a given Reynolds number and pin shape. In contrast to the friction factors, the array average Nusselt numbers showed more dependence on pin spacing than did the friction factors, as can be seen in Figure 3-8. For example, the tightest spaced diamond pins were able to achieve a 10-15% increase in heat transfer over the widest spaced pins at a $Re_D = 10,000$. This increase in heat transfer can be attributed to the increased effects of the wake regions behind the pins in the tightest streamwise spacing as compared to the widest as well as the increased surface area. The impact of the increased number of pins becomes less significant as the flow becomes more turbulent, as shown on the right of Figure 3-8 at $Re_D = 20,000$.

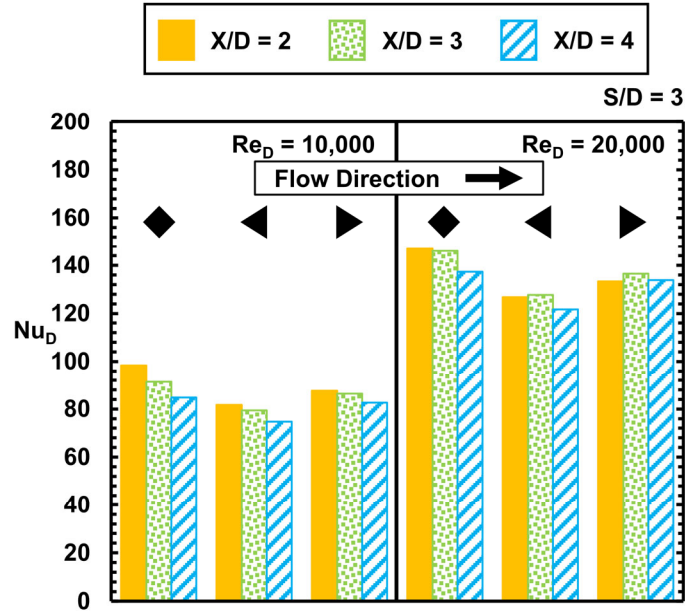


Figure 3-8. Nusselt number values for pins of varying shape and streamwise spacings at $Re = 10,000$ and $20,000$.

3.10. Overall Array Performance

To fully characterize the performance of an internal cooling design, it is important to understand the relative increase in pressure drop compared to the increase in heat transfer. One method of comparison is to determine the efficiency index of the design, which reveals the relative increase in heat transfer performance per increase in required pumping power. The form used in this study was adapted from Gee and Webb [60] and seen as Equation 3-5.

$$\eta = \frac{Nu_{Dh}}{Nu_0} \left(\frac{f_{Dh}}{f_0} \right)^{\frac{1}{3}} \quad (3-5)$$

To appropriately scale the data for this parameter, the Nusselt number was modified to be a function of the duct hydraulic diameter (D_h) rather than pin diameter, and the friction factor for the test coupons was calculated similar to that of channels, seen as Equations 3-6 and 3-7.

$$Nu_{Dh} = \frac{D_h h}{k} \quad (3-6)$$

$$f_{Dh} = \frac{2\Delta P}{\rho u_{mean}^2} \left(\frac{D_h}{L} \right) \quad (3-7)$$

This modification to the definitions is required as both the Nusselt number and friction factor are being normalized using the smooth channel correlations shown as Equations 3-3 and 3-4. Additionally, the values obtained from Equations 3-3 and 3-4 were calculated using the duct Reynolds number, which uses the duct hydraulic diameter as the length scale. This method for

normalizing the Nusselt number and friction factor augmentations is identical to the method used by Ostanek [73].

The efficiency index performance of arrays with diamond and triangle shaped pins at a streamwise and spanwise spacing of $X/D = S/D = 3$ is compared to a traditionally manufactured array with cylindrical shaped pins of the same spacing in Figure 3-9. It should be noted that these results are given as a function of the pin Reynolds number, rather than the duct Reynolds number. It can be seen in Figure 3-9 that the AM coupons perform very similarly to the traditional coupons, despite the AM roughness effects. This indicates that the heat transfer and friction factor are increased proportionally due to the increased surface roughness. However, the triangles pins in the face orientation have a lower efficiency index due to the substantial increase in pressure loss for only moderate increases in heat transfer as the flow impinged on the face of the pin.

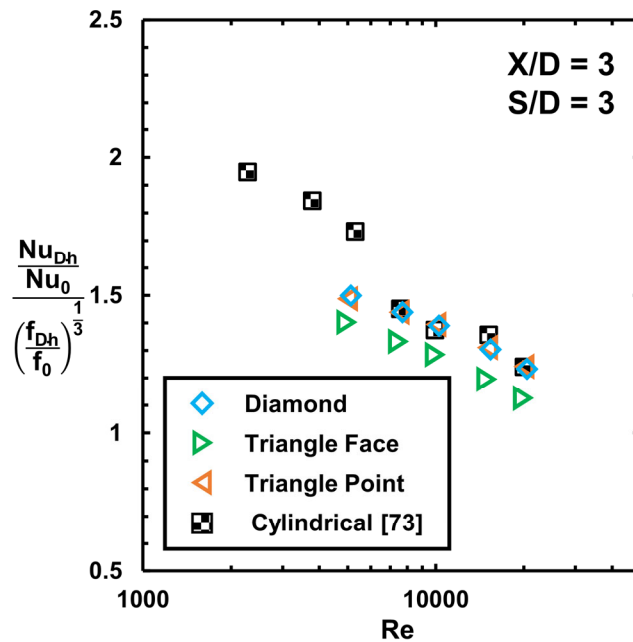


Figure 3-9. Efficiency index performance of coupons tested in the current study compared to a traditionally manufactured pin fin array of the same spacing.

3.11. Correlating roughness with performance

A pin fin array channel containing cylindrical pins was intended to serve as a comparison to prior results from the same laboratory [33,72], but a significant deviation from prior performance was found. A brief overview of the coupons analyzed in these prior investigations can be seen in Table 3-2, where it should be noted that these studies all used the same definition for Reynolds number, Nusselt number, surface area, and surface roughness. The results indicated measurable differences in Nusselt numbers when comparing the previous coupons with those that were made for this study with both using additive manufacturing. The heat transfer performance for the

cylindrical pins is compared to similar array spacings found in literature in Figure 3-10. The performance of the coupon developed for this study has significantly lower heat transfer than the previous AM pin fin arrays by Kirsch and Thole [33], but still considerably greater heat transfer from the smooth pin fin arrays (not using AM) by Lawson et al. [72].

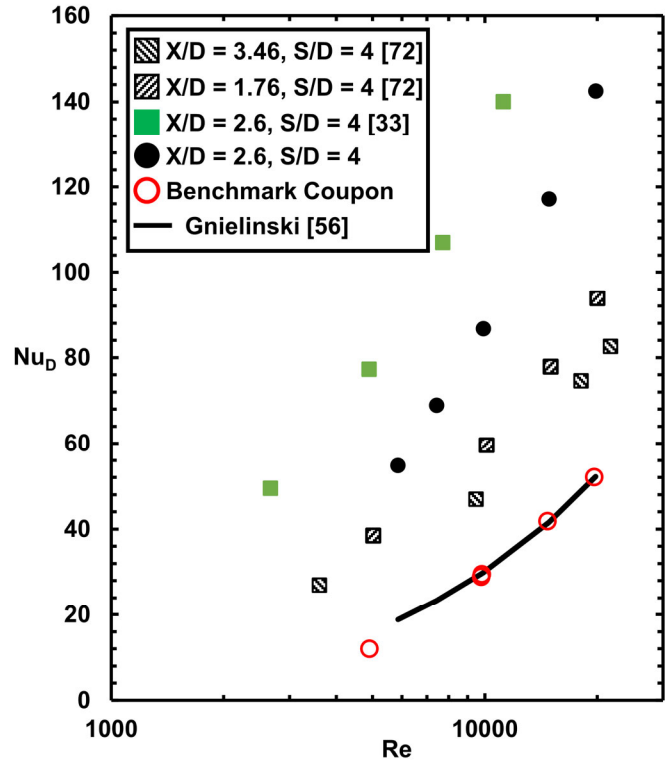


Figure 3-10. Nusselt number for various cylindrical pins of similar spacing found in literature compared to data from current study.

The differences in heat transfer shown in Figure 3-10 are a result of the significant role the endwall surface roughness has in low aspect ratio pin fin arrays. To compare the roughness effects, the endwall roughness was normalized by the duct hydraulic diameter, D_h , and is reported in Table 2. There was a significant difference in relative roughness between the current and prior AM studies [33,34], with the latter having over twice the relative roughness of the former as seen in Table 3-2. This increase in heat transfer of small internal passages as a function of relative roughness has been explored previously by Stimpson et al. [51] indicating higher heat transfer with relative roughness. What the results in Figure 3-10 also illustrate are the improvements in the additive manufacturing processing parameters with respect to reducing the roughness levels over time by comparing the Kirsch and Thole [33] study in 2017 to that of the current study in 2021.

Table 3-2. Geometric Characteristics of Test Coupons

Study	Pin Shape	X/D Range	S/D Range	H/D	Ra/Dh
Current Study	Varied	2 - 4	3 - 4	1.5	0.011 - 0.015
Kirsch et al. [33]	Cylindrical	1.3 - 2.6	1.5 - 4	1	0.039 - 0.053
Ferster et al. [34]	Varied	1.3 - 2.6	1.5 - 4	1	0.040 - 0.050
Ostaneck [73]	Cylindrical	2.16 - 3.03	2	1	0
Lawson [76]	Cylindrical	1.73 - 3.46	4	1	0
Metzger et al. [21]	Cylindrical	1 - 5	2.5	1	0

In developing a correlation for pin fin arrays with realistic AM roughness levels, prior correlations from literature were evaluated. Many of the correlations used to predict the heat transfer took the form of a common series of multiplied independent variables raised to a constant [21,70,73,76], as seen in Equation 3-8.

$$Nu_D = C_1 \left(\frac{X}{D}\right)^{C_2} \left(\frac{S}{D}\right)^{C_3} Re_D^{C_4} \quad (3-8)$$

Where C_1 through C_4 are correlation constants. To account for the relative roughness, an additional term is being proposed by our work to the series, resulting in the modified form seen in Equation 3-9.

$$Nu_D = C_1 \left(C_5 \left(\frac{R_a}{D_h}\right)^{C_6} + 1 \right) \left(\frac{X}{D}\right)^{C_2} \left(\frac{S}{D}\right)^{C_3} Re_D^{C_4} \quad (3-9)$$

To determine the correlation constants, a non-linear multivariable regression analysis was used on the experimental testing results of the current study including all of the pin fin shapes, as well as all available heat transfer data from the studies by Kirsch et al [33], Lawson [76], and Ostaneck [73]. The objective of the analysis was to minimize the root mean square (RMS) error between the prediction and experimental values. This data set included both additively and traditionally manufactured coupons of a variety of spacings and pin shapes.

Using this method, the constants for the correlation were solved and are shown in Table 3-3. The predictions using the new correlation are given in Figure 3-11. Despite the variations in pin shape, spacing, manufacturing, relative roughness, and size, that the correlation can predict heat transfer within 10% for almost all data used to fit the correlation. The correlation is compared against previous work in Table 3-4, where the valid ranges of geometric characteristics and Reynolds numbers are shown.

Table 3-3. Correlation Constants

$$Nu_D = C_1 \left(C_5 \left(\frac{R_a}{D_h} \right)^{C_6} + 1 \right) \left(\frac{X}{D} \right)^{C_2} \left(\frac{S}{D} \right)^{C_3} Re_D^{C_4}$$

C_1	C_2	C_3	C_4	C_5	C_6
0.127	-0.066	0.054	0.657	16.22	0.752

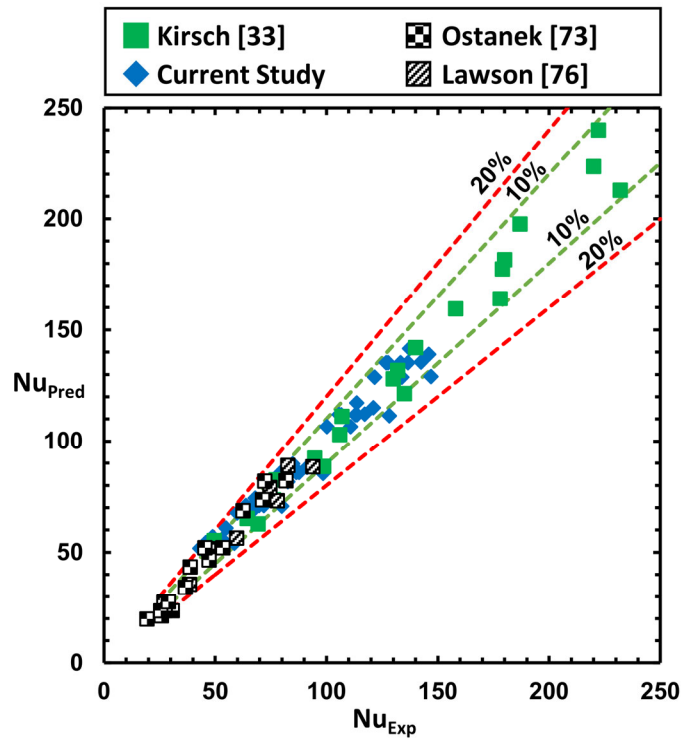


Figure 3-11. Prediction accuracy of developed correlation against data in literature.

To further validate the performance of the correlation, it was used to predict the heat transfer of additional data sets from Ferster et al. [34] and Metzger et al. [21]. The results of this comparison can be seen in Figure 3-12, where the correlations developed by Chyu et al.[70] and Metzger et al. [21] are also displayed. The previously reported correlations accurately capture the heat transfer of prior smooth coupons for $Re < 10,000$ as shown using various black markers. Likewise, the correlation developed in this study can be seen to predict very similar performance from the smooth pin fins, collapsing almost entirely onto the correlation developed by Chyu et al. [70].

The correlation developed in our study can be seen in Figure 3-12 to go one step further and predict the heat transfer performance of AM coupons as well indicated with the various colored markers. Notably, the developed correlation shows the ability to accurately predict the performance of various pin shapes despite not including a term to capture this geometric variation. This is due

to the relatively small impact that the changes in pin shape had on the heat transfer performance as compared to the large changes that were the result of the increased endwall roughness.

Table 3-4. Correlations for Pin Fin Array Heat Transfer

Study	Pin Shape	X/D	S/D	H/D	Reynolds	Correlation
Metzger et al. [21]	Cylindrical	1.5 - 5.0	2.5	0.5 - 3	2,000-100,000	$Nu_D = 0.135 \left(\frac{X}{D}\right)^{-0.34} Re_D^{0.69}$
Chyu et al. [70]	Cylindrical	2.5	2.5	1	10,000-30,000	$Nu_D = 0.14 Re_D^{0.65}$
Ostaneck [73]	Cylindrical	2.16 - 3.03	2 - 3	1	1,000 - 100,000	$Nu_D = 0.41 \left(\frac{X}{D}\right)^{-0.2} \left(\frac{S}{D}\right)^{-0.26} Re_D^{0.57}$
Lawson [76]	Cylindrical	1.73 - 3.46	2 - 4	1	5,000 - 25,000	$Nu_D = \left[0.128 \left(\frac{S}{D}\right)^{0.165} \left(\frac{X}{D}\right)^{-0.310} \left(\frac{S}{D}\right)^{+1.182} \dots Re_D \wedge \left[0.680 \left(\frac{S}{D}\right)^{-0.023} \left(\frac{X}{D}\right)^{0.048} \left(\frac{S}{D}\right)^{-0.2} \right]$
Current Study	Varied	2 - 4	2 - 4	1 - 2	2,000 - 50,000	$Nu_D = 0.127 \left(16.22 \left(\frac{R_a}{D_h}\right)^{0.752} + 1 \right) * \dots \left(\frac{X}{D}\right)^{-0.066} \left(\frac{S}{D}\right)^{0.054} Re_D^{0.657}$

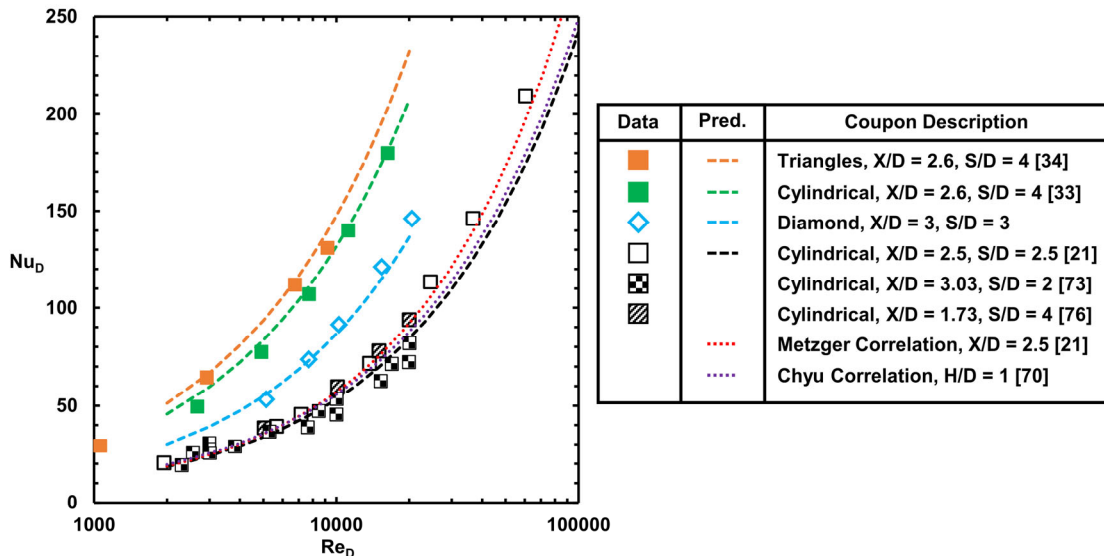


Figure 3-12. Developed Nusselt number correlation compared to data and correlations found in literature.

While not reported in this particular study due to unavailability of published data, it is expected that this correlation could be used to predict the heat transfer of traditionally rough cast components as well. Given the sensitivity of heat transfer to relative roughness, having a correlation that includes one such term can be highly useful for engineers designing components exposed to

high thermal loads. This correlation can be employed as a way of scaling the performance of prototypes made through additive manufacturing to final cast components.

3.12. Conclusions

The current study investigated the impacts of three elements of pin fin array design: pin geometry, spacing, and surface roughness. Several pin fin array designs were packaged into additively manufactured test coupons with these parameters varied and experimentally tested. Geometric characterization showed that pins were able to be largely accurately reproduced, though pins were all slightly undersized. The characterization of the coupons also revealed higher surface roughness on array endwalls relative to the roughness on the pins.

Experimental results indicated that the triangle shaped pins with their point directed into the flow resulted in the lowest overall friction factor, where reversing the triangle orientation resulted in the highest friction factor. The highest heat transfer was achieved by the diamond shaped pins, likely as a result of the increased levels of turbulence in the wake region, that were further enhanced by the rough endwalls. It was shown that pin streamwise spacing had little overall impact on the friction factor in the ranges tested, which is a result of the relative roughness dominating spacing effects as contributors to friction factor. The heat transfer was found to slightly increase with tighter spaced coupons at low Reynolds numbers. The efficiency index for the additively manufactured pin fin arrays was shown to be same as traditionally manufactured arrays for a range of Reynolds numbers, indicating that the ratio of heat transfer benefit to pressure loss is similar for both AM and traditional arrays.

Correlations in literature for heat transfer were found to significantly underpredict the heat transfer performance of the additively manufactured pin fin arrays because of the roughness. Comparisons of the data in literature showed a significant relationship between Nusselt number and relative roughness. To account for the roughness, a new correlation was developed with an additional term to capture the impact of the relative roughness of the array. This correlation was developed such that it can be used to predict the heat transfer of both highly rough and smooth pin fin arrays of a variety of spacings and shapes.

As additive manufacturing continues to prove to be a valuable asset in prototyping and cooling design development, it is critical to understand how the as built geometry impacts pin fin array performance. Furthermore, it is essential that designers have the required tools to predict the performance of these arrays, so that comparisons between manufacturing methods can be made before going through the manufacturing process. The results presented in this study bridge this gap so that designers can more effectively use AM in gas turbine cooling design.

4. Large Eddy Simulations of Kagome and Body Centered Cubic Lattice Cells⁴

4.1. Introduction

Heat exchangers are a prevalent part of modern life, with use cases spreading from small electronics cooling to power plants for distributing and dissipating thermal energy. Lattice structures have high surface area-to-volume ratios, making them an ideal candidate for use as a cooling technology. Several studies have recently evaluated lattice structures for cooling in the trailing edge of turbine blades [77,78] and in heat exchangers [24,79].

A lattice is most typically composed of a single “unit” cell in a repeating pattern in both streamwise and spanwise directions. The two most common types of lattice unit cells are triply periodic minimal surfaces (TPMS) that are complex surfaces defined by a mathematical function, or strut-based lattices that are composed of struts arranged in a variety of patterns. While lattice structures have been able to be produced through other means in the past [24], additive manufacturing (AM) opens up the opportunity to implement and curate these features faster and cheaper than was feasible previously.

Several groups in recent years have begun investigations into lattice structures for cooling applications, featuring both TPMS [80–84] and strut based lattices [78,83,85–102]. Many types of lattice unit cells have been investigated in these studies, with some of the most prominent unit cells including Kagome [78,83,86–89,96–98], body centered cubic (BCC) [83,89,99–102], face centered cubic (FCC) [83,87,103], cube [77,95], and octet [77,95]. These unit cells have been investigated in a range of scales, between 10 mm unit cells [77,85] down to 2 mm [83,86]. Additionally, the unit cells have been integrated into test coupons in several ways, including incorporated into channels with various spanwise and streamwise spacings [77,83], as well as used to form a three-dimensional grid [95]. Generally speaking, the thermo-hydraulic performance of lattice structures was greater than that of an empty duct, and have been seen to thermally develop in roughly 3-5 unit cells [89,95]. The specific focus of the current study is on two different unit cell geometries: the BCC and Kagome unit cells.

Recent investigations using Kagome lattice unit cells have leveraged both experimental and steady RANS simulations to explore performance. Hou et al. [104] completed a study on Kagome lattice where the orientation of the geometry was varied. They found that orienting the center struts parallel to flow direction resulted in enhanced heat transfer performance due to large

⁴ Corbett, T. M., and Thole, K. A., 2024, “Large Eddy Simulations of Kagome and Body Centered Cubic Lattice Cells,” *Int. J. Heat Mass Transf.*, **218**, p. 124808.

recirculation zones that occurred between lattice unit cells. This recirculation in the near wall region has been noted by several other researchers as well [83,86,89,97] and was found to be a function of the interactions of the vortices that develop just behind and in front of the lattice struts. The formation of these vortices resulted in a heat transfer bias, where one surface of the lattice design had significantly greater heat transfer than the other, as shown by Liang et al. [89]. There have also been a number of studies that have investigated how changes to the core Kagome geometry impact performance, including modifications to the strut shape [87], length [98], and number impacted the lattice performance [86]. Of these modifications, changes to strut length had the greatest impact on both heat transfer and pressure loss performance, with Kemerli and Kahveci [98] reporting an almost 230% increase in Nusselt number as unit cell sizes halved and cell porosity increased.

Similar to the Kagome lattice, there has been a significant research effort to better understand the performance of the BCC lattice. Several studies investigated laminar flow through a BCC lattice, and highlighted the impact of porosity [99–101] and developed analytical models to predict heat transfer [102]. Studies by Dixit et al. [99], Takarazawa et al. [100], and Shahrzadi et al. [101] found that as the porosity of the unit cell decreased, the heat transfer and pressure drop increased considerably. Dixit et al. [99] explained this change in performance to be the result of the increase in surface area increasing the skin friction as well as enabling greater heat transfer. Another study by Ernot et al. [102] developed an analytical model to predict the heat transfer of laminar flow through a BCC lattice, but they found that there were strict limitations on appropriate inlet flow rates, highlighting the difficulty in accurately predicting heat transfer of BCC lattice using simplified models. Two studies by Liang et al. [83,89] investigated turbulent flow through BCC lattice arranged with a streamwise and spanwise spacing similar to a pin fin geometry using experiments and steady RANS simulations. They found in high Reynolds number flows the vortex development in the wake of the BCC lattice resulted in increased average heat transfer on the endwalls relative to the average performance of the Kagome lattice. Despite the increased heat transfer the measured pressure drop was similar to Kagome lattice, giving rise to a greater thermal efficiency, or relative increase in heat transfer for a given amount of pumping power [89].

While these prior studies have explored many aspects of lattice designs, there is currently no work comparing the unsteady flow features in representative lattice structures, or studies that made use of higher order modeling techniques beyond steady RANS. The current study expands on the prior work on lattice structure performance by first exploring how the flow develops through subsequent rows of tightly packed Kagome and BCC lattices using experimentally validated large eddy simulations. Additionally, the turbulence generation and underlying transient structures are investigated, and their impact on local heat transfer is described.

4.2. Computational Setup

4.2.1. Modeling Domain and Methods

Two forms of lattice unit cells were investigated as part of this study, namely the body centered cubic (BCC) and Kagome lattices, which are shown in Figure 4-1(a) and 1(b). Each BCC lattice unit cell had a total of eight struts that were defined such that they connected opposing corners of the cubic unit cell. Each Kagome lattice featured a total of six struts that were defined similarly, though the unit cell shape was hexagonal with a width to height ratio of 3:2, similar to what was used by Parbat et al. [86]. The height of both designs investigated in this study was defined as 1.905mm, which was a size relevant to a variety of small-scale microchannels previously studied by the authors [105,106]. Because of the aspect ratio of the Kagome lattice, it was slightly wider than the BCC unit cell for this study with an aspect ratio of 1:1. Due to the differences in unit cell shape, the total volume of the Kagome lattice unit cell was physically larger than that of the BCC design. Both of the designs were modeled such that they had a porosity, defined as the empty volume over total unit cell volume, of 75%. The strut diameter was varied between the two designs to maintain this level of porosity as given in Table 1.

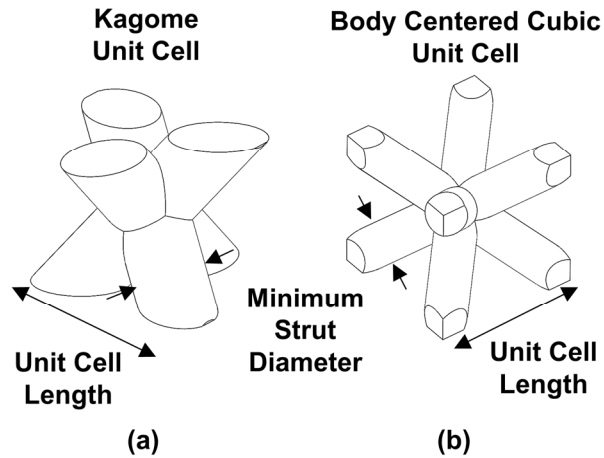


Figure 4-1. (a) Kagome and (b) body centered cubic lattice definitions.

Table 4-1. Geometric Properties and Experimental Results of Simulated and Tested Lattice

Analysis Method	Test Type	Unit Cell	Porosity	Cell Size [mm]	Strut Diameter [mm]	Fully Developed f	Fully Developed Nu	Fully Developed Nu, As-Designed Surface Area
LES	Both	BCC	0.75	1.905	0.46	7.1	245	245
LES	Both	Kagome	0.75	2.560	0.80	9.1	240	240
Exp.	Pressure Loss	BCC	-	1.905	0.58	8.6	-	-
Exp.	Pressure Loss	Kagome	-	2.560	0.93	8.7	-	-
Exp.	Heat Transfer	BCC	0.75	1.905	0.41	-	196	231
Exp.	Heat Transfer	Kagome	0.72	2.560	0.86	-	230	269

The unit cell size was defined as the width of the design, which was 1.91 mm for the BCC unit cell and 2.54 mm for the Kagome unit cell. Unit cells of the respective lattice were arranged into a “core” region, where cells were spaced at exactly one unit cell width, an arrangement which is shown in Figure 4-2. For each unit cell type, ten rows of lattice were combined into a “core” region, where the rows were arranged along the flow direction. In addition to the core region, there was an empty entry region, five unit cells in length, and an empty outlet region the length of ten unit cells. The domain was modeled this way to determine if the design of the lattice impacted the flow upstream or downstream of the core region. The two sides of the domain were modeled using a periodic boundary, which in effect captured an infinitely wide duct containing many columns of the lattice designs.

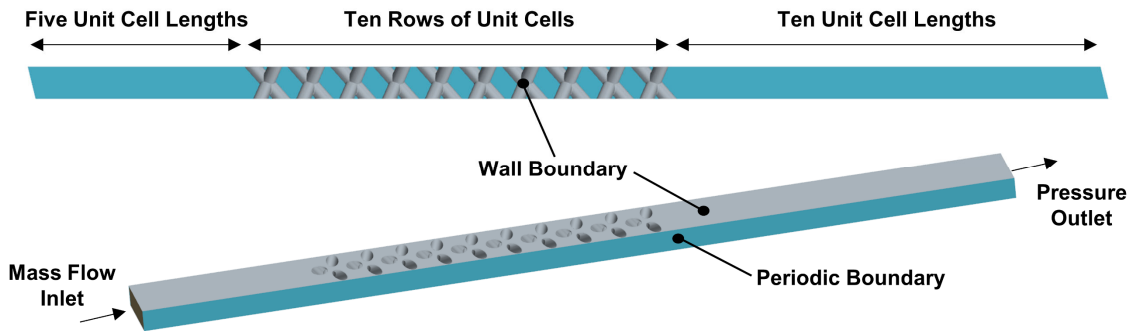


Figure 4-2. Computational domain used for simulations.

To ensure that the relevant flow features and transient flow dynamics were captured in this simulation, the domain was modeled using Large Eddy Simulations (LES) using a commercial computational fluid dynamics (CFD) solver [107]. The modeled fluid was air, where density was calculated using the ideal gas law and the dynamic viscosity and thermal conductivity of were modeled using Sutherland’s law. Air entered the domain through a mass flow inlet that imposed an internal Reynolds number of approximately $Re = 21,000$, and a pressure outlet boundary condition. The walls of the domain were set to a constant temperature of 75°C , and the temperature of the

inlet mass flow was set to 23°C. These conditions were set to mirror an experimental validation that will be discussed Section 2.3. The Wall-Adapting Local Eddy-viscosity (WALE) sub-grid turbulence model was used to capture sub-grid scale turbulence, as it most appropriate for wall bounded turbulent flows [108]. Time steps were determined such that the Courant number was less than one for the entire domain.

While lattice structures have gained significant interest for applications in conjunction with metal additive manufacturing, the computation model used for this study did not account for the typical surface roughness intrinsic to metal additive components. Modeling the surface roughness requires significantly more complex meshes or wall models [109,110], which is further exasperated by the variability in metal additive surface roughness. Given the already great computational cost of this analysis due to modeling using LES, the walls in the domain for this study were modeled as smooth.

4.2.2. Mesh Generation and Validation

A region of the two meshes that were generated and used for these simulations are shown in Figure 4-3(a) and 3(b). Both meshes were generated using the same commercial tool used for modeling, and made use of polyhedral cells. The mesh featured prism layers in order to accurately resolve thermal and velocity gradients in the near wall region with y^+ values to approximately one.

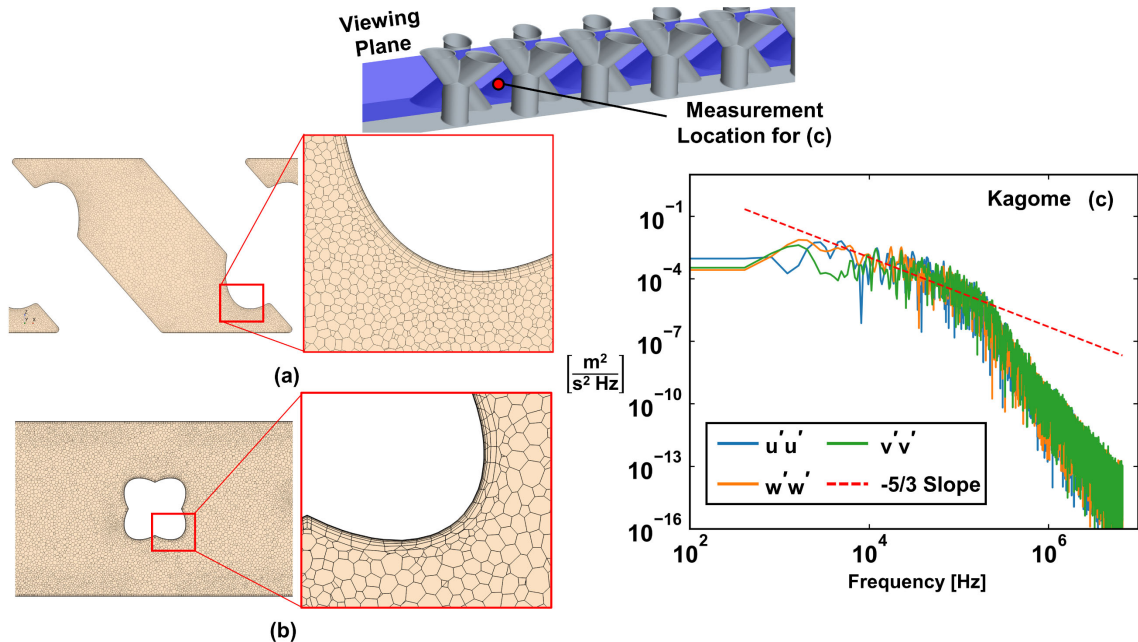


Figure 4-3. (a) Kagome and (b) body centered cubic mesh at the midplane of the domain and (c) the spectral power density of the three velocity components as a function of frequency at a point downstream of the first row of Kagome lattice.

Initial simulations of both geometries were computed using a steady Reynolds averaged Navier Stokes (RANS) simulation. These initial simulations were used in three capacities: to

determine the residence time in each domain, to approximate the Taylor micro and Kolmogorov length scales, and to serve as the initial conditions that were used for the LES simulations. The residence time was determined by tracking the amount of time it took an average particle to travel along a streamline from the domain inlet to the domain outlet. The residence time was approximately two milliseconds for both geometries. Estimations of the local Taylor micro and Kolmogorov turbulent length scales were extracted using built in software functions, and the domains were re-meshed such that the cell size fell between these two length scales, as recommended by the software user manual [107]. This remeshing process resulted in an average cell size in the core of the domain of approximately 28.2 microns for both lattices. The final mesh sizes were 13 million cells for the BCC lattice, and 15 million cells for the Kagome lattice. The non-dimensional grid scales $+\Delta x$ and $+\Delta z$ were estimated to be similar for both geometries, with an average value of approximately 50. The non-dimensional y grid scale $+\Delta y$ was one or lower for the entire domain. The re-meshed domains were then run using RANS until they were converged again, and these updated solutions were used as the initial state for the LES simulations.

The first step in determining whether a mesh is sufficiently resolved using LES is to determine the amount of turbulent kinetic energy (TKE) that was explicitly captured as compared to the amount that was modeled using the sub-grid model. The explicitly captured TKE was then compared to the TKE modeled using the sub-grid turbulence model, as recommended by Pope [111]. It was found that the turbulence captured was greater than 99% for the flow outside of the core mesh region, and greater than 95% for the vast majority of the flow inside of the core region, indicating that the mesh was well resolved.

As a secondary characterization of the mesh quality, a point was selected downstream of the second row of lattice where significant turbulence generation occurred. A time history of all three components of velocity were recorded at this point for a total of two residence times. Each component of the velocity was then converted into a spectral power density which was then plotted against frequency. An example of this analysis as completed for the Kagome lattice is shown in Figure 4-3(c), though the BCC lattice had a very similar response. The fluctuations in the three components of velocity at this point were roughly equivalent, indicating that the turbulence in this region was isotropic. All three components of the velocity from this analysis followed the expected $-5/3^{\text{rds}}$ slope from a frequency of approximately 10^4 Hz to 10^5 Hz, indicating that the mesh was sufficiently resolved.

After mesh validation was completed, the temperature, pressure, density, and three components of velocity were time averaged at each location in the entire domain for three full residence times in order to capture the bulk fluid motion and thermal transport. A time step was

considered converged when all residuals dropped by at least three orders of magnitude. Compute times for both simulations were on the order of several months using 100 cores on a computing cluster. The results of these simulations will be explored in detail in Section 3.

4.2.3. Benchmarking with Experimental Simulations

Comparisons of numerically predicted and measured heat transfer and friction factor were made to benchmark the simulations. For the heat transfer experiments, two coupons were manufactured using laser powder bed fusion (L-PBF) on an EOS M280 using Hastelloy-X. A similar sized coupon to those used in prior studies by the authors [105,106] was used to house the lattices. Unlike the modeled domain these coupons contained several more rows of lattice to ensure the flow became fully developed by the coupon exit. Additionally, there were not empty entrance and exit regions in these coupons like in the computational models, and instead the entire interior of the coupons consisted of the lattice core region of the modeled domain. Because of the differences in unit cell size, the manufactured Kagome coupon contained 19 rows of lattice unit cells, and the BCC design contained 25. There were seven lateral columns of the Kagome lattice in each coupon, and 10 columns in the BCC design. The coupons were CT scanned to validate that they were printed close to the design intent, and a section of the surfaces captured from these scans are shown in Figure 4-4(a) and 4(b). The as-printed porosity was $\varepsilon = 0.72$ for the Kagome lattice and $\varepsilon = 0.75$ for the BCC lattice. It should be noted that because the strut diameter of the BCC lattice was approaching the limits of what could be manufactured on the L-PBF system, there were consequently some variations in the as-printed strut diameter between individual unit cells. This variability and inherent surface roughness resulted in a 17% increase to surface area for both designs as compared to what was computationally modeled, which was the original design intent.

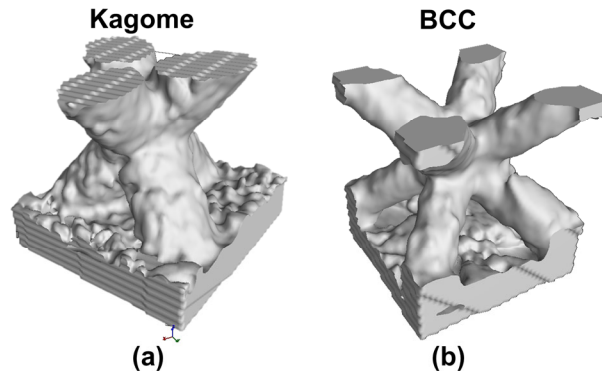


Figure 4-4. Single unit cell from CT scan of metal (a) Kagome and (b) BCC lattice test coupons.

To compare the predicted and measured pressure losses, two additional coupons were printed on a standard Stereolithography (SLA) 3D printer that represented the computational domain more precisely. These SLA coupons featured the upstream and the downstream regions

without lattice that was present in the computational domain. These coupons were also instrumented with pressure taps along the streamwise length to capture local static pressures. Following testing these coupons were cut open and the struts were measured using calipers. Both designs featured struts larger than the design intent, with the diameter of the BCC struts measured to be 0.58 ± 0.06 mm and the Kagome struts were measured to be 0.93 ± 0.06 mm.

Experiments were performed in a benchtop test that has been described in detail in prior publications by the authors [105,106]. In brief, the test rig features an upstream mass flow controller that meters the flow of air through an instrumented test section. This test section features two plenums that condition the flow entering the coupon to be of uniform velocity, and the flow exhausting from the plenum to undergo sudden expansion, ensuring that the inlet and outlet flow conditions were known. Each plenum was instrumented with a pressure tap and a differential pressure transducer was used to capture the static pressure loss across the coupon. The pressure inside of the test section was determined using a gauge pressure sensor that measured the downstream static pressure, and the local atmospheric pressure was used to determine the absolute pressure. The plenums in the rig were also instrumented with a series of thermocouples that were used to calculate the temperature of air upstream and downstream of the plenum. Isentropic flow relations were used to determine the temperatures and pressures exactly at the coupon inlet and outlet.

To quantify the internal heat transfer coefficients, a heating assembly was installed on both sides of a test coupon that impose a constant surface temperature boundary condition. These assemblies consisted of a surface heater placed between insulating foam and a copper block. Six thermocouples were placed precisely halfway through the thickness of the copper block in each heating assembly. Throughout both the foam blocks and the plenums there were a series of thermocouples which were used to determine the conduction losses, which were typically less than 1%. The temperature from the thermocouples in the copper blocks and the total heater power minus any losses were used in a one-dimensional conduction analysis to determine the coupon surface temperature. An energy balance was also performed during the experiments providing better than 3% closure.

Both test coupon geometries were tested at the same conditions used in the computational setup. The only deviation for the testing from the computational model was for the SLA coupons used to measure the local pressure loss, which were conducted at room temperature.

4.2.4. *Data Reduction*

There are many scaling methods used throughout the literature in studying lattice structures specifically related to the performance of their designs. Those variations include a range of

geometric features representing the length scales used such as duct hydraulic diameter, largest pore diameter, some combination of surface area and volume, and porosity. Caket et al. [112] have recently assembled a comprehensive summary of studies investigating the performance of lattice structures and noted that due to the unclear length scales it is difficult to directly compare the performance of lattice between studies.

For this study the Reynolds number (Re), friction factor (f), and Nusselt number (Nu) were scaled using the open duct hydraulic diameter. Since the computational results featured an infinitely wide duct due to the periodic boundary conditions, the hydraulic diameter definition reduces to twice the height of the duct, or $2H$. For the experimental results the test coupon hydraulic diameter was used, though it should be noted that due to the high aspect ratio of the test coupon duct (10:1), the resulting hydraulic diameter was 10% smaller than that of the infinite duct. For the velocity scale the mass average inlet velocity for a fully open duct was used for both the experimental and the computational domains. As such, the definitions for the Reynolds number (Re), friction factor (f), and Nusselt number (Nu) are given in Equations 4-1 through 4-3.

$$Re = \frac{u_{m,in} \cdot \rho_{in} \cdot D_h}{\mu} \quad (4 - 1)$$

$$f(x) = \frac{D_h}{\frac{1}{2} \rho u_{m,in}^2} \frac{\partial \bar{P}}{\partial x}(x) \quad (4 - 2)$$

$$Nu(x) = \frac{h(x) \cdot D_h}{k} \quad (4 - 3)$$

The local pressure gradient was found by first taking the average of the streamwise pressure, and then using a third order central differencing scheme to extract the gradient of this pressure as a function of streamwise position. The local heat transfer coefficient was determined using Equation 4-4, which was found by combining the equation for internal heat transfer with a constant surface temperature and the first law of thermodynamics.

$$h(x) = \frac{\dot{m} \cdot c_p \cdot (T_m(x) - T_{in})}{A_s(x)} \cdot \frac{\ln\left(\frac{T_{wall} - T_{in}}{T_{wall} - T_m(x)}\right)}{T_{in} - T_m(x)} \quad (4 - 4)$$

The surface area at a given streamwise position is defined as the area from the inlet to that position.

Finally the local fluid temperature throughout this study was normalized using Equation 4-5.

$$\theta_{x,y,z} = \frac{T(x, y, z) - T_{in}}{T_{wall} - T_{in}} \quad (4 - 5)$$

4.3. Results and Discussion

4.3.1. Local Pressure Drop and Heat Transfer

Measurements from the SLA test coupons and predictions of the development of the pressure loss in terms of a friction factor as a function of number of unit cells is shown in Figure 4-5(a). The results shown in Figure 4-5(a) indicate relatively good agreement between the pressure measurements and predictions, especially for the Kagome geometry. The trend in the results for the BCC agree with the experiments, however, there is a slight overprediction of the friction factor as the flow becomes fully developed. This disagreement is attributed to the sensitivity to the strut diameter for the BCC lattice. As previously discussed, the strut diameter approached the size limit for what could be printed and resulted in slightly larger struts than intended as shown in Table 4-1. Consequently, the pressure drop from the BCC coupons was measured to be higher than predicted computationally. Both the strut diameters and the unit cell size were larger for the Kagome lattice than they were for the BCC lattice. This meant that even though the SLA Kagome lattice coupons had a similar level of deviation from the intended strut diameter as the BCC lattice, the impact on the overall lattice porosity was smaller, translating to a smaller impact on the expected pressure drop. Given that the Kagome and BCC lattice used similar computational setups and that the experimental measurements from the Kagome lattice had good agreement with the computational results, it was concluded that the simulations represented the internal flow field from the test coupons.

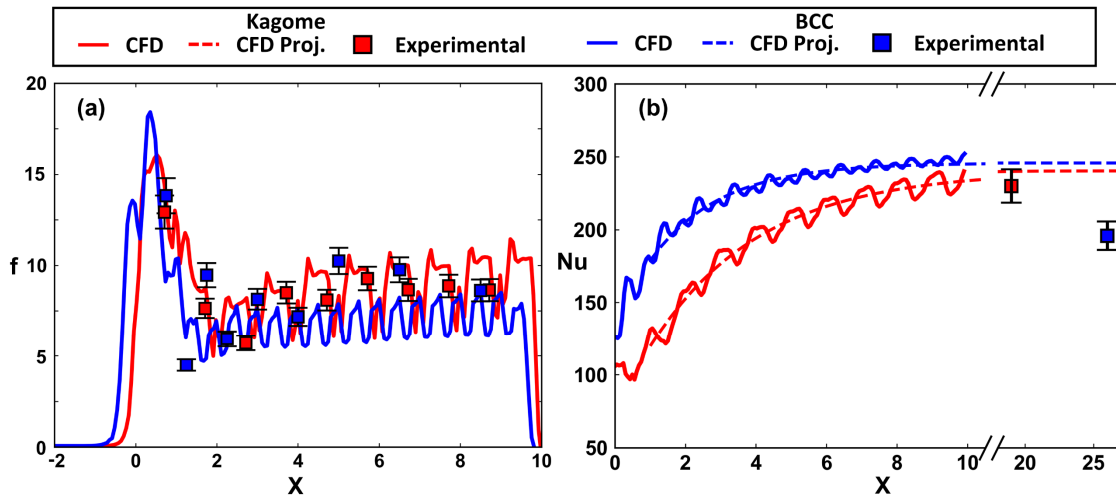


Figure 4-5. (a) Friction factor and (b) Nusselt number as a function of X.

The computational predictions show an oscillatory trend in friction factor beyond the first row for both the BCC and Kagome lattice as shown in Figure 5(a). These oscillations correlate directly with the flow's interactions with lattice struts. The areas of tightest flow constriction in each of the lattice designs force the flow to accelerate, increasing the pressure loss and consequently

increasing the local friction factor. Additionally, the flow stagnates on the lattice struts, which increases the static pressure in front of the lattice followed by a decrease in the static pressure in the wakes that form behind the struts. Because these high- and low-pressure regions are a function of the flow's interactions with lattice struts, the increased number of struts in the BCC lattice as compared to the Kagome lattice results in a higher oscillation frequency for the BCC lattice relative to the Kagome. Because the Kagome lattice struts are larger than the BCC lattice, larger wakes with more significant flow area reductions are induced causing the amplitude of Kagome lattice's oscillations to be greater than those seen in the BCC lattice.

For the Kagome lattice, the friction factor oscillates around a constant value after approximately four unit cells, whereas the BCC lattice's friction factor oscillates around a constant value after two unit cells. This near constant oscillation is indicative of the flow becoming hydrodynamically fully developed. Taking the average of friction factor in the region between $X = 5$ and $X = 9$ shows that fully developed value for the Kagome lattice is $f = 9.1$ and the fully developed value for the BCC lattice is $f = 7.1$. For comparison, the friction factor of the Kagome and BCC lattice were found experimentally to be $f = 8.7$ and $f = 8.6$ respectively. The deviation for the BCC lattice is the result of the overbuild struts, as mentioned previously. The Kagome lattice experimental results were within experimental uncertainty of the computational results. This difference in friction factor can be attributed to differences in local wall shear stress and in the strength and distribution of eddies in the wake regions of each lattice, which will be discussed in greater detail in Sections 3.2 and 3.3 respectively.

In addition to the development of the local friction factor profiles, there is significant interest in the development of the local Nusselt number, which is shown in Figure 4-5(b). Since the computational domain had fewer unit cells than the experiments with the measured heat transfer values being only a global average, the direct comparisons between the predicted and measured were not possible. However, the predictions in Figure 5(b) indicate nearly a fully thermally developed BCC lattice while the Kagome appears to continue to increase at the end of the domain. To compare the predicted to the measured Nusselt numbers, shown in Figure 4-5(b), a curve fit between row values of $X = 0.5$ and $X = 9.5$ for both lattices were done and are shown using a dashed line. The fully developed projected Nusselt value approaches $Nu = 245$ compared to the measured being $Nu = 196$ for the BCC lattice whereas the projected and measured values for the Kagome lattice were $Nu = 240$ and $Nu = 230$, respectively. The BCC and Kagome lattices reaches 95% of the projected fully developed value by $X = 4.5$ and $X = 8.3$. This difference in predicted heat transfer is the result of differences to the local thermal profiles, which is discussed in more detail in Sections 3.2 and 3.3.

Comparing the experimental data to the computational data, it is clear that the Kagome lattice LES matches the experimental value within uncertainty, but the BCC design does not. The Nusselt number of these lattice is primarily impacted by two things: the porosity and surface area of the lattice. The porosity of the experimental BCC lattice was the same as the computational model, whereas the experimental Kagome lattice was slightly less porous due to overbuilding during manufacturing and surface roughness features. Because the experimental Kagome lattice coupons were less porous than computational model, the experimental heat transfer should have been greater than the simulated heat transfer [99], but instead it was slightly lower. Both of the experimental lattice coupons had 17% greater surface area than intended due to local roughness features present on the surfaces of the struts. If the as-designed surface area was used to calculate the Nusselt number, the fully developed value increases to $Nu = 231$ and $Nu = 269$ for the BCC and Kagome lattice respectively. This adjustment to the surface area makes the BCC lattice performance agree with the computational model within experimental uncertainty, and makes the experimental Kagome lattice have a significantly greater Nusselt number than the computational model, as would be expected due to the decreased porosity. The better agreement using the as-designed surface area implies that the added surface roughness did not effectively increase heat transfer. The fully developed Nusselt number and friction factor for the experimental and computational analysis are summarized in Table 4-1, using both the as-printed and as-designed surface areas.

Similar to the momentum development there is a distinct spatial periodicity in the Nusselt number of the Kagome lattice, oscillating as the flow navigates around each row of lattice. This periodicity reaches a minimum at the center of a Kagome unit cell, indicating the sudden flow area reduction results in a local decrease to the Nusselt number. The BCC lattice's Nusselt number was notably less periodic by comparison, with a somewhat uniform increase in Nusselt number as a function of number of unit cells. The variation in oscillations between the two lattices is a function of local velocity and thermal profiles, which will be discussed later in Section 3.2.

3.3 Flow and Thermal Developing Region

To better understand how the flow develops through the entry region of the lattice structures, normalized, time-averaged thermal and velocity profiles at five streamwise planes were taken normal to the flow. The profiles for the Kagome lattice are shown in Figure 4-6. Starting with the Kagome lattice shown in Figure 4-6(a-j), the predictions indicate significant secondary flows including flow reversals that result in thermal fields with large variations. The secondary velocities for the Kagome lattice take the form of a vortex pair that drives the flow to have the highest velocities near the bottom juncture with the adjacent cell. Between the 1st (Figure 4-6(b)) and 2nd

(Figure 4-6(c)), rows of lattice there are also smaller, weaker vortices present in the bottom corners of the Kagome lattice, which dissipate after the 3rd (Figure 4-6(d)) row of lattice. These smaller vortices are the result of the upstream horseshoe vortex which forms just in front of the first row of the Kagome lattice. In the later rows of the Kagome lattice, the time-averaged horseshoe vortices are not visible resulting from the unsteady shedding from the struts. The thermal profiles for the Kagome lattice, shown in Figure 4-6(f-j), result explicitly from the secondary velocities with the cooler air near the bottom of the channel convecting towards the top of the channel.

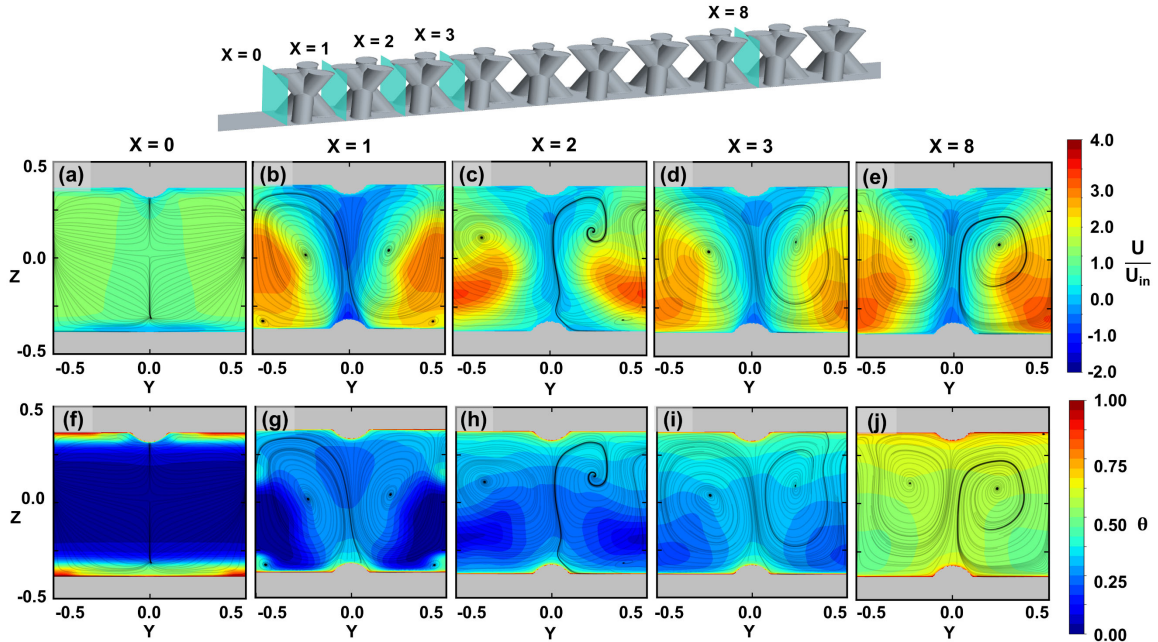


Figure 4-6. Normalized time-averaged (a-e) velocity and (f-j) thermal contours at five streamwise planes for the Kagome lattice.

The velocity distribution presented in Figure 4-6(c) indicates that after the second unit cell the flow accelerates as it transitions to fully developed from the distribution shown in Figure 4-6(b) and Figure 4-6(d). During this transition, there is a significant increase in turbulence intensity, which will be discussed in Section 3.3. The bulk of the flow can be seen to be moving on either side of the wake of the lattice in the first row (Figure 4-6(b)) with the secondary flows appearing to be similar between the third (Figure 4-6(d)) and eighth rows (Figure 4-6(e)). This similarity between the 3rd and the 8th rows of lattice is represented in the friction factor shown in Figure 4-5(a), where after the third row the trend in friction factor becomes spatially periodic. For the fully developed flow, there are regions of high velocity near the base of both sides of the lattice unit cell as shown in Figure 4-6(d). The biased flow resulted in 15% greater heat transfer on the base of the channel than on the top surface, similar to what was reported previously by Liang et al. [83]. To

explore this formation in greater detail, contours of the time-averaged normalized vorticity with in-plane streamlines are shown for three streamwise planes in Figure 4-7.

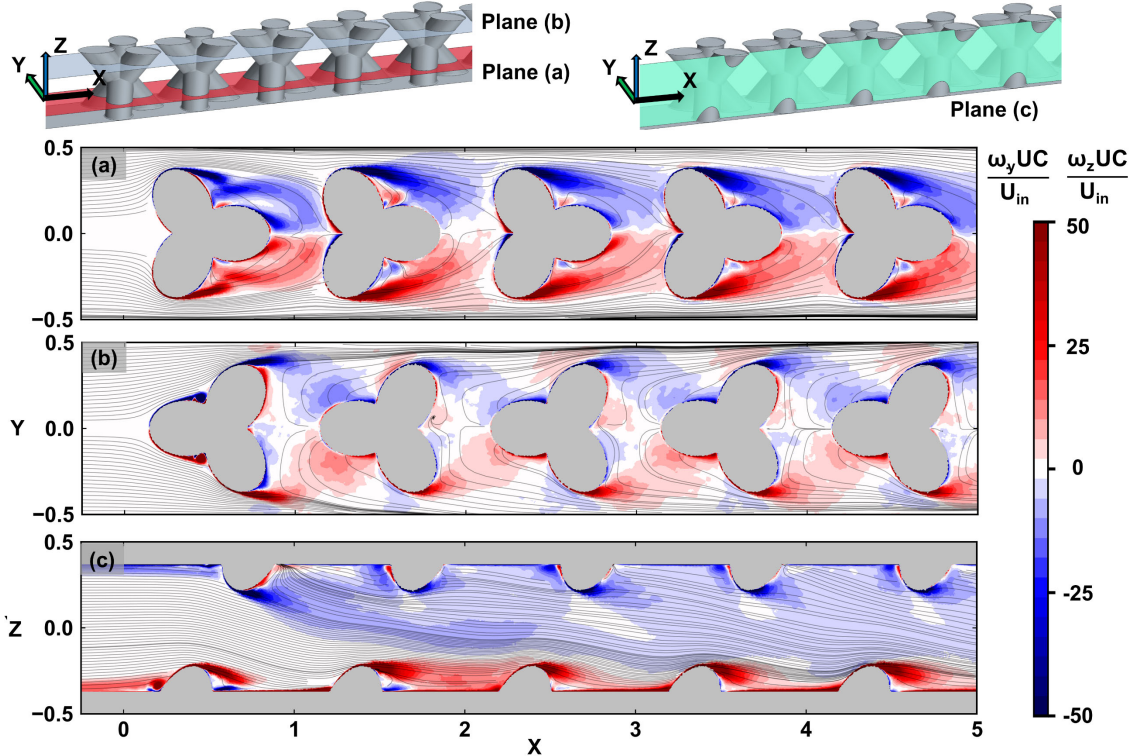


Figure 4-7. Normalized time-averaged vorticity in three streamwise planes for the first five rows of the Kagome lattice (a-c).

As the flow encounters the first Kagome unit cell, it impinges on the two front facing struts in the base of lattice and the one front facing strut at the top of the lattice. While the flow navigates around the base of the lattice, a region of vortical flow can be seen in Figure 4-7(a) on either side of the first unit cell, showing the formation of a wake. Some amount of the flow that encounters this first row passes between the bottom two struts and is injected into this wake, forming another vortex pair that extends to the following unit cell. The flow that is captured in these wakes is directed into the backwards facing strut near the base of the channel. This strut forces the fluid in the center of the unit cell upwards. Along the top of the channel the flow is diverted to either side of the unit cell by the single front facing lattice strut, and then collides with and subsequently separates from the two back facing struts as seen in Figure 4-7(b). As the wake forms from these separation points it is interrupted by the front facing strut from the second lattice unit cell. This interruption forces the flow and wake downwards, as shown by the streamlines in Figure 4-7(c). The composite effect between the interior flow being directed upwards and the exterior flow near the periodic boundaries being directed downwards results in the rotational secondary flows between cells that were seen previously in Figure 4-6.

Continuing downstream, the flow along the base of the channel passes over the front facing struts of the second row of lattice, and a larger wake forms that occupies the full width between the second and third unit cells. Because the top surface wake from the first unit cell is also continuing downstream, the flow area becomes effectively reduced and results in the high velocity region that was identified in Figure 4-6(c). Beyond the third lattice unit cell, the wake from the top struts of the first unit cell diffuses as the flow becomes highly mixed. This reduces the maximum flow speeds, however the rotational flow between cells continues to drive the fluid near the periodic boundaries downwards, and the flow in the interior upwards, as was seen in Figure 4-6.

The Kagome lattice flow fields are significantly different from the BCC lattice's, as shown in Figure 4-8 (a-e). There are many more vortices present for the BCC lattice than for the Kagome, with each BCC strut generating a pair of vortices. The generation of these vortices leads to periodic performance in friction factor seen in Figure 5(a), and the vortices smaller size relative to the Kagome vortices result in less pressure drop. The BCC vortices increase mixing from the near wall region, distributing flow from the center of the channel with higher velocities at the junction between the cells and in the near wall regions. After three unit cells ($X=3$), the velocity distribution shows the highest velocities occurring between the cell junctures. These high velocity regions transport the upstream cooler fluid downstream as shown in the thermal fields in Figure 4-8(j). Increased mixing from the secondary flows in the wakes of the BCC lattice resulted in higher Nusselt numbers as compared to the Kagome lattice, as was seen in Figure 4-5(b).

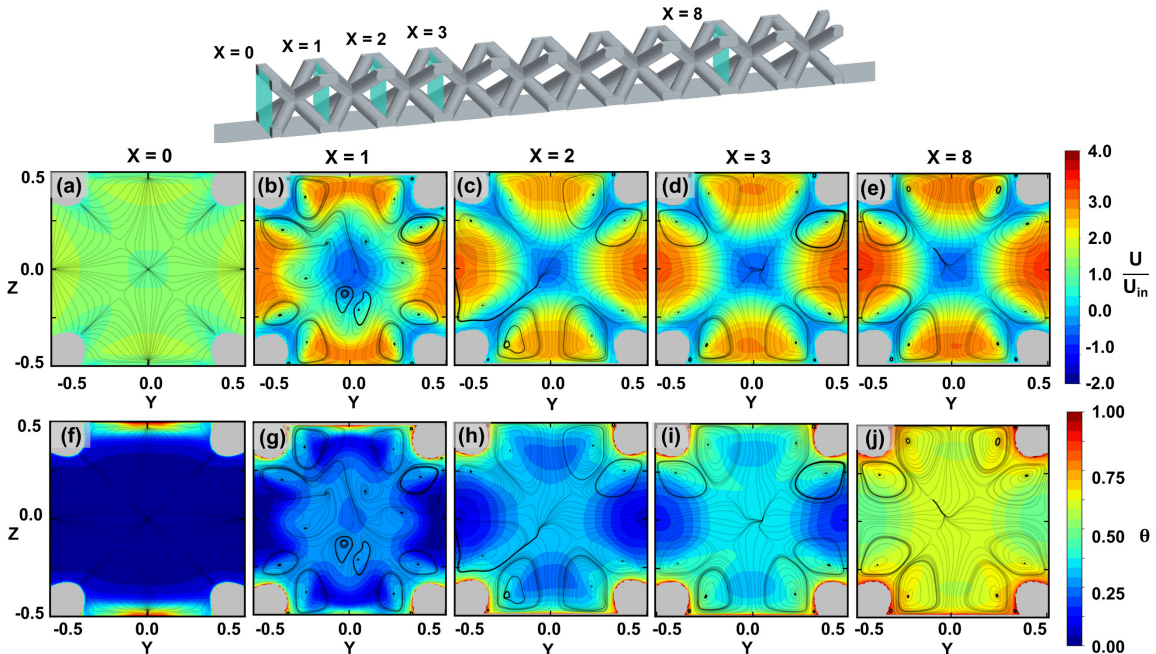


Figure 4-8. Normalized time-averaged (a-e) velocity and (f-j) thermal contours at five streamwise planes for the BCC lattice.

Just after the first row of lattice Figure 4-8 (b)), the flow is largely distributed to the regions near the center of the periodic boundary at $Y = -0.5$ and $Y = 0.5$ and along center of the top and bottom walls at $Z = -0.4$ and $Z = 0.4$. After the second row ($X = 2$), there is a notable bias of the flow to the cell junctures as shown in Figure 4-8(d), as the bottom and top walls induce increased drag reducing the overall flow through these regions. The flow distribution at these planar locations remains largely the same after the second row. Unlike the flow distributions seen with the Kagome lattice, there is a distinct symmetry to the flow distributions present for the BCC lattice, stemming from the overall symmetry of the geometry.

The time-averaged streamwise thermal and velocity fields at a vertical and horizontal midplane section for the Kagome and BCC lattice are shown in Figure 4-9 and Figure 4-10, including zoomed in regions after the 1st and 8th cells. Along the base of the channel in the core region of both lattice the thermal boundary layer is very thin relative to the developed boundary layer just upstream of the lattice at $X = 0$ due to the locally increased flow speeds, as shown in Figure 4-9(b) and Figure 4-10 (b). These thin boundary layers enhance heat transfer significantly by enabling a higher thermal gradient near the wall. In addition to short thermal boundary layers, the heat transfer is also enhanced by the boundary layer detachment in the wake region of the lattice, and the subsequent turbulent mixing which will be explored in Section 3.3. These wakes result in recirculation zones just behind the center of the unit cells, which are shown in Figure 4-9(c-d) and Figure 4-10(c-d) which further enhance mixing and heat transfer. The velocity in these recirculation zones is much slower than those near the periodic boundary, with the flow in some regions being nearly stagnant. In these regions the fluid is able to heat up significantly, such as near the top of the Kagome lattice as shown in Figure 4-9(e-f). However, in the region between two rows of lattice, cooler fluid is transported into this wake by the cooler fluid that was identified in Figure 4-6 and Figure 4-8. This transport results in a decrease in local fluid temperature downstream of the wake, and an example of this phenomenon can be seen in Figure 4-9(c) and Figure 4-10(c). This streamwise thermal gradient is significantly steeper for the Kagome lattice than the BCC lattice due to the increased mixing in the BCC lattice from the secondary flows identified in Figure 4-8. The difference in thermal gradient between the two lattice causes the local Nusselt number of the Kagome lattice to have greater peak-to-peak variation than the BCC lattice, as seen in Figure 4-5(b).

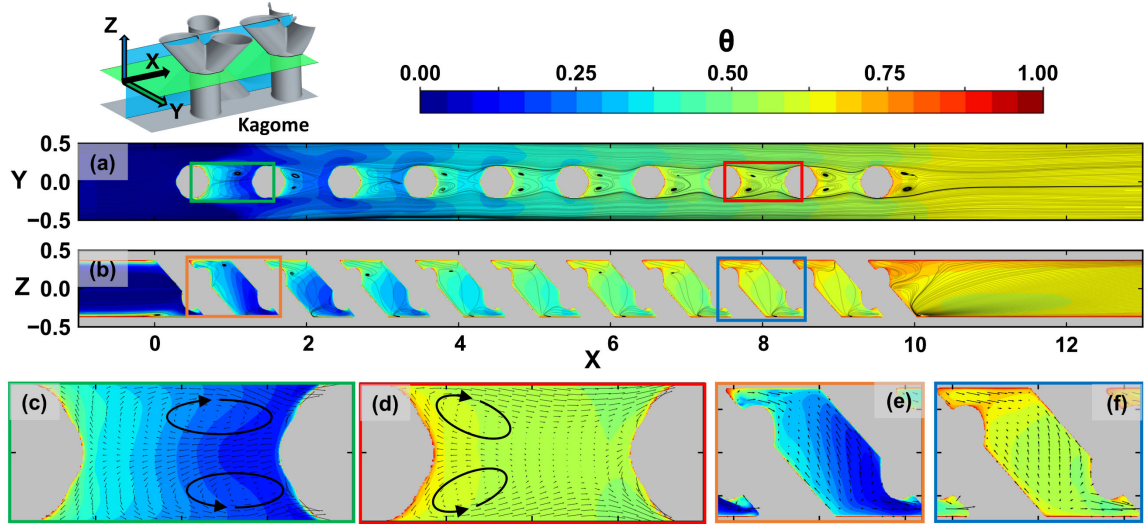


Figure 4-9. Normalized time-averaged thermal contours with streamlines in the (a) horizontal and (b) vertical midplane of the Kagome lattice with highlighted regions of interest (c-f).

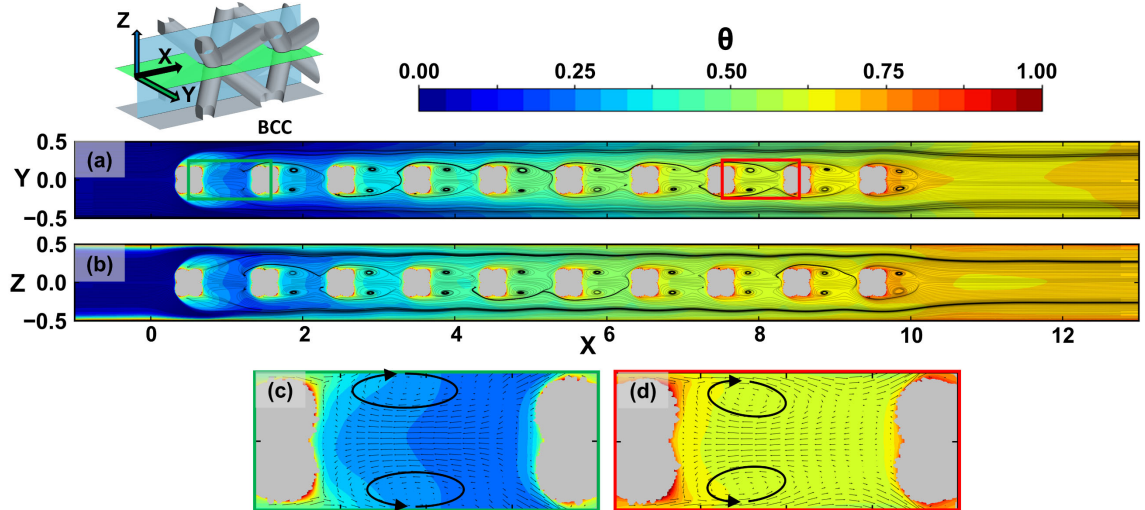


Figure 4-10. Normalized time-averaged thermal contours with streamlines in the (a) horizontal and (b) vertical midplane of the BCC lattice with highlighted regions of interest (c,d).

The streamlines in the horizontal planes displayed in Figure 4-9(a) and Figure 4-10(a) show that the wake behind the first row of both lattice types is notably larger than the downstream wakes. These wakes result in an effective reduction in flow area for this first row, which in tandem with the flow impinging on the first unit cell surface lead to the substantial pressure drop and friction factor presented in Figure 4-5(a). The wakes between the second ($X = 3$) and ninth ($X = 8$) rows are similar for both lattice, showing again that the flow has transitioned to being fully developed. A pair of vortices form in the wake region of behind each row of the Kagome and BCC lattices and are indicated using two ovals in Figure 4-9(c-d) and Figure 4-10(c-d). The location of the vortices relative to the center of the BCC unit cell is very similar for all rows of the BCC lattice, but change for the Kagome lattice after the second row. The center of the vortices in the wake of the first row

($X = 1$) are located approximately 0.6 unit cells away from the center of the first row. In all subsequent rows, the center of the wake vortices shifts to be approximately 0.3 unit cells away from the center of the unit cell.

For the BCC unit cell, the vortical formations are the same in both the vertical (Figure 4-10(a)) and horizontal (Figure 4-10(b)) planes due to symmetry. In contrast, the flow field in the horizontal (Figure 4-9(a)) and vertical (Figure 4-9(b)) planes of the Kagome lattice are distinct. Looking to Figure 4-9(e-f), the flow in the vertical plane can be seen to move through the bottom struts of the lattice, and then move upwards towards the top of the channel, following the streamlines that were shown in Figure 4-7. Unlike the flow in the horizontal plane, the secondary flows in the vertical plane of the core region were not significantly a function of the streamwise location for the Kagome lattice.

The flow in the wake behind the core region for both lattice designs return to the flow distribution found between parallel flat plates after several additional rows of lattice. The flow downstream of the BCC lattice shows a fully developed internal flow distribution approximately two unit cells after the core region, but the Kagome lattice takes as many as five unit cell lengths. The fully developed distance downstream of the lattice cells is a function of the Kagome lattice having highly skewed flow along the base of the channel, as was seen in Figure 4-6, which continues well after it leaves the core region, as shown using streamlines in Figure 4-9(b) after $X = 10$.

4.3.2. *Turbulence and Unsteady Flows*

The turbulence intensity contours for the two lattices are shown in Figure 4-11(a-d) for two different streamwise planes. In general, the turbulence intensity levels are much higher for the Kagome than for the BCC lattices. The Kagome lattice shown in Figure 4-11(b) has a peak in turbulence intensity just after $X = 2$ of $TI = 1.61$. The maximum of TI for the Kagome lattice is located where the velocity profiles in the Kagome lattice are not yet fully developed as was seen in Figure 4-6, with the high turbulence intensities indicating high flow unsteadiness. The BCC lattice has lower turbulence intensities, shown in Figure 4-11(c) and Figure 4-11(d), with a maximum turbulence intensity of $TI = 0.87$. Regions of high turbulence intensity for both types of unit cell relate to regions of increased heat transfer. Highly rotational regions like those in the wake of a given unit cell experience increased turbulence intensity resulting from the unsteady flow due to the wakes shedding from the struts. The increased turbulence intensity for the Kagome lattice as compared to the BCC lattice is reflected in the friction factor results presented in Figure 4-5(a), as the higher turbulence intensity leads to increased pressure drop and subsequently higher friction factor. While generally speaking increases to turbulence intensity results in increases to heat

transfer, prior researchers have identified that there is a limit to how much enhancement increased turbulence intensity can provide [113]. This limit is reflected in the heat transfer results, where despite the Kagome lattice having a greater overall turbulence intensity, it has a lower Nusselt number than the BCC lattice.

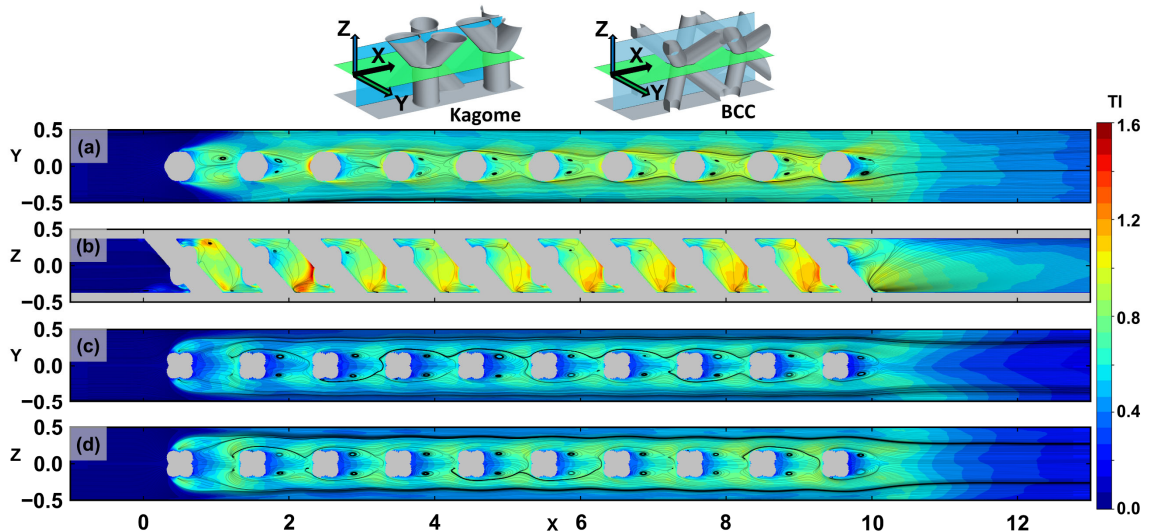


Figure 4-11. Turbulence intensity at two planar locations for the (a-b) Kagome and (c-d) BCC lattice.

To identify unsteady flow structures present in these areas of high turbulence intensity, the unsteady y-component of vorticity and temperature were captured at distinct time intervals for the Kagome and BCC lattice and is shown in Figure 4-12 and Figure 4-13. Beginning with the Kagome lattice in Figure 4-12(a), there are many instantaneous vortices in the regions between the first three rows of unit cells in Figure 4-12(a). These vortices indicate the flow is highly mixed, especially in the regions of highest turbulence intensity as shown in Figure 4-11(b). There does not appear to be any coherent or consistent structures, but instead this flow appears to be dominated by turbulent mixing. Regions of high vortex strength directly correlate with regions of increased thermal transport, as seen in instantaneous theta contours shown in Figure 12(b). Particularly the vortices that form due to wake shedding, such as those at approximately $Z = 0, X=0.8$, there is substantial thermal transport from the near wall region to the bulk flow. In certain areas of the flow, such as near the top wall at $X=2$, there is a recirculation zone that limits local heat transfer, denoted by the local vortical flows and temperatures approaching $\theta = 0.5$.

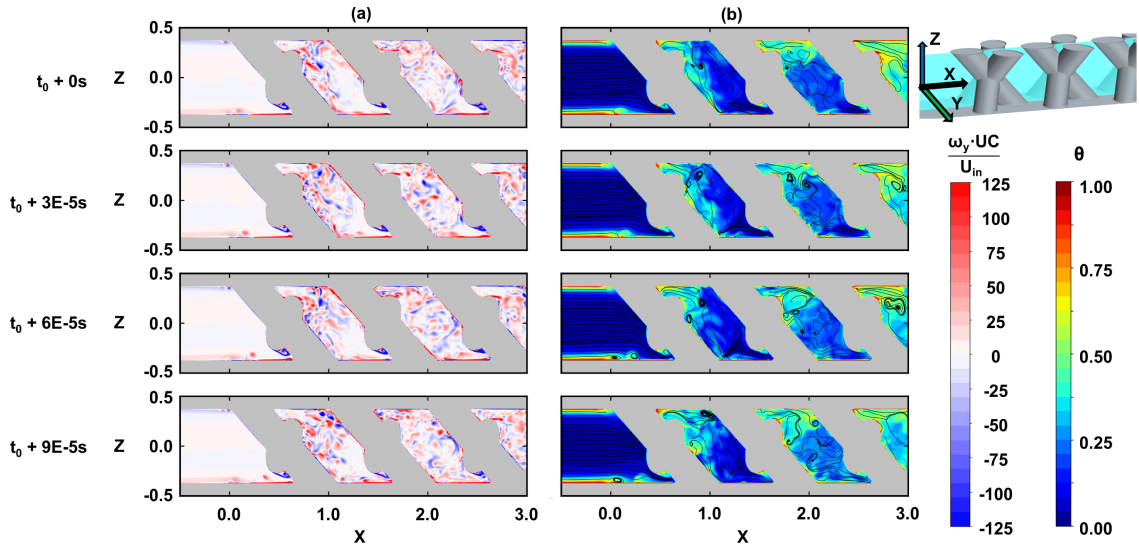


Figure 4-12. Instantaneous (a) vortices and (b) thermal profiles around the Kagome lattice at four time intervals.

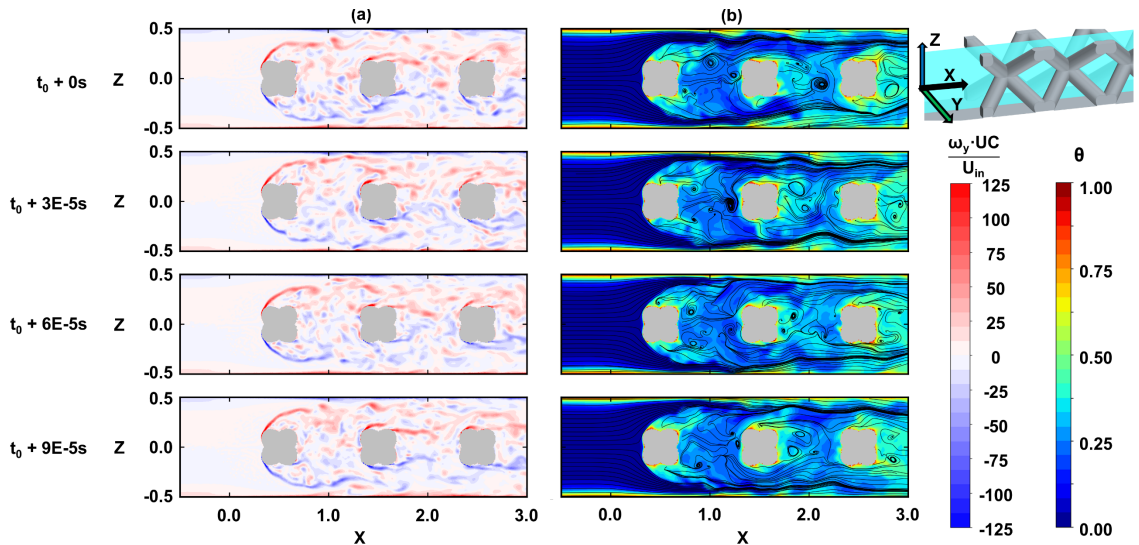


Figure 4-13. Instantaneous (a) vortices and (b) thermal profile around the BCC lattice at four time intervals.

Just upstream of the Kagome lattice a horseshoe vortex forms along the bottom wall periodically in time and is ingested into the core region of the lattice. This vortex forms, grows in strength, detaches from the wall, and is ingested 16 times per flow through time of the domain. This vortex formation and destruction can be seen at $X = 0.1$ in Figure 4-11(b), where there is a slight increase in turbulence intensity, and in the time averaged thermal profiles shown Figure 4-9(b), where the boundary layer just upstream of the first row of lattice dissipates before coming into contact with the actual unit cells.

The flow between rows of the BCC lattice has more coherent vortical structures than the Kagome lattice, as shown in Figure 4-13(a). At the interface of the upstream flow and the wake of the first row of BCC lattice there is a region of vorticity that is constant in time, indicating flow

separation. The separated flow region enables significant thermal transport, as shown in Figure 4-13(b). Following the first row, the span of the wake that forms from the center of the unit cell is only the width of the center region, and much of the flow around the lattice is mixed. The mixing in these rows enhances the thermal uniformity of the fluid through the BCC lattice. As these vortices shed from the center of the BCC unit cell, they interact with the boundary layer forming on the endwall, pulling it away from the near wall region. This vortex-boundary layer interaction causes the size of the thermal boundary layer to vary substantially as the fluid passes through the core region and indicates that the fluid near the endwall is circulated into the bulk flow more effectively than was seen for the Kagome lattice. The result of this more substantial interaction is a more uniform increase in the thermal profile than was seen in the Kagome lattice when time averaged, as was shown in Figure 4-9 and Figure 4-10. Subsequently, the local BCC lattice Nusselt number had smaller amplitude oscillations than the Kagome lattice, and the magnitude of the Nusselt number was also greater as shown in Figure 4-5(a).

To understand the fundamental motions of the vortices being shed from the two types of lattices, a transient spectral analysis was completed to determine the dominant frequencies in the U component of velocity. This analysis was completed by saving the instantaneous velocities at every location in the planes shown in Figure 4-9(a) and Figure 4-9(c). The time histories of these velocities were reconstructed, and a fast Fourier transform (FFT) was completed at each point to convert the velocity into the frequency domain. The power spectrum was calculated from the FFT to identify which frequency dominated the local velocity signal. The magnitude of the power spectra of these locally dominant frequencies varied considerably depending on the location in the spatial domain. To identify the regions of the most significant periodic flow, the frequencies whose magnitude were in the top 25% of all of the locally dominant frequencies were isolated. To normalize the isolated dominant frequencies (n), the local Strouhal number was calculated and is shown in Figure 4-14. The length scale for the Strouhal number was the width of the maximum flow obstruction at the center plane, and the velocity scaling was the local time-averaged velocity.

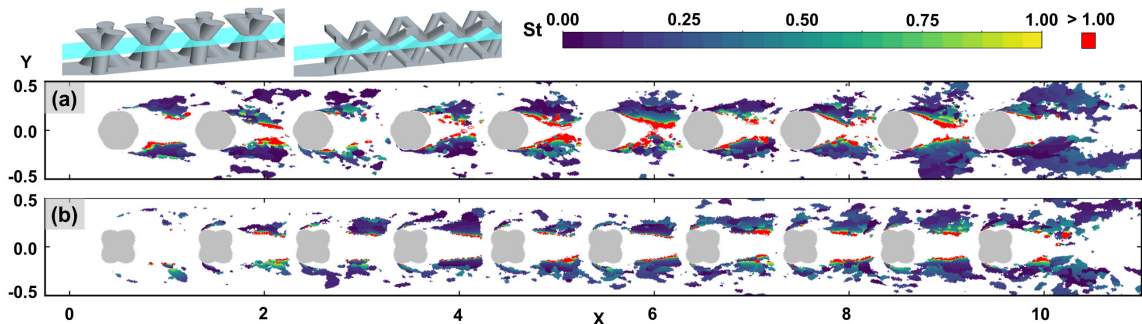


Figure 4-14. Local Strouhal number in the wake region of the (a) Kagome and (b) BCC lattice.

The Strouhal number is defined as the ratio of unsteady acceleration to the advective acceleration for a flow. For a single bluff body in cross flow, the expected Strouhal number is $St = 0.2$ in flows with a Reynolds number between $Re = 1,000$ and $Re = 100,000$ [114]. However, prior investigations have identified that augmentations to the yaw of the cylinder can decrease the Strouhal number [115], and that cylinders in a bank arrangement, such as pin fins, can cause the Strouhal number to increase beyond values of $St = 0.4$ using velocity scaling similar to what was used in this analysis [116].

For the present investigation the regions where the wake shedding occurs is clear, with wakes shedding halfway along the streamwise span of the center of a Kagome lattice unit cell (Figure 4-14(a)) and almost immediately after coming into contact with the center of the BCC lattice unit cell. Both locations represent areas where the span of the geometry decreases, which results in a boundary layer separation. The Strouhal numbers associated with these regions near the point of separation and just downstream of it lie in the range of $St = 0.05$ to $St = 0.5$, which is similar to what has been seen in prior pin bank experiments [116], due to large scale alternating eddy shedding [117]. The local Strouhal number increases to well in excess of $St = 1.0$ at the wake interface just behind the center of a given lattice unit cell due to high frequency vortices present in the wake region, as was seen in Figure 4-12 and Figure 4-13. In these regions the high frequency vortices that form in the shear layer of the wake dominates local oscillations in the flow and the associated Strouhal number, as compared to lower frequency instabilities due to the alternating eddy shedding. In the wake of the final row of lattice, the regions of the flow where $St > 1.0$ for both the BCC and Kagome designs are less prominent, but there are larger regions of more moderate Strouhal numbers ($St = 0.05-0.4$). In these regions the alternating eddies from the final row of lattice propagate downstream and are not interrupted by additional rows of lattice, allowing the vortices shed in this region extend out to full span, unlike what was seen in the earlier rows. For the Kagome lattice shown in Figure 4-14(a), the regions of the flow outlined by Strouhal numbers greater than one are cylindrical in all but the regions behind the first and last row, whereas these regions are largely rectangular in shape for the BCC lattice shown in Figure 4-14(b). In the regions of the flow where $St > 1.0$, the time averaged local velocities approach 0 as the flow transitioned to being reversed in the wake of the lattice, as was seen in Figure 4-9 and Figure 4-10. As was seen in Figure 4-12 and Figure 4-13, the local flow instabilities characterized by the Strouhal number enhanced thermal transport, which subsequently increased the local Nusselt number. These periodic flow mechanisms also increased viscous dissipation, resulting in significant pressure losses and friction factor values.

4.4. Conclusion

Two lattice structure designs were explored using large eddy simulations to understand underlying physical phenomena regarding thermal and momentum development, as well as unsteady flow features that result in high turbulence regions. Simulations were compared to experimental results and showed generally good agreement, and reasons for deviations between the two methods were identified. The friction factor for Kagome and BCC lattice was seen to become fully developed after four and two unit cells respectively, with the Kagome lattice friction factor being greater than the BCC lattice friction factor. The number of unit cells before the flow became fully developed was found to be a function of the local velocity distribution. The flow thermally developed within approximately four unit cells for the BCC designs and after eight unit cells for the Kagome, which was found to be the result of variations in the velocity profile and changes to the secondary flow structures as the fluid moved downstream. Once fully developed, the flow in the Kagome lattice was skewed, with one side of channel featuring two high velocity regions. The two high velocity regions were found to develop due to the interactions between the rotational wake regions and the lattice struts. The turbulence intensity was found to be a function of lattice unit cell design, with the Kagome lattice having higher local turbulence intensity than the BCC design. This variation was found to be the result of highly unsteady flow that formed as the Kagome lattice approached a fully developed flow condition. Vortices shed from both the BCC and Kagome lattice interacted with the endwalls, resulting in periodic boundary layer detachment in the wake region of the lattice designs, which ultimately enhanced heat transfer. Spectral analysis revealed that the wake shedding in the core lattice region occurred at a similar Strouhal numbers to prior pin bank experiments, with some regions of periodic flow dominated by large scale alternate eddies and other regions dominated by vortices present in the wake shear layer.

This study uniquely identified the time dependent structures present in the Kagome and BCC lattice designs, and further classified the development of friction factor and Nusselt number through rows of these lattice. The specific flow structures that contributed to this development were also determined and described in detail. This study also highlighted the use of large eddy simulations as a viable and valuable method for exploring lattice structure performance. Future work will be needed to explore additional styles of lattice structures, and identify how best to scale their performance to enable use in a myriad of applications.

5. SCALING HEAT TRANSFER AND PRESSURE LOSSES OF NOVEL ADDITIVELY MANUFACTURED RIB DESIGNS⁵

5.1. Abstract

Rib turbulators are a key cooling feature that enable increased heat transfer on the interior of gas turbine components. As metal additive manufacturing becomes available for developing turbine parts, it is becoming increasingly important to understand how the surface roughness intrinsic to this manufacturing method impacts the performance of rib turbulators. To explore what impact roughness has on rib turbulator performance, several relevant scale test coupons were manufactured from a variety of super alloys on a range of additive machines. Additionally, several coupons were built at large scales to effectively reduce the relative roughness size impacts and determine scale effects. A range of different wavy broken rib designs, varying both rib wavelength and orientation within a channel were evaluated. Coupon geometry and surface roughness were characterized using both computed tomography scans and optical profilometry. Variations between the print methods were found to have limited impact on the surface roughness, but significant impact on the accuracy to meet the design intent with rib heights varying by 30%. Following characterization, coupons were flow tested and it was found that the ribs that more regularly disturbed the flow as a function of their geometry most significantly enhanced heat transfer and pressure drop. The performance index of the broken wavy ribs was similar to other advanced rib designs, such as broken or V shaped ribs, but augmentations to heat transfer and pressure drop were generally lower. The rib performance was compared as a function of relative roughness, and it was found that increases in relative roughness resulted in increased friction factor and heat transfer, especially at higher Reynolds numbers

5.2. Introduction

The gas turbine engine is critical element of modern life, powering as many as 26,600 active aircraft worldwide with projections estimating a 22% increase to total turbine aircraft over the next decade [118]. As more turbine engines enter operation, guaranteeing they operate as efficiently as possible will be critical to both the environment, as well as to reducing fuel waste. One way to improve the efficiency of a gas turbine engine is to ensure that the cooling air used to improve the life and durability of individual components is used as effectively as possible by leveraging advanced internal cooling schemes.

⁵ Corbett, T. M., Thole, K.A. “Scaling Heat Transfer and Pressure losses of Novel Additively Manufactured Rib Designs” GT2024-122792, *under review*

Cooling schemes typically implemented in gas turbine components feature a wide range of internal features including pin fins, microchannels, and the focus of the current study, surface ribs [3]. Over the past few decades, surface ribs have received significant attention for use in a gas turbine environment, as summarized by Han [119]. Recent studies have explored the use of increasingly complex rib designs, managing to continue to improve heat transfer performance by encouraging complex secondary flows.

One way that complex rib designs can be studied is by leveraging additive manufacturing (AM), which is typically cheaper and faster than traditional cast components for development parts [120]. Additive manufacturing does not come without its own complications however, typically in the form of reduced mechanical strength and significant surface roughness. While the impact of surface roughness on certain internal designs has been explored at length, the impact of surface roughness on the performance of rib designs is still not well understood.

This study experimentally and computationally investigated a suite of additively manufactured surface rib designs and compared how differences in their design impacted their local and bulk heat transfer and pressure loss characteristics. Additionally, this study investigated coupons manufactured at multiple scales, while continuing to match non-dimensional parameters and Reynolds numbers, to identify how diminishing relative roughness impacted thermohydraulic performance.

5.3. Literature Review

Early studies into rib features focused on ribs at various angles relative to the flow direction in rectangular channels, and on the aspect ratio (width over height) of the rectangular channel. Historically, ribs were studied on two opposite sides of a rectangular channel, spanning the length of the width. These early studies identified that the relative rib height, (e/D) and the channel aspect ratio (AR) dominated the performance rib designs. As relative rib heights increase or as the channel aspect ratios become narrower, there is an enhancement in heat transfer and an increase to the pressure drop. Rib heights for gas turbine components are typically around $e/D = 0.1$, though they vary depending on the design [121]. Prior studies have investigated channel aspect ratios between 1/4 to 4/1 to mirror the aspect ratios expected in modern vanes and blades. Rib pitch spacing (P/e) also has an impact on the heat transfer and pressure drop performance. One study by Taslim and Lengkon [122] highlighted how decreasing rib pitch spacing below five was detrimental to the overall thermohydraulic performance, due to the substantial increase in pressure drop for an relatively small enhancement in heat transfer.

It is expected that there will be some variation to the rib profile due to manufacturing limitations, and several researchers have studied how changes to these profiles impact performance.

Han et al. [123] implemented wedges on the leading and trailing edges of 90° ribs. They found that these wedges lowered the friction factor relative to ribs without wedges, but heat transfer at Reynolds numbers greater than 7,000 was not impacted. Han et al. attributed the insensitivity of the heat transfer to the rib design to the increased turbulence in the completely rough regime. A later study by Lockett and Collins [124] found that by rounding edges of a square rib, the wake heat transfer becomes a function of Reynolds number due to a less defined flow detachment and reattachment location. Other authors [125,126] investigated fillets at the leading and trailing edges of ribs, finding that the rounding of corners resulted in a moderate reduction in heat transfer depending on the rib aspect ratio, but significantly reduced pressure drop, especially at wider rib pitch spacings. Rallabandi et al. [127] recently evaluated filleted angled ribs with a square cross section and found that at Reynolds numbers greater than 30,000, that the fillets had a relatively small impact on heat transfer, but did reduce friction factor considerably.

Later rib studies focused on more advanced designs which varied the orientation of the rib relative to the oncoming flow direction and rib shape. These advanced rib designs encouraged the development of secondary flows that resulted in significant heat transfer enhancement while minimally impacting the overall pressure drop. Examples of this style of rib include V-shaped ribs [128], W-shaped ribs [129], and wedge shaped ribs [130]. In addition to augmenting the orientation and shape of the rib, prior authors implemented “broken” ribs, where ribs would feature gap regions which further enhanced heat transfer without substantially impacting the design pressure drop [131,132].

One more recently studied style of advanced rib designs are wavy ribs [133–137]. These wavy ribs feature a rectangular profile that follows a sinusoidal pattern along the streamwise direction of a rectangular channel. Similar to the other advanced rib designs, the curvature of the wavy ribs is intended to produce beneficial secondary flows. Wang et al. [134,135] computationally investigated a straight channel with a central wavy rib, and independently varied the rib waviness and height. The results of these studies were compared against a more common V-shaped rib. The authors found that the rib height had the greatest impact on the channel performance, which they attributed to a beneficial increase in surface area. Wang et al. found that taller ribs with minimal curvature could result in similar heat transfer performance as compared to the V-shaped ribs. A follow up investigation by the same authors looked at a wavy rib in a stationary and rotating U-shaped channel [136], and found that on a wall with the wavy rib feature that the thermohydraulic performance was greater than that of a V-shaped rib. Chang et al. [137] experimentally evaluated the performance of a wavy rib and wavy U-channel design, and found that the addition of the

streamwise oriented wavy rib doubled pressure losses and heat transfer over a wavy duct without a rib design.

Many of the prior studies investigating rib performance have done so using ribs that were composed entirely of smooth surfaces. In true engine components, these internal features have some level of surface roughness as a result of the casting process. Additionally, as more manufacturers turn to additive manufacturing as a means for producing gas turbine components [9], understanding the impact of surface roughness on the performance of rib designs is critically important for effective component design. Kilpatrick and Kim [138] used computational modeling to predict the impact that surface roughness would have on the performance of additively manufactured surface ribs. The model that they developed showed that very high roughness levels ($R_a > 100$ micron) would limit the strength of secondary flows, resulting in a reduction in heat transfer while still increasing overall pressure drop. Roy et al. [35] and Searle et al. [36] experimentally and computationally investigated additively manufactured ribs at Reynolds numbers in excess of 80,000. Both studies saw enhanced heat transfer for a constant amount of pumping power for the additively manufactured geometries, and concluded that rougher surfaces likely would offer further heat transfer enhancement, though only showed this enhancement computationally.

The current study will build on the work of prior investigators by identifying how differences in the surface morphology of additively manufactured surface ribs impacts the performance of an advanced rib design. In particular, five additively manufactured wavy rib designs were explored. These designs were characterized using optical profilometry and computed tomography (CT) scans. The bulk heat transfer and pressure loss of these designs was measured experimentally, while a set of computational simulations were used to explore the local performance. Additionally, several coupons were manufactured at increased scale, which were used to analyze the impact of reduced relative roughness on the performance of these ribs.

5.4. Geometric Description

A series of test coupons were used to experimentally characterize the performance of a family of wavy rib designs. Each test coupon featured an open duct with a hydraulic diameter of 3.46mm, similar to those previously investigated by the co-authors [139]. The duct was designed to be 50.8mm long, and have an aspect ratio of 1:10 with a height of 1.91mm.

A total of six designs were evaluated in this study. A diagram of the six designs is shown in Figure 5-1 with a summary of the geometric conditions given in Table 5-1. The first design was a simple open channel, with no internal geometry to serve as a baseline for performance. The next three designs investigated wavy ribs of three different wavelengths, named the 0.5λ , nominal, and 1.5λ cases. For these designs, a wavy rib with a relative rib height of $e/H = 0.1$ and spanwise pitch

of $S/e = 10$ were integrated onto one of the wide sides of the coupon duct. The amplitude for each of these designs was constant at 2.0mm. The wavelength of the nominal case was 10.2 mm, making the wavelengths for the 0.5λ and 1.5λ cases 5.1 mm and 15.2 mm respectively. In addition to the waviness, these ribs were also broken, with breaks that were $2e$ wide that occurred at every quarter of the wavelength. The fifth and sixth coupon designs featured a wavy rib with the same geometry as the nominal wavelength case, but implement on both sides of the duct in either an aligned or offset orientation. The aligned orientation featured ribs that were simply mirrored across the midspan of the test coupon, and the offset design shifted the wavelength on the opposite side of the test coupon by half a period, resulting in helix pattern when viewed from above as shown in Figure 5-1.

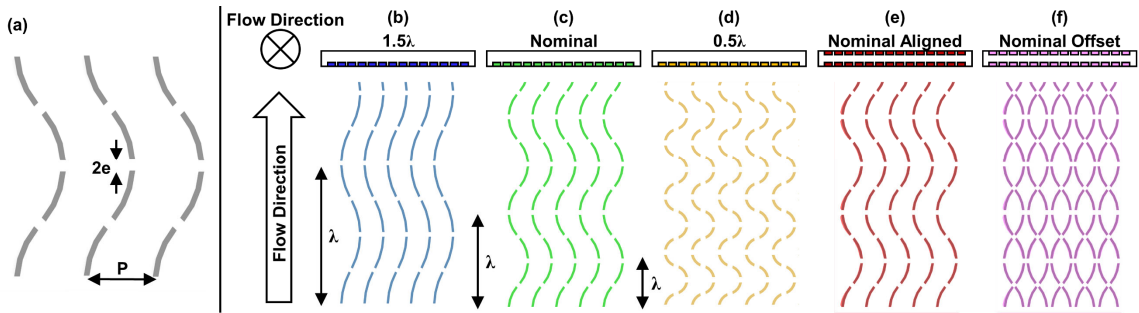


Figure 5-1. (a) Pitch and broken spacing for all rib geometries, and (b-f) diagrams of rib location in the coupon duct and rib design.

Table 5-1. Coupon Designs Investigated in the Current Study

Design	Scale	Wavelength [mm]	Amplitude [mm]	Position in Duct	Increase in SA [%]
0.5λ	1x	5.1	2.0	One Wall	10.4
Nominal	1x	10.2	2.0	One Wall	8.2
1.5λ	1x	15.2	2.0	One Wall	8.0
1.0λ -BS	1x	10.2	2.0	Two Walls	16.3
1.0λ -BSO	1x	10.2	2.0	Two Walls	16.3
$3x - 1.0\lambda$	3x	30.6	6.0	One Wall	8.2
$5x - 1.0\lambda$	5x	51.0	10.0	One Wall	8.2

In addition to the six previously mentioned designs, the nominal wavy rib case was also tested at multiple scales. Specifically, coupons were printed at a 1x, 3x, and 5x scale relative to coupon size previously mentioned. These larger coupons were intended to identify how reducing the relative roughness impacted the performance of the wavy rib designs.

Test coupons were additively manufactured out of IN718 on two printers: a GE M2 and a VELO Sapphire. On the GE printer, all of the design variations were printed, with the exception of the 5x scale coupon due to limitations on the print size. On the VELO printer, only four coupon variations were printed, those being the empty duct, and the nominal wavy rib printed at all three scales. The feedstock IN718 powder for all coupons was the same, and industry standard process parameters were used. All coupons were built in a vertical orientation, such that the flow and build directions were parallel. Self-supporting structures were integrated into the flanges of the coupon designs, which were removed following the build via milling. Additionally, coupon surfaces which mated with the test rig were machined to tolerance to allow the parts to seal.

5.5. Geometric Characterization

The test coupon geometries were characterized using computed tomography (CT) scans. CT scans were completed on the 1x coupons using a voxel size of 35 μ m, the 3x samples were scanned with a voxel size of 82 μ m, and the 5x sample was scanned at a voxel size of 100 μ m. It should be noted that features smaller than the voxel size would not be captured using these CT scans. This CT scan analysis revealed significant variation in recreation of the rib profile depending on the additive printer used. To showcase these variations, the rib cross section at approximately 75% of the rib height for the five coupons featuring the nominal wavy channel design is shown in Figure 5-2. In addition to the rib cross sections, streamwise rib profiles were extracted at the location of the green line which are shown to the right of each rib cross section.

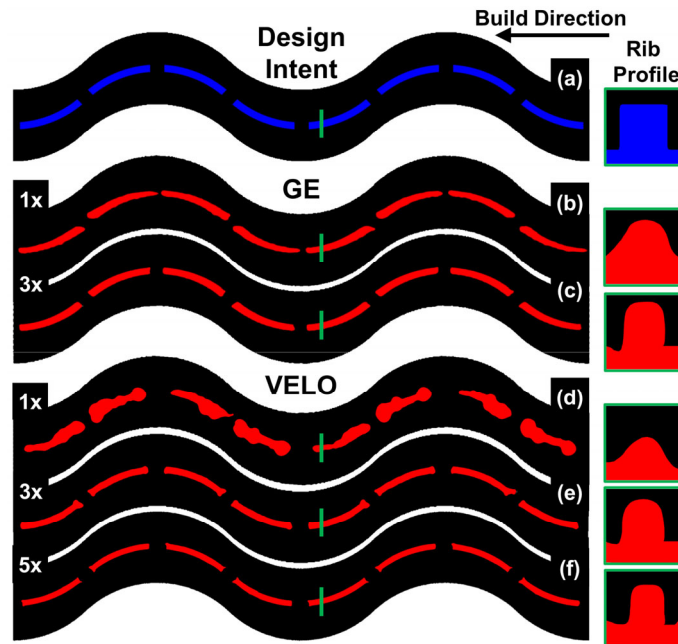


Figure 5-2. Profile of the nominal rib design intent (a) compared against the five printed variants (b-f).

As can be seen in Figure 5-2(b) and Figure 5-2(d), the 1x GE and 1x VELO coupons featured significant rounding at any of the corners of the design, deviating significantly from the intended rectangular profile. Along the streamwise direction, the areas where the rib was intended to be broken for the GE 1x test coupon were overbuilt, resulting in some cases where the rib was unbroken entirely. By comparison, the VELO 1x coupon included underbuilt ribs in the broken section, resulting in gaps approaching 4e instead of the intended 2e. The VELO 1x coupon also featured irregular ball structures along the length of the rib which significantly increased the local rib height. At the 3x scale, the GE (Figure 5-2(c)) and VELO (Figure 5-2(e)) coupons were significantly more similar, both to each other and to the design intent. This similarity is as expected, given that the scale of the rib is increasing, while the scale of the additive tolerancing is constant across all coupon scales. However, it should be noted that the irregular balling identified in the 1x VELO coupon also appears near the broken sections of the 3x VELO rib, resulting in a rib profile resembling a bone. At the 5x scale shown in Figure 5-2(f), the profile of the rib is largely identical to that of the design intent, with only small fillets on the corners of the surface.

These reconstructed surfaces were processed using an inhouse code was used to break up the surface into approximately 1000 slices along the flow direction. For each slice, the channel width and height were estimated, and then used to calculate the local perimeter and cross-sectional area. Using these values, the hydraulic diameter was calculated, and averaged across all streamwise slices for each test coupon. In addition, the coupon rib height was also calculated by averaging the distance between the top of each rib and the coupon surface for each streamwise slice. Given that the ribs were broken, the regions of the test coupon where the ribs were broken were excluded from the rib height averaging. The rib height determined through this analysis is shown in Figure 5-3.

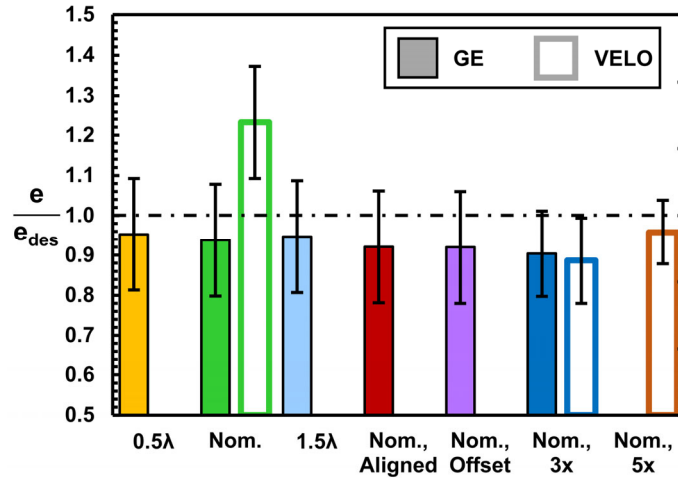


Figure 5-3. Relative rib height determined from the CT scans for the nine test coupons featuring ribs.

The rib height analysis shown in Figure 5-3 revealed that the almost all of the ribs slightly underbuilt their design intent, though most ribs were within uncertainty (defined as half of the voxel size). The one notable exception is the 1x nominal VELO coupon, which was significantly taller than intended, due to the irregular balling on the rib identified in Figure 5-2(d). Conversely, the coupon built most accurate to the design intent was the VELO 5x nominal case.

To characterize the surface quality of the test coupons, the open channel coupons were cut open using wire EDM to allow optical access. Given that prior work from the authors has shown that coupons printed in the same build with the same orientation have statistically similar roughness profiles [139], the two open channel test coupons were assumed to be representative of the roughness profile for their respective builds. To capture the roughness profiles, optical profilometry measurements were taken using a laser confocal optical profilometer at a 20x scale. Eighteen surface measurements were taken for each coupon to ensure statistical significance. Each measurement was analyzed using the software provided with the optical profilometer, which characterized the surface to within 0.8 μm. For surface measurements, planes that were approximately 500 by 700 μm were fit to the measured surface. A variety of roughness statistics were extracted from these planes and averaged for each sample, and are reported in Table 5-2.

Table 5-2. Roughness Measurements from the Open AM Channels

Machine	Sa [μm]	Sz [μm]	Sq [μm]	Ssk
GE M2	3.2	55.1	4.4	1.6
VELO Sapphire	4.2	48.8	5.6	1.1

Generally speaking, the roughness profiles and magnitudes from the two samples were similar, with the GE coupons having moderately lower arithmetic mean and root mean square roughness levels. The measured roughness is low as compared to prior investigations [27,140], likely a function of the beneficial build orientation and well refined process parameters for IN718. The roughness on both of these parts was largely a function of small particulate that was dispersed over the surface, in addition to layer lines which caused more regular but smaller disruptions to the surface topography.

5.6. Experimental Setup

The experimental setup for the 1x coupons in this study is identical to that used in prior investigations by the authors [139]. The experimental rig consists of a test section fed compressed air from a mass flow controller. The test section consists of two plenums on either side of a test coupon, which impose known flow conditions to the inlet and exit of the test coupon. The upstream plenum imposes a uniform velocity profile, whereas the downstream plenum features a sudden expansion in flow area, which enables defining a known loss coefficient at the coupon inlet and outlet. Both plenums are instrumented with a pressure tap to capture the pressure drop across a test coupon and the test section gauge pressure, as well as thermocouples to capture the thermal rise. Typical gauge pressure in the rig ranged from 70-700kPa. The pressure transducer used to measure the pressure drop across the coupon featured swappable diaphragms enabling accurate capture of a range of pressure drops. Temperatures and pressures at the coupon inlet and exit are calculated using isentropic flow relations, which are used in the calculation of the non-dimensional bulk flow characteristics. Downstream of the test section is a needle valve, which allows for independent control of Reynolds number and Mach number. Mach numbers in the test coupon were kept below $Ma = 0.1$ to minimize compressibility effects. During heat transfer testing two heating assemblies were installed on either side of the test coupon, which imposed a constant surface temperature boundary condition. Each heating assembly consisted of a heater positioned between a foam block and copper block. Each copper block had six thermocouples located precisely in halfway along the copper thickness. Using a one-dimensional thermal resistance network accounting for the remaining copper, thermal paste, and coupon wall thickness, the wall temperature on the interior of the test coupon was calculated. In addition to the thermocouples in the copper, there were several additional thermocouples placed throughout the foam blocks and in the material of the plenums. These thermocouples were used to estimate the losses from the heaters to the rig itself, rather than to the flow passing through the test coupon. Losses were typically less than 3% of the total heat input. To calculate the bulk convection coefficient, the equation for the heat transfer from an isothermal wall was used, as shown in Equation 5-1.

$$h = \frac{(Q - Q_{\text{loss}})}{A_s \Delta T_{\text{LMTD}}} \quad (5 - 1)$$

The total wetted surface area as determined from the CT scans was used when calculating the bulk convective coefficient.

For the 3x and 5x test coupons, larger scale plenums and heating assemblies as compared with the 1x were used with the same instrumentation. The only modification to the scaled-up plenums and heating assemblies was the integration of additional thermocouples to improve capture of temperatures inside the plenums and copper blocks.

Pressure loss from the test coupons was normalized using the friction factor, and the heat transfer was normalized using the Nusselt number. To ensure that the results from the test rig matched expectations, plenums of all scales were initially tested using a coupon featuring smooth cylindrical channels. Pressure loss results from this analysis was compared against the Colebrook correlation [55], and was within 5% for $Re > 3000$ for all coupon scales. The Nusselt number results from the 1x scale were compared against the Gnielinski correlation [56] and agreed within 3%. Additionally, during a heat transfer test, the energy input into the test coupon is compared against the first law of thermodynamics. These comparisons were within 6% for all test coupon scales, indicating accurate capture of the heat transfer in the system.

5.7. Uncertainty Quantification

Uncertainty for the experimental results was calculated using the method of propagation of uncertainty as described by Dunn [57]. The uncertainty in the Reynolds number and friction factor was greatest at lower Reynolds numbers, with uncertainties approaching 7% and 15% at a Reynolds number of 2000. At Reynolds numbers in excess of 5000, uncertainties in Reynolds number and friction factor approached 2% and 6%. These parameters were repeatable within 1% and 3%. The major contributors to uncertainty in the Reynolds number was the mass flow rate and the test section pressure. The local pressure drops and CT scan measurements of the coupon height and width were the major contributors to the uncertainty in the friction factor measurements. The uncertainty in Nusselt number was approximately 3%, and was repeatable within 1%. The copper block temperatures and the outlet temperature measurements were the greatest contributors to uncertainty in Nusselt number.

5.8. Computational Setup

In partnership with the various experimental test coupons evaluated in this study, a computational analysis was completed to further explore the underlying flow structures. A total of six simulations were run: one for each of the five geometric variations, and another case using the same mesh and domain settings with no ribs to validate the computational setup. For the five cases

looking at geometric variations, the corners of the ribs were rounded with very small fillets to improve mesh quality and reduce computational error. These simulations were developed using a commercial CFD solver [107], and the computational domain can be seen in Figure 5-4(a-b). The domain consisted of a test section the length of a single test coupon and an empty region the length of five duct-heights behind the test section to minimize reversed flow near the outlet. Flow entered the domain through a mass flow inlet, which was set to achieve a Reynolds number of 20,000. Flow exits the domain through a constant pressure outlet condition set to a typical pressure used during experimental testing. On either of the spanwise walls of the domain, a periodic flow boundary condition was used to mimic an infinite width duct containing the wavy ribs. The other domain surfaces were set as smooth no slip walls. These walls were set to a constant temperature of 75°C and the mass flow entering the domain was set to a temperature of 23°C. The flow was modeled as turbulent, using the K- ω SST turbulence model. The constitutive relationship, which describes the relationship between the Reynolds stresses and the mean strain rate, was modeled as cubic to increase the accuracy of highly swirled flows with anisotropic turbulence, like would be expected in the wake of the ribs. The modeled fluid was air, where the density was calculated using the ideal gas law, thermal conductivity and dynamic viscosity were modeled using Sutherlands law, and the specific heat was modeled using a polynomial as a function of local fluid temperature. The walls for the computational domain were modeled as smooth.

Polyhedral meshes were generated for each of the geometries using the commercial solver, and an example of one such mesh can be seen in Figure 5-4(c). In the near wall region, inflation layers were used to reduce the local y^+ values to approximately unity, with a growth rate of 1.1 to ensure the thermal and momentum boundary layers in the sub viscous region were accurately resolved. The nominal wavy rib case underwent a mesh independence study, with mesh sizes varying between 200,000 and twenty million cells and is shown in Figure 5-4(e). A mesh size of approximately 14 million cells was found to resolve the flow in the domain, and the mesh settings used to capture this performance was used for all other domains.

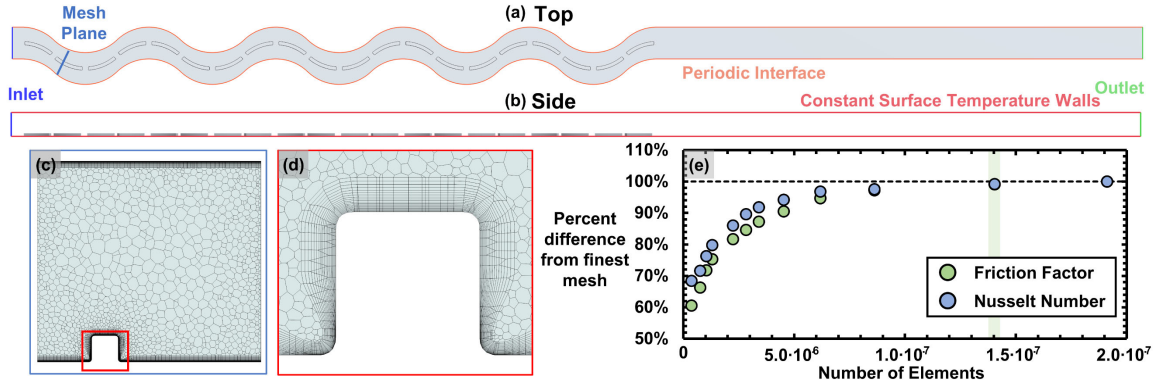


Figure 5-4. The (a) top and (b) side profiles of the computational domain, (c) zoomed out and (d) zoomed in view of the computational mesh, and (e) mesh independence study for the nominal case.

5.9. 1x Wavy Rib Performance

To begin identifying how the changes to the 1x wavy rib geometry impacted the performance of the wavy ribs, the friction factor and Nusselt number performance was quantified as a function of Reynolds number, and is shown in Figure 5-5.

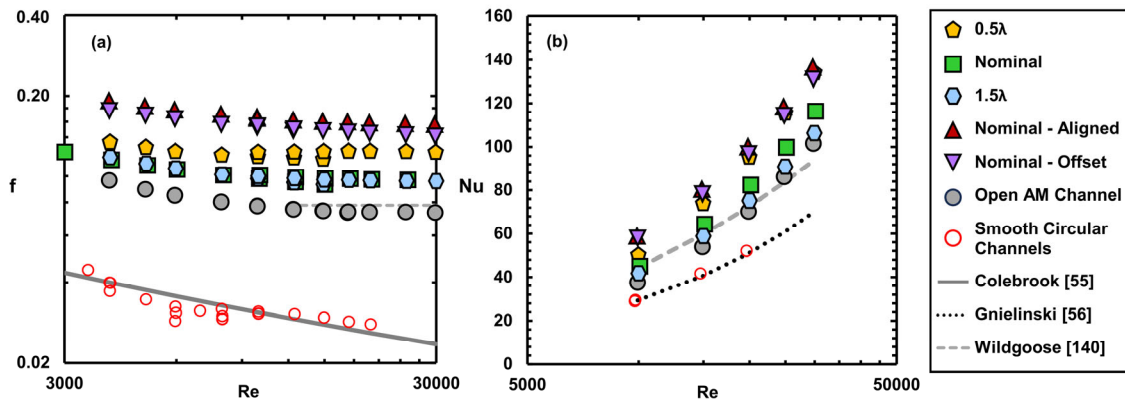


Figure 5-5. Measured (a) friction factor and (b) Nusselt number as a function of Reynolds number for the varying rib designs for 1x scale.

Looking to the five different wavy ribs designs, there was a clear upwards trend in both pressure drop and heat transfer as a function of increased flow disruptions. Starting with the three designs of varied wavelength, the nominal and 1.5λ designs had similar friction factor performance, whereas the 0.5λ design had a 30% greater friction factor. In contrast, the heat transfer differed between the three designs with the 1.5λ having 9% lower heat transfer than the nominal case, and the 0.5λ having 15% greater heat transfer than the nominal case on average. The cause for these differences in heat transfer is due to the more regular disruptions to the near wall flow from the 0.5λ design as compared to the nominal and 1.5λ designs. For the nominal designs printed on both sides, there was significant increase to both the heat transfer and the pressure drop over that of the nominal design printed on one side of the coupon. However, the difference in performance between the two designs featuring ribs on both sides was largely within experimental uncertainty. The

coupon that had the lowest friction factor and heat transfer enhancement was the open additive channel. Both the heat transfer and friction factor from the open channel agreed within 15% of a prior correlation proposed by Wildgoose et al. [140], which leverages the root-mean-square roughness and the skewness of a sample to predict a fully developed friction factor and Nusselt number.

To more precisely examine the differences in performance between the different test coupon designs, a bar plot of the friction factor augmentation and Nusselt number augmentation at a Reynolds number of 20,000 is presented in Figure 5-6. The bulk results from the computational setups are also presented in Figure 5-6, where it was seen that the computational results followed the same trends as the experimental results, and in some cases matched the experimental results within uncertainty. The most significant exception to this agreement is in the case of the empty duct, which instead approached the values of the Colebrook and Gnielinski correlations due to the lack of modeling surface roughness in the computational domain. This agreement implies that the additional surface roughness present on the GE designs did not significantly alter the performance of these features, which is the result of the already enhanced near wall turbulence that was developed as a function of the rib geometry. The heat transfer from the designs featuring ribs on both sides of the duct was marginally greater than the experimental results, which may be due to the computational model using the design intent rib height, increasing the local flow blockage and velocity.

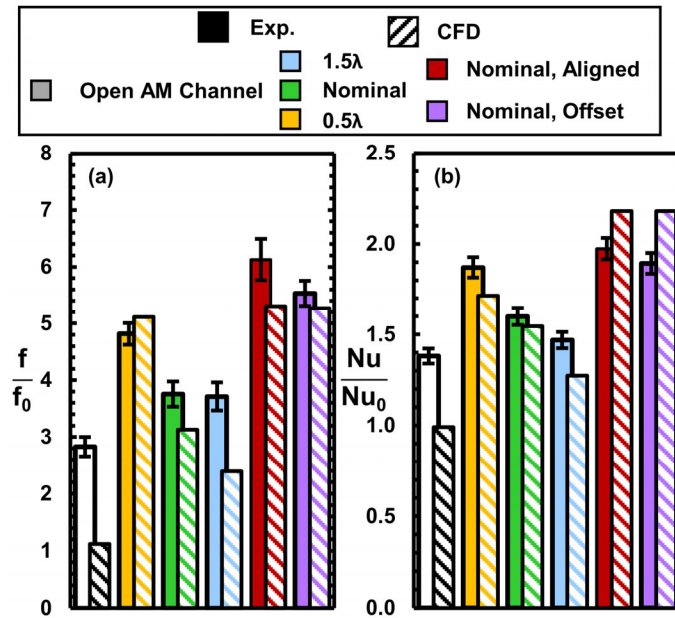


Figure 5-6. Friction Factor and Nusselt number augmentation at a Reynolds number of 20,000.

To further understand why the different designs performed as they did, contours of the non-dimensional temperature with overlaid streamlines were created and are presented in Figure 5-7.

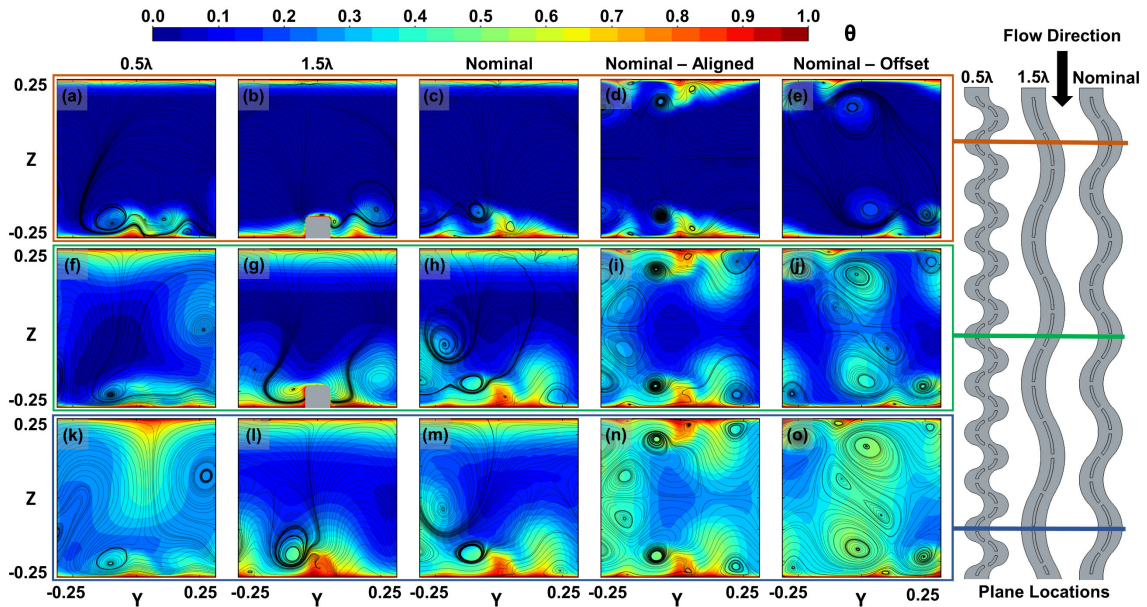


Figure 5-7. Contours of Theta for the five different wavy rib designs at three streamwise planes.

The first plane for the nominal design (Figure 5-7(c)) is located at half of a wavelength along the streamwise direction. Two vortices are shed from the first two broken rib segments, which pull up the boundary layer in the wake of these segments and enhance local convection. As these vortices travel downstream of the rib surface, they are disrupted by subsequent rib segments, causing new vortices to be regularly established. The orientation of the vortex is dependent on the alignment of the rib surface relative to the oncoming flow, meaning that the vortex changes orientation twice for each rib wavelength. Between the first and second plane, many more vortices are shed from each of the different segments, and a counter rotating vortex forms near the center of the channel. This vortex can be seen near the middle left of Figure 5-7(h). This counter rotating vortex forms as a result of the vortices shed from the rib surfaces, and similarly changes orientation twice over a given wavelength. At the final streamwise plane, shown in Figure 5-7(m), this central vortex extends to the top of channel, and begins to enhance the heat transfer on the opposing surface of the domain.

The formation and destruction of the vortices are also present in the 0.5λ and 1.5λ designs, though the interval of the formation is tied to the rib wavelength. The strength of the vortex formation, and the resulting interaction with the thermal boundary layer, is tied to the angle of attack of the broken rib segments. This difference in vortex strength means that the 0.5λ design

enhances heat transfer both through an increased number of wakes being shed, but also by the strength of these vortices. The impact of these more regular and stronger vortices are reflected in the greater bulk temperatures in Figure 5-7(k) than in Figure 5-7(l) or Figure 5-7(m), which all feature ribs on only a single channel surface. As a result of these vortices, the 0.5λ rib design had the greatest Nusselt number and friction factor as shown in prior figures and the 1.5λ design had the lowest overall Nusselt number and friction factor of the ribbed designs.

When comparing to the designs that featured rib designs on both sides of the channel, there is an apparent increase in the overall number of vortices, as shown in Figure 5-7(d) and Figure 5-7(e). In the aligned case the vortex formations downstream of the first period are symmetric, as seen in Figure 5-7(i), mirroring the symmetry of the design. In the offset case, the vortex formations are symmetric across the diagonal, as can be seen in Figure 5-7(j). The increased number of vortex interactions enhance the thermal mixing considerably, as well as serve as an additional pressure loss mechanism. Additionally, because these ribs are located on both channel surfaces, these designs disturb the flow and enhance the heat transfer performance on both channel surfaces, resulting in enhanced heat transfer performance relative to the designs featuring a rib on only one wall.

The wavy rib design induces significant near wall vorticity, which results in localized regions of increased and reduced flow speeds. To explore this effect, contours of the near wall normalized y-component of vorticity for the nominal wavy rib design are shown in Figure 5-8, but it should be noted that all of the designs shared similar local near wall vorticity formations.

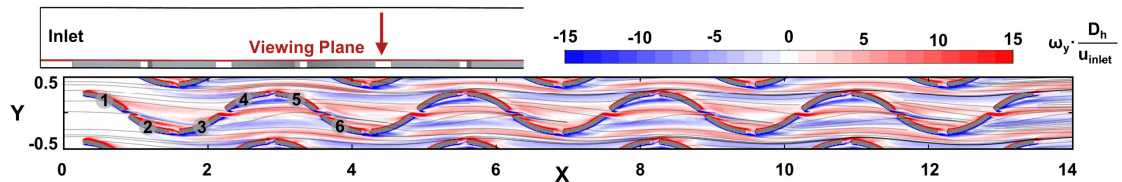


Figure 5-8. Contours of the near wall normalized y-component of vorticity for the nominal case.

As the flow crosses over the first period of the rib, it becomes skewed to the negative y direction due to the low-pressure region behind the first two rib segments. Some of this skewed flow then passes through the opening between the third and fourth rib segments, resulting in two regions of enhanced vorticity and increased flow speeds just below the fourth and fifth rib segments. In this region the skewed flow is corrected to travel again normal to the X-axis. Then, as the flow passes over the fifth and sixth rib segments it again becomes skewed in the negative Y direction. This pattern of the flow becoming skewed and then corrected repeats along the entire length of the rib design. Because of the broken rib segments, there are many regions of opposing vorticity near the wall. The regions of opposing vorticity either serve to locally increase or decrease

local velocities depending on their orientation, which lead to enhanced or deterred local heat transfer. To further characterize the local heat transfer performance, contours of the local Nusselt number enhancement were created for all designs and are shown in Figure 5-9. To calculate these local Nusselt numbers, the spanwise averaged log mean temperature difference was calculated as a function of length.

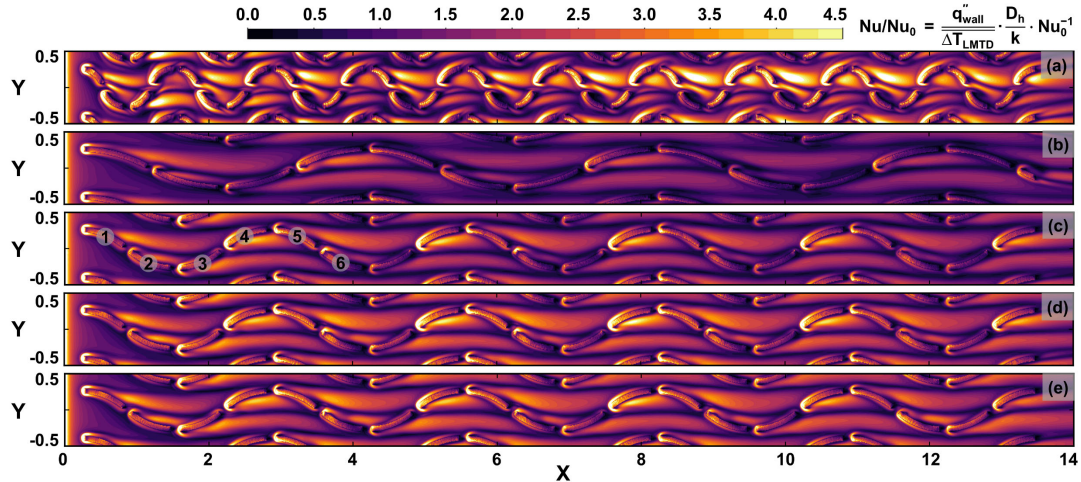


Figure 5-9. Local Nusselt number augmentation for the (a) 0.5λ , (b) 1.5λ , (c) Nominal, (d) Nominal Aligned, and (e) Nominal Offset rib geometries.

Starting with the nominal case presented in Figure 5-9(c), there is an evident bias to the heat transfer, where every fourth rib segment has increased heat transfer in the wake region. This region of enhanced heat transfer aligns with the enhanced flow velocity region created by the constructive vortex formations identified in Figure 5-8. Additionally, there are regions of reduced heat transfer that cross along the interior of a given rib period, which correspond to the regions of reduced flow speed caused by the destructive vortex formations shown in Figure 5-8.

Comparing the nominal case to the 0.5λ and the 1.5λ cases, shown in Figure 5-9(a) and Figure 5-9(b), the Nusselt number profile changes considerably. Notably for the reduced wavelength case that is a more dramatic region of increased Nusselt number augmentation, and the increased wavelength case has relatively minimal increase to the local Nusselt number. For the channels with ribs on both sides, the local Nusselt number profiles are slightly greater than those found for the nominal case on one wall, but have the same form. The similarity in distribution indicates that the changes to the local flow structures in the interior of the channel seen in Figure 5-7 did not change the structure of the near wall heat transfer performance, but did increase the magnitude.

5.10. Overall Performance

To understand the performance of these rib geometries against other advanced rib geometries, a plot of efficiency index was created that features ribs from Park et al. [141], as well as Wright et al. [129] as a function of Reynolds number and is shown in Figure 5-10. It should be noted the data reported in this plot from prior authors was originally reported using the area of an empty duct, but was corrected in the current study to use the wetted surface area to offer a fair comparison between studies. A summary of the properties of these advanced rib designs is presented in Table 5-3.

Table 5-3. Geometric Characteristics of Designs Investigated In Prior Studies

Study	Rib Design	Rib Height	Rib Spacing (P/e)	Channel Aspect Ratio (W/H)
Current	Wavy	0.131	-	10
Park et al. [141]	90°	0.078	10	4
Wright et al. [129]	45°	0.078	10	4
Wright et al. [129]	Discrete W	0.078	10	4

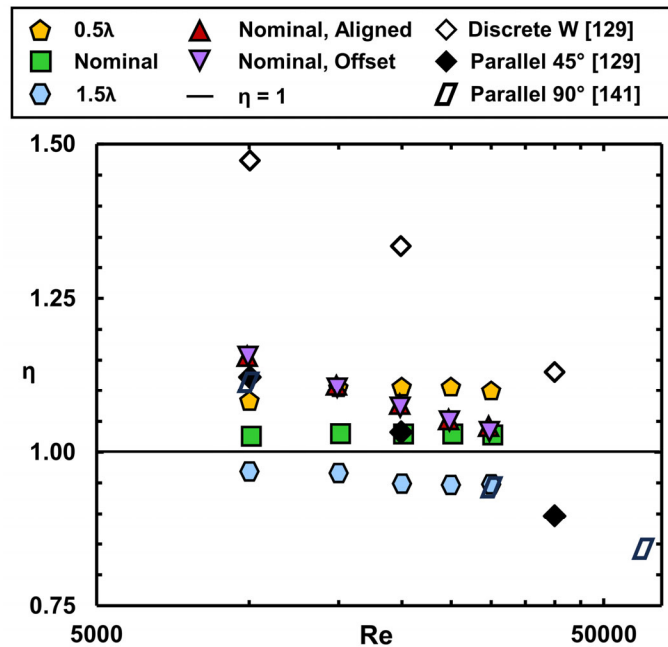


Figure 5-10. Efficiency index versus Reynolds number of the wavy rib geometries against other advanced rib designs.

First looking to the efficiency index of the designs investigated in this study, it can be seen that the designs with ribs on only one side of the duct have a efficiency index that is largely independent of Reynolds number in the range tested. As the wavelength of these designs decrease, the efficiency index increases, following the same trends as the heat transfer performance. For the ribs that were integrated on both sides of the duct, there is a clear downward trend as a function of

the Reynolds number. At a Reynolds number of 10,000, only the ribs on both sides of the duct outperformed the 90° ribs reported by Park et al. [141]. At Reynolds numbers of 20,000 and greater, all but the lowest wavelength ribs outperformed 90° ribs and the angled ribs studied by Wright et al. [129], indicating that the wavy ribs investigated in this study may be more suitable than angled ribs at greater Reynolds numbers. The W-shaped rib studied by Wright et al. [129] outperformed the wavy ribs investigated in this study at all investigated Reynolds numbers.

To further characterize the relative performance of the ribs in this study against other advanced rib designs, an augmentation plot was created and is presented in Figure 5-11.

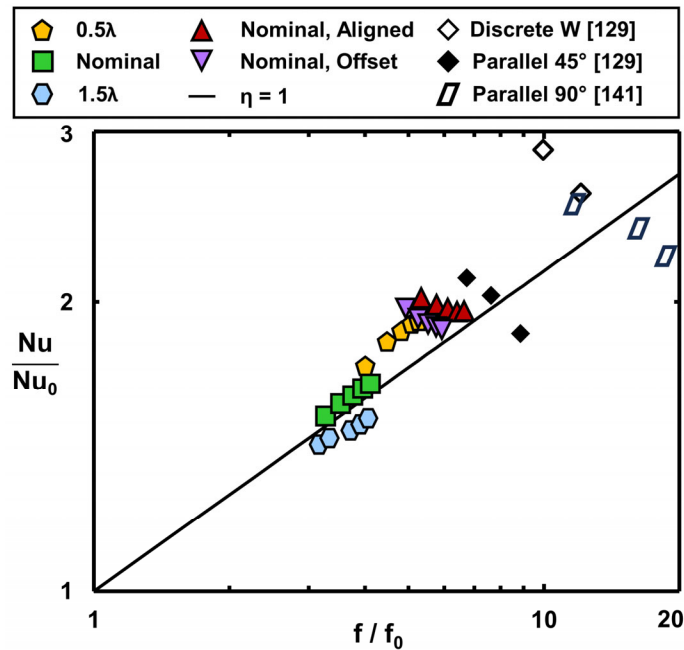


Figure 5-11. Augmentation plot of the wavy rib designs investigated in this study compared against designs from literature.

Relatively speaking, the designs in this study offered low augmentation values for both friction factor and heat transfer as compared to the other advanced designs. These reduced augmentation values are likely the result of relatively low rib spanwise spacing, and the fact that the majority of the wavy rib designs had the rib oriented largely along the flow direction. Additionally, the ribs investigated as part of this study also did not extend across the full span of the channel, where the other advanced rib designs did, resulting in significantly greater overall Nusselt number and friction factor augmentations.

5.11. Scaled Testing

To begin to isolate the impact of the roughness on the surfaces of these rib designs against their performance, the nominal test coupons built at three scales were tested over a range of

Reynolds numbers to capture both the heat transfer and pressure loss. These results were normalized by the 5x design, and are shown in Figure 5-12.

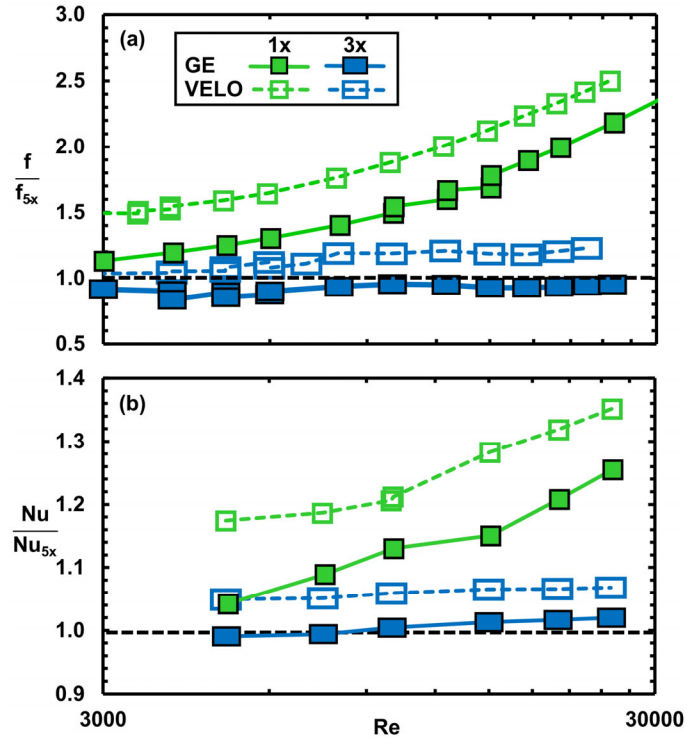


Figure 5-12. Friction factor and Nusselt number augmentation for the nominal design at several scales.

In both Figure 5-12(a) and Figure 5-12 (b) all scales are trending towards the same friction factor and Nusselt number at a lower Reynolds number, with the exception of the 1x VELO coupon. Given that the geometry is matched and the Reynolds number is matched, we would expect the augmentation from the 5x case to be uniformly unity for all coupons. However, at higher Reynolds numbers the increased relative roughness of the 1x scale coupons enhanced the heat transfer performance by as much as 20-30% while resulting in an increase to friction factor by 200-250%. The 1x VELO coupon deviation in performance can likely be attributed to the extremely irregular rib profile and height that deviated significantly from the design intent as was shown previously in Figure 5-2(d). The 3x VELO coupon had nodules that formed near the corners of the ribs, which protruded above the overall rib height. It is suspected that these protrusions, partnered with the slightly greater relative roughness, lead to the greater friction factor and Nusselt number as compared to the 3x GE coupon.

To further explore the impact that the additive surface roughness had on the test coupons, an additional analysis compared the friction factor and Nusselt number against the relative roughness of the channel, and is reported in Figure 5-13.

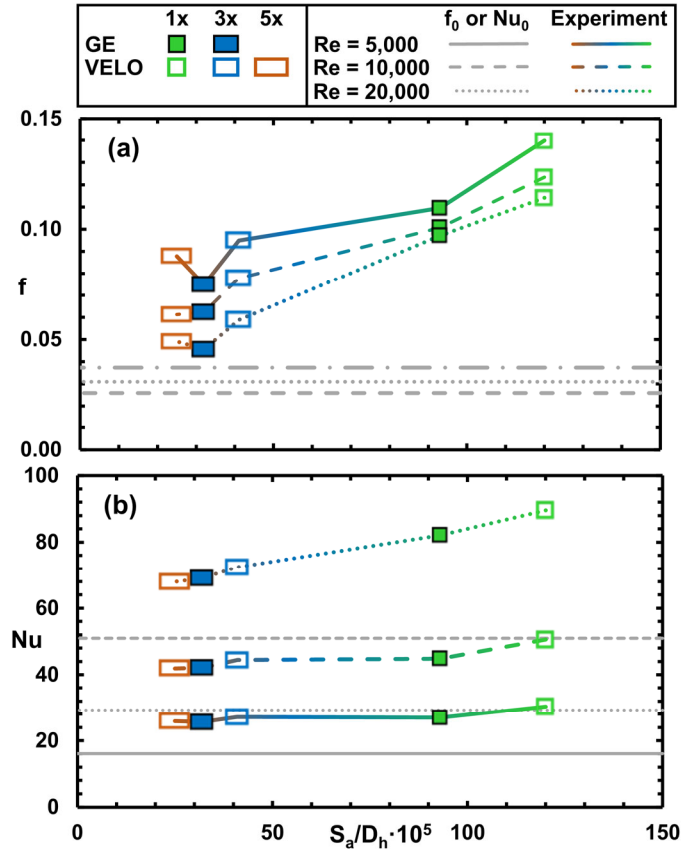


Figure 5-13(a) Friction factor and (b) Nusselt number as a function of relative roughness at three Reynolds numbers for the scaled test coupons.

Starting with the friction factor results shown in Figure 5-13 (a), there is an evident upward trend in friction factor as relative roughness increased for all Reynolds numbers. Three coupons with the smoothest relative roughness, those being the coupons printed at 3x and 5x scale, had relatively similar values for friction factor, though as was shown in Figure 5-12(a), the 3x VELO coupon had slightly greater friction factor values due to the irregularities along the rib surface in addition to the increased surface roughness. Looking to the heat transfer results shown in in Figure 5-13(a), we can see that at lower Reynolds numbers the relative roughness had a relatively small impact on the overall heat transfer. At greater Reynolds numbers, there was a linear increase in heat transfer with increasing relative roughness, which agrees with the computational trends predicted by Roy et al. [35]. However, Roy et al. [35] also predicted that the friction factor would only marginally increase as a function of relative roughness, which is counter to the results shown in Figure 5-13 (a), indicating that more work should be done to accurately capture the impact of additive surface roughness on the performance of ribbed surfaces.

5.12. Conclusions

This paper explored the performance of a suite of advanced broken wavy rib designs. Designs were integrated into additive coupons of three different scales and built on two different direct metal laser sintering printers. Test coupons were characterized using computed tomography scans to characterize the accuracy to design intent, and determine the hydraulic diameter and rib height. It was found that the coupons manufactured on a GE machine were manufactured largely similar to the design intent, but the 1x scale VELO coupons were manufactured with significant variability in both the rib height and the rib profile. Surface roughness measurements were taken on a single coupon from both printers featuring an open duct using an optical profilometer to accurately describe the surface topography. It was found that GE coupons had slightly lower surface roughness, but that the topography of the surface roughness was similar.

Coupons were experimentally tested over a range of Reynolds numbers to characterize both the heat transfer and pressure loss performance. Computational studies were also completed to analyze the internal flow structures that lead to the measured performance. Experimental results showed that reductions to the wavelength of the rib resulted in increases to the overall pressure loss and heat transfer, but that integrating ribs on both sides of the duct had the greatest impact on the overall performance. Ribs integrated in either an aligned or offset orientation performed very similarly from a heat transfer and pressure loss perspective. The trends of the computational results aligned well with the experimental results, and revealed that there was complex vortex generation in the near wall region due to repeated vortex shedding from the rib surfaces. These near wall vortex formations resulted in a bias to the local heat transfer across the ribs.

Comparing the experimental results determined from this study against the results determined by prior researchers, it was determined the augmentation to both heat transfer and pressure loss were lower than typical 90° ribs, and significantly lower than that of more advanced rib designs. This difference in performance was attributed to the reduced angle of attack from these rib surfaces as opposed to those in literature, as well as the lack of the rib extending the full span of the endwall surface.

To identify the impact of the relative roughness of the design against the overall performance, coupons at multiple scales were tested at a range of Reynolds numbers. It was expected that the coupons built at different scales should perform the same at a given Reynolds number, however it was found that greater levels of relative roughness increased the friction factor significantly. The Nusselt number at low Reynolds numbers approached the same value for the test coupons that accurately represented the intended geometry, but at more turbulent Reynolds numbers there was a linear increase in heat transfer as a function of relative roughness.

The results from this study provide designers with a potential new cooling technology that could be used to enhance the internal cooling of various gas turbine components. Further work should be completed to identify how the spanwise spacing of these ribs impacts the performance of wavy rib designs. Additionally, an unsteady computational analysis should be completed to better understand the flow bias mechanics given the inherent unsteady nature of vortex shedding.

5.13. Acknowledgements

This research was sponsored by the US Department of Energy, Office of Energy Efficiency and Renewable Energy (EERE), Advanced Materials & Manufacturing Technologies Office (AMMTO), under Contract DE-AC05-00OR22725 with UT-Battelle LLC. This work was performed in part at the Oak Ridge National Laboratory's Manufacturing Demonstration Facility, an Office of Energy Efficiency and Renewable Energy user facility.

6. THERMOHYDRAULIC PERFORMANCE AND FLOW STRUCTURES OF DIAMOND PYRAMID ARRAYS⁶

6.1. Abstract

Surface features are a common heat transfer enhancement method used in a myriad of applications including gas turbines and heat exchangers. One such style of surface features is diamond pyramids, which offer significant heat transfer augmentation for moderate increases in overall pressure losses. This study investigated a suite of additively manufactured pyramids in a variety of sizes and arrangements at relevant scale contained in test coupons. Designs were printed with low surface roughness relative to typical additive components, and pyramids were printed near to the design intent. Experimental and computational results indicate that the pressure penalty and heat transfer increased as the pyramids increased in size with aligned pyramids on both channel walls having higher values than staggered pyramids. It was found that implementing the pyramids onto a rough surface had a lesser impact on the friction factor than implementing on a smooth surface, but that the relative increase in heat transfer was the same regardless of the roughness of the endwall. The greatest enhancement to local heat transfer and pressure loss was offset from the location of minimum flow area due to local acceleration around the wake regions. The vortices formed in the wake of the pyramid structures significantly enhanced the endwall heat transfer and shear stress. The overall performance of the pyramids investigated in this study follows a similar trend to prior studies investigating smooth rib geometries, though certain rib designs had higher heat transfer at lower pressure losses.

6.2. Introduction

Power generation gas turbines serve as a major source of energy, with natural gas contributing as much as 41% of the total electricity generation in the United States as of May 2023 [142]. As energy demand continues to grow even with the commissioning of renewable sources, identifying avenues for improving performance of these engines is of the utmost importance. One such avenue is the improvement of the internal cooling schemes used in a variety of hot section components. In an engine, cooling air is siphoned from the main gas path in the compressor, before the combustor. Extracting cooling air from this location means that a significant amount of work goes into the air, but only a fraction of that work can be extracted from it. Therefore, an efficient cooling design needs to limit the amount of cooling air but yet cool components enough to meet the design life.

⁶ Corbett, T. M., Thole, K.A. “Thermohydraulic Performance and Flow Structures of Diamond Pyramid Arrays” GT2024-122359, *under review*

Innovative and efficient internal cooling schemes are a cornerstone in the design of high-performance gas turbine components. Tailoring each scheme for its unique set of boundary conditions requires a wide range of internal cooling features including pin fins, ribs, impingement jets, and more [3]. As additive manufacturing becomes an increasingly viable means for manufacturing stationary components for gas turbine engines [9] and enables faster and cheaper product design cycles [120], there is ample opportunity to investigate and integrate new cooling schemes. One such style of internal cooling technology with limited research is diamond pyramid surface features.

This study leverages additively manufactured test coupons to explore diamond pyramids differing in height and internal arrangement. Surface roughness measurements and geometric characterizations were completed to fully describe as-printed parts while computational fluid dynamics simulations were used to further understand the underlying flow dynamics. Flow features were explored and directly tied to the impact on overall heat transfer and pressure loss. The overall thermohydraulic performance of these features were evaluated as function of Reynolds number and performance was compared to other common heat transfer augmentation technologies.

6.3. Literature Review

Surface features are a common method for enhancing heat transfer as they both increase the overall surface area and encourage flow detachment which enhances heat transfer near the wall. Several research groups have investigated various forms of solitary surface features, including rectangular prisms [23,143,144], hemispheres [23], cones [145], and pyramids [23,146–149]. One study by Chyu et al. [23] investigated a range of surface features, including a rectangular prism, hemisphere, diamond, and pyramid, and found significant variations in the heat transfer in the wake region behind these shapes. They attributed these variations largely to changes in formation of the upstream horseshoe vortex in front of and the different wake vortex formations behind of the differing surface geometry. This study by Chyu et al. also identified that the most effective use of these types of features would be in staggered array, with diamond shapes likely requiring the least number of elements to effectively increase overall heat transfer.

Solitary diamond and pyramid shaped surface features were explored by Martinuzzi et al. [146–148] through several studies. In their first investigation, Martinuzzi and AbuOmar [146] classified diamond pyramid shapes into either slender or broad pyramid shapes depending on the apex angle. When the oncoming boundary layer was laminar, slender and broad pyramids had differing vortex patterns in the wake. If the oncoming boundary layer was turbulent, where the boundary layer height exceeded that of the pyramid height, both slender and broad pyramids had similar wake structures. The most notable structure was a recirculation region that formed just

behind the tip of the pyramid, which Martinuzzi and AbuOmar named a rotor vortex. In a follow up study, Martinuzzi et al. [147] expanded on the wake flow and local pressure distribution of surface mounted bluff bodies. They found that the mean pressure coefficient profiles were similar for several types of bluff body if the streamwise distance was normalized by the reattachment length.

Beyond the single diamond pyramid in cross flow, there are several studies that investigate a very similar geometry called a delta rib in an array. A delta rib is in effect a pyramid with a triangular base, where the apex of the pyramid is slanted towards the flow direction. Han et al. [130] conducted an early investigation identifying that the heat transfer performance of delta ribs in an array produced heat transfer enhancements 2.5-3.2 times that of a smooth channel, which outperformed a common square-edged 90° ribs. This heat transfer enhancement came at the cost of a 5-6 times increase in friction factor. A study by Henze and Von Wolfersdorf [150] investigated delta ribs computationally, and found that the heat transfer was a function of the how far into the boundary layer the ribs protruded, with more pronounced designs causing more significant increases to heat transfer. An investigation by Valentino et al. [151] found that by strategically placing either full or partial delta ribs on alternating walls of a channel they could improve their overall thermal performance by encouraging secondary flows.

All of the previously discussed studies investigating surface turbulators featured smooth surfaces. When leveraging new manufacturing techniques, like metal additive manufacturing, part surfaces have an inherent surface roughness. Prior literature exploring the impact of the inherently rough additive surfaces on surface turbulating geometry is limited [35,36,138]. A study by Roy et al. [35] computationally investigated the performance of turbulators at internal Reynolds numbers in excess of 100,000 and saw an enhancement in heat transfer with only a moderate increase to friction factor as the surface became rougher.

The prior investigations on diamond pyramids and delta rib turbulators have identified how various geometric aspects of these surface features impacted heat transfer, pressure loss, and vortex formation. However, there is limited information on how pyramids of different heights in an array configuration, as would be expected in cooling designs, impact the thermohydraulic performance. Prior work also does not identify how the vortices from this style of surface feature interact with each other, or how those vortices impact the local heat transfer. Finally, there is a lack of work investigating additively manufactured surface features, identifying how the inherent surface roughness impacts the part performance. This study will build on the work of prior investigators by exploring these aspects of diamond pyramid surface features, enabling engineers developing gas turbine cooling schemes to apply this cooling technology effectively.

6.4. Geometric Description

Several test coupons were fabricated to experimentally explore a range of diamond pyramid arrays. The test coupon envelope for this study was the same as prior studies by the authors [105,139] being 50.8 mm long, 25.4 mm wide, and 3.05 mm tall. The diamond pyramids were integrated into a duct of the same length, with a width of 19.05 mm and a height of 1.91 mm. An example of this coupon can be seen in Figure 6-1.

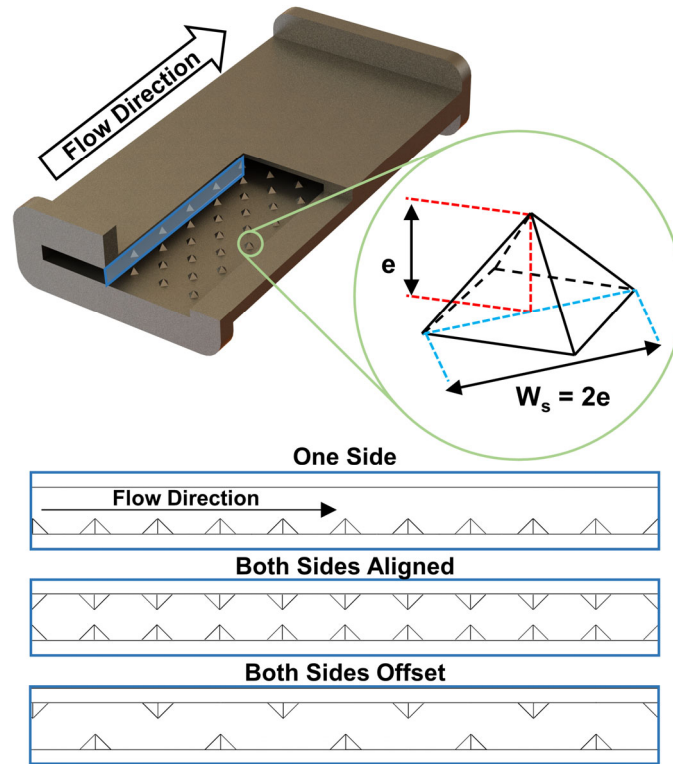


Figure 6-1. Example of test coupon with dimensioned pyramid, and side profiles of the different pyramid arrangements.

A summary of the different geometries investigated as part of this study is shown in Table 6-1. To isolate the impact of pyramid height on performance, three sizes of pyramids were investigated. The pyramid heights were $e = 0.25$ mm, $e = 0.43$ mm, and $e = 0.63$ mm tall, which correlates to a pyramid height over channel height ratio of $e/H = 0.131$, 0.231 , and 0.328 . The frontal width of the pyramid was defined as twice the height resulting in an apex angle of 90° , which is categorized as “broad” according to Martinuzzi et al. [147]. Pyramids were arranged in a staggered array on one or both sides of the test coupons, as shown in Figure 6-1. For pyramids of differing heights, the pyramids were only integrated on one endwall of the test coupon. The spacing of the array was normalized using the projected frontal width of the base of the pyramid, defined as W_s (equal to two times the pyramid height). The pyramids were distributed in a staggered arrangement, with a streamwise spacing of $x/W_s = 2$ and spanwise spacing of $S/W_s = 3$.

Table 6-1. Coupon Geometric Descriptions

Coupon Name	Pyramid Arrangement	Design S_x Open Channel S_x	Designed	Measured	Designed e/H	Measured e/H	Endwall R_a [μm]	Endwall R_z [μm]
			Pyramid Height [μm]	Pyramid Height [μm]				
Open Channel	None	1	-	-	-	-	3.00±1.2	21.7±2.1
Small Pyramids	One Side	1.05	250	151.2±4.8	0.13	0.08	3.58±1.2	23.0±2.4
Medium Pyramids	One Side	1.05	440	349.8±10.1	0.23	0.18	4.00±1.3	25.9±3.0
Large Pyramids	One Side	1.05	635	547.6±23.6	0.33	0.29	4.15±1.3	28.7±5.2
Large Pyramids, Both Sides Aligned	Both Sides Aligned	1.08	635	543.8±12.9	0.33	0.29	3.30±1.3	27.9±2.4
Large Pyramids, Both Sides Offset	Both Sides Offset	1.05	635	531.8±11.3	0.33	0.28	4.25±1.2	32.6±3.2

In addition to the three designs that varied pyramid height, two designs were manufactured that varied the pyramid arrangement, as shown in Figure 6-1. The first arrangement was the “aligned” case, where pyramids were placed on both walls of the test coupon as if they were mirrored across the midspan. The second was an “offset” case, where the pyramids of opposing rows were placed staggered on either side of the test coupon. These additional cases were designed to elucidate any potential impacts of variations to the array arrangement on heat transfer and pressure losses. Finally, there was one additional test coupon featuring an open channel and no surface features. This coupon’s purpose was to serve as a baseline for the expected performance of an empty additive duct and to give perspective on how much increase in performance could be expected by implementing any of the pyramid designs.

The six test coupons were manufactured out of IN718 on a GE M2 printer with industry standard process parameters. Coupons were manufactured in a vertical orientation at a constant radius from the laser source, as this has been shown in the past to minimize variations to local surface roughness [152]. Support structures were integrated into the flanges of the design to enable this print orientation. After the build, parts were cleared of powder and heat treated to remove residual stresses. Finally, coupon flanges were machined to size to allow them to mate with the experimental test rig and support structures were removed.

6.5. Geometric Characterization

To characterize the accuracy to build intent, test coupons were scanned using Computed Tomography (CT) using a voxel size of 35 μm . Using a commercial software the surfaces determined by the CT scans were reconstructed to within 3.5 microns [54], though it should be noted that features smaller than the voxel size were not resolved from this analysis. These reconstructed surfaces were digitally split into approximately 1000 slices along the flow direction.

For each slice the perimeter and cross-sectional area of the duct was determined, which were then used to determine the duct hydraulic diameter for each slice. The slice values were averaged for each coupon, and showed that each duct was built within 3% of the design intent.

After characterization by CT scan and performing the heat transfer and pressure drop testing, the coupons were cut open using wire electro discharge machining to reveal the internal surfaces. The extracted coupon surfaces were then measured by focus variation on an optical profilometer (OP) to more precisely measure pyramid heights and roughness statistics. Scans were taken using a 10x resolution, which resolved features approximately one micron and larger. Using the profilometer software, three geometric characteristics from the pyramids were measured: the average height, the streamwise length and the spanwise width. These measurements were taken on a minimum of seven pyramids for each design to ensure statistical significance. The normalized heights, streamwise lengths, and spanwise widths of the pyramids are summarized in Figure 6-2. To make these measurements, lines were defined across the streamwise and spanwise width of the pyramids, similar to what is shown in the diagram of Figure 6-2. These lines captured the average profile of the pyramid along the length of the line. To determine the spanwise width and streamwise length of the pyramid, the location where the surface extended beyond the height of the local surface roughness was identified, as shown by the red and blue “X”s in Figure 6-2. The distance between these two “X”s was defined as the span or length of the pyramids respectively. The height of the pyramid was defined as the average of the max height found from the spanwise and widthwise profiles, and is shown using a green “X”.

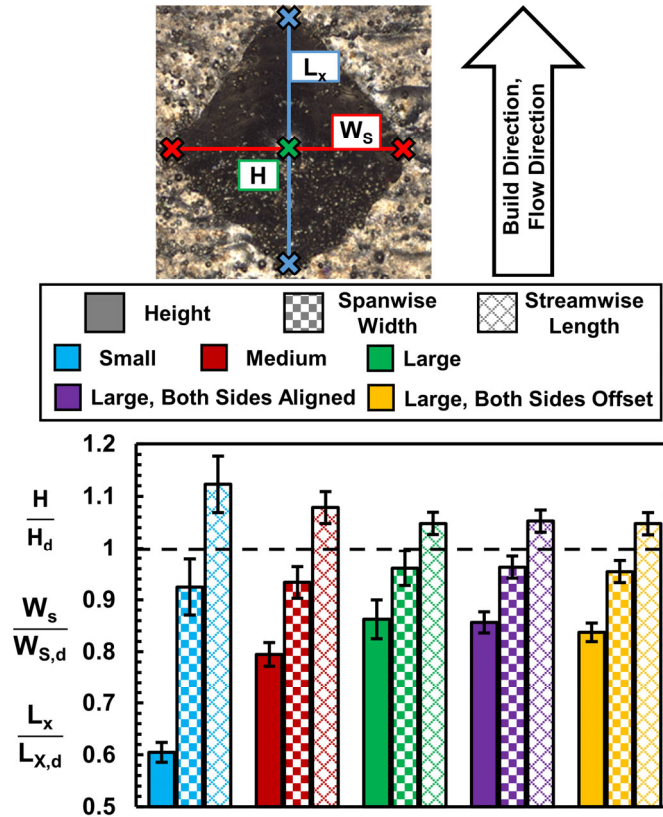


Figure 6-2. Measurements of pyramid height, spanwise width, and streamwise length from optical profilometry scans.

All of the pyramids were notably shorter than the design intent shown by the solid bars in Figure 2 with the small pyramid being only 60% of its intended height. The deviations reported in Figure 2 correspond to each design printing approximately 100 μm shorter than intended. This deviation can be attributed to the rounding of the top of the pyramid, due to limitations of the weld pool size during the manufacturing process. The spanwise width and streamwise length of the pyramid were manufactured within 10% of the design intent, with the spanwise width being smaller than intended and the streamwise length being larger than intended. The lengthening along the streamwise direction was the result of the powder being unsupported on the downskin face of the pyramid during the print. Despite the height, spanwise width and streamwise length deviating from the design intent, the surface area was within 2% of the design intent for all designs due to additional surface area from the roughness features.

The software used to operate the optical microscope was also used to extract roughness statistics. For each coupon a minimum of 12 locations were scanned to extract roughness measurements. Before calculating any roughness statistic from these measurements, a surface correction was applied to account for any tilt the sample had during the measurement. Additionally, a filter was applied that removed non-physical noise from the scan measurement. After these

corrections were applied, four line profiles were defined parallel and perpendicular to the build direction for each measurement location. From the profiles two roughness statistics were extracted: the arithmetic mean surface roughness, R_a , and the average roughness height, R_z .

Roughness measurements from the optical scans revealed that the average R_a for the end walls of all coupons were within measurement uncertainty, with an average value of $3.7 \pm 1.2 \mu\text{m}$. A summary of all of the roughness values is shown in Table 6-1. This value of R_a is relatively low as compared to prior work on published additive surfaces [29], which was likely the result of highly refined process parameters and the ideal surface orientation of the test coupons. R_z measurements were also found to be very similar across all coupons, with an average value of $26.0 \pm 1.4 \mu\text{m}$. This means that the roughness features on the surface of the part were between 5-17% of the height of the as-built pyramids. The magnitude of the R_z measurements were largely a function of the of partially sintered particles present on the surface, in tandem with the layer lines distributed along the build direction.

Qualitatively, the upward facing surfaces of the pyramids are even more smooth than the endwalls, as seen in Figure 6-2, with only a few partially sintered particles dotting the surface. The downskin faces of the pyramid are significantly rougher than the upskin faces due to a collection of particulates that partially fused to the downskin surface. This particulate is the result of the laser fusing more powder than intended during the additive build process, as would typically be expected of downskin surfaces.

6.6. Experimental Setup

Bulk thermal and pressure drop measurements were captured using an experimental rig that has been described in great detail in previous papers by the authors [105,139]. In short, upstream of the test section the flow is metered using a mass flow controller. The flow then passes through an upstream plenum, through the test coupon, and then exhausts from a downstream plenum. These plenums are used to modulate the flow to known conditions, with the upstream plenum providing a uniform velocity distribution, and the downstream plenum providing a sudden expansion allowing for known minor loss coefficients. Both plenums are instrumented with pressure taps and thermocouples to capture the pressure drop and thermal rise across the coupon during testing. Isentropic flow relations are used to capture the exact flow conditions at the inlet and exit of the test coupon. Downstream of the test section a needle valve is used to regulate the internal pressure to ensure the Mach number stays less than 0.2 during testing. During heat transfer testing, a heating assembly is installed on both sides of the test coupon which imposes a constant surface temperature boundary condition. The heater for these assemblies is situated between a copper block and a foam block. The copper block features precisely machined holes for

six thermocouples, which were used in a 1D conduction analysis to find the coupon surface temperature. Losses in the test section were estimated using thermocouples installed in the foam and the plenum respectively.

Pressure drop from the test coupons was normalized using the friction factor, which is defined in Equation 6-1.

$$f = \frac{2 \cdot \Delta P}{\rho \cdot u_m^2} \cdot \frac{D_h}{L} \quad (6-1)$$

Heat transfer was normalized using the Nusselt number and is defined in Equation 6-2.

$$Nu = \frac{h D_h}{k} \quad (6-2)$$

The bulk heat transfer coefficient was defined assuming a constant surface temperature boundary condition and accounted for the losses to the test rig, as shown in Equation 6-3.

$$h = \frac{Q_{in} - Q_{loss}}{A_s \Delta T_{LMTD}} \quad (6-3)$$

While running the heat transfer experiments an energy balance was performed that compared the heater power minus the calculated thermal losses to the first law of thermodynamics. For all experimental tests this energy closure was within 3%, indicating that the energy in the system was well captured.

The bulk friction factor and Nusselt number are commonly normalized by the equivalent friction factor or Nusselt number for a straight cylindrical channel. The smooth friction factor was determined using the Colebrook correlation [55] assuming a smooth wall, shown in Equation 6-4, and the smooth Nusselt number was determined using the Gnielinski correlation [56], shown in Equation 6-5.

$$\frac{1}{\sqrt{f_0}} = 2.0 * \log \left[\frac{f_0}{Re} \right] \quad (6-4)$$

$$Nu_0 = \frac{\frac{f_0}{8} (Re - 1000) Pr}{1 + 12.7 \sqrt{\frac{f_0}{8}} \left(Pr^{\frac{2}{3}} - 1 \right)} \quad (6-5)$$

To benchmark the test rig, a coupon containing only straight smooth channels was tested, and showed good agreement with the previously mentioned correlations for the test range evaluated in this study. The results from this test coupon are shown in later sections.

In addition to the rig used to evaluate the bulk friction factor and Nusselt number, an additional test rig was used to determine any variation in the local surface temperature of the designs. A diagram of this experimental test rig is shown in Figure 6-3. This setup consisted of a rectangular channel with a hydraulic diameter of 13.6mm that was fed using a mass flow controller

upstream of the test section. In the test section mainstream temperatures and pressures were measured just upstream of the test section using thermocouples in the flow, and a pressure tap located in the top surface of the square channel. One half of a test coupon that was cut up for optical profilometry measurements was bonded to a heating assembly that was similar to those used for the bulk heat transfer measurements using thermal paste. This heating assembly applied a constant surface temperature boundary condition on the base of the channel. A cover plate was installed over the edges of the coupon to secure it during testing, and ensure a gradual transition from the rectangular channel surface to the rough surface of the test coupon. There was a Zinc Selenide window above the test section to allow optical access for a high-resolution (1280x1024) infrared (IR) camera to measure the coupon surface temperature. The test coupon was painted black to increase surface emissivity for IR camera measurements. The thickness of this paint was expected to be approximately 25 microns thick, based on prior measurements of the paint thickness on similar samples in the same lab. This paint thickness meant that the smallest roughness features may have been smoothed out, but the largest features which contributed more significantly to the local flow performance would still be visible. Surface thermocouples were bonded to the coupon for in situ IR calibration during testing. Thirty images of the coupon surface were taken and averaged for the results reported in this investigation.

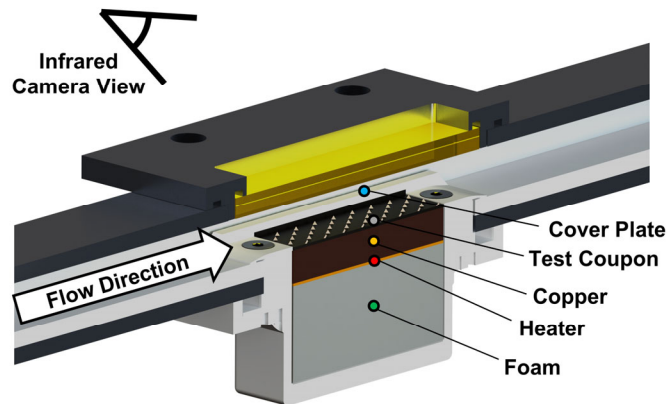


Figure 6-3. Cross section of rig used to take IR images of coupon surface.

Surface temperatures for the IR measurements were normalized using the fin temperature, defined using Equation 6-6.

$$\frac{T_s - T_\infty}{\overline{T}_s - T_\infty} \quad (6 - 6)$$

The base temperature, T_s , was determined by taking the area-average endwall temperature excluding areas with the pyramid geometries.

6.7. Computational Setup

To analyze internal flow features, computational fluid dynamics (CFD) simulations were completed using a commercial software [107]. A diagram of the computational domain that was used to evaluate this geometry is shown in Figure 6-4. The computational domain mimicked the experimental test coupons, but included an additional empty upstream section that was five duct heights long, and an empty downstream section that was ten duct heights long. The inlet to the domain was a mass flow inlet which imposed a Reynolds number of 20,000, and the outlet of the domain was a pressure outlet at 60psi. To simplify the model, symmetry planes were used on opposing walls of the duct such that only one sector of pyramids were modeled. The walls of the domain were isothermal, set to a temperature of 75°C. The walls were modeled as smooth, as prior investigations have shown explicitly modeling additive roughness is typically complex and requires either advanced wall modeling or highly refined surface meshes. The goal of these computations was to describe the largest flow features that drove the heat transfer and pressure loss in the domain. Modeling the domain in this way also offered the opportunity to delineate how the AM roughness impacted the performance of the different features, since these models should in effect be capturing the smooth version of these designs.

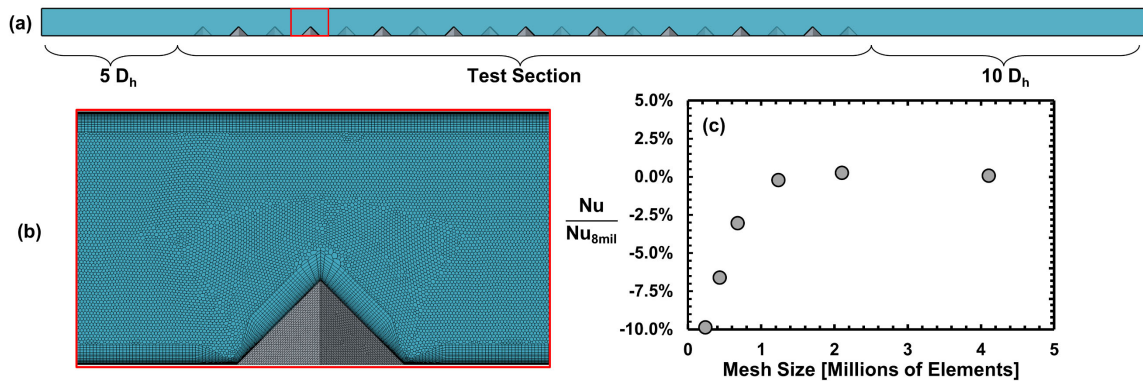


Figure 6-4. (a) Domain used for computations, (b) mesh used for computations, (c) mesh convergence study.

The domain was meshed using a polyhedral mesher in the far field and using prism layers in the near wall region. The prism layers were defined such that the near wall y^+ was approximately one, and the growth rate was set at 1.1 to accurately capture the thermal and velocity gradients near the wall. A mesh sensitivity study was completed on the domain containing the large pyramids on one wall, with meshes ranging from 240 thousand cells to over 8 million, and the result of this analysis is shown in Figure 6-4(c). It was found that after a mesh size of approximately 2 million cells that further refinement did not change the value of the calculated bulk Nusselt number or friction factor. However, because of available computational resources all of the domains were meshed using the settings that resulted in the highest density mesh of approximately 8 million cells.

The flow was modeled using Reynolds Averaged Navier Stokes (RANS) with the k-omega SST turbulence model using a linear constitutive relationship. No wall functions were used and the boundary layer was fully resolved. The modeled fluid was air. Density in the domain was calculated using the ideal gas law, and the thermal conductivity and viscosity of the fluid were determined using Sutherland's Law.

Since one of the cases run for this study was a simple empty duct, results from this duct were compared against the values predicted by Colebrook and Gnielinski correlations, similar to what was done for the experimental data. It was found that the empty duct case was within 0.005 (19%) for friction factor, and within 1.79 (4%) for Nusselt number, indicating that the near wall flow features were relatively accurately captured.

6.8. Uncertainty Quantification

The uncertainty in the experimental calculations was determined by the method of propagation of uncertainty as described by Dunn [57]. The uncertainty of Reynolds number was less than 2% for all Reynolds numbers greater than 5,000. For the friction factor measurements, uncertainties were approximately 6% at Reynolds numbers greater than 10,000 with repeatability lower than 4.5% for all test cases. The largest contributors to uncertainty were the pressure drop across the coupon and the dimensional accuracy from the CT scans. The uncertainties for the heat transfer tests were approximately 4%, with repeatability within 2%. The greatest contributors to uncertainty for the heat transfer tests were the wall temperatures and the outlet temperature thermocouple measurements. Uncertainty in the accuracy for the fin temperature measurements made using the IR camera were 0.05, though the precision of these measurements was 0.002.

6.9. Surface Temperature Measurements

The normalized fin temperature ratios as determined from the IR measurements are shown in Figure 6-5. The coupon endwall is largely at a uniform temperature, with a slight increase along the flow direction due to the flow developing across the coupon surface. There were local decreases in surface temperature on the pyramid surfaces in the same location as the partially fused roughness elements present near the tip of the pyramids on the downskin surfaces. Because these particles were only partially fused to the coupon surface, their conduction resistance was significantly enhanced resulting in a reduction in the local surface temperature. Additionally, the flow impinged onto the front of the diamond pyramids which further decreased the temperature. Several tests were run at a variety of different copper block temperatures and Reynolds numbers and the fin temperature ratios were found to be independent of the tested conditions. Given that the majority of the surface area of this design had a fin non-dimensional temperature approaching unity, the

assumption that the surface could be treated as isothermal was validated for the bulk heat transfer tests.

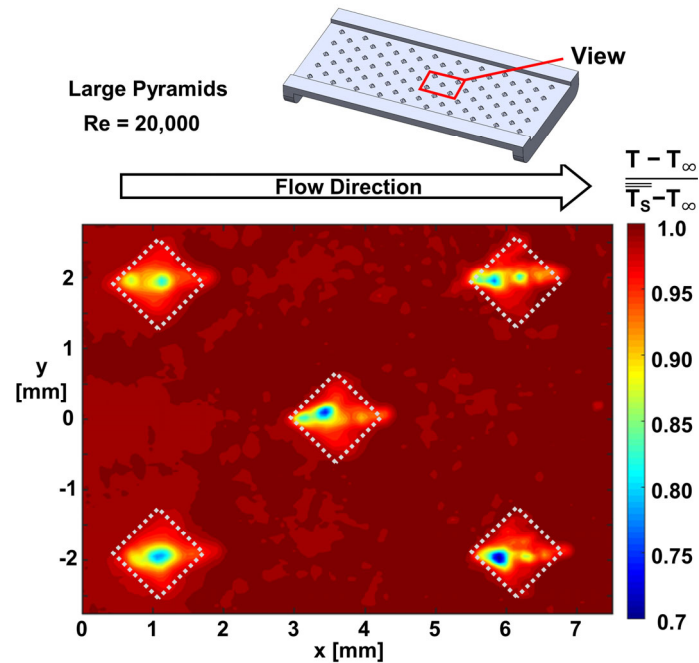


Figure 6-5. Temperature distribution on the surface of the large pyramids case.

6.10. Developing and Developed Flow

To gauge the performance of the different pyramid geometries, the bulk friction factor and Nusselt number are presented as a function of Reynolds number in Figure 6-6 and are compared against straight cylindrical AM channels from Wildgoose et al. [53]. All forms of pyramid geometry had increased pressure loss and heat transfer over the AM open channel case, showcasing how even the smallest geometry had an impact on the bulk flow characteristics. Comparing the three pyramids of different sizes, both the pressure drop and heat transfer increased with increasing pyramid size. Specifically, the Nusselt increased by approximately 8% and the friction factor increased by 11-17% for each increase in pyramid size. As the pyramids became larger they imparted a more significant flow disturbance, causing wake vortices to increase in strength, as will be shown in later sections.

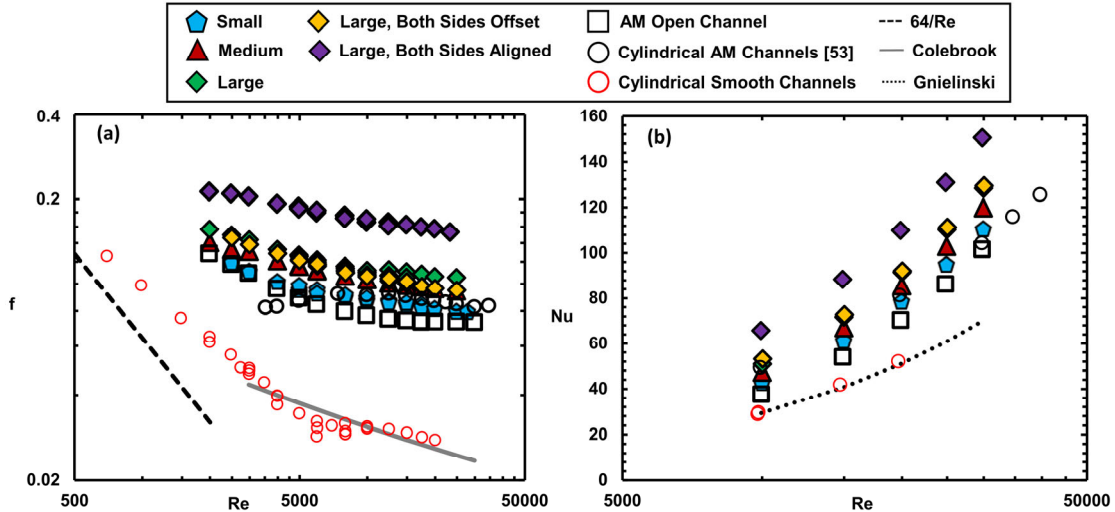


Figure 6-6. (a) Friction factor and (b) Nusselt number as a function of Reynolds number for the various diamond pyramid configurations.

The arrangement of pyramids on the two channel surfaces also had a significant impact on the thermohydraulic performance, as shown in Figure 6-6, with aligned large pyramids on both sides of the channel resulting in the greatest overall pressure drop and heat transfer. This increase in heat transfer and pressure decrease can be attributed to the reduction in flow area from the pyramids on both sides, resulting in substantial local flow convective acceleration. The large pyramids on one side and the offset large pyramids on both sides had very similar friction factor and heat transfer performance over the range of Reynolds numbers evaluated. This similarity in performance can be attributed to similar heat transfer enhancement regions behind the two designs, which will be quantified in later sections.

Comparing the heat transfer from the open channel printed for this study with the cylindrical AM channels characterized by Wildgoose et al. [53], the cylindrical channels have greater friction factor and Nusselt numbers augmentations. These greater values are expected, as the channels studied by Wildgoose et al. were moderately rougher ($R_a \sim 10\mu\text{m}$) than those in the current study ($R_a \sim 4\mu\text{m}$), and also had a smaller hydraulic diameter ($D_h = 1.25\text{mm}$). At high Reynolds numbers when the flow becomes highly turbulent, the Nusselt number, as reported by Wildgoose et al., and the open channel case in the current study become the same within the uncertainty. This similarity in results implies that there is a limit to the heat transfer enhancement from the roughness elements as the flows become highly turbulent, while still being detrimental to pressure losses.

For the open channel results in Figure 6, the rough AM channel transitioned to turbulent flow at a lower Reynolds number than the smooth cylindrical channels, as indicated by the significantly greater friction factor at the textbook transition Reynolds number of approximately

2,000. This transition occurs due to various roughness features present on the surfaces of the additive parts turbulating the flow. Additionally, the open channel became fully turbulent at a Reynolds number of approximately 10,000, as the friction factor became independent of Reynolds number. In contrast, the friction factor of the various pyramid geometries did not become independent of Reynolds number within the range tested. In some cases, like the aligned large pyramids on both sides, continued to decrease above Reynolds numbers of 20,000. This continued decrease at high Reynolds numbers is the result of separated flow regions that will be discussed in greater detail in a later section.

To more precisely examine the differences in performance between the different pyramid designs, the experimental and computational friction factor data at a Reynolds number of 20,000 was normalized in two ways. The first way normalized both data sets by the Colebrook friction factor, f_0 , to find the augmentation over a smooth channel. The second method normalized the friction factor by the open channel case, f_e , to find the augmentation of the pyramids over a rough channel. For the latter, the computational studies were normalized by the computational open channel, and the experimental results were normalized by the additive open channel. The results of these normalizations are shown in Figure 6-7, with bars to denote the experimental uncertainty.

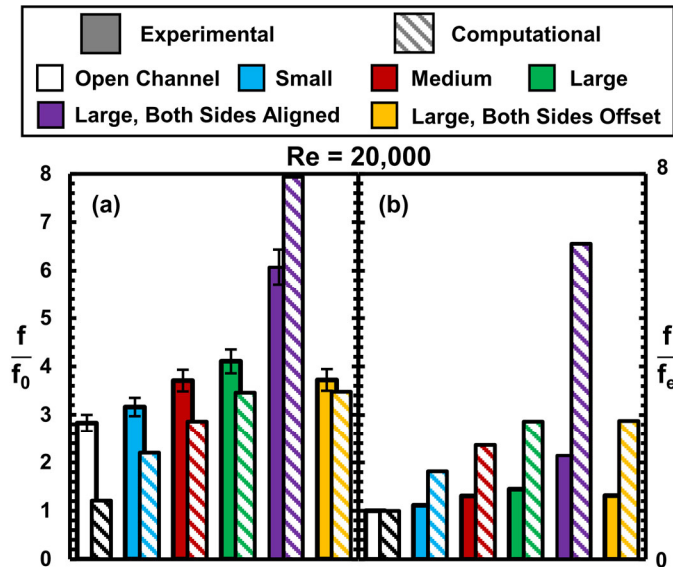


Figure 6-7. Friction factor augmentation from a (a) smooth duct and the (b) empty duct cases at a Reynolds number of 20,000.

Looking first to the results presented in Figure 6-7(a), it can be seen that as the size of the pyramid increases from the small pyramids design to the large pyramids design, there is a consistent increase in overall friction factor augmentation both experimentally and computationally. The computational augmentations predicted especially for the small pyramids and the empty duct are significantly lower than the experimental results, indicating that the inherent surface roughness is

having a notable impact on the overall friction factor for these designs. As the pyramids grow in size, the influence of the design overtakes the influence of the roughness and the simulated friction factor approaches the experimental. For example, computational and experimental results agree much more for the large pyramids than for the small pyramids. For the aligned pyramids on both walls, the computational augmentation was significantly greater than what was found experimentally. This difference in performance can be attributed to the limitations of the computational turbulence model and differences between the computational and experimental geometry which will be discussed shortly. Because the current analysis is focused on the largest flow features, whose forms are expected to be largely independent of turbulence and small geometric differences the computational models were deemed valid for the current study.

The experimental data in Figure 6-7 indicates that the large pyramids on one side had a slightly higher friction factor augmentation than the pyramids on both sides, even though the computational results indicated that their performance should be nearly identical. This difference in performance is suspected to be the result of how the roughness on the endwall surfaces impacted the attachment and reattachment behavior of the offset large diamond pyramids on both sides.

Looking to the results normalized by the open channel case in Figure 6-7(b), all cases showed the computational augmentations are significantly greater than the experimental augmentations. This deviation between the two sets of results suggests that implementing these pyramids on a smooth surface would have a more significant impact on the internal pressure loss than an implementation on a rough surface.

A similar analysis to what was shown in Figure 6-7 was completed using the Nusselt number with the smooth Nusselt number estimated by the Gnielinski correlation and is shown in Figure 6-8, with bars to represent the experimental uncertainty.

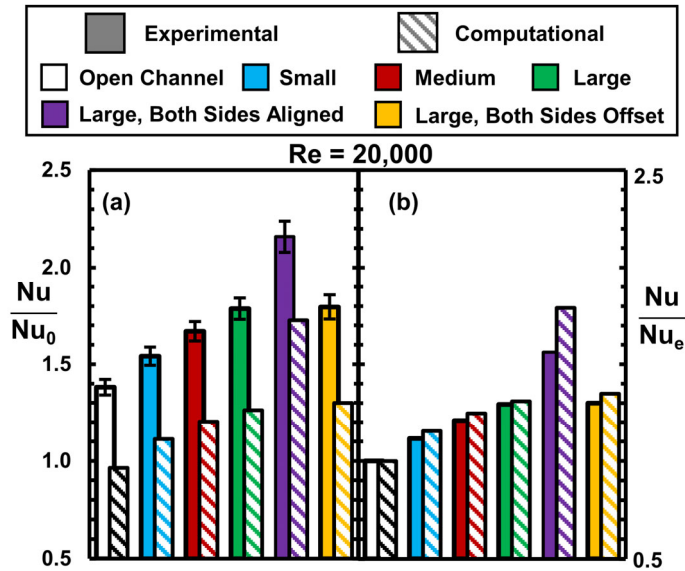


Figure 6-8. Nusselt number augmentation from a (a) smooth duct and the (b) empty duct cases at a Reynolds number of 20,000.

Starting with Figure 6-8(a), it can be seen that the heat transfer augmentations are significantly smaller than the friction factor augmentations, as indicated by the scale on the y-axis. There is again a clear trend of increasing augmentation as the size of the pyramid increases both experimentally and computationally. The aligned large pyramids design has the highest heat transfer augmentation, measured at $Nu/Nu_0 = 1.72$ and predicted at $Nu/Nu_0 = 2.16$. Similar to the friction factor results, the predicted Nusselt number was notably lower than the experimental augmentations. This can be largely attributed to the lack of surface roughness present in the computational setup. Unlike the friction factor results, the difference between the computational and experimental results are nearly constant, with a bias of approximately $Nu/Nu_0 = 0.45$. This result implies that for the conditions evaluated in this paper, the impact of surface roughness on heat transfer was additive, similar to what was shown by previous authors investigating external flows [153].

Transitioning to Figure 6-8(b) both the computational and experimental augmentations from the open channel case show good agreement. This agreement also shows that the CFD accurately captured the heat transfer from the various pyramid designs. The one exception to this agreement was the aligned large pyramids on both sides which slightly over estimated augmentation values relative to the experiments.

One of the key differences between the experimental and computational cases was the unintended fillets on the experimental pyramid surfaces due to manufacturing limitations. To isolate the impacts of these fillets, an additional simulation was run on the design featuring aligned pyramids on both sides, where fillets were applied to all pyramid edges that approximated the

geometric deviations found in the experimental coupons. The bulk friction factor and Nusselt number from this “rounded edges” case was captured at a Reynolds number of 20,000 and is shown in Figure 6-9.

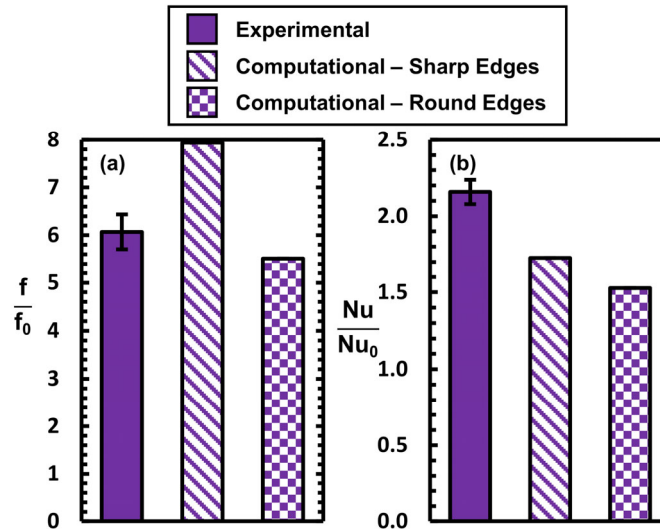


Figure 6-9. (a) Friction factor and (b) Nusselt number augmentation for three variations to the aligned pyramids on both sides case.

Comparing the friction factor augmentation between the three cases shown in Figure 6-9(a), the computational case with rounded edges had a 36% lower friction factor than the case with sharp edges. Despite the large change to the friction factor augmentation, the case with rounded edges had only 12% lower heat transfer enhancement than the sharp edges case as shown in Figure 6-9(b). This greater decrease in friction factor as compared to Nusselt number for filleted surfaces features is similar to results seen in prior rib studies [125,126]. The filleted case pressure drop agrees more closely with the experimental results than the sharp case, though there is a greater discrepancy in heat transfer. Similar to Figure 6-7, the agreement in friction factor augmentation between the rounded case and the experimental results indicates that the shape of the surface feature dominates the pressure drop over the inherent additive surface roughness. However, the additive roughness still plays an important role in enhancing the experimental heat transfer. While the round edges case more closely models the true experimental coupon geometry, the performance trends and flow features as they pertain to this study from the rounded and sharp edges cases were similar as will be shown in later sections.

To explore the flow development, the local friction factor and Nusselt number for the five sharp-edged designs and the empty channel were determined from the computational domains. The local friction factor was ascertained by finding the local pressure drop between the test section inlet and a given streamwise location in the computational domain. The velocity scaling for the local friction factor was the mass-averaged inlet velocity, and the length scaling used the local

streamwise position relative to the test section inlet. The local Nusselt number was determined using the average local convective coefficient, which itself was defined by combining the first law of thermodynamics with the equation for heat transfer using a constant surface temperature boundary condition, and is shown in Equation 6-7.

$$\bar{h} = \frac{\dot{m} \cdot c_p \cdot (T_m - T_{in})}{A_s \cdot \Delta T_{LMTD}} \quad (6 - 7)$$

The surface area used to find the local convection coefficient was defined as the surface area between the domain inlet and the current streamwise position. Because the local temperatures and pressures used in this analysis were streamwise averaged values, the local friction factor and Nusselt number reported in this analysis are also a streamwise averaged value. The results from this analysis are shown in Figure 6-10.

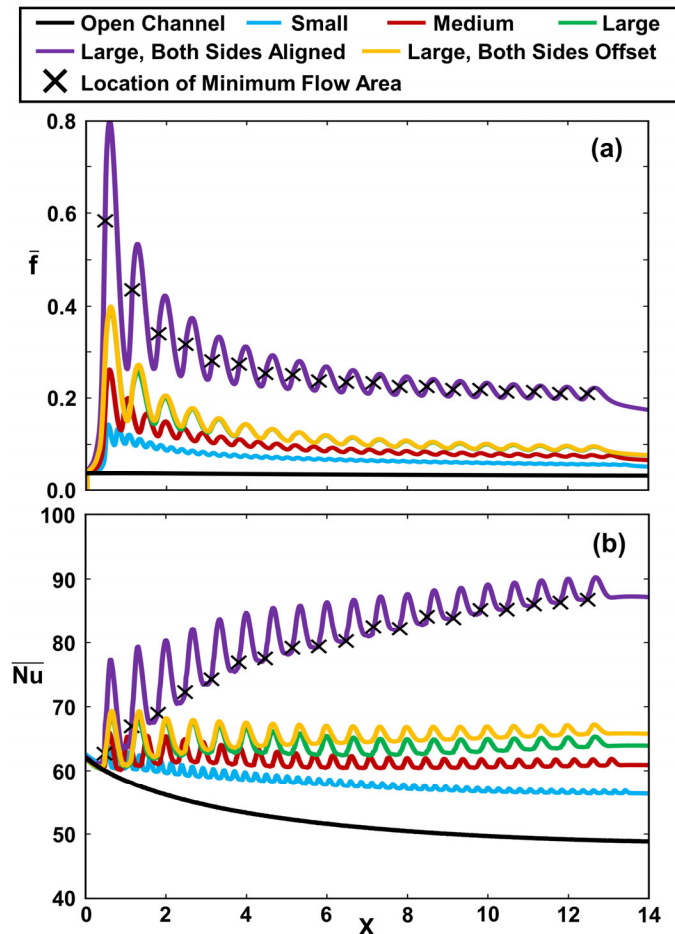


Figure 6-10. Development of local (a) Friction factor and (b) Nusselt number as a function length along the duct with locations of minimum flow area highlighted for the large, both sides aligned case.

The friction factor, shown in Figure 6-10(a), for each design decreases to within 3% of the fully developed value within approximately 10 hydraulic diameters along the length of the channel. The Nusselt number development length varies considerably between designs, with the medium,

large, and large pyramids on both sides offset being within 3% of their fully developed Nusselt number in less than two channel hydraulic diameters. The aligned large pyramids on both sides and small pyramids took 8.2 and 5.2 hydraulic diameter lengths respectively. The flow structures that developed between rows were stronger for the aligned large pyramids, and took more rows to approach a fully developed condition. The small pyramids did not cause large changes to the bulk flow, limiting thermal transport in the regions between rows, resulting in a longer entry region. These differences in development length are driven by the pyramids causing boundary layer detachment, resulting in increased mixing in the near wall region. As the flow through these designs approach a fully developed state there is a clear oscillatory response in the local pressure drop and heat transfer. The amplitude of these oscillations is directly correlated with the flow blockage of each design, with the small diamond pyramids having the lowest flow blockage and lowest oscillation amplitudes, and the aligned large pyramids on both sides having the greatest flow blockage and greatest oscillation amplitude.

In Figure 6-10, a black “X” has been indicated on the aligned large pyramids to illustrate the location of maximum geometric flow blockage, which is located at the apex of a given row of pyramids. It is apparent that this location does not correspond with the maximum of the local friction factor, and instead the minimum flow area is a quarter of period ahead of the maximum friction factor. Additionally, the maximum flow obstruction occurs at the location of the minimum Nusselt number. This local performance can be attributed to the regions of flow attachment and detachment around the pyramid geometry, along with the acceleration of the cooler upstream flow, which will be explored in greater detail in the next section.

Much like the bulk performance, the local friction factor for the large pyramids on one side and the offset large pyramids on one side develops similarly. Despite this similarity, the offset large pyramids on both sides had slightly higher heat transfer augmentation than the large pyramids on one side. This increase in heat transfer for the offset case is related to the formation of wakes behind the two designs, which will also be discussed in the next section.

6.11. Flow Structures and Thermal Fields

The normalized thermal profile of the five designs evaluated as part of this study are shown in Figure 6-11. Comparing the three pyramids of different heights shown in Figure 6-11(a-c), the thermal profile differs significantly. Between rows of the small diamond pyramids there was an area of flow with high temperatures, showcasing the limited thermal transport between this region and bulk flow. Because of the layer of high temperature fluid, this region experiences reduced heat transfer relative to the other pyramid designs. Between rows of the medium diamond pyramids cool air moves into the wake region, enabling more significant heat transfer enhancement than was seen

for the small pyramids. For the large diamond pyramids, the thermal wake is the least pronounced, with cooler fluid able to circulate into the wake region between rows of pyramids, significantly enhancing heat transfer. These flow phenomena directly tie to the bulk performance found in Figure 6-6 (b), with the heat transfer increasing proportionally with pyramid height.

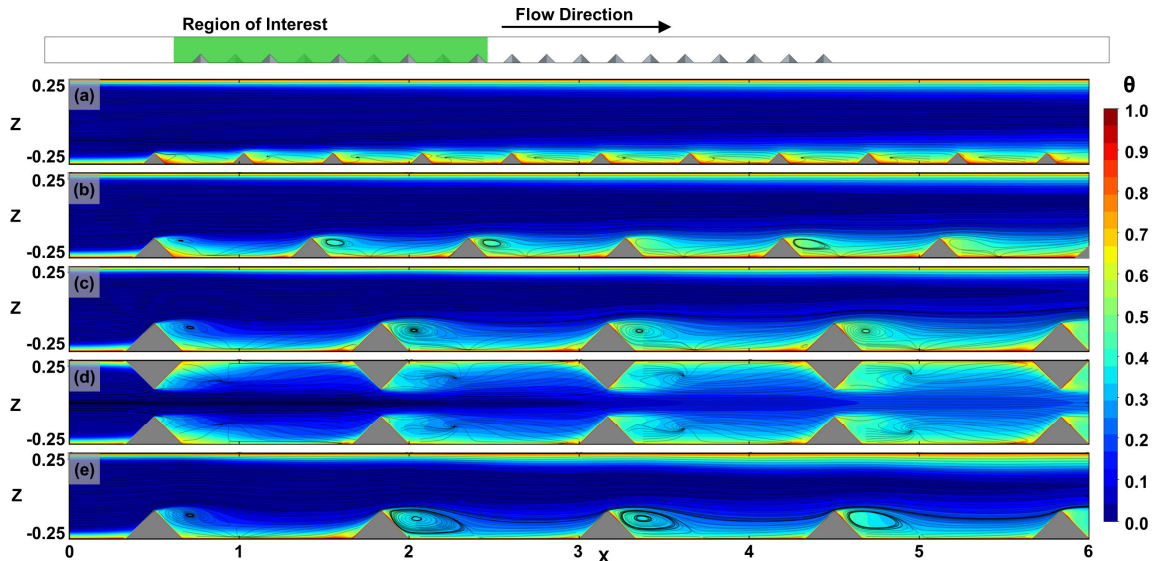


Figure 6-11. Contours of normalized temperature for the (a) small, (b) medium, (c) large, (d) large both sides aligned, and (e) large both sides offset for a streamwise oriented plane in the entry region.

The streamlines and thermal profiles of the large pyramids in the one sided (Figure 6-11(c)) and staggered (Figure 6-11(d)) arrangements were almost identical, despite the differences identified in Figure 6-10. This implies that the major differences in heat transfer between the two designs occurred away from the symmetry plane. In the aligned pyramids on both sides case, the thermal profiles and streamlines have an inherent symmetry along the design midspan due to the geometric symmetry. Because of the greater blockage ratio of the aligned large pyramids, the local flow velocities were increased, and subsequently local heat transfer was also increased. This is indicated by the greater local fluid temperature as compared to the other cases, which aligns with the expectations set by the experimental tests which showed the aligned large pyramids on both sides having the greatest bulk Nusselt number.

Several vortex cores can be identified using the streamlines shown in Figure 6-11. Upstream of the pyramid the flow detaches and a horseshoe vortex forms, which results in a region of increased heat transfer just upstream of the pyramids. For all of the diamond pyramid designs, there was a recirculation zone located beyond the peak of the pyramid, named a rotor vortex by Martinuzzi and AbuOmar [146]. The size of this vortex and the location where the flow re-attaches to the surface behind the vortex was found to be consistent with Martinuzzi and AbuOmar's findings for the three designs varying pyramid height. For the aligned pyramids on both sides the

reattachment location is driven further downstream due to the increased local flow speeds. These recirculation zones are a function of Reynolds number, stretching downstream as Reynolds number increases. These zones effectively act as slip walls, resulting in the reduction to friction factor as a function of Reynolds number as was seen in in Figure 6-6(a).

To continue to understand the impact of round edges on the performance of the diamond pyramids, thermal contours and streamlines were plotted for the third row of the aligned large pyramids case with and without the filleted edges and are shown in Figure 6-12. While there are some changes to the thermal field, such as the cooler upstream fluid traveling further downstream in the rounded case (Figure 6-12(a)) than the sharp case (Figure 6-12 (b)), the general form of thermal field is similar. This slight drop in thermal pickup was expected based on the 12% drop in Nusselt number reported in Figure 6-9(b). The rotor vortex is further downstream of the pyramid for the sharp edge case than the round edge case because of the greater flow constriction of the sharp edge case. For the rounded case, the flow detachment location is less defined than in the sharp edge case, where the flow will detach along the sharp edge of the pyramid.

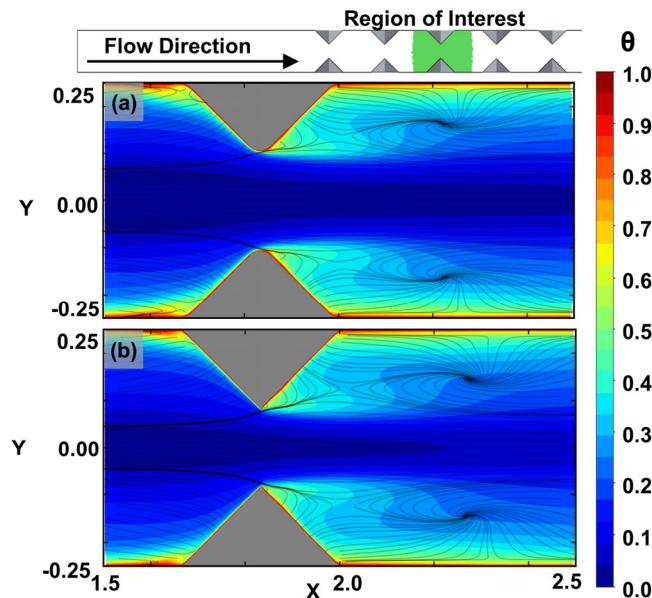


Figure 6-12. Thermal contours with streamlines for the third row of the (a) round edge and (b) sharp edge aligned pyramids on both sides case.

A further description of the thermal profile for the five sharp edged designs is presented in Figure 6-13, which shows the temperature profile with streamlines at two streamwise locations. Looking to the thermal profile at the upstream plane (Figure 6-13(a-e)), there is a region of flow where the thermal boundary layer is thin due to the interactions between a horseshoe vortex and the rotor vortex shown in Figure 6-11. This region of reduced boundary layer thickness allows for increased heat transfer from the wall to the bulk flow in the channel. At the downstream plane (Figure 6-13(f-j)) this region of reduced thermal boundary layer thickness is largely dissipated due

to the mixing that occurs as a function of the frequent boundary layer detachment from the pyramid protrusions. For the small pyramid design shown in Figure 6-13(f) the thermal boundary layer at the downstream plane is similar for the bottom wall with pyramid features and the top wall without features. The similarity in thermal profile between the smooth wall and the wall with pyramids indicates that the small pyramids did not significantly alter the thermal profile beyond the immediate interactions with the pyramid geometries. These results imply that the majority of the increase in heat transfer for the small pyramid design was due to impingement on the front faces of the pyramids.

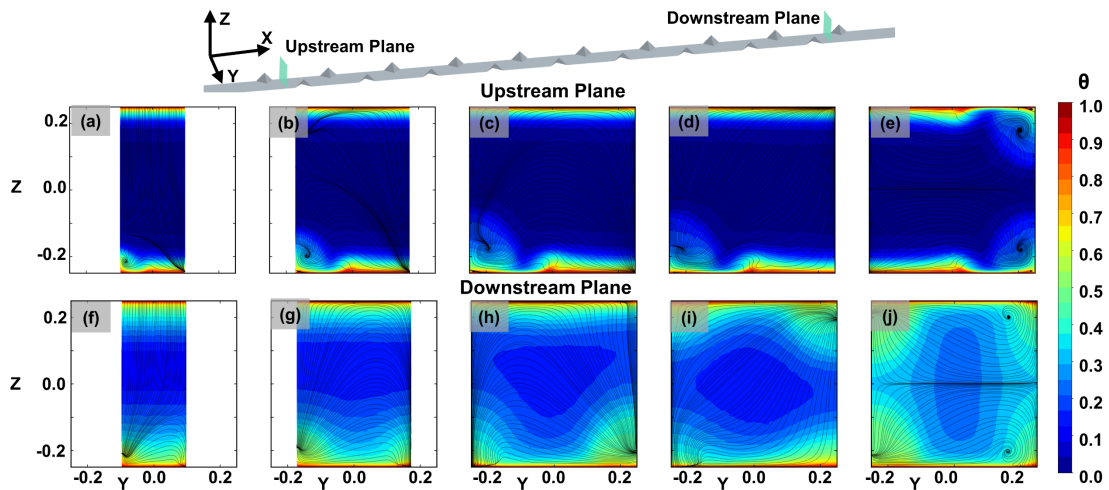


Figure 6-13. Contours of normalized temperature for the (a) small, (b) medium, (c) large, (d) large both sides aligned, and (e) large both sides offset for planes normal to the streamwise direction.

In the wake of all of the pyramid designs at the first planar location there is a pair of counter rotating vortices that form and propagates downstream, as shown in Figure 6-13. These vortices improve heat transfer downstream of the rotor vortex identified in Figure 6-11, but also acts as a source for increase wall shear stress and pressure loss.

To investigate the impact of the previously identified flow structures on the endwall heat transfer, contours of the endwall Nusselt number augmentation were extracted and are shown in Figure 6-14. This endwall Nusselt number was calculated using the local heat flux and the streamwise averaged log mean temperature difference. It is clearly evident comparing the regions with locally reduced thermal boundary layers shown in Figure 6-11 and Figure 6-13 to the surface contours in Figure 6-14, that these areas experience significantly enhanced local heat transfer. As the vortex strength increased, the heat transfer on the endwall also increased. In the case of the offset pyramids on both sides, the vortical zone in the wake was not as constricted as with either the large pyramids on one wall, or the aligned large pyramids on both walls. This lack of constriction allowed for an overall increase to the heat transfer as compared to large pyramids on

only one wall despite having the same overall surface area, which is reflected in the streamwise averaged Nusselt number profiles provided in Figure 6-10.

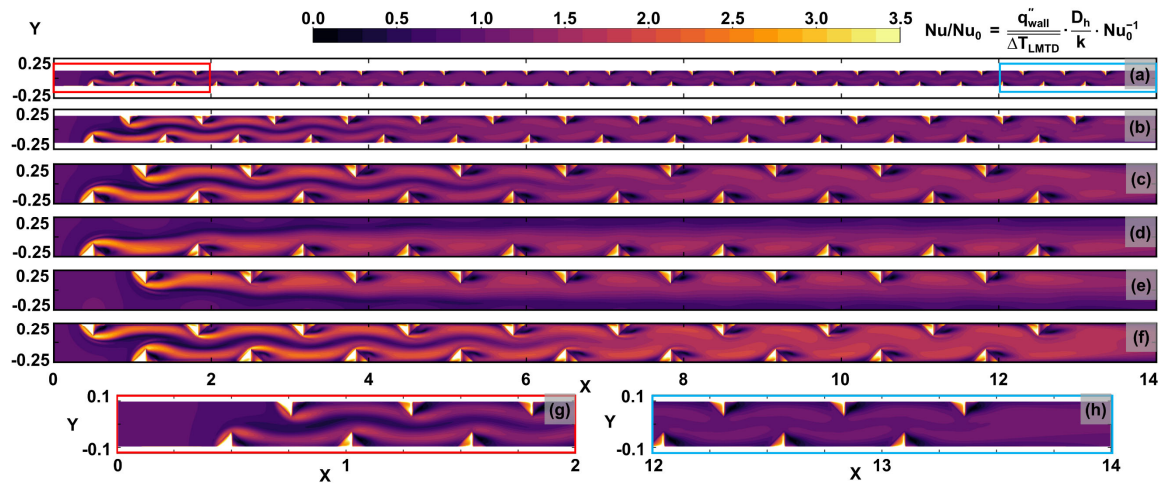


Figure 6-14. Contours of the endwall Nusselt number augmentation for the (a) small, (b) medium, (c) large, (d) large both sides offset bottom wall, (e) large both sides offset top wall, and (f) large both sides aligned cases, with a zoomed in view of the (g) upstream and (h) downstream region of the small pyramids case.

The faces that experience the greatest Nusselt number are the front faces of the pyramids, as cool air impinges on the front face resulting in significant heat transfer. These high Nusselt number regions line up with the IR measurements reported in Figure 6-7, where it was found that the front faces of the pyramids had the lowest surface temperature, indicative of increased convective heat transfer overwhelming the conductive heat transfer through the coupon.

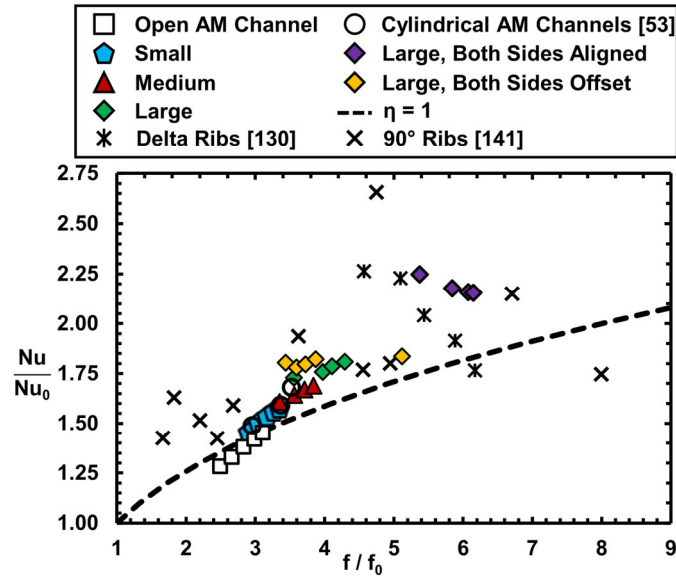
In the later rows of the diamond pyramids of all varieties, the areas of Nusselt number enhancement become less defined, and the enhancement region extends to the full span of the domain. However, the recirculation zones present just behind the spanwise corners of the pyramids continue to exhibit poor endwall heat transfer for all rows of pyramids, and the forward-oriented faces of the pyramids continue to have significantly enhanced heat transfer. The broadening of these heat transfer enhancement regions is the result of the less intense but larger regions of mixing that occur in the near wall region as the flow becomes highly mixed.

6.12. Overall Performance

There is a wide scope of surface feature designs that have been explored in prior literature. A summary of the geometric properties from two such studies by Park et al. [141] and Han et al. [130] is shown in Table 6-2. The experimental data from the current study is compared against the data from these prior studies on an augmentation plot shown in Figure 6-15.

Table 6-2. Geometric Summary of the Current and Prior Investigations on Surface Features

Study	Geometry	e/H	Streamwise Pitch	Property Varied
Current Study	Diamond Pyramids	0.08 - 0.28	4e	Diamond Pyramid Array Height and Arrangement
Park et al. [141]	90° Ribs	0.03 - 0.13	10e	Channel Aspect Ratio
Han et al. [130]	Delta Ribs	0.12	5e	Arrangement of four different surface features

**Figure 6-15. Augmentation plot comparing investigated designs to prior data.**

The black “X”s in Figure 6-15 represents data from a study by Park et al. [141] who examined ribs on two sides of ducts of several different aspect ratios, and the black “*” represents data from a study by Han et al. [130] who investigated delta shaped ribs on two sides of a square duct. Both of these prior investigations did not include the surface area from the surface features in their calculations of the heat transfer coefficient. To offer a fair comparison to the data in the current study, the data from these studies was adjusted to account for additional feature surface area. The range in Nusselt number and Friction factor augmentations found by Park et al.’s study was similar to those found in this study, indicating that the additional roughness elements on the additive samples did not significantly alter the performance enhancement that could be expected from surface features. However, at low friction factor augmentations Park et al. did find their ribs offered moderately greater heat transfer enhancement than what was found from the designs in this study. Comparing against the data provided by Han et al., the performance of delta ribs is comparable to the performance of the diamond pyramids on both sides, which makes sense given the similarity between the two designs. The cylindrical AM channels from Wildgoose et al. [53] were found to

perform very similarly to the designs in this study, with performance falling largely on top of the small and medium pyramid design data.

6.13. Conclusions

This study investigated five variations on diamond pyramid designs to identify how the pyramid height and arrangement impacted the overall design performance. Test coupons containing the augmentation features were additively manufactured using current best practices. As-printed pyramids were shorter than intended due to surface filets, but were otherwise printed very close to their design intent. Roughness measurements taken from test coupon endwalls revealed that the samples had lower roughness values than had been reported previously in literature for as-built additive parts.

To evaluate the performance of the designs computational and experimental methods were used. As expected based on prior work, an empty additive duct had enhanced heat transfer and pressure loss as compared to a smooth duct. Introducing pyramids further enhanced pressure drop and heat transfer, increasing both proportionally to the size of the pyramid. The pyramids that were arranged on both sides aligned had the greatest pressure loss and heat transfer of the designs considered. Normalizing the design's friction factor by the friction factor of an additive empty duct showed that introducing pyramids on a rough surface had a significantly smaller effect on performance than introducing the pyramids on a smooth surface. Doing the same scaling for heat transfer revealed that introducing pyramids on either the additive or the smooth surfaces resulted in similar levels of heat transfer enhancement.

Investigations into the local heat transfer and pressure loss revealed that the peaks in performance did not align with the location of minimum flow area, but instead were offset. This offset was the result of local convective acceleration, which caused regions of increased heat transfer and pressure loss, especially in the wake region behind the pyramid. The structure and strength of the vortices in the wake of the pyramids were similar to that seen by prior authors exploring singular diamond pyramids. Finally, the designs explored in this analysis were found to be highly comparable to prior surface feature designs, including 90° ribs and delta shaped vortex generators. Future work should identify the role channel aspect ratio has on the performance of diamond pyramid geometries, to offer a more direction comparison to some prior rib studies and greater applicability to turbine blade and vane cooling.

The results from this study uniquely identify the key flow mechanisms and expected heat transfer enhancement for a family of diamond pyramids. Designers can use the information provided in this study to incorporate this type of cooling technology into their own additive cooling schemes.

6.14. Acknowledgement

This research was sponsored by the US Department of Energy, Office of Energy Efficiency and Renewable Energy (EERE), Advanced Materials & Manufacturing Technologies Office (AMMTO), under Contract DE-AC05-00OR22725 with UT-Battelle LLC. This work was performed in part at the Oak Ridge National Laboratory's Manufacturing Demonstration Facility, an Office of Energy Efficiency and Renewable Energy user facility.

7. EXPANDING MATERIAL SELECTIONS FOR ADDITIVELY MANUFACTURED COOLING DESIGNS⁷

7.1. Abstract

Gas turbines feature many components that require superalloys capable of handling extreme thermal environments. Increasing the selection of materials available for these components is important to their use in these extremely high temperature environments. This study investigated two recently developed materials intended to be used for additive manufacturing (AM) with one superalloy based on Cobalt and the other on Nickel. Sets of four test coupons were built using the materials, in addition to the commonly used Inconel-718, on multiple laser powder bed fusion (L-PBF) machines. Several build conditions were varied between coupon sets including coupon orientation, contour settings, and upskin and downskin treatment. Each set of test coupons featured four unique cooling designs to explore how different cooling technologies would be impacted by the variations in build conditions. After being built, coupons were CT scanned to determine accuracy to design intent and quantify the surface roughness. The CT scans indicated that horizontally built test coupons had significantly higher deviation from design intent and higher surface roughness than those built vertically. Results also indicated that the Cobalt-based alloy consistently had a smoother surface quality with lower surface roughness compared to the nickel-based alloy. After geometric characterization, the cooling performance of the test coupons was measured experimentally. Pressure losses were found to correlate with increases in surface roughness; however, in some cases the convective heat transfer did not increase proportionally to the pressure loss as a result of surface features significantly blocking the flow without proportionally increasing convective heat transfer.

7.2. Introduction

Improving the efficiency of gas turbine engines by even a small amount can result in substantial reductions in fuel consumed to either generate thrust for aerospace applications or torque for power generation applications. One means of improving the turbine stage efficiency is by increasing the turbine inlet temperature. Developments in superalloys and sophisticated internal cooling schemes have enabled turbine inlet temperatures up to 1600°C as of 2010, which is in excess of the softening temperature of the metals used to make the parts [1].

Advancements in manufacturing, such as casting of hot section components with internal cooling features, have aided much of this development. However, not only can the casting process

⁷ Corbett, T. M., Thole, K.A., Ryan, D., Sudhakar, B, Kirka, M. M., Ledford, C., “Impacts of Superalloys on The Surface Quality of Additively Manufactured Channels” GT2023-102569

be expensive, but parts can take months, if not years, to manufacture [65]. Recently, some turbine manufacturers have been turning to additive manufacturing (AM), specifically laser powder bed fusion, to manufacture parts. While the low creep strength of AM components relative to single crystal cast components inhibits feasibility for AM turbine blades, other components within the hot section of the turbine under lighter loads may be able to be manufactured via AM [6]. However, there is a limited selection of AM materials capable of handling the extreme environments in this section of the engine [154,155].

To address the limited material selection, two new superalloys have been recently developed for AM gas turbine components, with one being based on Nickel and the other being based on Cobalt [156]. Before using these new alloys for parts with integrated cooling features, it is important to understand how different build conditions, such as the laser parameters and part orientation, can impact accuracy to design intent and surface roughness. To better understand this surface quality and subsequent internal heat transfer, the two new alloys were used to manufacture eight sets of four test coupons containing different internal cooling geometry. Test coupons were printed on a variety of printers with several build conditions. Internal surfaces were characterized using computed tomography scans, and test coupons were then experimentally tested to determine heat transfer and pressure loss characteristics.

7.3. Literature Review

The surface morphology of additive parts is highly dependent on various aspects of the build process, such as part orientation and laser process parameters. While external faces of additive parts can be smoothed through secondary machining operations, internal cooling geometries can be difficult to post process due to lack of line-of-sight access and small features sizes. Therefore, it is important to understand how these aspects of the build process impact the as-built quality of internal additive surfaces.

Many researchers have investigated how part orientation impacted accuracy to design intent and roughness [52,157–159]. When parts feature surfaces that are downward facing and unsupported, known as downskin faces, it is anticipated that there will be a substantial increase in surface roughness and deviation from design intent without modifications to as-designed geometry [52]. These surface deviations are a function of the laser permeating beyond a single layer of powder due to increased powder absorptivity relative to the bulk material, resulting in dross roughness features [160]. Faces that are oriented upwards and are supported beneath by solid material, known as upskin surfaces, have been shown to typically more accurately capture the design intent and have lower magnitudes of surface roughness than downskin and sidewall surfaces [157].

In addition to part orientation, there have been several studies that have investigated the influence of variations to the laser and process parameters, including changes to the laser speed, power, hatch spacing, and layer size [161–165]. These investigations identified the surface quality was a function of the conjugate interactions between these parameters, and should therefore be combined into a single parameter known as the volumetric energy density (VED). VED is defined as the laser power divided by the product of the laser scan speed, hatch distance, and layer size. An investigation by Wang et al. [165] showed there was a parabolic relationship between VED and surface roughness, where either too great or small VED can cause increased surface roughness. Additionally, Zhang and Yuan [166] identified that while higher VED can reduce the surface roughness of upward facing surfaces to some extent, vertically oriented surfaces actually saw an increase in surface roughness with increasing VED.

Some researchers have also investigated curating the laser parameters for specific regions of a part. Several studies by Charles et al. [160,167] have shown that the VED used on downskin faces was directly related to the deviation from design intent and surface roughness, indicating that optimizing parameters for multiple regions of a part is important to achieve better quality surfaces. A study by Tian et al. [162] identified that use of contour scans, which are a laser pass around the exterior surfaces of part at the end of each layer, reduced the overall surface roughness regardless of other build conditions.

Further complicating the matters of appropriate laser process parameters are variations in material. Because of differences in absorptivity, the ideal laser process parameters varies when considering different materials [168]. In addition to the surface quality, one must also consider how the material porosity, microstructure, and residual stresses are impacted by the process parameters, which has also been shown a function of the VED [168,169]. Balancing these considerations may result in parameters that provide a part with better internal grain structure and density, but result in increased surface roughness.

The surface quality of additive parts has a significant impact on the cooling performance of the part. There have been many studies that have identified how the high relative surface roughness of AM microchannels augmented the cooling performance considerably [51]. One study by Kirsch et al. [170] identified that changing the material between Hastelloy X, IN718, and CoCr could cause as much as 30% variations between channel hydraulic diameters, in addition to impacting the quantity and magnitude of roughness elements present on part surfaces. These features and deviations caused the friction factor to vary by as much as 300%. Despite these substantial changes to the friction factor, heat transfer augmentations were relatively similar

between designs printed from different materials, indicating that variations to the surface quality impacts pressure loss more so than convective heat transfer [170].

The as-built surface quality and accuracy to design intent for designs manufactured by L-PBF out of the two newly developed superalloys presented in this study have not yet been reported. To explore the range of surface morphology that can be expected using the current state of the art processing parameters for these materials, test coupons were printed in two orientations and with variations in contour settings. CT scans were completed on test coupons to identify deviations from design intent and quantify surface roughness. After characterizing the test coupons, flow testing was completed to identify how the as-built surfaces impacted the cooling performance.

7.4. Test Matrix Description

The primary focus of this study was to understand the as-built surface quality of two newly developed superalloys for gas turbine applications, and determine the subsequent impacts this surface quality had on the cooling performance on internal cooling designs. The first superalloy used in this study was based on Cobalt and was developed by UC-Santa Barbara[171]. This alloy shows promise to exhibit higher ultimate tensile strength and durability as compared to prior Ni-based superalloys, making it a good choice for gas turbine applications [156,171,172]. The second material was based on Nickel and was developed by Carpenter Technologies Corporation [173], whose composition was curated to enable enhanced additive manufacturing processability. These new alloys were developed for use in the laser powder bed fusion process, and had the same particle size distribution, with particulate ranging from 15-53 μ ms. In addition to these new alloys, IN718 was also used in this study to serve as a point of comparison for the current state of the art materials available for AM gas turbine components.

To understand the as-printed quality of these new alloys, several designs were incorporated into the same general coupon shape which is shown in Figure 7-1. All coupons were designed to be 50.8 mm long, 25.4 mm wide, and 3.05 mm tall. Four different internal cooling geometry designs were investigated as part of this study, with three designs featuring wavy channels, and a fourth design featuring pin fins. A diagram showing the four different designs can be seen in Figure 7-2. The first wavy channel design used in this study was based on the nominal case design presented by Corbett et al. [106], with the additional two cases increasing the channel width by a factor of 1.5 and 2.0 times respectively. Variations to the aspect ratio of the channel have been seen to alter the cooling performance of periodic channels in a prior study due to changes to the strength of the dean vorticities that form along the walls of the channel [45]. Additionally, it was anticipated that the larger channel hydraulic diameter would minimize the deviation from design intent. The nominal case channel was designed to have a hydraulic diameter of 1.27 mm,

with the 1.5X width and 2.0X width channels having a diameter of 1.63 mm and 1.91 mm respectively. Channel lengths were defined such that the flow would become fully developed throughout the length of the channel, with L/D values of approximately 30 at a minimum.

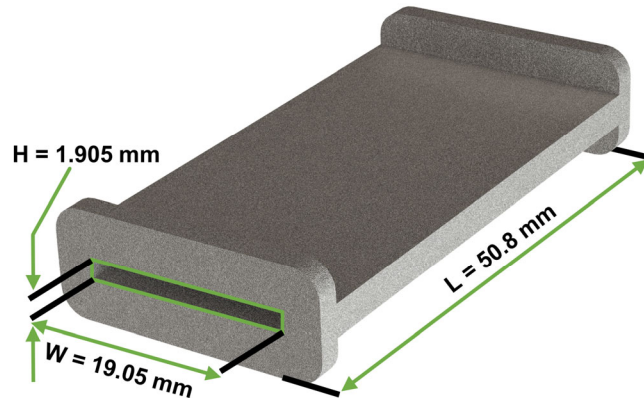


Figure 7-1. General shape of all test coupons used as part of this study.

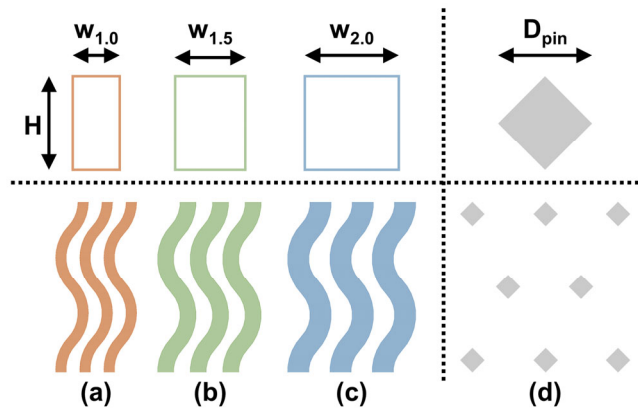


Figure 7-2. Channel hydraulic diameter and internal channel geometry for the (a) nominal width, (b) 1.5 width, and (c) 2.0 width wavy channels, in addition to the pin geometry and spacing for the pin fin design.

The pin fin array that was used as part of this study was based on a study by Corbett et al. [105], and featured pins that had a diamond cross section and were spaced at a spanwise and streamwise spacing of three pin diameters. The pin diameter was defined as the width of the maximum flow obstruction, which was designed to be 1.27mm.

To understand the variety of surface quality that could be achieved using the two newly developed materials, a test matrix was developed that included several L-PBF machines and sets of build conditions which are summarized in Table 7-1. For each variation in build conditions, all four cooling designs were printed to understand how the build conditions impacted each design independently.

Table 7-1. Test Set Build Conditions

Material	Machine	Coupon Orientation	Layer Size [mm]	Upskin and Downskin Treatment	Bulk Material Settings			Contour Settings	
					Power [W]	Velocity [mm/s]	Volumetric Energy Density [J/mm ³]	Power [W]	Velocity [mm/s]
Ni-Alloy	Renishaw	Horizontal	0.05	None	200	678	67.8	-	-
Ni-Alloy	Renishaw	Horizontal	0.05	Applied	200	678	67.8	-	-
Ni-Alloy	Renishaw	Horizontal	0.05	None	200	678	67.8	100	882
Ni-Alloy	Renishaw	Horizontal	0.05	Applied	200	678	67.8	200	667
Ni-Alloy	Renishaw	Vertical	0.05	None	200	678	67.8	100	882
Co-Alloy	EOS M280	Vertical	0.03	None	167	1198	58.1	-	-
Co-Alloy	EOS M280	Vertical	0.03	None	167	1198	58.1	250	400
IN718	GE M2	Vertical	-	-	-	-	-	-	-

The first variation to the build conditions was modifying the coupon build orientation, as can be seen in Figure 7-3(a). The vertical build orientation was anticipated to enable the best quality surfaces, as much of the internal surfaces of the channel coupons would be self-supported. The horizontal build orientation was anticipated to be representative of the worst-case build direction, as much of the internal channel surface was unsupported during the build. It should be noted that for the pin fin designs the pins were unsupported within the duct for both the vertical and horizontal print orientation.

The second variation involved enabling or disabling specialized process parameters for different regions of a given layer during the print. A breakdown of the different regions of a given layer can be seen in Figure 7-3(b), wherein the core, upskin/downskin, and contour regions can be seen. Within the context of L-PBF, the core region consists of the bulk interior material of the part. Upskin and downskin regions refer to the top and bottom external surface of part respectively. Process parameters can be curated for the upskin and downskin regions separate from the core region, and ideally setting unique parameters should reduce roughness elements around the part, and can result in improved accuracy to design intent. Lastly, a contour is a laser pass around the profile of the part for a given slice. Contours are typically used to reduce the surface roughness around the outside profile of a part.

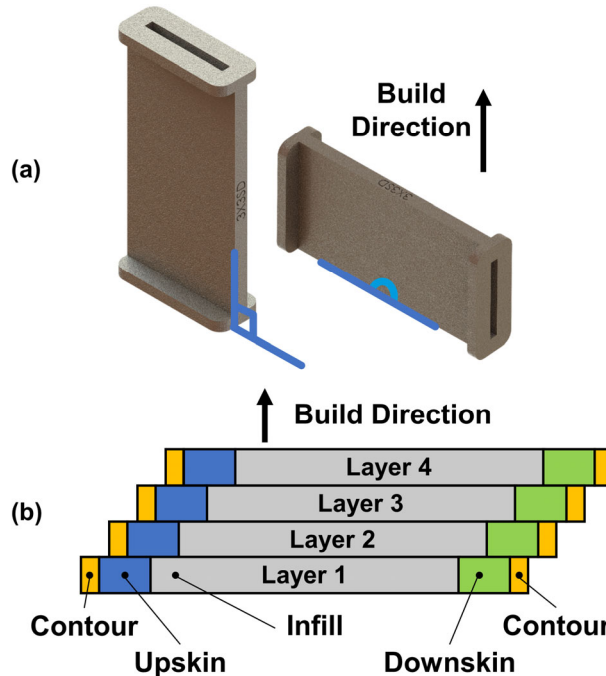


Figure 7-3. (a) Vertical and horizontal print orientations and (b) schematic of different zones in a layer during a L-PBF build that may use different process parameters.

Because there were three different materials that were used as part of this study, the process parameters used in the core region also differed and can be seen in Table 7-1. It should be noted that given that these new materials have only just recently been developed, the process parameters that were used as part of this study are also still under development and are expected to improve over time. Additionally, due to time and material constraints, the Ni-alloy coupons and the Co-alloy coupons were built on two different additive systems, with the Ni-alloy coupons being built on a Renishaw AM250, and the Co-alloy being built on an EOS M290. The IN718 coupons were built on a GE M2 machine by a third party vendor, whose internal process parameters were proprietary, though are representative of the current standard parameters for current AM superalloys. One key difference between the three machines used to manufacture the parts for this study were their lasers, where the GE M2 and EOS M290 use a continuous wave laser and the Renishaw AM250 used a pulsed wave laser. These two laser types interact with the weld pool differently, resulting in greater instability in the case of the pulsed wave laser relative to the continuous wave laser, and additional process parameters that require tuning to manufacture the best possible surface.

7.5. Geometric Characterization

All test coupons manufactured as part of this study were visually inspected immediately after manufacturing to determine if they were printed successfully. Some coupons, like those shown in Figure 7-4, had almost completely blocked channels. In particular, the horizontally built coupons with specialized parameters for the “skin” regions significantly overbuilt into the channels, resulting in completely blocked flow areas. In fact, of the four sets of coupons printed horizontally, only the set with one contour and no skin treatment printed successfully. Since the blocked channels would significantly inhibit flow testing, only two sets of the coupons printed from the Ni-alloy were tested: the coupons built vertically and the coupons built horizontally with one contour and no skin treatment.



Figure 7-4. Pictures of several as-built test coupons.

The remaining five sets of test coupons printed without issue, and underwent additional evaluation through computed tomography (CT) scans. The CT scans were completed using a CT scanner with a voxel size of 35 μm . CT scans were post processed using a commercial software, which was able to resolve the resolution of the scan to 1/10th the voxel size, or 3.5 μm [54]. Using this software, coupon surfaces were re-constructed and exported for additional analysis using in-house post-processing code.

The wavy channel designs were processed by splitting channel into hundreds of cross-sectional slices along the flow direction, similar to what was completed in by Corbett et al. [106]. The perimeter and cross-sectional area were then determined for each slice, and averaged for an entire channel, and then channels were averaged for an entire coupon. This methodology was also used to measure the wetted surface area of the channel coupons which was used in the later analysis. The pin fin coupons were analyzed using a similar but different methodology, which sliced the coupon along the streamwise direction as well as along the length of the pins inside the duct. The slices oriented in the streamwise direction were used to calculate the duct hydraulic diameter using the same method that was described for the wavy channels. The slices oriented along the height of

the channel were used to capture the pin diameter and wetted surface area for each pin independently, which was then averaged for each coupon.

To begin evaluating the as-built quality of the geometries, the deviation from design intent for the hydraulic diameter and pin size, which can be seen in Figure 7-5. There were significant variations in the as-built designs, with hydraulic diameters varying by as much as 15% for the nominal width channels, and with the pin diameter varying by over 20% for the pin fin designs. The channel with the least variation in hydraulic diameter was the 2.0X width channel, varying in diameter by less than 10% between build conditions.

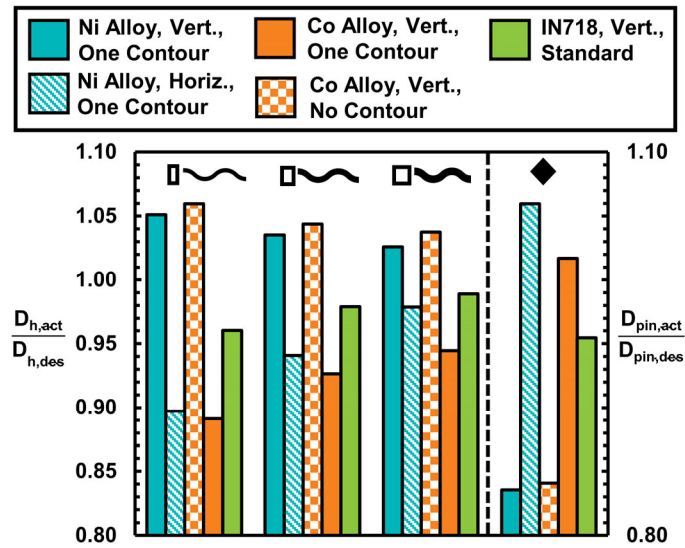


Figure 7-5. Deviation from design intent for the twenty test coupons that underwent experimental testing.

To gain insight into the driving features that impacted the channel hydraulic diameter and pin diameter, the channel profile at two locations along the channel length and the midsection of two pins can be seen in Figure 7-6. Starting with the channel designs, the first channel cross section was taken at Plane I shown in Figure 7-6(a-c). Plane I was oriented orthogonal to the build direction of the coupons built vertically, and parallel to the build direction of the coupons build horizontally. For all three wavy channel designs printed horizontally out of the Ni-alloy, the top wall protruded significantly into the flow area, with irregular shapes forming on all walls. Since the vertically oriented Ni-alloy channel was better supported at the Plane I, it more closely matched the overall design intent as compared to the horizontal coupons. Despite the favorable orientation, the vertically oriented Ni-alloy channel still had significant and large irregular shapes along all walls. In contrast, the Co-alloy channels had much smoother walls, regardless of contour setting. The difference in surface quality between the two materials was likely a function of two things: the difference in power, laser scan speed, and layer size in the contour region, as well as the difference in machine used to manufacture the two materials. Renishaw machines use a pulsed laser whereas

EOS machines use a continuous laser. Prior studies have identified parts made by a Renishaw machine have increased surface roughness relative to EOS and SLM machines [174], which is suspected to be a function of the difference in laser type between machines. The two sets of Co-alloy coupons had similar build performance at the first planar location, though it should be noted that the coupons without contours had slightly larger flow areas than those built with contours. Of the build conditions evaluated, the IN718 designs printed closest to the design intent, which was anticipated due to the more refined process parameters.

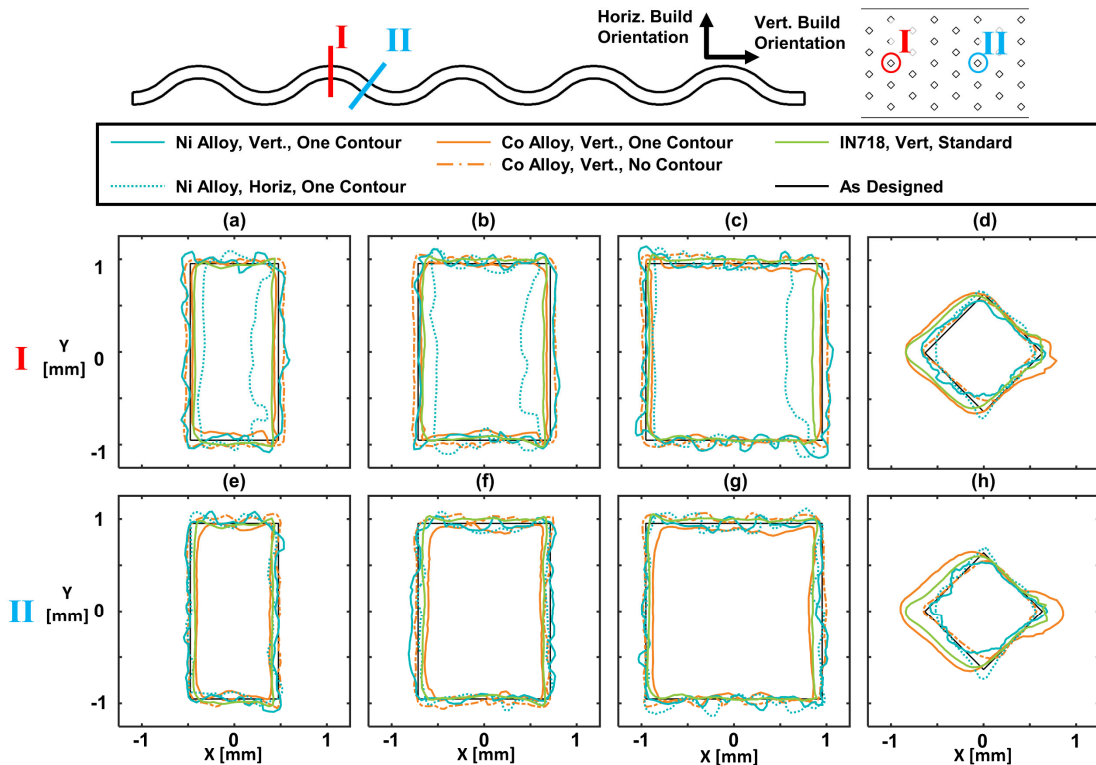


Figure 7-6. (a-c, e-g) Wavy channel and (d,h) diamond pin fin profiles at two discrete locations.

The second planar location (Plane II) shown in Figure 7-6(e-g) is at an approximately 45° plane to both build directions, meaning the vertically and horizontally built channels should have had a similar level of support during the build. This support is evident when comparing the Ni-alloy coupons built vertically and horizontally, as their profiles for all three wavy channel designs are very similar. The profiles are close to the design intent, indicating that the deviation from the hydraulic diameter for the horizontally built coupons that was seen in Figure 7-5 was largely a function of channel profile in the orientation shown at Plane I. Conversely, the Co-alloy coupons had greater deviation from design intent than at the Plane I, with the coupons printed with contours being overbuilt and the coupons without contours were slightly underbuilt. This variation in print performance is also reflected in Figure 7-5, where it can be seen that the samples built with one

contour from the Co-alloy had a smaller than intended hydraulic diameter, and the samples without contours had a larger than intended hydraulic diameter. The magnitude of the deviation from the design intent was not a function of the width of the channel for each build condition evaluated. These deviations therefore had a greater impact on the hydraulic diameter of the smaller width channels than the greater width channels, which is reflected in Figure 7-5. Generally speaking, the profiles of the IN718 coupons show they captured the design intent more accurately than the other conditions.

The build conditions impacted the pin fins differently than they impacted the channels. The pin fins were unsupported for all test cases, resulting in significant stretching along the build direction as shown in Figure 7-6(d) and Figure 7-6(h). The stretching of pin is especially noticeable for the Co-alloy coupons printed with contours, where not only are the pin surfaces extended significantly behind the pin, but also the surfaces are overbuilt in front of the pin. Despite the increase in overall pin size, the Co-alloy coupon with contours was able to more accurately capture the pin diameter than any other design, as the pin diameter was defined as the area of maximum flow obstruction. The extension into the flow area behind the pin had a significant impact on the performance which will be discussed in later sections. Similar to the Co-Alloy, the IN718 pin fins slightly overbuilt the front of the pin, but pins did not have the tails stretching into the flow area behind the pins. The horizontally built coupon similarly featured stretched pins, but the stretching occurred along the spanwise direction, or along a given row of pins. The stretching of the pins in the horizontally built test coupon resulted in an over-sizing of the pin diameter, as well as a blunting of the front of the pin, which can be a source of significant pressure loss. Both sets of pin fin coupons made of the Co-alloy had relatively smooth pin surfaces, which is in stark contrast to those made from the Ni-alloy that featured highly irregular surfaces, similar to the channels. This irregularity can cause early and localized flow detachment from the pin surface, which can significantly increase pressure loss.

To further quantify the surface quality of the coupons printed out of the new superalloys, the arithmetic mean surface roughness was determined for the three different channel designs. While the surface roughness of the pin fin designs was also of interest, CT scans of the pin fin endwalls had substantial noise limiting the author's ability to resolve the surface. For the purposes of this study, it was anticipated that the surface roughness of the pin fin coupons was similar to that which was measured for the wavy channel designs.

The surface roughness of the coupons was measured from the same CT scan surfaces that were used to determine the channel hydraulic diameter. In house code determined the surface roughness by first breaking up the channel into hundreds of slices, and then fitting a line to each

surface in each slice, and determining the average surface deviation from that line. Surface roughness values for each channel surface were then determined by averaging roughness values across all channel slices for each surface independently. Then the channel surface roughness was found by applying a surface area weighted average all channel surfaces. Finally, the coupon roughness value was determined by averaging the surface roughness of all channels in a coupon.

The final roughness values found for the wavy channel coupons is presented in Figure 7-7. Similar to what was seen in Figure 7-6, the Ni-alloy coupons were built considerably rougher than their Co-alloy counterparts. In fact, roughness values for the Ni-alloy coupons were as much as three times as great as those built from the Co-alloy coupons. With respect to the big jump in roughness between materials, the build orientation only moderately impacted the channel surface roughness, with the horizontally built coupons being between 9% to 18% greater than those being manufactured vertically. As was seen in Figure 7-6, the IN718 coupons had the lowest surface roughness of the designs, which again was anticipated based on the improved process parameters. The variation in surface roughness is most likely another result of the difference in additive machine and settings in the contour region during the build, as the Co-alloy coupons were built with a greater power and lower speed relative to the Ni-alloy coupons.

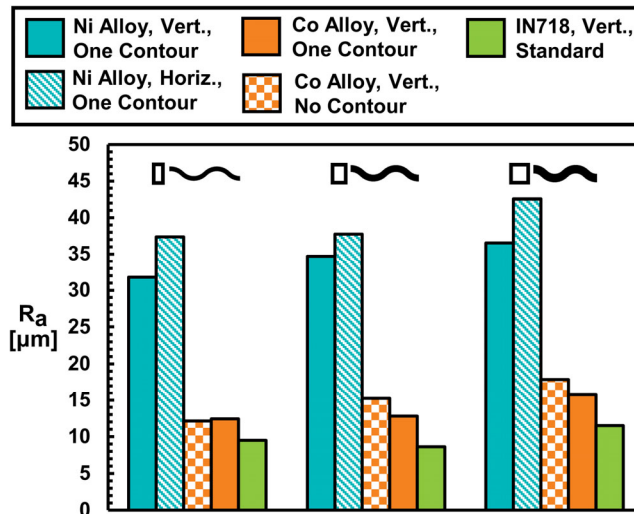


Figure 7-7. Measured Ra for the wavy channel designs.

The final analysis to evaluate the surface quality of the different designs was to image the as-built surface using an in-house microscope, and the resulting images from this analysis are shown in Figure 7-8. Starting with the 2.0X wavy channel surfaces seen in Figure 7-8(a), the Ni-alloy designs have many large roughness elements that protrude significantly into the flow area, as would be expected from the results presented in Figure 7-7. Both the IN718 and Co-alloy without contours coupons appear to have many small partially sintered particles distributed on the channel walls. The Co-alloy coupon with contours appears to have significantly fewer partially sintered

particles, but layer lines are more prominent on these walls than on the other coupons. These differences in surface quality show that despite having similar magnitudes of R_a , the underlying form of the roughness is different between build conditions. The upskin surfaces of the diamond pins in the various build conditions are shown in Figure 7-8(b). Mirroring the channel morphology, the Ni-alloy coupons have many large irregularly shaped nodules located along the length of the pin. The Co-alloy without contours pin fins have many small roughness features along all surfaces. In contrast, the IN718 and Co-alloy with contour coupons had relatively smooth pin surfaces with only a few partially sintered particles.

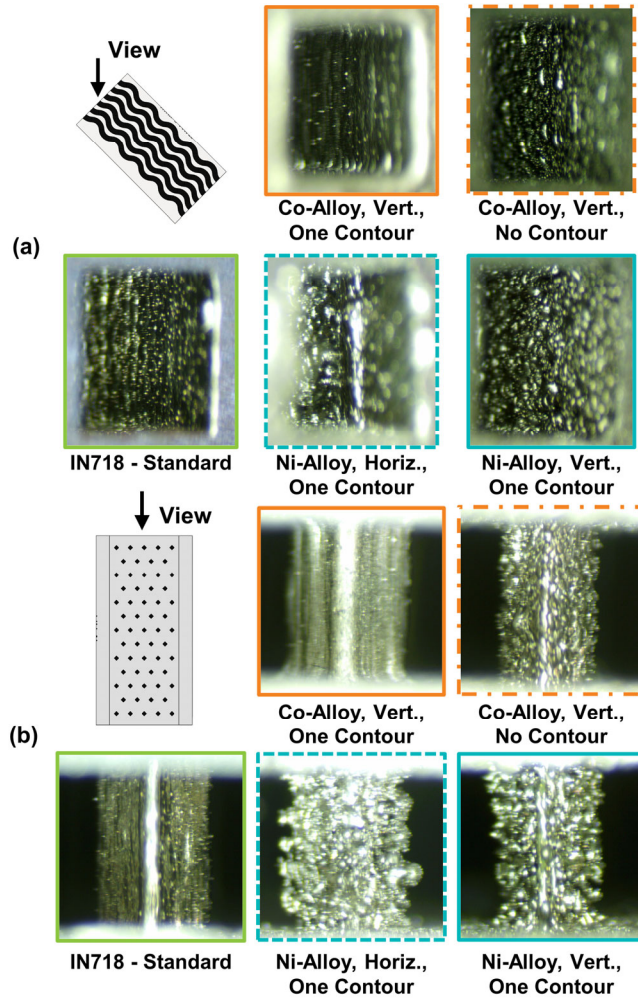


Figure 7-8. Surface morphology for the (a) 2.0X width wavy channels and the (b) upskin pin fin surfaces

7.6. Thermal Conductivity

When intending to use a material for high thermal applications, it is important to quantify the material properties, especially the conductivity. To measure the thermal conductivity of the materials investigated in this study, several thermal conductivity tests were conducted according to

ISO 22007-2 using a semi-infinite medium assumption. Measurements were conducted in a controlled oven at steady state conditions, and five measurements were taken and averaged for each data point to ensure accuracy. Measurements were taken in 50°C increments as the temperature was ramped up and down between 50°C and 250°C. A 95% confidence interval of these measurements indicated that the results were within 1.5% of the reported value.

The results of the thermal conductivity testing can be seen in Figure 7-9. Between 50°C and 250°C the thermal conductivities of the Co-alloy and Ni-alloy were between 16% and 26% lower than the conductivity of the IN718 material. However, the relative increase in thermal conductivity with increase in temperature was similar for all three materials. The difference in thermal conductivities between the two newly developed alloys was only 3% at 50°C and 5% at 250°C. These results indicate that thermal conductivity of the Co-alloy and the Ni-alloy were very similar, though it should be noted that the difference in thermal conductivity between the two materials will likely increase at higher temperatures.

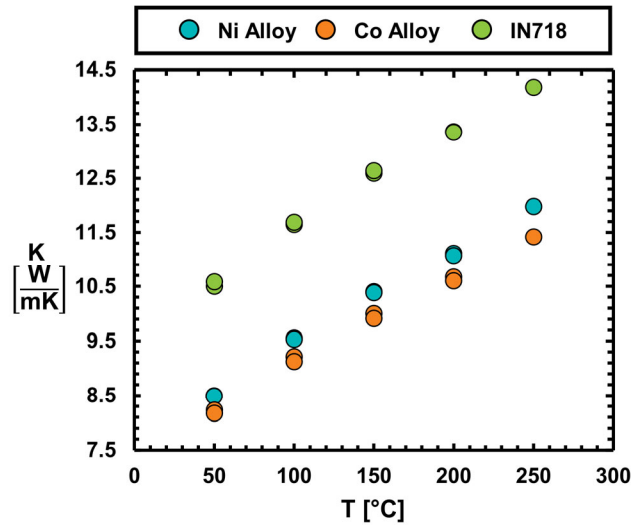


Figure 7-9. Thermal conductivity of newly developed superalloys compared against standard IN718.

7.7. Experimental Methods

Once the coupon surfaces characterized, coupons were experimentally tested to capture their heat transfer and pressure loss performance. The test rig used in this study was the same as was reported in prior studies by the authors [105,106], and can be seen in Figure 7-10.

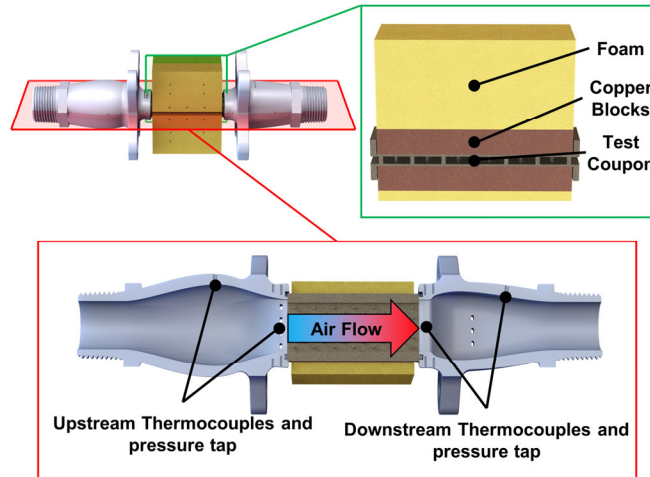


Figure 7-10. Test section of test rig used in this study.

Air flow was metered upstream of the test section using a mass flow controller, which feeds into the upstream plenum. The upstream pressure was measured using a gauge pressure sensor, and temperature was measured through several thermal couples placed into the flow. The plenum conditioned the velocity profile of the air to be almost completely flat as it entered the test coupon. The air then passed through the test coupon and was vented to the downstream plenum, where more thermocouples placed into the flow captured the temperature and a downstream pressure tap captured the pressure drop across the coupon. To ensure accuracy in reported values, the pressure, temperature, velocity, and density was calculated precisely at the coupon entrance and exit using isentropic flow assumptions. Back pressure in the test section was controlled using a downstream needle valve, which enabled independent control over Mach number and Reynolds number.

For heat transfer tests, two heating assemblies were placed on either side of the test coupons to impose an isothermal wall condition. An example of one such assembly can be seen in Figure 7-10. This assembly consists of a custom designed heater placed between a foam block and a copper block. Each heater was independently powered using a variable power supply. The foam blocks were instrumented with thermocouples to capture the thermal losses of the system. The copper block featured thermocouples whose position was precisely measured. Thermal paste was used between the copper block and the coupon to minimize conduction resistance, and additional losses to the plenums was also accounted for through additional thermocouples. Using the heater power and the thermocouples located in the copper, a one-dimensional (1D) conduction analysis as described by Stimpson et al. [51] was used to determine the temperature on the internal surface of the test coupon, accounting for the conduction losses. Using all of the measured temperatures and heat fluxes, the bulk convective coefficient was then calculated using Equation 7-1.

$$h = \frac{Q_{in} - \sum Q_{loss}}{A_s \cdot \Delta T_{lm}} \quad (7 - 1)$$

Before measuring the performance of the coupons investigated in this study, the test rig was benchmarked using a traditionally manufactured smooth cylindrical channel test coupon. The friction factor measurements for the smooth coupon in the fully turbulent regime were compared against the Colebrook Equation [55], seen as Equation 7-2.

$$\frac{1}{\sqrt{f}} = -2 \log_{10} \left(\frac{k_s}{3.7D_h} + \frac{2.51}{\text{Re} \sqrt{f}} \right) \quad (7 - 2)$$

It was assumed that the benchmark coupon's surface roughness, k_s , was zero. The smooth cylindrical channel friction factor, f_0 , was then found by iteratively solving Equation 2 with no surface roughness. Heat transfer testing in the turbulent regime was similarly benchmarked by comparing the heat transfer results to the Gnielinski correlation [56], seen as Equation 7-3.

$$\text{Nu} = \frac{\frac{f}{8}(\text{Re} - 1000)\text{Pr}}{1 + 12.7 \sqrt{\frac{f}{8}} \left(\text{Pr}^{\frac{2}{3}} - 1 \right)} \quad (7 - 3)$$

Where f_0 was used to calculate the smooth cylindrical channel Nusselt number, Nu_0 . The complete results of the benchmark testing can be seen in prior investigations by the authors [105,106], where it was seen that smooth coupon results agreed well with the stated correlations.

When determining the friction factor and the Nusselt number, either the diameter of the duct that contained the pin fin array or the wavy channel hydraulic diameter were used as the length scale. Defining the friction factor and Nusselt number using these length scales was done to enable more direct comparisons between the cooling performance augmentation in the later results sections.

7.8. Measurement Uncertainty

Uncertainty was calculated using the methods of propagation of error as described by Dunn [57]. Below a Reynolds number of 5,000, Experimental uncertainty in friction factor calculations was found to be approximately 10%, but was 4% or lower for Reynolds numbers in excess of 5,000. To evaluate repeatability, coupons were completely removed test rig following testing, and then reinstalled and tested again. This showed that friction factor tests were repeatable within 3%.

Experimental uncertainty was calculated to be 8% or lower for Nusselt number measurements for all Reynolds numbers, and heat transfer tests were repeated similar to the friction factor tests and were found to also be repeatable to approximately 8%. To ensure that all of the energy entering and leaving the test rig was accounted for, the heat input from the heaters minus the measured thermal losses was compared to the heat entering the system as calculated from the first law of thermodynamics. This energy balance showed that a minimum of 95% of the energy entering and leaving the system was accounted for all heat transfer tests, which was deemed suitable for this study.

7.9. Wavy Channel Cooling Performance

The friction factor augmentation and heat transfer augmentation for the wavy channel designs can be seen in Figure 7-11, in addition to data from a prior study [106] featuring the same geometry. Starting with the friction factor plots shown in Figure 7-11(a-c), it is immediately apparent that the Ni-alloy coupons had a substantially higher friction factor augmentation than the Co-alloy coupons. In Figure 7-11(a), the Ni-alloy built horizontally had an almost 5 times higher friction factor augmentation than the Co-alloy coupon with one contour, showcasing the result of the increased surface roughness of the Ni-alloy coupons. The friction factor performance mirrors the surface roughness measurements shown in the prior sections, where increases in roughness are met with increases in friction factor augmentation. It is speculated that the large roughness features that were present on the surface of the Ni-alloy parts caused frequent and substantial disturbances to the boundary layer inside of the channels, resulting in boundary layer detachment and subsequent increases in pressure loss. While the IN718 coupons had the lowest measured surface roughness, the designs performed very similar to the Co-alloy coupons without contours. It is suspected that this similarity in performance is a function of the similar surface morphology that was seen in Figure 7-8. Despite the differences in design, all wavy channel designs had very similar increases in friction factor with increases in Reynolds number for a given build condition. This similarity between designs indicated that the impact of the surface roughness dominated the pressure loss performance over the design of the channel.

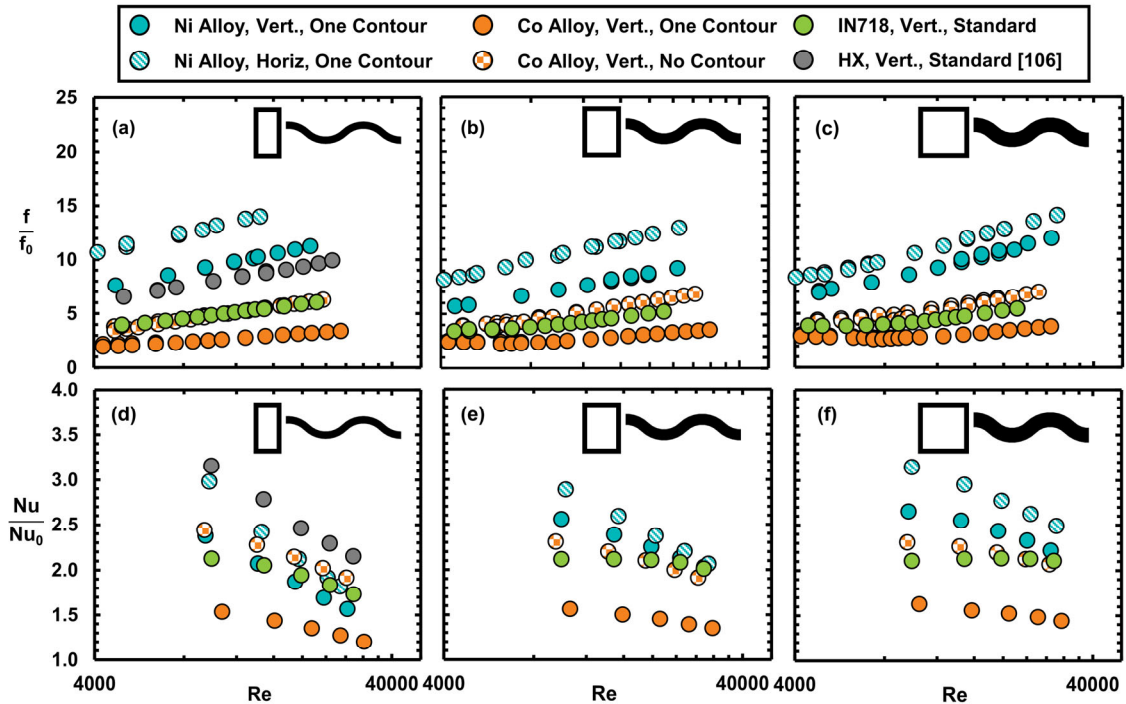


Figure 7-11. (a-c) Friction factor augmentation and (d-f) Nusselt number augmentation for the three wavy channel designs.

To more clearly illustrate the difference in performance between the channel designs, the friction factor augmentation for the three wavy channel designs at two Reynolds numbers can be seen in Figure 7-12. At a Reynolds number of 10,000 the friction factor augmentation was more so a function of the build conditions than the design. In particular, the friction factor augmentation of the Co-alloy coupons without contours was almost the same regardless of the width of the wavy channel. This independence from the design was not the case with the Ni-alloy coupons, where the poor build performance paired with the high surface roughness caused significant differences in the friction factor. At a Reynolds number of 30,000 the Co-alloy coupon performance was again independent of design, with friction factor augmentation for between the three wavy channels varying by only 10%. It should be noted that at Reynolds numbers above 15,000 the channel friction factors were constant.

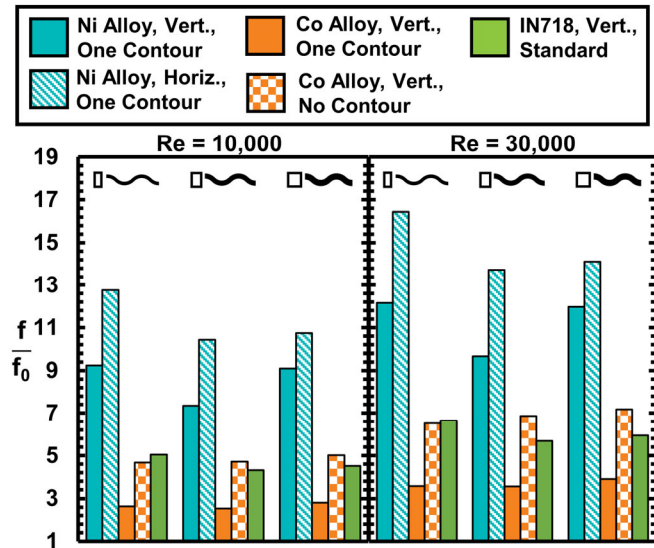


Figure 7-12. Friction factor augmentation of the wavy channel coupons at Reynolds number of 10,000 and 30,000.

While the friction factor performance was consistent between the three channel designs, the heat transfer performance was not. The Nusselt number augmentation of the nominal width wavy channel shown in Figure 7-11(d). At a Reynolds number of 10,000 the horizontal Ni-alloy coupons were only moderately out-performing the Co-alloy coupons without contours, and as the Reynolds number approached 30,000 the Ni-alloy coupons performed worse than the Co-alloy coupon without contours. In contrast, the 1.5X width and 2.0X width channels, shown in Figure 7-11(e) and Figure 7-11(f) respectively, show the same trend in performance that was seen in the friction factor augmentation. The roughest coupons, the horizontal Ni-alloy coupons, had the highest heat transfer augmentation, and the smoothest coupons, the single contour Co-alloy coupons, had the lowest heat transfer augmentations. The IN718 coupons had very similar performance to the Co-alloy coupons without contours, as was expected based on the similar surface morphology between the test coupons. These results indicate that the high surface roughness and surface irregularity that was seen with the nominal width channels made from the Ni-alloy were ineffectively transferring heat to the mainstream flow, despite increasing the channel pressure drop. Furthermore, since these effects are not seen in the 1.5X width and 2.0X width channels, it is expected that this performance is a function of the size of the roughness elements relative to the channel hydraulic diameter.

The heat transfer augmentation values at two Reynolds numbers for the three wavy channel designs can be seen in Figure 7-13. Similar to the friction factor augmentations, the Nusselt number augmentations are largely a function of the material and build conditions used at a Reynolds number of 10,000, with variations in channel design only moderately impacting the heat transfer. At a

Reynolds number of 30,000 the performance of the channels varies with changes in design. There is an apparent increase in Nusselt number augmentation as the channel width increases, particularly for the Ni-alloy coupons. This increase in performance indicates wavy channels with a greater cross-sectional area may be more suitable for heat transfer applications at higher Reynolds numbers.

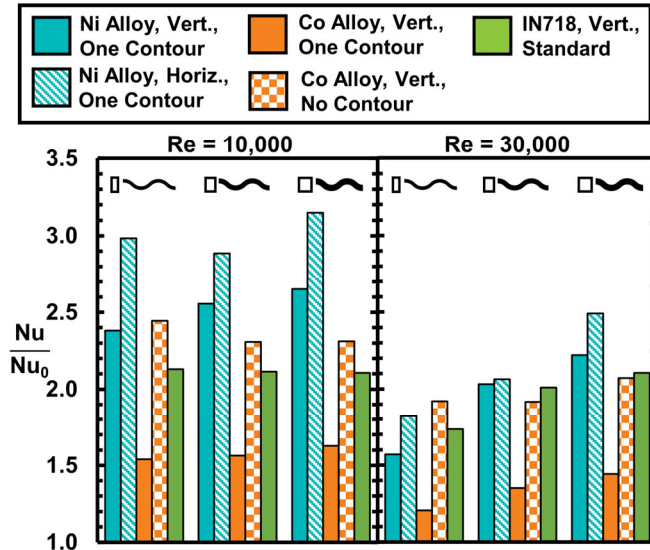


Figure 7-13. Nusselt number augmentation of the wavy channel coupons at Reynolds numbers of 10,000 and 30,000.

7.10. Pin Fin Array Cooling Performance

The friction factor and Nusselt number augmentations for the pin fin array design can be seen in Figure 7-14, in addition to data from a prior study [105] featuring the same geometry. The friction factor augmentation for the pin fin designs was substantially greater than for the wavy channel designs. This difference in magnitude was a function of the fundamental differences in what causes pressure loss between the designs. Internal channels experience pressure loss as a function of the viscous forces that attach the flow to the walls of the channel. In addition to the pressure loss experienced at the wall, pin fin designs also introduce large flow blockages in the form of the pins. These pins both locally disrupt and mix the flow, as well as develop wakes that interact with other geometry in the duct as well as other pin wakes. This critical difference in flow dynamics means that the pressure loss performance of a pin fin array is a function of both the geometry of the pin, as well as the quality of the endwall surface. The trend and magnitude of the friction factor augmentation is therefore significantly different than was seen for the wavy channel coupons.

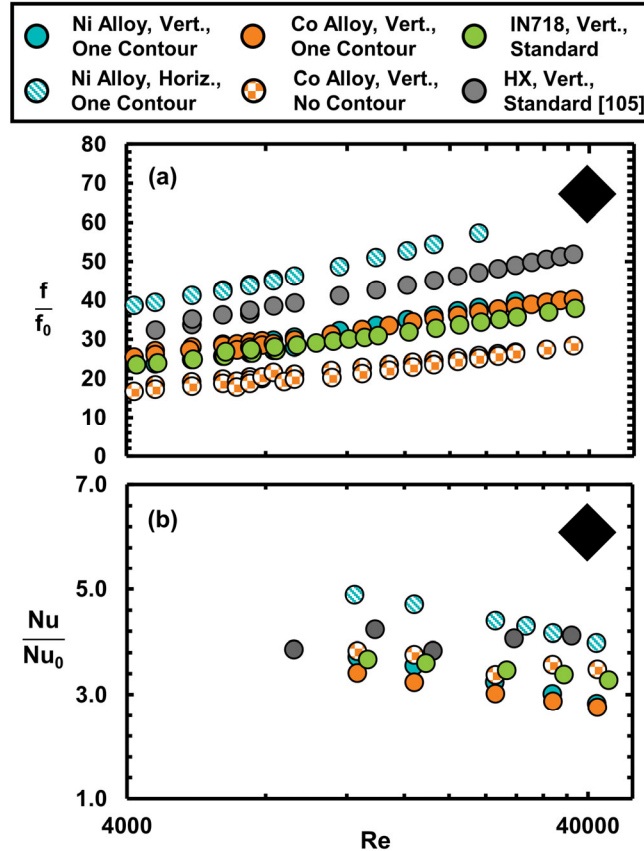


Figure 7-14. (a) Friction factor augmentation and (b) Nusselt number augmentation for the pin fin designs.

The lowest friction factor augmentation was for the Co-alloy with no contour, which can be attributed to the overall accuracy to design intent and small size of the pin as was seen in Figure 7-6. The Co-alloy pin fin coupon printed with contours can be seen to have a similar level of friction factor augmentation as the vertically printed Ni-alloy and IN718 coupons, due to the substantial deviation from the design intent of the pins. Similar to the wavy channel designs, the Ni-alloy coupon printed horizontally had the highest measured friction factor, which is suspected to be a function of the pin's elongation along the streamwise direction that was seen in Figure 7-6. This elongation would not only result in an increase in the overall flow blockage, but also the blunter shape of the pin would induce a more significant flow detachment in the pins wake.

The heat transfer performance of the pin fin designs is shown in Figure 7-14(b). Despite having a notably higher friction factor augmentation, the Co-alloy coupon built with contours and the Ni-alloy coupons built vertically both had lower Nusselt number augmentation values than the Co-alloy without contours. The increase in Nusselt number augmentation does loosely align with increases in the suspected surface roughness. It is expected based on a prior study by the authors that the endwall roughness played a significant role in the overall heat transfer performance of AM pin fin arrays[105]. Since it was expected that the endwall roughness of AM pin arrays drives the

increased heat transfer, and that the design of the pin drove the pressure loss, the heat transfer and pressure loss performance of these coupons was anticipated to be decoupled to some degree.

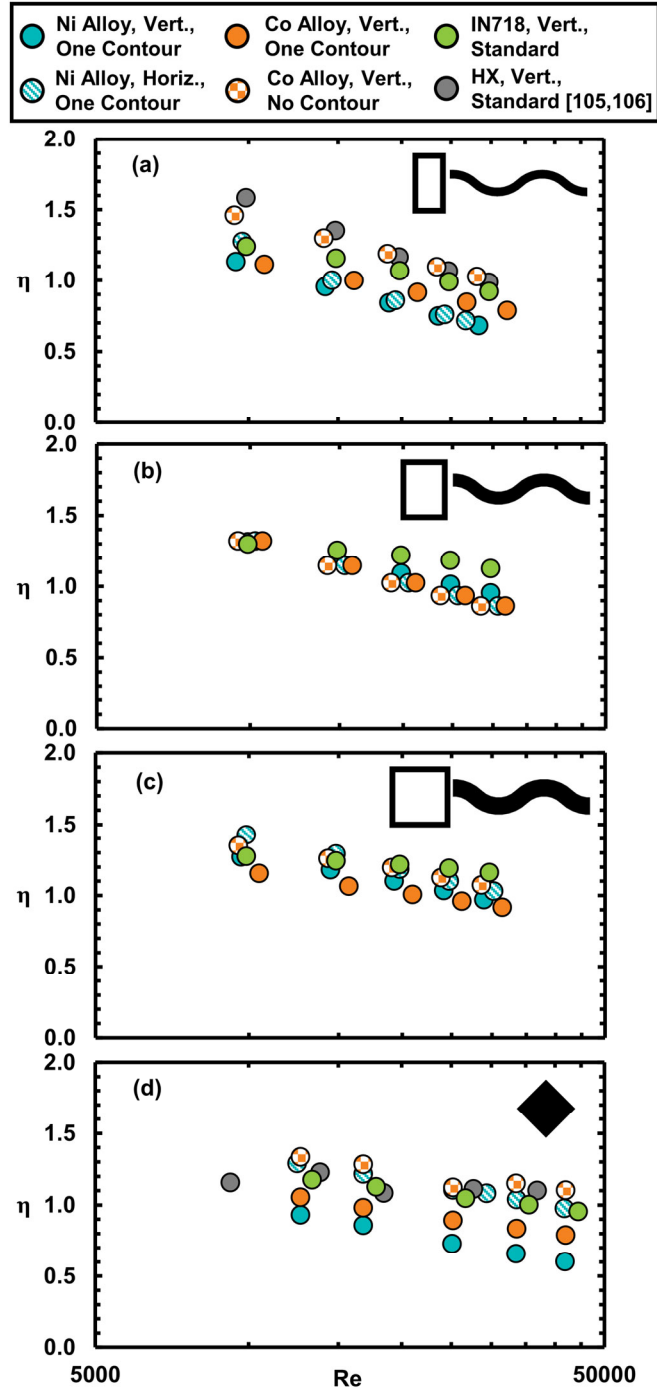
7.11. Efficiency Index of Tested Designs

Using the prior augmentations, the efficiency index as defined by Gee and Web [60] was calculated using Equation 7-4.

$$\eta = \left(\frac{Nu}{Nu_0} \right) \cdot \left(\frac{f}{f_0} \right)^{-\frac{1}{3}} \quad (7 - 4)$$

The efficiency index is way to indicate the relative increase in heat transfer for an increase in pressure drop. A value of one would indicates the performance of a smooth, straight, cylindrical channel. The efficiency index was plotted as a function of Reynolds number for all tested coupons and can be seen in Figure 7-15, in addition to data from prior studies featuring the same geometries [105,106]. As expected based on the Nusselt number augmentation results, the nominal width wavy channel efficiency index results shown in Figure 7-15(a) are somewhat mixed. As the Reynolds number increased, the efficiency index of the Ni-alloy coupons decreased significantly more than the performance of the Co-alloy coupons. The efficiency index of the Ni-alloy coupons fell below one for much of the tested Reynolds range, indicating that the relative increase in pressure drop was not met with sufficient increase in heat transfer. For the other two wavy channel designs, shown in Figure 7-15(b) and Figure 7-15(c), the results from all build conditions collapse onto one value. This collapse indicates that the relative increase in heat transfer for a given pressure drop was similar between these designs, and the roughness features on the surfaces of the coupons simply amplified the magnitude of the respective friction factor and Nusselt number augmentations. As the Reynolds number was increased to 30,000 for the 1.5X and 2.0X width wavy channels, the performance index was trending towards one and would likely be lower than one at even greater Reynolds numbers.

Despite the significant differences in the magnitude of the friction factor and Nusselt number augmentations between the channel and pin fin designs seen in prior figures, the efficiency index of the pin fins shown in Figure 7-15(d) is very similar to that of the wavy channels. This similar level of performance is indicative that the pin fins have a similar ratio of heat transfer to pressure loss to the wavy channel designs. There is a wider spread in the performance of the pin fin designs however, and it is suspected that this is the result of the significant variations to the pin shape seen in Figure 7-6, and differences in the surface roughness on the endwall surfaces.



7.12. Conclusions

This study investigated the print surface quality of two newly developed superalloys for additive manufacturing. A variety of internal cooling designs were printed into test coupons, which were printed with a variety of build conditions. Surface quality of the designs varied substantially, and was largely a function of the material, machine, laser processing parameters, and build orientation. Surface roughness was largely a function of the build conditions regardless of internal design, with the Ni-alloy coupons having significantly greater surface roughness than the Co-alloy coupons.

Thermal conductivity testing revealed that the newly developed materials had an approximately 20% lower thermal conductivity than standard IN718. Friction factor results showed that the poor surface quality of the Ni-alloy coupons caused high pressure losses for the wavy channel designs. The deviation from design intent for the pin fin designs caused the Co-alloy coupon built with contours and the Ni-alloy coupon built horizontally to have a significantly increased friction factor. Increases in friction factor were not always met with increases to heat transfer, as was the case for the wavy nominal width wavy channel built from the Ni-alloy. However, the 1.5X width and 2.0X width wavy channels did see improved heat transfer performance with increases in friction factor. Efficiency index calculations showed that the 1.5X and 2.0X width channels had a similar increase to heat transfer for a given amount of pressure loss, but that the nominal width wavy channel built from the Ni-alloy had worse performance than a smooth, cylindrical channel at Reynolds numbers greater than 20,000. This reduction in performance is suspected to be a function of the large surface roughness relative to hydraulic diameter inhibiting heat transfer.

7.13. Notice Of Copyright

This manuscript has been authored by UT-Battelle, LLC under Contract No. DE-AC05-00OR22725 with the US Department of Energy. The United States Government retains and the publisher, by accepting the article for publication, acknowledges that the United States Government retains a non-exclusive, paid-up, irrevocable, world-wide license to publish or reproduce the published form of this manuscript, or allow others to do so, for United States Government purposes. The Department of Energy will provide public access to these results of federally sponsored research in accordance with the DOE Public Access Plan (<http://energy.gov/downloads/doe-public-access-plan>).

7.14. Acknowledgements

Research was sponsored by the US Department of Energy, Office of Energy Efficiency and Renewable Energy (EERE), Advanced Manufacturing Office, under Contract DE-AC05-00OR22725 with UT-Battelle LLC. This work was performed in part at the Oak Ridge National Laboratory's Manufacturing Demonstration Facility, an Office of Energy Efficiency and Renewable Energy user facility.

8. IMPACTS OF MATERIALS AND MACHINE ON THE VARIATION OF ADDITIVELY MANUFACTURED COOLING CHANNELS⁸

8.1. Abstract

While additive manufacturing (AM) can reduce component development time and create unique internal cooling designs, the AM process also introduces several sources of variability, such as the selection of machine, material, and print parameters. Because of these sources, wide variations in a part's geometrical accuracy and surface roughness levels can occur, especially for small internal cooling features that are difficult to post-process. This study investigates how the selection of machine and material in the AM process influences variations in surface quality and deviations from design intent. Two micro-scale cooling geometries were tested: wavy channels and diamond-shaped pin fins. Test coupons were fabricated with five different additive machines and four materials using process parameters recommended by the manufacturers. The as-built geometry was measured non-destructively with computed tomography (CT) scans. To evaluate surface roughness, the coupons were cut-open and examined using a laser microscope. Three distinct roughness profiles on the coupon surfaces were captured including upskin, downskin, and channel walls built at 90 degrees to the build plate. Results indicated that both material and machine contribute to producing different roughness levels and very different surface morphologies. The roughness levels on the downskin surfaces are significantly greater than on the upskin or sidewall surfaces. Geometric analysis revealed that while the hydraulic diameter of all coupons was well captured, the pin cross section varied considerably. Along with characterizing the coupon surfaces, cooling performance was investigated by experimentally measuring friction factor and heat transfer. The variations in surface morphology as a function of material and machine resulted in heat transfer fluctuating by up to 50% between coupons featuring wavy channels and 26% for coupons with pin fin arrays. Increased arithmetic mean surface roughness led to increased heat transfer and pressure drop; however, a secondary driver in the performance of the wavy channels was found to be the roughness morphology, which could be described using the surface skewness and kurtosis.

8.2. Introduction

The additive manufacturing (AM) process, specifically direct metal laser sintering (DMLS), creates parts by using a laser to melt layers of metal powder particles in patterns that make up thin slices of the intended design. To implement AM as a viable manufacturing method

⁸ Altland, A. Y., Corbett, T. M., Thole, K.A. "Impacts of Materials and Machine on the Variation of Additively Manufactured Cooling Channels" GT2024-122409, *under review*

for gas turbine components, additive parts need to be fabricated with reproducible mechanical properties, surface qualities, and geometric tolerances. In engine operating conditions, these qualities have a significant impact on a component's durability and performance. For example, the microscale roughness and surface morphology created inside small internal cooling channels influence the design's cooling performance, especially because these regions are difficult to post-process. Not only does roughness vary from part-to-part, but different regions of one AM part have varying roughness profiles that are influenced by build orientation and where the part is located on the build plate.

With recent advancements in AM, some gas turbine manufacturers have been 3D printing turbine components with unique cooling designs and reduced lead times [175]. However, compared to traditional manufacturing methods, metal AM is not yet capable of repeatably producing parts. During a build, each step and selection in the AM process impacts the quality of all the individual layers formed, and imperfections in one layer can propagate in succeeding layers in the build. Because this technology involves many complex interactions, several sources lead to variability in printed components, such as print parameters, materials, and machines [176]. Additional variations are introduced in the training and experience of the people operating the machines because operators are involved in many steps of the metal AM process.

Characterizing how different vendors, machines, and materials contribute to variation across parts is needed to create reproducible AM methods. This study aims to find how the selection of material and machine affect part variation for AM cooling channels, and then understand how these variations impact the thermohydraulic performance. Two cooling geometries, diamond pin fins and wavy channels, were manufactured using five vendors, five machines, and four materials. Optical profilometry and computed tomography (CT) scans were used to characterize the internal surface roughness, surface morphology, and geometric deviations of the test coupons. Test coupons were experimentally tested to measure how roughness variations produced from the AM process influence the heat transfer and pressure loss.

8.3. Literature Review

Multiple studies have investigated how print parameters like hatch spacing, contours, and laser energy affect the surface morphology and defect formation for additive parts [177–182]. Laser parameters set for a build are highly influential in the final surface roughness produced because the laser varies the geometries of individual melt tracks that compose the part. As laser power increases, surface roughness decreases if the scan speed remains constant [178,180]. For different surface angles of a part, there is usually a trade-off in the parameters to create lower roughness profiles

[181]. Specifically looking at defect formation in DMLS, Sanaei et al. [182] observed that location on the build plate significantly impacted the defect distributions in a part.

Because DMLS machines have differences in hardware and operators, additive part variation is further impacted. Some researchers have focused on additive part variation across different machine systems. For example, Wildgoose et al. [159] found that the surface roughness for multiple AM samples, including full gas turbine vanes, was higher for an EOS M400-1 machine compared to an EOS M290-1 machine. Dunbar et al. [183] examined in situ distortion for additive parts built on two machines and observed that a Renishaw AM250 machine's build vertically distorted 10.6% more when compared with the same build on an EOS M280 machine. This distortion difference was attributed to the different default print parameters recommended for each machine and the different hardware components in the machine systems. Expanding on the range of additive machines investigated, Clark et al. [184] explored how five different machines impact surface morphology and roughness variation. Findings showed that surface morphology and roughness were significantly different for samples based on the build angle of the surface. Some machines produced upskin surfaces with low roughness and top surfaces with high roughness, while other machines produced opposing roughness profiles on these surfaces. A benchmarking study conducted by Yasa et al. [185] corroborated that roughness levels produced on different build angles varied based on machine. Additionally, Yasa et al. concluded that features of a sample that captured the design intent varied depending on the machine vendor.

When selecting different materials for DMLS, more variability is introduced into the fabrication of additive parts. Several studies have investigated the differences in geometry and surface qualities of printed parts when using different metal powder materials in DMLS. For metal powders, the powder size distribution in combination with layer thickness are determining factors in the as-built surface roughness [186–188]. Other aspects of metal powder materials like particle shape [189,190], flowability [191], and reuse [192,193] also impact the surface quality and microstructure produced in additive parts.

In addition to powder composition influences on the surface quality, several studies have looked at how different materials affect the as-built geometry of internal cooling channels. Kirsch et al. [170] found that changing material for a build can introduce up to 30% variation in the hydraulic diameters compared to only 18% variation using the same material. Corbett et al. [139] examined the geometries and roughness morphologies produced in additive cooling channels using two newly developed superalloys. The observed differences in the channel geometries and surface roughness were suspected to vary because of the different materials and print parameters used for each build. Building on AM capability studies, Snyder et al. [27] explored the feasibility of

customizing print parameters for AM cooling channels to create surfaces that enhance thermohydraulic performance. Findings showed that certain roughness levels and surface morphology combinations improve the performance of AM microchannels.

The objective of this current study is to understand how preliminary sources of variability in the additive process, selection of vendor, machine, and material, impact variations in performance of internal cooling geometries. Non-destructive and destructive methods were used to characterize the surface quality and as-built geometry. Using two different internal cooling geometries, wavy channels and diamond pin fin arrays, the impact of the additive roughness on the heat transfer performance is measured.

8.4. Description Of Test Matrix

This study aims to understand how the selection of materials and machines in the AM process contributes to variation in additive parts, and the succeeding effects on the performance of different cooling geometries. To see how variation across additive parts impacts different types of internal cooling schemes, two cooling geometries were integrated into a general coupon shape, as shown in Figure 8-1. All test coupons are 50.8 mm long with a total channel width of 19.1 mm and height of 1.9 mm. For each manufacturing selection shown in Table 8-1, there is a set of two test coupons, including a diamond pin fin geometry and a wavy channel geometry. The pin fin geometry used in this study is based on the array presented by Corbett et al. [105], where the cross-sections of the pins are diamond-shaped. Pin spacings in these channels are designed to be three pin diameters in the spanwise and streamwise directions, and a design pin diameter of 1.3 mm. The wavy channel geometry used in this study is based on the nominal wavy channel geometry described by Corbett et al. [106] with the hydraulic diameter of each channel designed to be 1.3 mm.

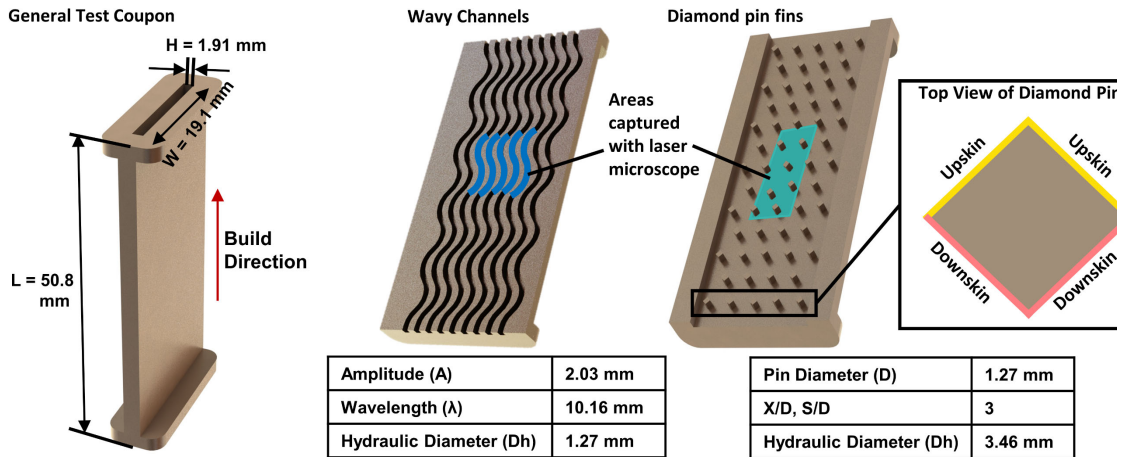


Figure 8-1. The general coupon shape used in this study and regions of the test coupons imaged using a laser microscope.

Table 8-1. Test Coupon Manufacturing
Test Coupon Sets – includes one wavy channel and one pin fin geometry

Manufacturing Methods	■	■	■	■	■	▲	■	●
Vendor	[194]	[194]	[195]	[196]	[194]	[197]	[198]	[198]
Machine	EOS M290	EOS M290	EOS M280	EOS M280	Renishaw AM250	3D Systems Pro X	GE M2	Velo3D Sapphire
Layer Height [μm]	30	30	30	20	50	-	-	-
Material	Ni-Alloy	Co-Alloy	Co-Alloy	Hastelloy X	Ni-Alloy	IN718	IN718	IN718

Introduced in Table 8-1 are the five vendors, five machines, and four materials that were used to fabricate the total of 16 test coupons. The test coupons were externally manufactured using print parameters that were recommended by the manufacturers for the specific machines and materials. While some of the print parameters can be directly compared, other vendors included in this study have proprietary print parameters for their machines. For each build, only the vertical build orientation along the length of the test coupons and support structures were specified, as seen in Figure 8-1. By only specifying the build orientation, there was likely variation in not only the selection of layer size, but also in the bulk scan settings and the implementation of unique scan strategies for smaller features. Because much of this information was unavailable to the authors, the specific cause of some of the variations to the as-built quality and surface topography cannot be determined, but the main objective of this study was to identify how the different roughness profiles generated by these differences in parameters impacted the flow results.

To observe material effects on additive part variation, four materials were selected for this study. Two of these materials are newly developed superalloys for use in gas turbine engines, which are described by Corbett et al. [139]. The first new superalloy developed was nickel-based [173], while the second was a superalloy that was cobalt-based [171]. Commonly used in aerospace applications, the other two materials in this study are Inconel 718 and Hastelloy X, which are nickel-based superalloys. According to the external vendors, the four metallic powders in this study have similar particle size distributions, ranging from 15-53 μ ms, though these distributions were not measured by the authors explicitly.

From these various manufacturing selections, a test matrix was constructed with two independent variables to delineate the impacts of machine and material. A number of research groups assisted in the manufacturing of test coupons [194–198], which are summarized in Table 8-1. For materials, three of the materials described were printed on EOS machine systems. Two different EOS machines were used, those being an EOS M290 machine and an EOS M280 machine. The machine impacts were studied using test coupons fabricated with Inconel 718 on three different metal AM machines: 3D Systems ProX, GE M2, and Velo3D Sapphire. Additionally, one coupon was printed on a Renishaw AM250 out of the Ni-alloy. The Co-alloy was printed on an EOS machine twice, though the process parameters were refined between the two test sets. The parameters used will be referred to as Parameters 1 (P1) and Parameters 2 (P2). It should be noted that the print performance for any of these machines could likely have been improved through repeated builds with more curated process parameters.

By using five vendors and five machines to manufacture the test coupons, additive part variation due to the operators of the machines and machine components was observed. Because operators of metallic additive machines are involved in most steps of the AM process, the experience and training of the individuals producing additive parts affects the microstructure and surface qualities. All the machines used direct metal laser sintering (DMLS) to fabricate the test coupons. With the exception of the Renishaw AM250 machine, the machine systems use continuous wave lasers. The Renishaw machine uses a pulsed wave laser. The different temporal profiles between these two laser emissions cause differences in temperature fluctuations of the melt pool. From these temperature differences, pulsed wave lasers have been shown to produce scale-like melt tracks with deeper and narrower melt pools, while the continuous wave lasers result in smoother surface morphologies [199]. This difference in laser, in addition to the larger layer size used for the Renishaw AM250 printer as compared to the other coupons, was anticipated to result in significant irregularity in the coupon surface, as well as deviations from the design intent.

8.5. Surface Roughness Characterization

The surfaces of all the test coupons were captured with a laser microscope to determine the impact of the manufacturing process on surface morphology and surface roughness levels. Before calculating any roughness parameters, a surface correction was applied to remove sample tilt and non-physical noise was filtered out. As highlighted in Figure 8-1, different areas of the coupons were imaged, including all four sides of the diamond pins, the channel walls of the pin fin coupons, and the endwalls of the wavy channel coupons. These imaged regions correspond to three different roughness profiles. The top two surfaces of the diamond pins capture upskin surfaces, meaning that these surfaces were printed over layers of sintered metal. Because the pins were unsupported during the builds, the other two sides of the diamond pins were printed over unsintered powder, so that these sides represent downskin surfaces. The pin fin and wavy channel walls capture surfaces that were oriented 90 degrees to the build plate.

As seen in Figure 8-2, the eight different AM selections used to fabricate the coupons caused the surface morphologies of the pin fin channel walls to vary widely based on vendor, machine, material, and print parameters. These results show that the surface morphology varies widely depending upon material and machine but does not vary widely based on geometry. When the channel walls for the pin fins and wavy channel geometries have the same manufacturing selections, like in Figure 8-2(a) and Figure 8-2(b), the surface morphology appears very similar. Coupons fabricated with the same vendor and machine, such as in Figure 8-2(i,j) and Figure 8-2(k,l) have similar surface morphologies despite using different materials. The surface morphologies in Figure 8-2(g,h) and Figure 8-2(o,p) with the same vendor and material also have close appearances even though different machines were used. The similarities between these two cases demonstrate the influence of machine operators on the quality of additive parts. In contrast, Figure 8-2(k,l) and Figure 8-2(m,n) coupons printed on EOS M290 and Renishaw machines with the same vendor and material have very different surface morphologies. The Renishaw machine used in Figure 8-2(k,l) produced a surface with large globular features, while the EOS machine in Figure 8-2(m,n) fabricated a relatively smooth surface with distinct powder particles sintered to the surface. This variation in surface morphologies is suspected to be a function of the different machines and print parameters used. The coupons in Figure 8-2(a,b) and Figure 8-2(c,d) were printed on EOS M280 machines, but have different surface morphologies due to differences in the print parameters, material, and vendor. Printed using IN718, Figure 8-2(e,f) looks dissimilar to Figure 8-2(g,h) and Figure 8-2(o,p) fabricated with the same material because of the varying vendor, machine, and print parameters.

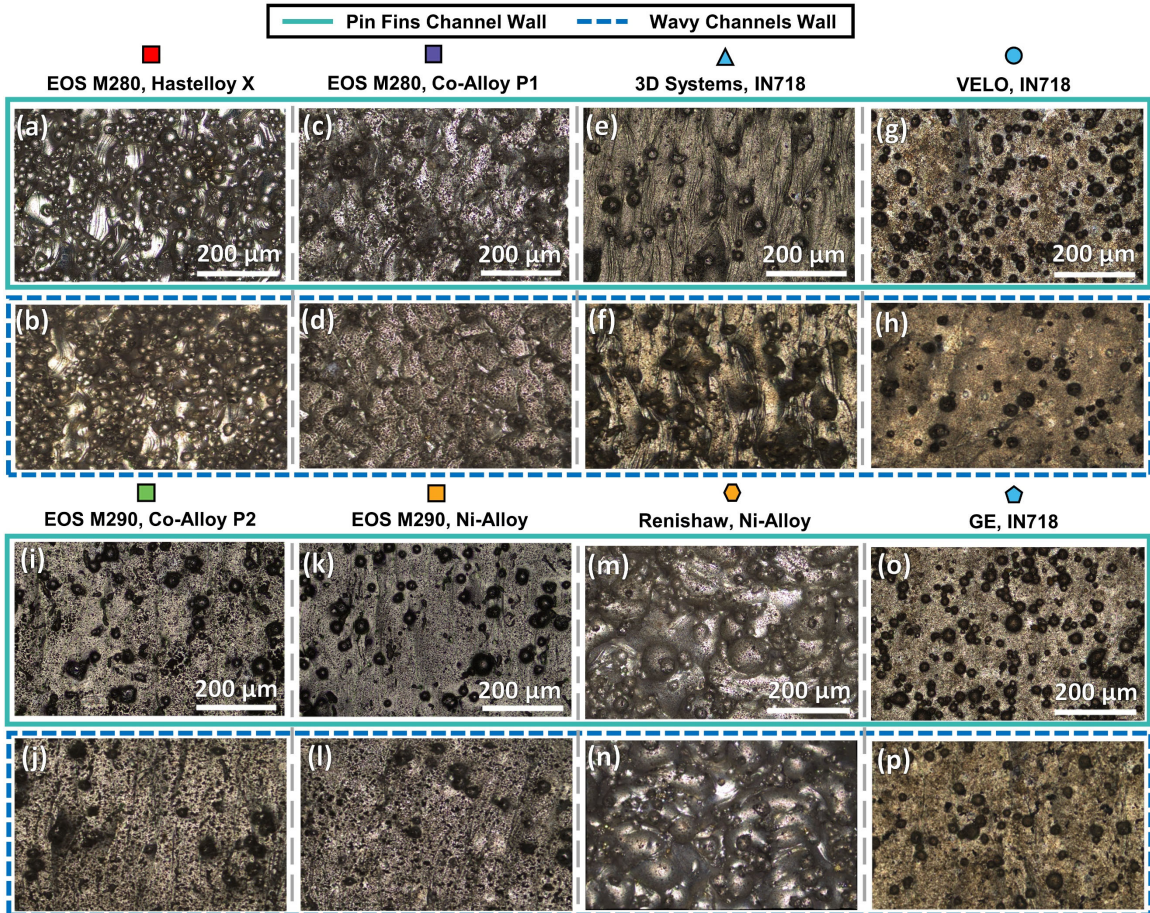


Figure 8-2. Images captured with a laser microscope of pin fin channel walls (a,c,e,g,i,k,m,o) and wavy channel walls (b,d,f,h,j,l,n,p) in the respective regions indicated in Figure 8-1.

Surface morphology does not only vary between different additive parts, but also vary across different regions on one additive part depending on the surface angle. Figure 8-3 shows the upskin and downskin images captured of the diamond-shaped pin surfaces. The downskin surfaces of the pins typically have increased numbers of partially sintered particles on the surface compared to the upskin surfaces, as seen on Figure 8-3(a) and Figure 8-3(b). Because downskin surfaces are printed over unsintered powder, surrounding powder particles partially melt onto the surface of the part during the build. Some coupons, like in Figure 8-3(p), also have large roughness features on the downskin surfaces, especially at the down-facing point of the diamond, because of powder particle agglomerations.

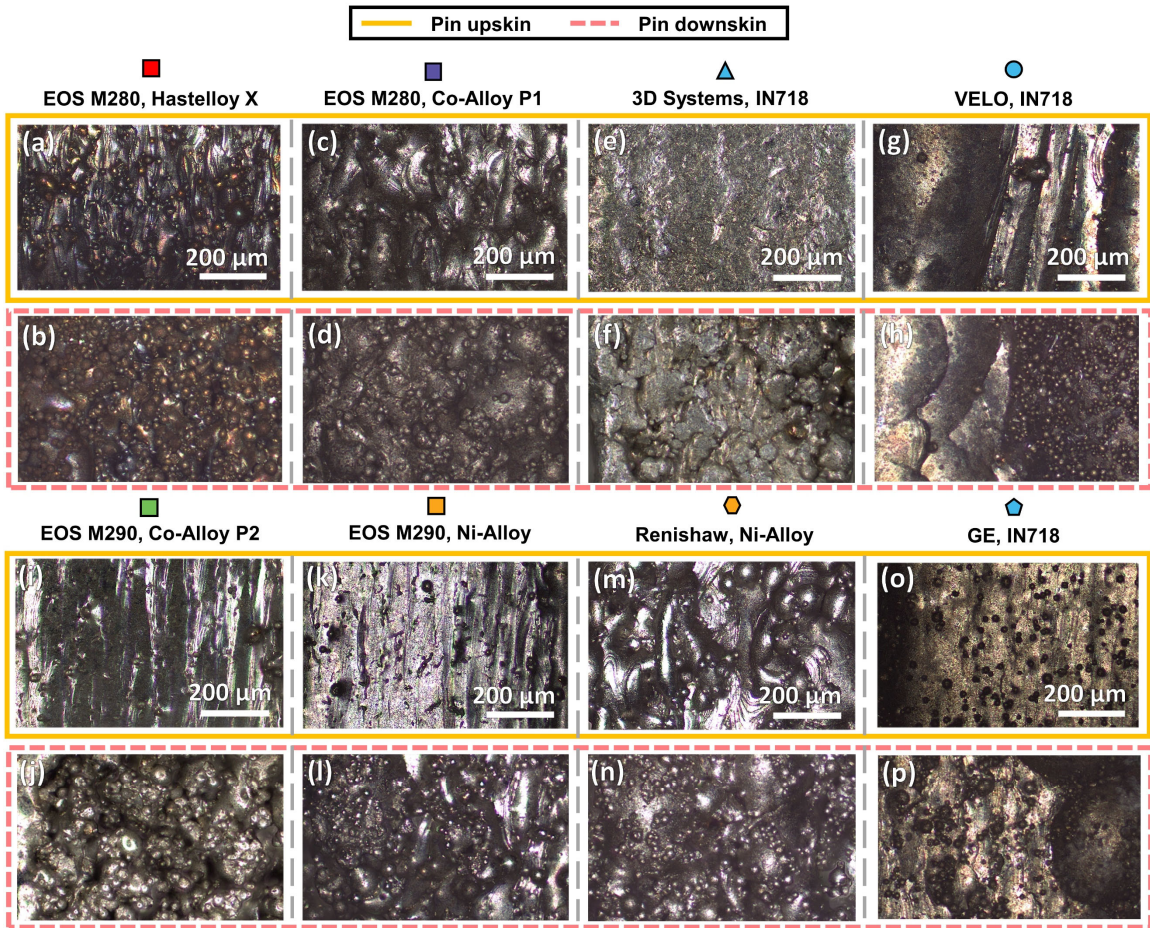


Figure 8-3. Images captured with a laser microscope of upskin surfaces of the diamond pins (a,c,e,g,i,k,m,o), and downskin surfaces of the diamond pins (b,d,f,h,j,l,n,p) in the respected regions shown in Figure 8-1.

To evaluate the coupons' surface roughness levels in this study, several roughness profile parameters were used, as seen in Figure 8-4. These roughness statistics were calculated from an average of seven individual measurements for each region of each sample. In total, four roughness parameters are discussed: arithmetical mean height (S_a), mean roughness depth (S_z), skewness (S_{sk}), and kurtosis (S_{ku}). For each coupon set that includes one wavy channel and one pin fin geometry manufactured with the same machine and material, S_a and S_z show similar trends in roughness for the four areas imaged in Figure 8-4(a,b). The regions with the greatest average deviations follow the similar trends as the greatest height deviations in the area. When manufactured with matching machines and materials, the channel walls for the pin fin and wavy channel coupons have very close S_a values. This similarity shows that roughness does not vary much for the same surface angles on two different parts using the same machines and materials. The highest S_a for the channel walls was observed for the Renishaw coupons which is suspected to be due to a high layer thickness

of 50 μm and the pulsed wave laser on the Renishaw machine. Other authors [139,183] have also seen high levels of roughness and deformation produced on Renishaw machines. Compared to the roughness on the channel walls, the Renishaw diamond pin surfaces have significantly higher roughness levels on the downskin regions. The EOS M290 machines produced the highest S_a levels observed across all roughness measurements on the downskin surfaces. Conversely, all the coupons have upskin S_a that is relatively close to the 90-degree channel walls' S_a values, with the exception of the Renishaw and Velo coupons that have upskin roughness levels close to the downskin regions.

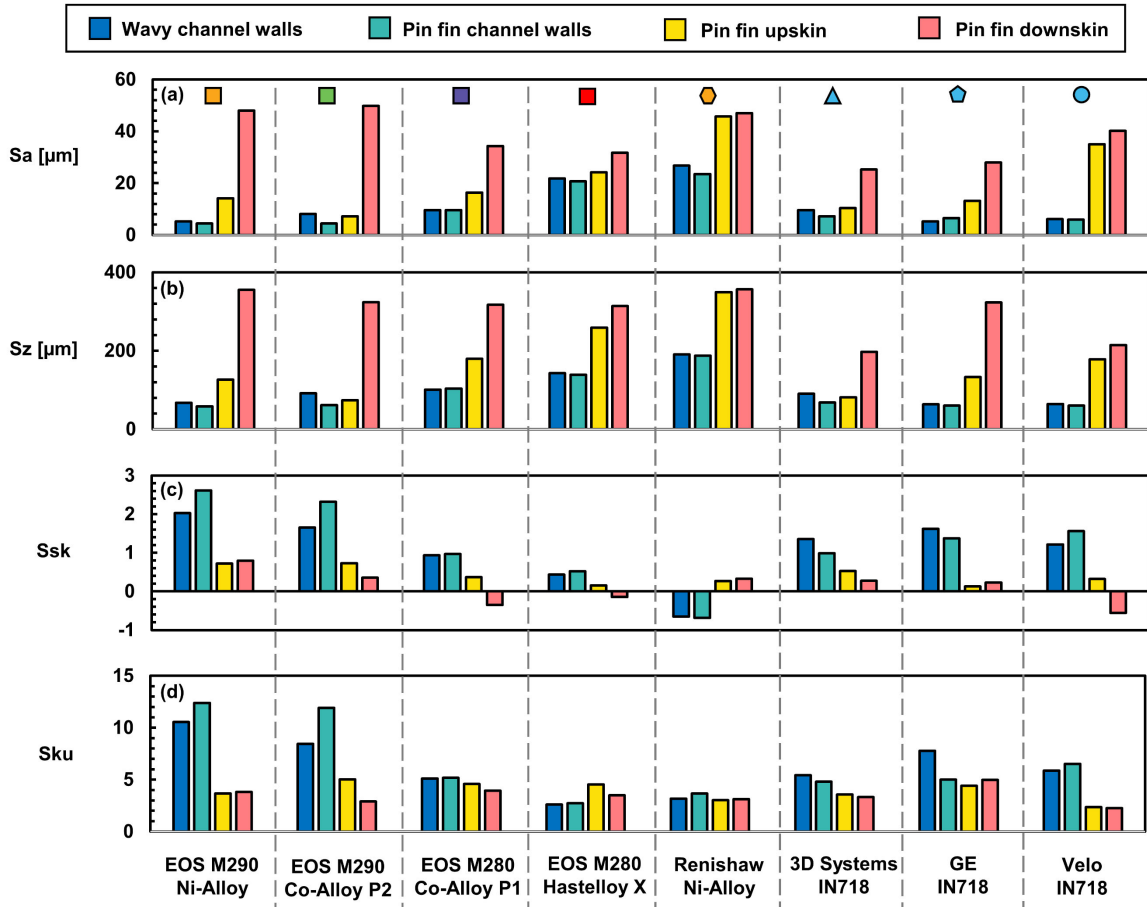


Figure 8-4. Roughness statistics for the imaged surfaces of the test coupons, including arithmetic mean roughness (a), mean roughness depth (b), skewness (c), and kurtosis (d).

The mean roughness depth on the downskin surfaces approached or even exceeded $300\mu\text{m}$, which is on the scale of the designed pin diameter of $1270\mu\text{m}$. The similarity in scale between the designed features and the roughness on them would imply that these roughness elements are not just acting as additional microscale roughness features, but instead as more macroscale cooling features, which will impact the flow in unintended ways as will be shown in later figures.

The four surfaces of the Velo coupon's pins were deformed with the four sides caved inward toward the middle, which will be shown later. This deformation on the Velo pins led to high deviations in the surface height. For the Renishaw coupons, all sides of the diamond pins exhibited very similar roughness profiles, which is attributed to the print parameters and machine.

Almost all of the coupons' surfaces have positive S_{sk} in Figure 8-4(c), which shows that the surfaces consist of peak features as opposed to valleys. Several surfaces show a negative S_{sk} close to zero, particularly on the downskin surfaces of the pin fins. This slightly negative S_{sk} value means that these surfaces are nearly balanced, but have slightly more valley-like features. In the channel walls data, coupon surfaces with larger S_a values tend to have lower S_{sk} meaning that these surfaces with higher average roughness tend to feature more crevasses. Coupons built with the same machines show similar trends in skewness for different surface roughness regions. For instance, the EOS M280 machines that built the Co-Alloy P1 coupon and the Hastelloy coupon have higher positive S_{sk} on both the channel walls, slightly positive S_{sk} on the upskin surfaces, and slightly negative S_{sk} on the downskin surfaces. This trend is corroborated by the coupons built on the EOS M290 machines with high S_{sk} on the channel walls, and positive S_{sk} for the diamond pin surfaces.

Most of the test coupons in Figure 8-4(d) have S_{ku} values around 3 which means the roughness profile is balanced between jagged and rounded features. However, a few surfaces have S_{ku} values above 3, meaning the roughness profile is sharp. A sharp roughness profile (jagged) is most likely indicating that there are particles which are not bonded well to the surface. This likelihood is the result of the measurement method imposing high gradients to the surface roughness height when there are overhangs, which are expected when only a small portion of the particle fuses to the surface. An example of this effect is shown in the illustration presented in Figure 8-5. The reduced contact area between the particles and the wall will result in increased conduction resistance and reduce the fin efficiency of the particulate.

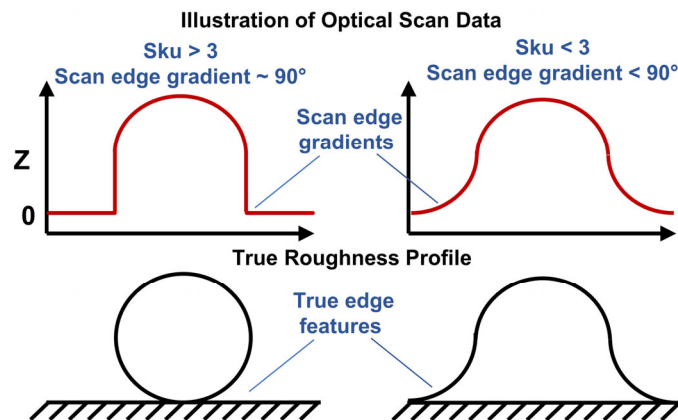


Figure 8-5. Illustration showing potential differences in measured and actual roughness profile.

Surfaces with lower S_a levels tend to have higher S_{ku} which correlates to a sharper roughness profile because these profiles are typically smooth with individual powder particles adhered to the surface causing sharp changes in height. Contrarily, the higher S_a profiles tend to have more rounded roughness features where powder particles have coalesced, which causes the profile to balance close to 3.

These types of roughness shapes can be viewed in Figure 8-6, which shows the channel wall roughness profiles for the pin fin and wavy channel coupons. The roughness profiles were obtained using the scans from the laser microscope, where a straight line was placed over small area of the surface to determine the height variations in the z direction for a given length in the x direction. As seen in previous roughness data, the channel walls for the pin fins and wavy channel geometries have very similar characteristics, while walls with different AM selections have wide variation. Height deviations can be seen for both the layer lines and the particulate adhered to the surface of the walls. For example, in Figure 8-6(a,b,g,h), the surface appears slightly wavy with occasional sharp deviations in height. The baseline rounded bumps are layer lines and the sharp spikes in the z direction are distinct powder particles that are partially sintered to the part's wall. As can be seen in Figure 8-6(f), the sharper height deviations have smoother gradients to connect the particles to the mean plane, meaning that there is less overhang and the particles are closely bonded with the surface. On the other hand, surfaces like Figure 8-6(a) have perpendicular deviations in height showing that overhang likely exists. Other surfaces, such as in Figure 8-6(c,e), are pitted with sharp deviations to deep valley features.

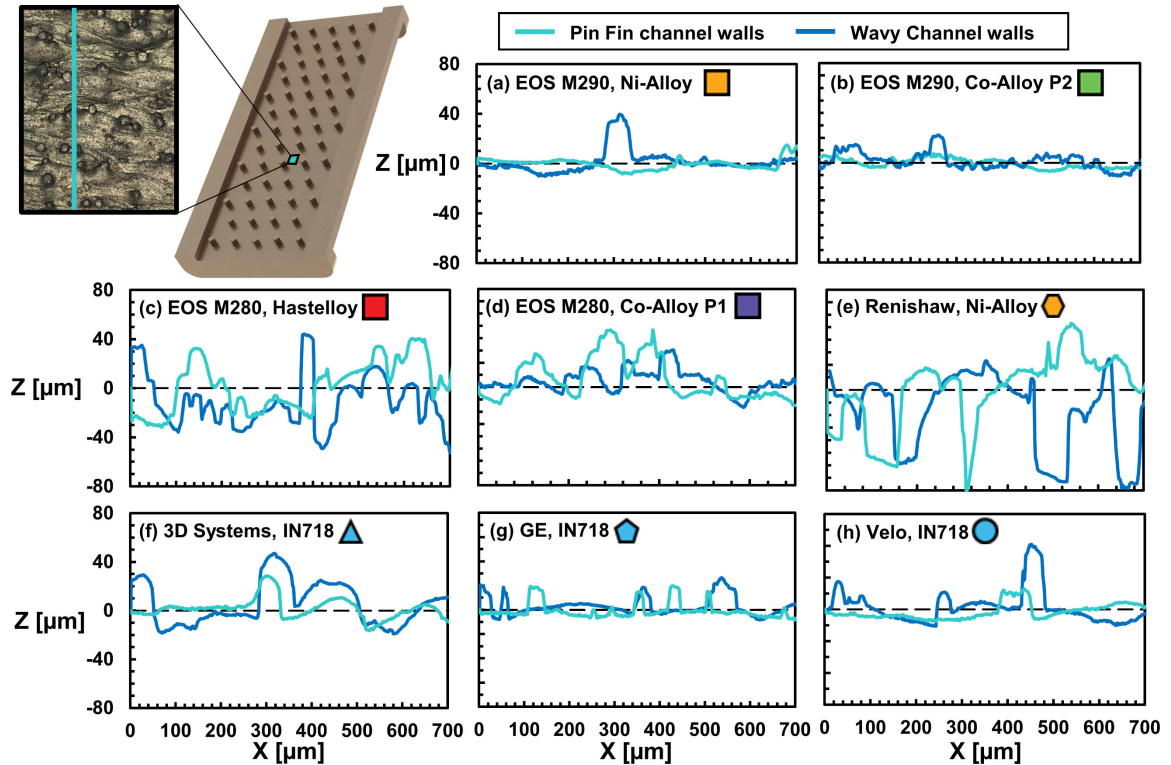


Figure 8-6. Height variation in the z-direction for the channel walls taken along a given length in the x-direction.

8.6. Geometric Accuracy Characterization

Further evaluation of the build quality for the test coupons was conducted using computed tomography (CT) scans. Investigating the as-built geometries of the cooling channels was completed by measuring deviation from design intent for the wavy channels and diamond pin fins using methods described by Corbett et al. [139]. An in-house processing code used point clouds obtained from the CT scans to measure slices of the as-built geometries and output averaged measurements of the hydraulic diameter and wetted surface area. For the pin fin coupons, all deviations from design intent in the hydraulic diameter fell within a range of 3.2%. The wavy channel geometries exhibited higher deviations for the hydraulic diameter geometry because the smaller channel widths and heights are difficult to print accurately. All wavy channel geometries were within a 6% deviation from design intent with the highest deviations in the EOS M280 Co-Alloy and Renishaw Ni-Alloy coupons.

While the hydraulic diameters were close to design intent for all the test coupons, the shape of the diamond pins varied greatly depending on the machine and material used to fabricate the cooling geometries. Figure 8-7 shows the cross-sectional shape of the as-built pins for the eight pin fin coupons compared to the intended design. Because the diamond pins are relatively small and

unsupported during the build, these cooling features tend to have more geometric deviation compared to other regions of the test coupons. Variation in the diamond pin diameters ranged as high as 16.5%. As seen in Figure 8-7(a), the EOS M290 coupons both had pins that were overbuilt on the upskin surfaces and underbuilt on the downskin surfaces. The downskin surfaces of these coupons are observed to have rounded down-facing points with higher roughness features. The EOS M280 Co-Alloy P1 pins printed close to design intent for the impingement point, but were undersized along the span direction and downskin point. In contrast, the EOS M280 Hastelloy pins printed close to design intent on the upskin sides with overbuilt surfaces on the downskin sides.

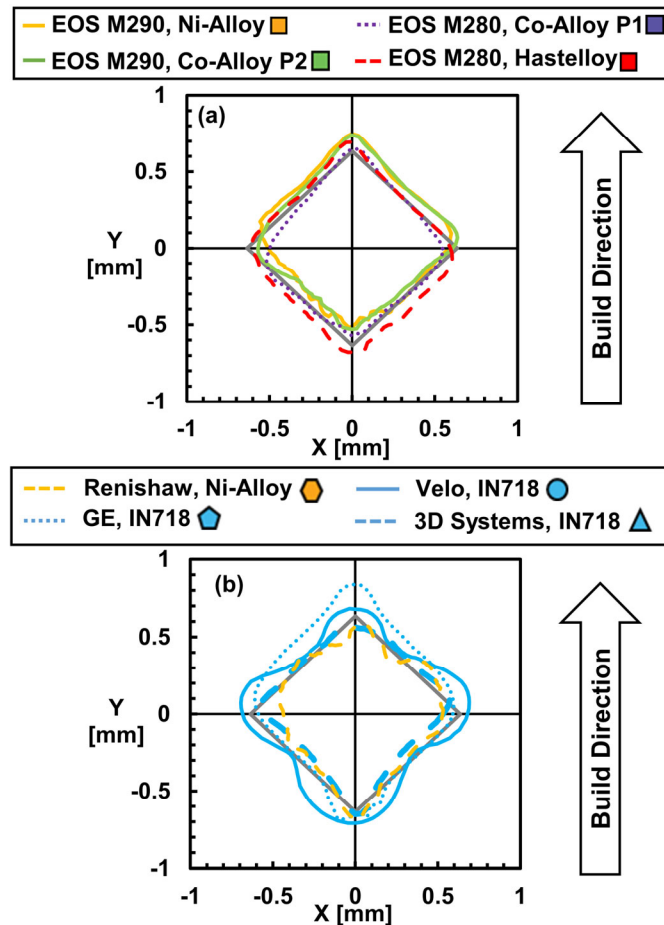


Figure 8-7. Analysis of the shape of the diamond pins for EOS machines (a) and IN718 material (b).

Looking at Figure 8-7 (b) with the coupons built using different machines and the same IN718 material, there is a notable increase in pin shape variation compared to the four coupons manufactured using EOS machines. This increased variation is suspected to be due to the different machines' hardware, print parameters, and operators. For example, the Velo IN718 pins were printed with a distinct plus sign shape where each of the four points of the diamond are overbuilt, so that the pin walls cave inward at the middle. In comparison, the GE IN718 coupon that was

fabricated with the same material and vendor had very different geometric inaccuracies in the diamond pins. The GE IN718 pins were significantly overbuilt on the upskin side of the coupon with a small tail in on the downskin side. Both the 3D Systems IN718 and the Renishaw Ni-Alloy pins were undersized with rounded upskin surfaces and tails on the downskin points. However, the Renishaw pins were also undersized in the spanwise directions leading to the highest deviations from the intended design diameter compared to the other coupons' pins. The Renishaw coupon had the largest known layer size of the evaluated test coupons, which was likely a key factor in the accuracy to design intent that could be achieved using this printer.

8.7. Experimental Methods

In addition to characterizing the build of the coupons, experimental testing was conducted to collect heat transfer and pressure loss results. For this study, the test rig was the same as reported in previous research [105,106,139]. Test coupons were installed between two plenums instrumented with pressure taps to capture the pressure drop across the coupon using a differential pressure transducer. A gauge pressure transducer was used to find the upstream pressure inside of the test section. Flow entering the test section was regulated using a mass flow controller located upstream. A needle valve located downstream was used to independently control Mach number, which was kept below 0.15 for all tests, and Reynolds number. The plenums imposed known boundary conditions on the inlet and outlet of the test coupon, which were accounted for using loss coefficients. In the plenum thermocouples were placed into the flow path which measured the temperature of air at the inlet and outlet of the coupon. Using the known pressures, temperatures, and the mass flow rate in the plenums, the temperature, pressure, velocity, and density of the air at the coupon inlet and outlet was calculated assuming 1D isentropic flow.

For heat transfer tests, heating elements were added to both sides of the test coupon on the test rig. The heating elements are comprised of a custom surface heater placed between a copper block and a foam block. To minimize conduction resistance, thin layers of thermal paste were added to the copper block surfaces when placed against the coupon walls for testing. The heating elements imposed a constant surface temperature boundary condition on the outside of the test system. Using thermocouples located in the copper blocks, a 1D conduction analysis was completed to determine the temperature of the surface of the test coupon. There were also thermocouples in the foam blocks and the plenums, which were used to determine thermal losses during an experiment were measured. Using these measured losses, the known inlet and exit temperatures, and the known power input, an energy balance was created that compared the measured heat in to the expected heat in from the first law of thermodynamics. This comparison showed that energy closure was typically within 3%, meaning the loss paths in the rig were well captured.

Pressure loss results are represented by the friction factor, and heat transfer results were normalized using the Nusselt number. Calculations of the bulk convective coefficient used the wetted surface area of the test coupons as determined from the CT scans. Before running tests in the rig, it was benchmarked using a test coupon featuring smooth, straight, cylindrical channels. The results from this test coupon were compared to Colebrook [55] and Gnielinski [56] correlations for friction factor and Nusselt number respectively. For the test range reported in the current study ($Re > 4000$), the benchmark coupon results were within 10% of the Colebrook correlation and within 5% of the Gnielinski correlation.

8.8. Measurement Uncertainty

To calculate uncertainty, the method of error propagation that is described by Dunn [57] was used. Experimental uncertainty for the friction factor values was calculated to be below 10% for all Reynold's numbers in excess of 4000, and were typically approximately 6%. The greatest contributors to the uncertainty were the measured pressure drop and the measurements geometric measurements taken from the CT scans. In the Nusselt number calculations, uncertainty was found to be below 7% for all data collected. The greatest contributors to uncertainty the temperature measurements for the thermocouple in the copper block, as well as at the exit of the test coupon. Uncertainty in the Reynolds number was also quantified, and found to be less than 3% for all tests. The greatest contributor to Reynolds number uncertainty was the measured mass flow rate.

8.9. Thermal Performance of Wavy Channels

The wavy channel friction factor and Nusselt number performance are reported as a function of Reynolds number in Figure 8-8. Also shown in Figure 8-8 are the results from Kirsch et al. [31] who studied similar wavy channel geometry.

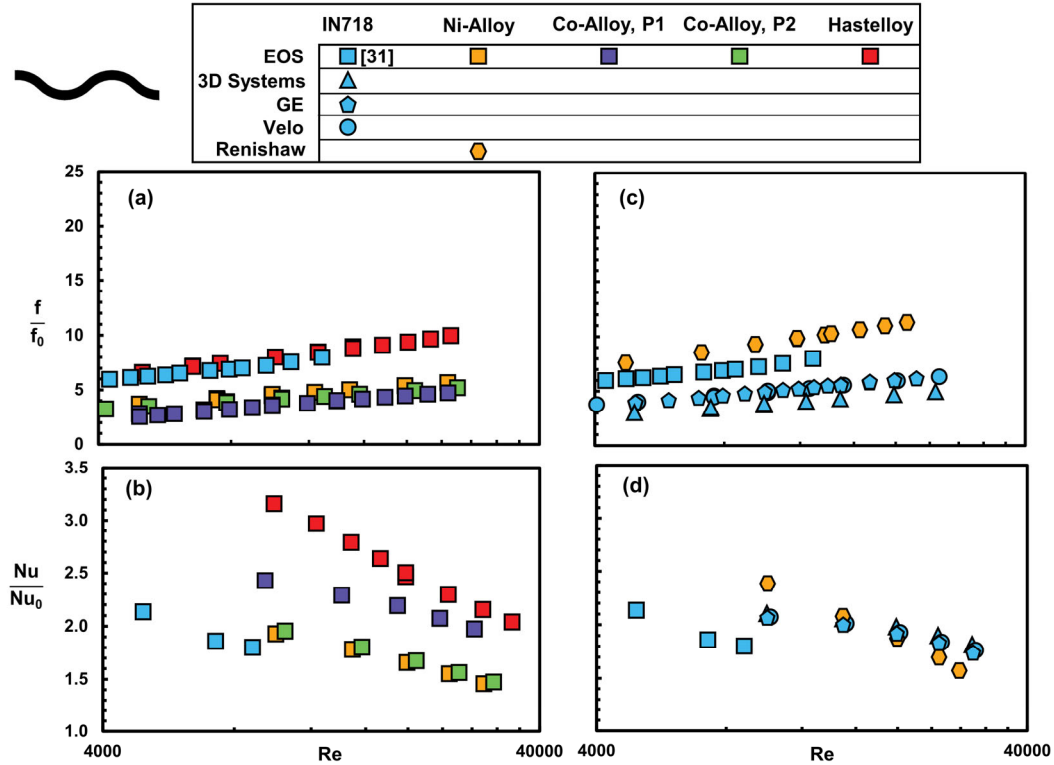


Figure 8-8. Wavy channel friction factor (a,c) and Nusselt number (b,d) augmentation as a function of Reynolds number.

Comparing all of the coupons made on an EOS machine in Figure 8-8(a) and Figure 8-8(b), it is clear that depending on the material used there is significant variation, despite all using the same printer manufacturer. In particular, the heat transfer flow results follow the same trends that were reported in the arithmetic mean and mean roughness height roughness results shown in Figure 8-4(a-b). The heat transfer performance and the pressure loss performance follow the same trends, with the Co-alloy P1 coupon being the only exception. This test coupon had scale-like roughness features below the partially fused particulate which can be seen in Figure 8-2(d). Between the Co-alloy P1 and Co-alloy P2 coupons, most roughness statistics were the same, despite the differences in surface morphology, as shown in Figure 8-4(a-c). The major difference between the two coupons was in the measured S_{ku} , which was lower for the P1 coupons than it was for the P2 coupons. As previously mentioned, the kurtosis describes the sharpness of the roughness profile, where a sharper profile has a higher S_{ku} . The increased S_{ku} of Co-alloy P1 coupon therefore implies that the roughness particles are poorly attached to the surface, resulting in reduced heat transfer performance relative to the Co-alloy P2 coupon.

Comparing between the Co-alloy P2 coupon and the Hastelloy coupon, there was as much as an 83% difference in friction factor augmentation, and a 47% difference in heat transfer, despite the designs sharing the same design intent. Additionally, the IN718 coupon in Figure 8-8 (a-b) had

the second highest friction augmentation and the lowest heat transfer augmentation, which can be attributed to the small differences in the design between the wavy channels studied by Kirsch et al. [31] and the design evaluated in the current study.

Comparing the results from the coupons manufactured from IN718 on different machines shown in Figure 8-8(c-d), there is less spread than was seen with the coupons of all the same machine. In fact, all of the heat transfer results conducted for this study are within experimental uncertainty. However, the coupon manufactured on the 3D Systems machine did have slightly lower friction factor augmentation than was measured on the other surfaces. It is suspected that this may be the result of the roughness on the downskin surfaces on the interior of the channel. The 3D Systems pin fin coupons had the lowest downskin S_a and S_z of the measured surfaces and the downskin surfaces on the interior of the wavy channels exhibited similar surface roughness characteristics. As such, this reduction to the channel downskin surface roughness led to improved friction factor results. The only coupon made of IN718 that did not have the same heat transfer performance was again the coupon design studied by Kirsch et al. [31]. Also shown in Figure 8-8(c-d) is the results from the Renishaw coupon made from the Ni-alloy. This coupon had a high value of both arithmetic mean and total roughness height. The roughness profile was extremely irregular, as shown in Figure 8-6(e), which resulted in increased friction factor results. The heat transfer from extremely rough surfaces does not increase proportionally with respect to pressure loss [139], and the heat transfer augmentation for this coupon can decay below the IN718 coupons at higher Reynolds numbers.

Prior authors have noted that differences in the structure of roughness elements can have an impact on the cooling performance of the designs [200]. Between the different wavy channels that were manufactured out of IN718, there was not significant variation in the structure of the surface roughness, as was shown in Figure 8-2(f), Figure 8-2(h), and Figure 8-2(p). However, Figure 8-2(b), Figure 8-2(p), and Figure 8-2(n) shows the apparent differences in the surface morphology between the coupons made of different materials. Take for the example the surfaces of the coupon made from Hastelloy, the IN718 coupon made on the GE machine, and the Ni-alloy coupon built on the Renishaw machine. Of these three coupons, the IN718 coupon has the lowest S_a , but the Ni-alloy and Hastelloy coupons had similar levels of S_a as shown in Figure 8-4. Flack and Shultz [201] as well as Wildgoose et al. [140] identified that the skewness of roughness elements is a key parameter in scaling performance, and there is an evident difference in S_{sk} between the Hastelloy and Ni-alloy coupons. The negative S_{sk} of the Ni-alloy coupons indicates that the roughness profile was composed of valleys, as opposed to the mountains that made up the profiles of the Hastelloy coupon.

Despite similar magnitudes of S_a between the Hastelloy and Renishaw coupons, visually the difference in roughness structure can be seen in Figure 8-2(b) and Figure 8-2(n). The Hastelloy coupon surface is dotted with a multitude of randomly distributed small particulate, whereas the Ni-alloy coupon features large mounds of material with crevasses located between, which are dotted with additional particulate imposed on top of the mounds. Therefore, the distributed small particulate on the surfaces of the Hastelloy coupon is a more effective finned surface as compared to the crevices surfaces of the Ni-alloy coupon, allowing for an increase to heat transfer, despite the augmentation to pressure drop being similar as shown in Figure 8-8.

To more broadly compare the performance of the different test coupons evaluated as part of this study, an augmentation plot was created and is presented in Figure 8-9. As with the prior augmentation results, the performance of much of the IN718 coupons fall on top of each other, with the exception of the 3D Systems coupons which offer similar levels of heat transfer enhancement for lower friction factor enhancement due to the previously discussed suspected low downskin surface roughness. The performance of coupons manufactured out of different materials varied depending on their respective roughness properties, where the smoother coupons enabled similar levels of heat transfer enhancement with lower friction factor enhancement. Across all of the designs, the slope of heat transfer versus friction factor augmentation was consistent, whereas the shift along the friction factor augmentation axis was largely just a function of the arithmetic mean surface roughness.

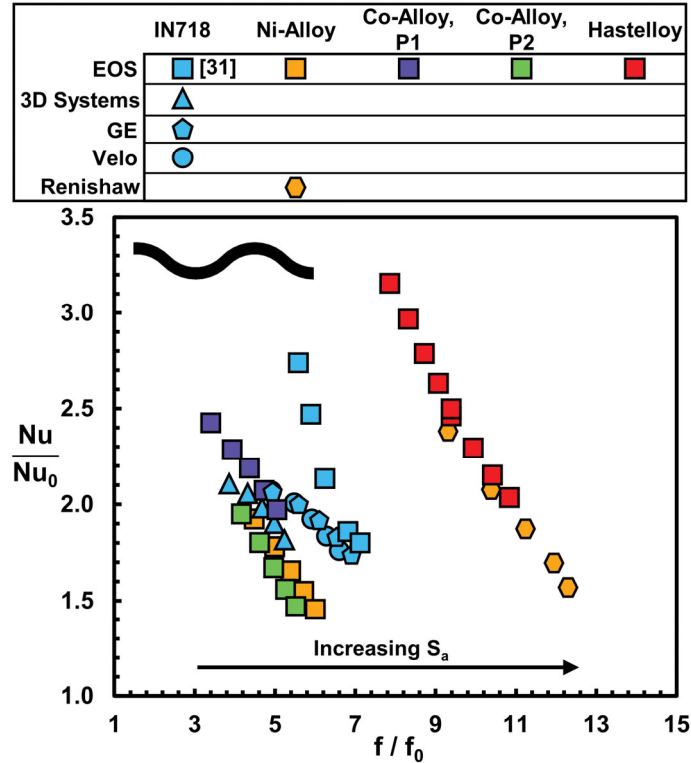


Figure 8-9. Augmentation plot of the wavy channel design from the nine different build conditions.

Comparing the results from the EOS Ni-alloy coupon to the EOS Co-alloy P1 coupon in Figure 8-9, there is an evident increase in the heat transfer despite a similar magnitude of friction factor augmentation. This difference in performance is the result of the poorly attached particles on the surface of the EOS Ni-alloy coupon as indicated by the higher levels of S_{ku} shown in Figure 8-4(d) and the images shown in Figure 8-2(d) and Figure 8-2(l) for the Ni- and Co-alloys, respectively. The scale-like roughness of EOS Co-alloy P1 coupons therefore more effectively transfer heat.

The flow results presented in Figure 8-9 also showcase that a primary factor to increasing the friction factor and heat transfer from a test coupon is the arithmetic means surface roughness. However, the structure of the roughness, which can be described using the S_{sk} and S_{ku} of the surface, plays a significant secondary role in determining the effectiveness of a surface morphology.

8.10. Thermal Performance of Pin Fins

The flow results from the pin fin coupons are presented in Figure 8-10. Starting with the coupons of varied materials shown in Figure 8-10(a,b), it should immediately be noted that the friction factor and Nusselt number augmentations are significantly greater than those found for the Wavy channel coupons presented in Figure 8-8. The cause for this increase is in part due to the normalization of the results, which uses the bulk inlet velocity instead of the maximum velocity,

and also the difference in the main contributors to pressure loss. Where for the wavy channels the wall shear stress in tandem with the internal secondary flow formations drive much of the pressure loss, the impingement onto pin surfaces and subsequent flow detachment and mixing is what drives the pressure loss and heat transfer in the pin fin arrays.

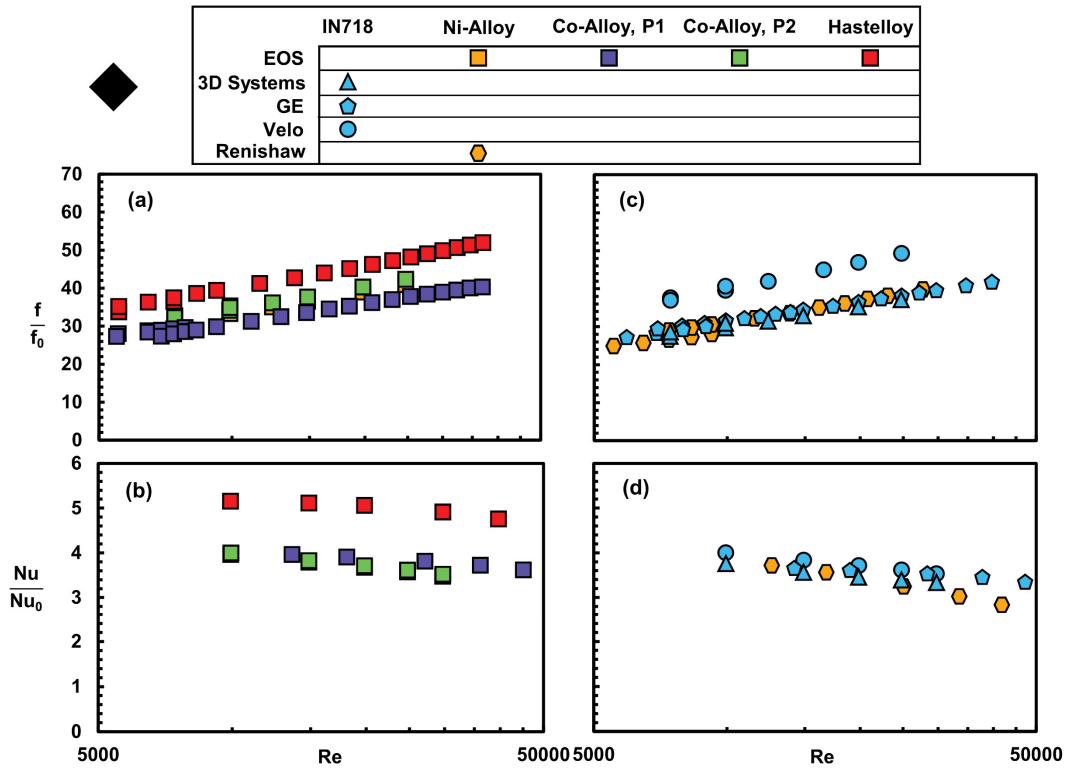


Figure 8-10. Pin fin friction factor (a,c) and Nusselt number (b,d) augmentation as a function of Reynolds number.

For all but the Hastelloy coupons, the pin fin coupons made of different materials had very similar friction factor augmentation. The cause for this difference is that the coupons from the other materials had lower roughness statistics than the Hastelloy coupons, as shown in Figure 8-4. The Nusselt number augmentations from the coupons of varied materials for most of the coupons was very similar, with the exception of the Hastelloy test coupon. The reason for this difference in performance is twofold: firstly, the average pin diameter for the Hastelloy coupons was slightly larger than the other coupons of different materials inducing more mixing, and secondly the endwall surface of the Hastelloy coupon was significantly rougher than that of the other coupons of varied materials. Within the coupons of the same material, there was as much as a 22% difference in friction factor for a given Reynolds number, and as much as a 26% difference in heat transfer.

Looking to Figure 8-10(c,d), the Renishaw Ni-alloy and the IN718 coupons made on the 3D systems and GE machines had almost identical friction factor performance for the range tested. The only coupon to deviate was the IN718 coupon made on the VELO machine. The reason why

the VELO coupon had the significant increase in friction factor was due to the shape of the pin that was formed during the build, as was shown in Figure 8-7 (b), where instead of the pins being a diamond in shape, they were instead shaped like a plus sign. This irregular shape lead to a greater percentage of the pin frontal area being normal to the oncoming flow direction, resulting in an increase in pressure loss from the flow impingement. This loss mechanism was partnered with an increased amount of pressure loss in the wake of each pin due to the recessed areas downstream of the pin. Despite the increased pressure loss, the heat transfer for the coupons made of IN718 was very similar. The Ni-alloy coupon made on the Renishaw machine also featured very similar performance to the coupons made of IN718, despite having increased levels of endwall arithmetic mean roughness relative to the IN718 coupons (Figure 8-4(a)). This was the result of the pins being considerably undersized, as shown in Figure 8-7 (b), limiting the effectiveness of this coupon as it compares to the Hastelloy coupon which shared a similar level of endwall surface roughness.

The final comparison of the pin fin test results is presented in Figure 8-11, which features an augmentation plot of all eight variations of test coupon. The coupons that shared similar levels of surface roughness also shared a similar augmentation performance, with many of the test results falling largely on top of each other in Figure 8-11. The Hastelloy coupon is an outlier, with significantly enhanced heat transfer for a given friction factor augmentation. This outlier is again the result of the increased endwall arithmetic mean surface roughness not substantially increasing the pressure drop but still increasing heat transfer, since the mechanism for pressure drop is more reliant on interactions with the pin fins themselves. This relatively low friction factor sensitivity to roughness is indicated by the relatively similar friction factor augmentations exhibited by all coupons studied.

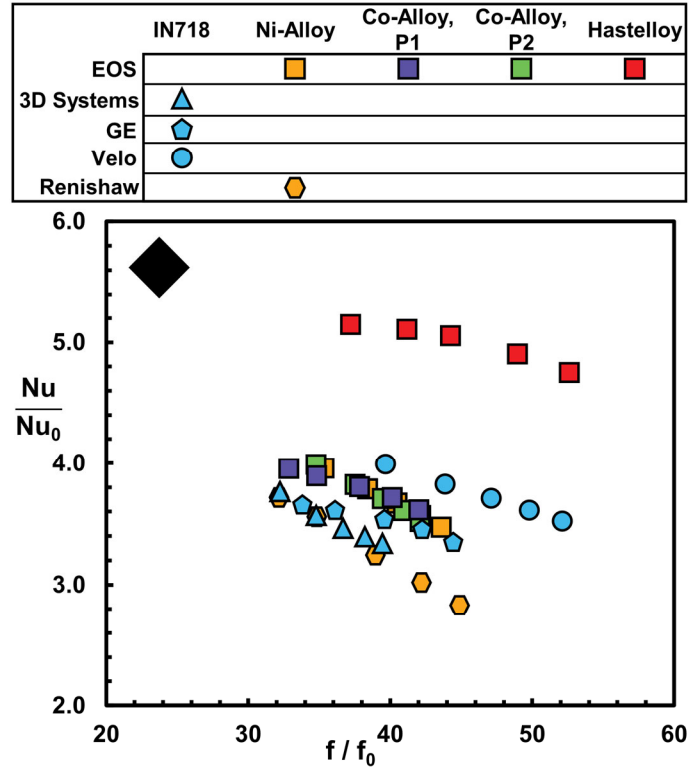


Figure 8-11. Augmentation plot of the pin fin design from the eight different build conditions.

As was seen with the wavy channel results, it is likely that the particulate that made up the endwall surface roughness on the Hastelloy coupon further improved performance over the other evaluated test coupons. Similar to the wavy channels, the morphology of the endwall surface roughness also furthered the reduction in heat transfer for Renishaw coupons relative to the other designs, as shown in Figure 8-11. However, due to the significant differences in pin geometry between the Hastelloy and Renishaw coupons in Figure 8-7, it is difficult to decouple the surface morphology from geometric impacts.

8.11. Conclusions

This study examined how additive machines and materials impact the surface roughness and geometric accuracy of AM cooling channels, which subsequently affects the cooling performance. Two different AM cooling geometries were incorporated into a general test coupon, including a wavy channel geometry and pin fin geometry. A total of 16 coupons were manufactured using five vendors, five machines, and four materials. All test coupons were printed using DMLS with specified support structures and build orientation, while the print parameters were selected according to manufacturer recommendations. To characterize the as-built qualities, the coupons were scanned using computed tomography and imaged using a laser microscope. Additionally, test coupon pressure loss and heat transfer were experimentally determined.

Both the selection of machine and material were found to influence an additive part's surface roughness, surface morphology, and geometric deviations. Not only do machine and material affect a part, but different manufacturers that are contracted to build parts can lead to variations in part roughness and geometry. Roughness levels can also significantly vary across one additive part based on a region's surface angle. The downskin surfaces printed over unsintered powder on the test coupons were found to have much higher average roughness compared to the 90-degree channel walls and upskin surfaces. However, there was very little variation in roughness observed for test coupons with different geometries that were built using the same build parameters.

For the geometric accuracy characterization, all the cooling channels were found to have hydraulic diameters very close to the design intent. However, the diamond pins introduced significant variability in geometry because they were built without supports and are relatively small in size. Looking specifically at the cross-sectional perimeters of the diamond pins, it was observed that some machines and materials fabricated the diamond shape more accurately than others. There was more variation in pin shape across different machines compared to varying the material.

This study identified that a primary driver in pressure loss and heat transfer was increased levels of S_a , but that a key secondary driver is the roughness morphology which can be described using S_{sk} and S_{ku} . In particular, it was observed that for wavy channels surfaces with a high S_a , highly distributed small particles (higher S_{sk}) enhanced the heat transfer performance over that of a surface with more crevice-shaped roughness features (lower S_{sk}). Additionally, it was observed that for wavy channel surfaces with lower levels of S_a that the kurtosis described how well particles bonded to a surface, whereby poorly bonded particles resulted in a reduction in surface heat transfer performance.

For the pin fin designs it was found that deviations from the pin design intent had the most significant impact on the pressure loss performance. However, in cases where there was significant endwall S_a , it was observed that the roughness further enhanced heat transfer and pressure loss. It was found that the different materials introduced more variation in a cooling geometry's heat transfer performance compared to the additive machine used for both the wavy channel and pin fin geometries. Heat transfer and friction factor varied by up to 50% and 83% between coupons featuring wavy channels and varied by up to 26% and 22% for coupons containing pin fin arrays and was highly dependent upon the surface morphology.

These results have identified exciting directions for improving heat transfer augmentation separately from pressure loss through identifying specific surface morphology effects. These results also lay the groundwork for further developing additive manufacturing processes to create tailor-made surfaces specific to the application. Though further work needs to be completed in

order to isolate the impacts of process parameters, particle size distribution, and laser type in the determination of the various surface topographies.

8.12. Acknowledgements

This research was sponsored by the US Department of Energy, Office of Energy Efficiency and Renewable Energy (EERE), Advanced Materials & Manufacturing Technologies Office (AMMTO), under Contract DE-AC05-00OR22725 with UT-Battelle LLC. This work was performed in part at the Oak Ridge National Laboratory's Manufacturing Demonstration Facility, an Office of Energy Efficiency and Renewable Energy user facility.

The authors would like to thank Mike Kirka at Oak Ridge National Laboratories (ORNL) and Carpenter Technologies for supplying several of the test coupons that were used in this study.

9. CONCLUSIONS

The seven studies that were covered in this dissertation explored how the inherent surface roughness of the additive manufacturing process impacted the performance of several families of internal cooling structures. Specifically, the prior chapters covered the performance of wavy channels, pin fin arrays of varying shapes, two varieties of strut-based lattice structures, surface diamond pyramids features, and broken wavy ribs. The parametric analyses around these designs offered greater insight into the range of performance that could be expected from similar styles of design. These internal features all saw enhanced heat transfer as a function of the increased surface roughness at some pressure deficit, however there was significant variation in the magnitude of the impact of the surface roughness. The partnered computational analyses that were completed in the prior studies offered significant insight into the underlying fluid dynamics and heat transfer that enable the experimentally measured performance, and also allowed for identification of when computational models may not match their experimental counterparts. Building the coupons on the myriad of machines out of a range of different materials allowed for a broader understanding of the impact of these two key aspects of the additive manufacturing process on the surface morphology and subsequent thermohydraulic performance of wavy channels and pin fin arrays.

The remainder of this chapter will review the overarching key findings from this dissertation. The first section will broadly compare the heat transfer and pressure loss results from the different internal cooling designs and the impact that the inherent surface roughness had on them. The second section will review how changes to the material and machine impacted the surface topography and ultimately the flow results from a series of internal cooling geometries. The last section will offer suggestions on future work to be completed to continue to explore the internal cooling additive manufacturing design space.

9.1. Comparisons Of Internal Cooling Designs

The bulk of this dissertation is composed of the exploration of a variety of internal cooling designs, identifying their key fluidic structures and interactions with roughness elements. A summary of the results from all of the investigated geometries is presented in Figure 9-1. Each dot in Figure 9-1 represents the results from a coupon of the associated color. While the majority of the data presented in Figure 9-1 has been shown previously, a handful of additional coupons investigating the same surface features and fully dense lattice structures previously discussed were included in the plot that did not make their way into a prior publication. It should be noted that the axis in Figure 9-1 are log scale, so as to visualize the extremely broad range of test coupon designs as determined from the analyses discussed in the prior chapters.

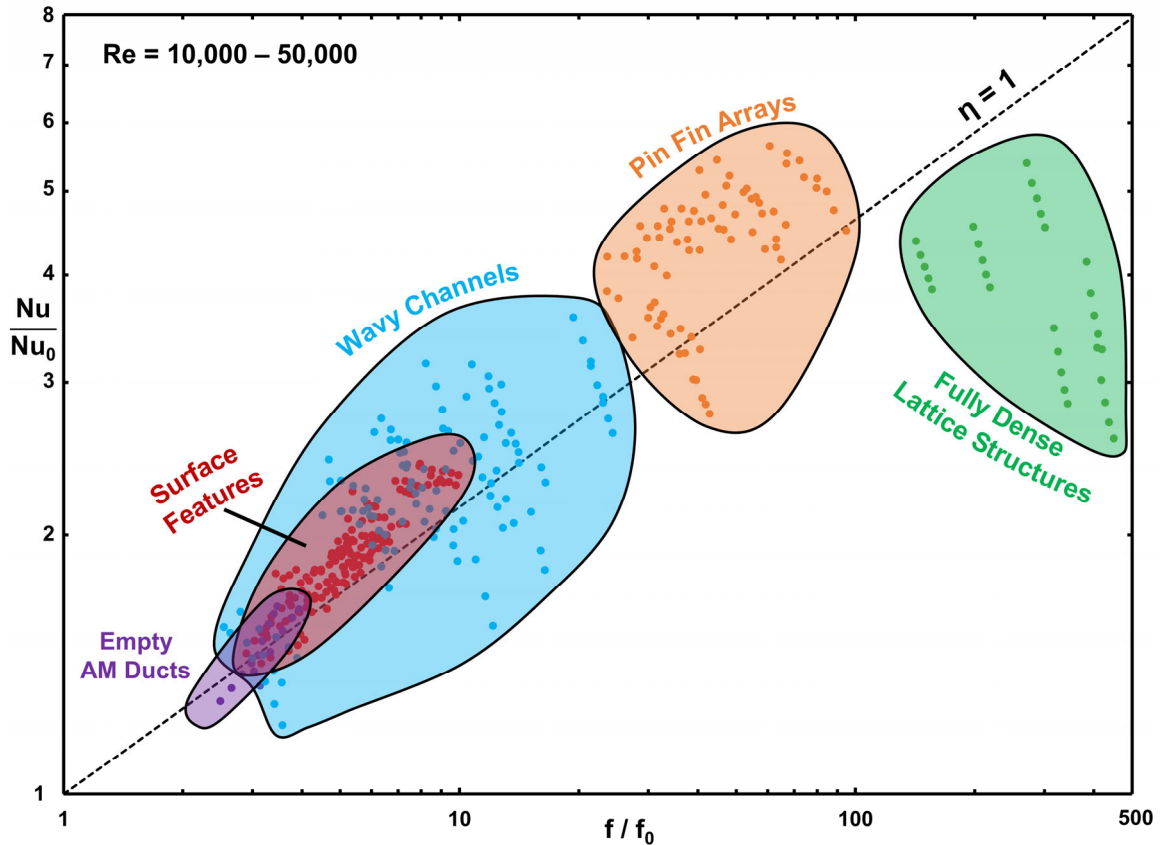


Figure 9-1. Augmentation plot of all designs tested in this dissertation.

In Figure 9-1, the definition used for friction factor was uniformly the definition used to describe the friction factor of channel geometries to ensure that the comparisons between each of the data points would be fair. From these comparisons, it can be seen that different types of cooling technologies augments the performance of a simple channel in vastly different magnitudes. From the coupons explored in the current body of work, the empty ducts had friction factor augmentations between 2.0 and 5.0 depending on the Reynolds number, with heat transfer augmentations between 1.2 and 1.7. Prior literature has shown that channels with more significant relative roughness can experience much more significant enhancements to performance, but within the work completed for this dissertation this range is representative.

Surface features offered additional enhancement, bringing friction factor augmentations between 3.0 and 10.0, and Nusselt number enhancements between 1.4 and 2.3, with the vast majority of the results following along the line of an efficiency index of one. These surface features largely enhanced the heat transfer through increasing the near wall vorticity and thermal transport, particularly in the near wake region behind a given feature. Experimentally, these flow structures

would interact with endwall roughness, which lead to an increase in both heat transfer and pressure loss.

The wavy channel designs, highlighted in blue, offer an additional region of enhancement, with friction factor augmentations of 3.0 up through 30 depending on the design and interior roughness of the wavy channel, and Nusselt number augmentations that spanned from 1.2 to above 3.0. The main mechanism for heat transfer enhancement in the wavy channel was the development of beneficial secondary flows, or Dean vortices, that formed as a function of the channel geometry. In the experimental channels, these secondary flows would interact with the rough channel walls, causing both increased heat transfer and pressure loss. In contrast to the surface features, the wavy channel designs span the efficiency index line, with some designs showing performance significantly below an efficiency index of 1. This low efficiency is due to the reduction in performance as a function of Reynolds number that was observed for the studied wavy channels. This reduction in performance was likely the result of the flow becoming more centered to the channel at greater flow rates, leading to larger recirculation zones and significant increases to pressure drop, while not equally enhancing heat transfer. This effect can be somewhat mitigated by increasing the aspect ratio of the wavy channel, as was seen in Chapter 7.

The next range of cooling technologies, the pin fins and fully dense lattice structures, far extend beyond the friction factor augmentations that were reported for the previously discussed geometries. Pin fin friction factor augmentations start at a value of 20 and extend to 100, whereas the lattice structure designs have augmentations that extend well above 500. As previously mentioned, this increase in friction factor augmentation is the result of the difference in how these geometries induce heat transfer and pressure drop. In either a pin fin or lattice array there are significant regions of reduced cross-sectional area which force the local velocity to increase, and strut geometry that the flow both impinges onto and also detaches from, resulting in wake formations and mixing. These significant increases to friction factor augmentations are paired with significant heat transfer enhancement, however the magnitude of these enhancements plateau at a Nusselt number augmentation just below six. While there is certainly a significant pressure penalty associated with the introduction of pin fin arrays, in certain instances the heat transfer enhancement from the arrays is worth the pressure penalty, such as in the trailing edge of a turbine blade. In the same way, there may be instances where the significant pressure drop that is induced from highly dense lattice structures may be worth it, especially in the cases of multifunctional designs where structural concerns are significant.

The designs presented in Figure 9-1 cover a broad range of thermohydraulic performance, but that doesn't necessarily mean the designs shown will achieve every conceivable thermal

requirement. As such, the designs studied in this dissertation should serve as a starting point for a cooling scheme, which can then be optimized for a given application. Though as was seen in Chapter 7 and Chapter 8, the surface morphology that will be accompanying these designs will need to be considered during this optimization.

9.2. Machine and Material Considerations in the DMLS Process

While the chosen cooling features used in an additive cooling design have obvious implications onto the performance of said design, the surface roughness present as a function of the process is also a driving factor in the overall performance. While, as shown previously, there are a myriad of different L-PBF parameters that ultimately impact the surface morphology, the results from Chapter 7 and 8 discuss the implications of how different machines and materials ultimately impact the performance of an additively manufactured cooling features. Broadly speaking, it was found that geometric accuracy was fairly similar when comparing multiple materials on a given machine, though there may be variations in the underlying roughness topography. Conversely, differences in machine resulted in fairly significant modifications to the geometric accuracy, with only small changes to roughness topography. Particularly, unsupported surfaces resulted in notable geometric changes between two machines. Between all of the builds studied, the friction factor of the same wavy channel design printed out of different materials differed by as much as 83%, and the heat transfer varied by as much 47%. For pin fins the friction factor augmentation varied by as much as 22% and the heat transfer varied by as much as 26% between coupons of different materials.

Due to limited access to some of the process conditions used during the manufacturing of several of the coupon sets, explicitly determining what aspects of the different machines impacted the surface quality and geometric accuracy was not possible. It was likely that for any given coupon set, repeated builds which could be used to hone in the different process parameters would have improved the overall quality of the parts tested, however the main point of interest in this work was to understand how different roughness morphologies impacted the flow performance, and was less focused on the specifics aspects of those processes that lead to the differences in surface quality.

The results presented in this dissertation also identified that increased arithmetic mean surface roughness led to increased friction factor and heat transfer enhancement for both pin fin and wavy channels. In the case wavy channels, it was also identified that the morphology of the surface roughness played a secondary role in determining test coupon performance. Small particulate that was well bonded to the channel surface was found to significantly enhance heat transfer, whereas crevasse shaped roughness features had limited enhancement. The quality of these features was found to correspond with the surface skewness and kurtosis.

9.3. Recommendations for Future Work

To fully understand each of the designs in this dissertation, a significant amount of work still needs to be completed. In particular, many of the designs investigated as part of this study featured unsteady flow structures, and in certain cases the heat transfer and pressure losses from the design was driven by complex unsteady flows. Because the vast majority of this work used time-averaged techniques, either with the experimental results or the implementation of Steady Reynolds Averaged Navier Stokes (RANS) models, there is a significant amount about these unsteady flows that have not been characterized. Particularly in the cases of the wavy ribs, diamond turbulators, or the pin fin arrays, a more detailed transient analysis may offer increased insight into the underlying fluid dynamics leading to the time-averaged performance. If possible, a detailed transient analysis into the fluid flow around additive surface roughness would also be valuable, since the flow separation induced by the roughness would also be inherently unsteady.

As mentioned in Chapter 4, there is not yet a widely agreed on method for scaling the hydrothermal performance of lattice structures, and there has been limited work investigating the performance of lattice structures at multiple scales. Preliminary results from a scaling analysis on lattice structures is presented in Appendix A, which shows that using channel definitions for characterizing the performance of lattice structures does not scale friction factor appropriately, but that using the definition for pin fins shows promise. Additional experimental work will need to be completed to validate an appropriate friction factor definition, and would be of great use to the heat exchanger community as leveraging lattice structures as a cooling design becomes more feasible. Additional criteria for evaluating the performance of these lattice structure should also be explored, such as comparisons of the gravimetric heat transfer [202], which may more directly compare the overall heat transfer for a given weight which is an important quality for aerospace heat exchangers.

One of the key outcomes from this dissertation was the mapping of cooling design space for additively manufactured internal cooling schemes. These largely experimental results have laid the ground work for an opportunity to explore an optimization space for advanced internal designs. Not every design investigated as part of this body of work will be suitable for every application, but many of the designs can be used in some combination to create an effective cooling scheme. Completing a first order optimization using the designs from this dissertation for a given application would be an effective use of the breadth of experimental data. From this first order optimization, further refinement could be completed using more computationally heavy optimization methods, such as adjoint optimization or voxel based genetic algorithms. Given the irregularity of additive surface roughness and the difficulty to simulate it with commercial computational fluids solvers, it

is recommended that a final step for this style of optimization should always be to validate the optimization using additional experimental testing.

While the latter half of this dissertation covered how additive surfaces varied depending on their manufacturing conditions, further research should be completed to understand what aspects of the additive machines was leading to the differences in surface morphology and geometric accuracy. Specifically, additional work should be completed on comparisons of parts between different additive machines while keeping a greater number of variables the same between builds, such as particle size distribution and layer height. Without a key understanding of the cause for the differences between machines, validation of additive manufacturing as a general manufacturing method will be impossible. Several of the studies completed in this dissertation involved coupons where the author did not know the process parameters used to manufacture the parts. Not knowing these parameters limited detailed discussion about accuracy to design intent and the impacts of the surface quality, and what aspects of the process resulted in these deviations. Future studies investigating additively manufactured internal cooling designs should be diligent in determining the process parameters used in a given build and extracting powder samples for particle size distribution measurements. Much like in industry, having a detailed log of as many aspects of entire additive process as possible, including the feedstock powder quality, process conditions used, operator of the machine, and final part heat treatment and machining, is a critical in being able to make the most detailed and definitive statements about how and why a given part printed the way it did.

REFERENCES

- [1] Saravanamuttoo, H. I. H., Rogers, G., Cohen, H., and Straznicky, P., 2009, *Gas Turbine Theory*, Pearson Prentice Hall, Harlow, England ; New York.
- [2] Gülen, S. C., 2019, *Gas Turbines for Electric Power Generation*, Cambridge University Press.
- [3] Ligrani, P., 2013, “Heat Transfer Augmentation Technologies for Internal Cooling of Turbine Components of Gas Turbine Engines,” *International Journal of Rotating Machinery*, **2013**, pp. 1–32.
- [4] Aust, J., and Pons, D., 2019, “Taxonomy of Gas Turbine Blade Defects,” *Aerospace*, **6**(5), p. 58.
- [5] Bollapragada, S., Zeng, X., Fox, M., Elam, B., Ryan, D., Thole, K., and Corbett, T., 2023, “INTERNALLY COOLED TURBINE TIP SHROUD COMPONENT.”
- [6] Wimmer, T., Ruehmer, T., Mick, Y., Wang, L., and Weigand, B., 2019, “Experimental and Numerical Investigation on an Additively Manufactured Gas Turbine Ring Segment With an In-Wall Cooling Scheme,” GT2019-90227.
- [7] McMasters, M. A., Benjamin, M., Mancini, A., and Lohmueller, S., 2014, “Fuel Nozzle.”
- [8] Kalb, B., Yaquinto, M., Vogel, G., and Keshava Bhattu, R., 2022, “Design and Validation of an Improved Lower Emission Additively Manufactured Combustor Pilot Nozzle for F Class Industrial Gas Turbine,” *Volume 7: Industrial and Cogeneration; Manufacturing Materials and Metallurgy; Microturbines, Turbochargers, and Small Turbomachines; Oil & Gas Applications*, American Society of Mechanical Engineers, Rotterdam, Netherlands, p. V007T17A017.
- [9] Cecconi, M., and Giovannetti, I., 2023, “Development of Additive Manufacturing Gas Turbine Hot Gas Path Vanes at Baker Hughes,” *GT2023-103043*, p. 8.
- [10] Lindbäck, M., Frankolin, K., Tuneskog, E., Karlsson, B., and Wang, L., 2023, “Development and Validation Under Engine Operation Environment of Additively Manufactured Hot Turbine Parts,” *Volume 13C: Turbomachinery — Deposition, Erosion, Fouling, and Icing; Design Methods and CFD Modeling for Turbomachinery; Ducts, Noise, and Component Interactions*, American Society of Mechanical Engineers, Boston, Massachusetts, USA, p. V13CT32A037.
- [11] Wei, X., Joshi, Y., and Patterson, M. K., 2007, “Experimental and Numerical Study of a Stacked Microchannel Heat Sink for Liquid Cooling of Microelectronic Devices,” *Journal of Heat Transfer*, **129**(10), pp. 1432–1444.

- [12] Han, J.-C., Park, J. S., and Lei, C. K., 1984, *Heat Transfer and Pressure Drop in Blade Cooling Channels with Turbulence Promoters*, NASA-CR-3837.
- [13] Northcutt, B., and Mudawar, I., 2012, “Enhanced Design of Cross-Flow Microchannel Heat Exchanger Module for High-Performance Aircraft Gas Turbine Engines,” *Journal of Heat Transfer*, **134**(6), p. 061801.
- [14] Weaver, S. A., Barringer, M. D., and Thole, K. A., 2011, “Microchannels With Manufacturing Roughness Levels,” *J Turbomach*, **133**(4), p. 041014.
- [15] Adewumi, O. O., Bello-Ochende, T., and Meyer, J. P., 2013, “Constructal Design of Combined Microchannel and Micro Pin Fins for Electronic Cooling,” *International Journal of Heat and Mass Transfer*, **66**, pp. 315–323.
- [16] Koo, J.-M., Im, S., Jiang, L., and Goodson, K. E., 2005, “Integrated Microchannel Cooling for Three-Dimensional Electronic Circuit Architectures,” *Journal of Heat Transfer*, **127**(1), pp. 49–58.
- [17] Lu, S., and Vafai, K., 2016, “A Comparative Analysis of Innovative Microchannel Heat Sinks for Electronic Cooling,” *International Communications in Heat and Mass Transfer*, **76**, pp. 271–284.
- [18] Zhao, C. Y., and Lu, T. J., 2002, “Analysis of Microchannel Heat Sinks for Electronics Cooling,” *International Journal of Heat and Mass Transfer*, **45**(24), pp. 4857–4869.
- [19] Dai, B., Li, M., and Ma, Y., 2014, “Effect of Surface Roughness on Liquid Friction and Transition Characteristics in Micro- and Mini-Channels,” *Applied Thermal Engineering*, **67**(1–2), pp. 283–293.
- [20] Sui, Y., Teo, C. J., Lee, P. S., Chew, Y. T., and Shu, C., 2010, “Fluid Flow and Heat Transfer in Wavy Microchannels,” *International Journal of Heat and Mass Transfer*, **53**(13–14), pp. 2760–2772.
- [21] Metzger, D. E., Shepard, W. B., and Haley, S. W., 1986, “Row Resolved Heat Transfer Variations in Pin-Fin Arrays Including Effects of Non-Uniform Arrays and Flow Convergence,” *Volume 4: Heat Transfer; Electric Power*, p. 9.
- [22] Chyu, M. K., Yen, C. H., and Siw, S., 2007, “Comparison of Heat Transfer From Staggered Pin Fin Arrays With Circular, Cubic and Diamond Shaped Elements,” *GT2007-28306*, p. 10.
- [23] Chyu, M. K., and Natarajan, V., 1996, “Heat Transfer on the Base Surface of Threedimensional Protruding Elements,” *International Journal of Heat and Mass Transfer*, **39**(14), pp. 2925–2935.

- [24] Kaur, I., and Singh, P., 2021, “Critical Evaluation of Additively Manufactured Metal Lattices for Viability in Advanced Heat Exchangers,” *International Journal of Heat and Mass Transfer*, **168**, p. 120858.
- [25] King, W. E., Anderson, A. T., Ferencz, R. M., Hodge, N. E., Kamath, C., Khairallah, S. A., and Rubenchik, A. M., 2015, “Laser Powder Bed Fusion Additive Manufacturing of Metals; Physics, Computational, and Materials Challenges,” *Applied Physics Reviews*, **2**(4), p. 041304.
- [26] Snyder, J. C., and Thole, K. A., 2020, “Understanding Laser Powder Bed Fusion Surface Roughness,” *Journal of Manufacturing Science and Engineering*, **142**(7), p. 071003.
- [27] Snyder, J. C., and Thole, K. A., 2020, “Tailoring Surface Roughness Using Additive Manufacturing to Improve Internal Cooling,” *Journal of Turbomachinery*, **142**(7), p. 071004.
- [28] Rehme, O., Emmelmann, C., and Morlock, M., 2010, *Cellular Design for Laser Freeform Fabrication*, Cuvillier, Göttingen.
- [29] Thole, K. A., Lynch, S. P., and Wildgoose, A. J., 2021, “Review of Advances in Convective Heat Transfer Developed through Additive Manufacturing,” *Advances in Heat Transfer*, Elsevier, pp. 249–325.
- [30] Mazzei, L., Soghe, R. D., and Bianchini, C., 2020, “CFD Modelling Strategies for the Simulation of Roughness Effects on Friction and Heat Transfer in Additive Manufactured Components,” *GT2020-15406*, p. 11.
- [31] Kirsch, K. L., and Thole, K. A., 2017, “Heat Transfer and Pressure Loss Measurements in Additively Manufactured Wavy Microchannels,” *J Turbomach*, **139**(1), p. 011007.
- [32] Kirsch, K. L., and Thole, K. A., 2018, “Isolating the Effects of Surface Roughness versus Wall Shape in Numerically Optimized, Additively Manufactured Micro Cooling Channels,” *Experimental Thermal and Fluid Science*, **98**, pp. 227–238.
- [33] Kirsch, K. L., and Thole, K. A., 2017, “Pressure Loss and Heat Transfer Performance for Additively and Conventionally Manufactured Pin Fin Arrays,” *International Journal of Heat and Mass Transfer*, **108**, pp. 2502–2513.
- [34] Ferster, K. K., Kirsch, K. L., and Thole, K. A., 2018, “Effects of Geometry, Spacing, and Number of Pin Fins in Additively Manufactured Microchannel Pin Fin Arrays,” *Journal of Turbomachinery*, **140**(1), p. 011007.
- [35] Roy, A., Searle, M., Ramesh, S., and Straub, D., 2022, “Investigation of Gas Turbine Internal Cooling Using Supercritical CO₂—Effect of Surface Roughness and Channel Aspect Ratio,” *Journal of Engineering for Gas Turbines and Power*, **144**(11), p. 111019.

- [36] Searle, M., Roy, A., Black, J., Straub, D., and Ramesh, S., 2022, “Investigating Gas Turbine Internal Cooling Using Supercritical CO₂ at Higher Reynolds Numbers for Direct Fired Cycle Applications,” *Journal of Turbomachinery*, **144**(1), p. 011007.
- [37] IATA, 2021, “Industry Statistics Fact Sheet.”
- [38] Manning, R. F., Acquaviva, P. J., and Demers, D. E., “Gas Turbine Airfoil With Axial Serpentine Cooling Circuits.”
- [39] Ahmed, M. A., Shuaib, N. H., and Yusoff, M. Z., 2012, “Numerical Investigations on the Heat Transfer Enhancement in a Wavy Channel Using Nanofluid,” *Int J Heat and Mass*, **55**(21–22), pp. 5891–5898.
- [40] Guzmán, A. M., Cárdenas, M. J., Urzúa, F. A., and Araya, P. E., 2009, “Heat Transfer Enhancement by Flow Bifurcations in Asymmetric Wavy Wall Channels,” *International Journal of Heat and Mass Transfer*, **52**(15–16), pp. 3778–3789.
- [41] Wang, G., and Vanka, S. P., 1995, “Convective Heat Transfer in Periodic Wavy Passages,” *International Journal of Heat and Mass Transfer*, **38**(17), pp. 3219–3230.
- [42] Nishimura, T., Otori, Y., and Kawamura, Y., 1984, “Flow Characteristics in a Channel with Symmetric Wavy Wall for Steady Flow,” *J. Chem. Eng. Japan / JCEJ*, **17**(5), pp. 466–471.
- [43] Xie, G.-N., Wang, Q.-W., Zeng, M., and Luo, L.-Q., 2007, “Numerical Investigation of Heat Transfer and Fluid Flow Characteristics inside a Wavy Channel,” *Heat Mass Transfer*, **43**(7), pp. 603–611.
- [44] Snyder, B., Li, K. T., and Wirtz, R. A., 1993, “Heat Transfer Enhancement in a Serpentine Channel,” *International Journal of Heat and Mass Transfer*, **36**(12), pp. 2965–2976.
- [45] Comini, G., Nonino, C., and Savino, S., 2003, “Effect of Aspect Ratio on Convection Enhancement in Wavy Channels,” *Numerical Heat Transfer, Part A: Applications*, **44**(1), pp. 21–37.
- [46] Karale, C. M., Bhagwat, S. S., and Ranade, V. V., 2013, “Flow and Heat Transfer in Serpentine Channels,” *AIChE J*, **59**(5), pp. 1814–1827.
- [47] Harikrishnan, S., and Tiwari, S., 2018, “Effect of Skewness on Flow and Heat Transfer Characteristics of a Wavy Channel,” *International Journal of Heat and Mass Transfer*, **120**, pp. 956–969.
- [48] Harikrishnan, S., and Tiwari, S., 2019, “Heat Transfer Characteristics of Sinusoidal Wavy Channel with Secondary Corrugations,” *International Journal of Thermal Sciences*, **145**, p. 105973.

- [49] Lin, L., Zhao, J., Lu, G., Wang, X.-D., and Yan, W.-M., 2017, “Heat Transfer Enhancement in Microchannel Heat Sink by Wavy Channel with Changing Wavelength/Amplitude,” *International Journal of Thermal Sciences*, **118**, pp. 423–434.
- [50] Zhou, J., Hatami, M., Song, D., and Jing, D., 2016, “Design of Microchannel Heat Sink with Wavy Channel and Its Time-Efficient Optimization with Combined RSM and FVM Methods,” *International Journal of Heat and Mass Transfer*, **103**, pp. 715–724.
- [51] Stimpson, C. K., Snyder, J. C., Thole, K. A., and Mongillo, D., 2016, “Roughness Effects on Flow and Heat Transfer for Additively Manufactured Channels,” *J Turbomach*, **138**(5), p. 051008.
- [52] Snyder, J. C., Stimpson, C. K., Thole, K. A., and Mongillo, D. J., 2015, “Build Direction Effects on Microchannel Tolerance and Surface Roughness,” *Journal of Mechanical Design*, **137**(11), p. 111411.
- [53] Wildgoose, A. J., Thole, K. A., Sanders, P., and Wang, L., 2021, “Impact of Additive Manufacturing on Internal Cooling Channels With Varying Diameters and Build Directions,” *J Turbomach*, **143**(7), p. 071003.
- [54] Reinhart, C., 2011, *Industrial CT & Precision*, Volume Graphics GmbH, Heidelberg, Germany.
- [55] Colebrook, C. F., 1939, “Turbulent Flow In Pipes, With Particular Reference To The Transition Region Between The Smooth And Rough Pipe Laws.,” *Journal of the Institution of Civil Engineers*, **11**(4), pp. 133–156.
- [56] Gnielinski, V., 1975, “New Equations for Heat and Mass Transfer in the Turbulent Flow in Pipes and Channels,” *NASA STI/Recon Technical Report A*, **41**, pp. 8–16.
- [57] Dunn, P. F., 2014, *Measurement and Data Analysis for Engineering and Science*, CRC Press, Taylor & Francis, Boca Raton.
- [58] ANSYS, 2018, “ANSYS Fluent.”
- [59] Pointwise, 2018, “Pointwise.”
- [60] Gee, D. L., and Webb, R. L., 1980, “Forced Convection Heat Transfer in Helically Rib-Roughened Tubes,” *International Journal of Heat and Mass Transfer*, **23**(8), pp. 1127–1136.
- [61] National Academies of Sciences, Engineering, and Medicine (U.S.), ed., 2020, *Advanced Technologies for Gas Turbines*, The National Academies Press, Washington, DC.
- [62] Ligrani, P., 2013, “Heat Transfer Augmentation Technologies for Internal Cooling of Turbine Components of Gas Turbine Engines,” *International Journal of Rotating Machinery*, **2013**, pp. 1–32.

- [63] Armstrong, J., and Winstanley, D., 1988, "A Review of Staggered Array Pin Fin Heat Transfer for Turbine Cooling Applications," *J Turbomach*, **110**(1), pp. 94–103.
- [64] Schilke, P. W., Foster, A. D., and Pepe, J. J., 1991, *Advanced Gas Turbine Materials and Coatings*.
- [65] Konter, M., and Thumann, M., 2001, "Materials and Manufacturing of Advanced Industrial Gas Turbine Components," *Journal of Materials Processing Technology*, **117**(3), pp. 386–390.
- [66] Žukauskas, A., 1972, "Heat Transfer from Tubes in Crossflow," *Advances in Heat Transfer*, Elsevier, pp. 93–160.
- [67] Sparrow, E. M., Stahl, T. J., and Traub, P., 1984, "Heat Transfer Adjacent to the Attached End of a Cylinder in Crossflow," *International Journal of Heat and Mass Transfer*, **27**(2), pp. 233–242.
- [68] VanFossen, G. J., 1982, "Heat-Transfer Coefficients for Staggered Arrays of Short Pin Fins," *Journal of Engineering for Power*, **104**(2), pp. 268–274.
- [69] Brigham, B. A., and VanFossen, G. J., 1984, "Length to Diameter Ratio and Row Number Effects in Short Pin Fin Heat Transfer," *Journal of Engineering for Gas Turbines and Power*, **106**(1), pp. 241–244.
- [70] Chyu, M. K., Siw, S. C., and Moon, H. K., 2009, "Effects of Height-to-Diameter Ratio of Pin Element on Heat Transfer From Staggered Pin-Fin Arrays," p. 8.
- [71] Metzger, D. E., Berry, R. A., and Bronson, J. P., 1982, "Developing Heat Transfer in Rectangular Ducts With Staggered Arrays of Short Pin Fins," *J of Heat Transfer-Transactions of the ASME*, **104**(4), pp. 700–706.
- [72] Lawson, S. A., Thrift, A. A., Thole, K. A., and Kohli, A., 2011, "Heat Transfer from Multiple Row Arrays of Low Aspect Ratio Pin Fins," *International Journal of Heat and Mass Transfer*, **54**(17–18), pp. 4099–4109.
- [73] Ostanek, J. K., 2012, "Flowfield Interations in Low Aspect Ratio Pin-Fin Arrays," The Pennsylvania State University.
- [74] Metzger, D. E., Fan, C. S., and Haley, S. W., 1984, "Effects of Pin Shape and Array Orientation on Heat Transfer and Pressure Loss in Pin Fin Arrays," *Journal of Engineering for Gas Turbines and Power*, **106**(1), pp. 252–257.
- [75] Chyu, M. K., Hsing, Y. C., and Natarajan, V., 1998, "Convective Heat Transfer of Cubic Fin Arrays in a Narrow Channel," *J Turbomach*, **120**(2), pp. 362–367.
- [76] Lawson, S. A., 2007, "Heat Transfer from Multiple Row Arrays of Low Aspect Ratio Pin Fins," Virginia Polytechnic Institute and State University.

- [77] Kaur, I., Aider, Y., Nithyanandam, K., and Singh, P., 2022, "Thermal-Hydraulic Performance of Additively Manufactured Lattices for Gas Turbine Blade Trailing Edge Cooling," *Applied Thermal Engineering*, **211**, p. 118461.
- [78] Shen, B., Li, Y., Yan, H., Boetcher, S. K. S., and Xie, G., 2019, "Heat Transfer Enhancement of Wedge-Shaped Channels by Replacing Pin Fins with Kagome Lattice Structures," *International Journal of Heat and Mass Transfer*, **141**, pp. 88–101.
- [79] Ho, J. Y., Leong, K. C., and Wong, T. N., 2020, "Additively-Manufactured Metallic Porous Lattice Heat Exchangers for Air-Side Heat Transfer Enhancement," *International Journal of Heat and Mass Transfer*, **150**, p. 119262.
- [80] Kaur, I., and Singh, P., 2021, "Flow and Thermal Transport Characteristics of Triply-Periodic Minimal Surface (TPMS)-Based Gyroid and Schwarz-P Cellular Materials," *Numerical Heat Transfer, Part A: Applications*, **79**(8), pp. 553–569.
- [81] Cheng, Z., Xu, R., and Jiang, P.-X., 2021, "Morphology, Flow and Heat Transfer in Triply Periodic Minimal Surface Based Porous Structures," *International Journal of Heat and Mass Transfer*, **170**, p. 120902.
- [82] Clarke, D. A., Dolamore, F., Fee, C. J., Galvosas, P., and Holland, D. J., 2021, "Investigation of Flow through Triply Periodic Minimal Surface-Structured Porous Media Using MRI and CFD," *Chemical Engineering Science*, **231**, p. 116264.
- [83] Liang, D., He, G., Chen, W., Chen, Y., and Chyu, M. K., 2022, "Fluid Flow and Heat Transfer Performance for Micro-Lattice Structures Fabricated by Selective Laser Melting," *International Journal of Thermal Sciences*, **172**, p. 107312.
- [84] Liang, D., Shi, C., Li, W., Chen, W., and Chyu, M. K., 2023, "Design, Flow Characteristics and Performance Evaluation of Bioinspired Heat Exchangers Based on Triply Periodic Minimal Surfaces," *International Journal of Heat and Mass Transfer*, **201**, p. 123620.
- [85] Kim, T., Hodson, H. P., and Lu, T. J., 2004, "Fluid-Flow and Endwall Heat-Transfer Characteristics of an Ultralight Lattice-Frame Material," *International Journal of Heat and Mass Transfer*, **47**(6–7), pp. 1129–1140.
- [86] Parbat, S., Min, Z., Yang, L., and Chyu, M., 2020, "Experimental and Numerical Analysis of Additively Manufactured Inconel 718 Coupons With Lattice Structure," *J Turbomach*, **142**(6), p. 061004.
- [87] Liang, D., Bai, W., Chen, W., and Chyu, M. K., 2020, "Investigating the Effect of Element Shape of the Face-Centered Cubic Lattice Structure on the Flow and Endwall Heat Transfer Characteristics in a Rectangular Channel," *International Journal of Heat and Mass Transfer*, **153**, p. 119579.

- [88] Xu, L., Chen, H., Xi, L., Xiong, Y., Gao, J., and Li, Y., 2022, “Flow and Heat Transfer Characteristics of a Staggered Array of Kagome Lattice Structures in Rectangular Channels,” *Heat Mass Transfer*, **58**(1), pp. 41–64.
- [89] Liang, D., Chen, W., Ju, Y., and Chyu, M. K., 2021, “Comparing Endwall Heat Transfer among Staggered Pin Fin, Kagome and Body Centered Cubic Arrays,” *Applied Thermal Engineering*, **185**, p. 116306.
- [90] Kaur, I., and Singh, P., 2021, “Numerical Investigation on Conjugate Heat Transfer in Octet-Shape-Based Single Unit Cell Thick Metal Foam,” *International Communications in Heat and Mass Transfer*, **121**, p. 105090.
- [91] Kaur, I., 2022, “Flow and Thermal Transport in Additively Manufactured Metal Lattices Based on Novel Unit-Cell Topologies,” Mississippi State University.
- [92] Kaur, I., and Singh, P., 2022, “Conjugate Heat Transfer in Lattice Frame Materials Based on Novel Unit Cell Topologies,” *Numerical Heat Transfer, Part A: Applications*, pp. 1–14.
- [93] Kaur, I., and Singh, P., 2022, “Direct Pore-Scale Simulations of Fully Periodic Unit Cells of Different Regular Lattices,” *J of Heat Transfer-Transactions of the ASME*, **144**(2), p. 022702.
- [94] Kaur, I., and Singh, P., 2020, “Flow and Thermal Transport Through Unit Cell Topologies of Cubic and Octahedron Families,” *International Journal of Heat and Mass Transfer*, **158**, p. 119784.
- [95] Aider, Y., Kaur, I., Cho, H., and Singh, P., 2022, “Periodic Heat Transfer Characteristics of Additively Manufactured Lattices,” *International Journal of Heat and Mass Transfer*, **189**, p. 122692.
- [96] Yang, G., Hou, C., Zhao, M., and Mao, W., 2019, “Comparison of Convective Heat Transfer for Kagome and Tetrahedral Truss-Cored Lattice Sandwich Panels,” *Sci Rep*, **9**(1), p. 3731.
- [97] Shen, B., Yan, H., Xue, H., and Xie, G., 2018, “The Effects of Geometrical Topology on Fluid Flow and Thermal Performance in Kagome Cored Sandwich Panels,” *Applied Thermal Engineering*, **142**, pp. 79–88.
- [98] Kemerli, U., and Kahveci, K., 2020, “Conjugate Forced Convective Heat Transfer in a Sandwich Panel with a Kagome Truss Core: The Effects of Strut Length and Diameter,” *Applied Thermal Engineering*, **167**, p. 114794.
- [99] Dixit, T., Nithiarasu, P., and Kumar, S., 2021, “Numerical Evaluation of Additively Manufactured Lattice Architectures for Heat Sink Applications,” *International Journal of Thermal Sciences*, **159**, p. 106607.

- [100] Takarazawa, S., Ushijima, K., Fleischhauer, R., Kato, J., Terada, K., Cantwell, W. J., Kaliske, M., Kagaya, S., and Hasumoto, S., 2022, “Heat-Transfer and Pressure Drop Characteristics of Micro-Lattice Materials Fabricated by Selective Laser Metal Melting Technology,” *Heat Mass Transfer*, **58**(1), pp. 125–141.
- [101] Shahrzadi, M., Davazdah Emami, M., and Akbarzadeh, A. H., 2022, “Heat Transfer in BCC Lattice Materials: Conduction, Convection, and Radiation,” *Composite Structures*, **284**, p. 115159.
- [102] Ernot, J., Verdin, P. G., Ahmad, H., and Indge, P., 2019, “Analytical and Numerical Predictions of the Thermal Performance of Multi-Layered Lattice Structures,” *International Journal of Heat and Mass Transfer*, **145**, p. 118752.
- [103] Yun, S., Lee, D., Jang, D. S., Lee, M., and Kim, Y., 2021, “Numerical Analysis on Thermo-Fluid–Structural Performance of Graded Lattice Channels Produced by Metal Additive Manufacturing,” *Applied Thermal Engineering*, **193**, p. 117024.
- [104] Hou, C., Yang, G., Wan, X., and Chen, J., 2019, “Study of Thermo-Fluidic Characteristics for Geometric-Anisotropy Kagome Truss-Cored Lattice,” *Chinese Journal of Aeronautics*, **32**(7), pp. 1635–1645.
- [105] Corbett, T. M., Thole, K. A., and Bollapragada, S., 2023, “Impacts of Pin Fin Shape and Spacing on Heat Transfer and Pressure Losses,” *Journal of Turbomachinery*, **145**(5), p. 10.
- [106] Corbett, T., Thole, K. A., and Bollapragada, S., 2022, “Amplitude and Wavelength Effects for Wavy Channels,” *J Turbomach*, **145**(3), p. 031011.
- [107] Siemens, 2021, “SimCenter STAR-CCM+.”
- [108] Nicoud, F., and Ducros, F., 1999, “Subgrid-Scale Stress Modelling Based on the Square of the Velocity Gradient Tensor,” *Flow, Turbulence and Combustion*, **62**(3), pp. 183–200.
- [109] Kaur, I., and Singh, P., 2023, “Effects of Inherent Surface Roughness of Additively Manufactured Lattice Frame Material on Flow and Thermal Transport,” *International Journal of Heat and Mass Transfer*, **209**, p. 124077.
- [110] Mazzei, L., Da Soghe, R., and Bianchini, C., 2021, “Calibration of a CFD Methodology for the Simulation of Roughness Effects on Friction and Heat Transfer in Additive Manufactured Components,” *Volume 5B: Heat Transfer — General Interest; Internal Air Systems; Internal Cooling*, p. 10.
- [111] Pope, S. B., 2000, *Turbulent Flows*, Cambridge University Press, Cambridge ; New York.
- [112] Caket, A. G., Wang, C., Nugroho, M. A., Celik, H., and Mobedi, M., 2022, “Recent Studies on 3D Lattice Metal Frame Technique for Enhancement of Heat Transfer: Discovering Trends and Reasons,” *Renewable and Sustainable Energy Reviews*, **167**, p. 112697.

- [113] Lowery, G. W., and Vachon, R. I., 1975, “The Effect of Turbulence on Heat Transfer from Heated Cylinders,” *International Journal of Heat and Mass Transfer*, **18**(11), pp. 1229–1242.
- [114] Delany, N. K., and Sorensen, N., 1956, *Low-Speed Drag of Cylinders of Various Shapes*, NACA TN 3038, NACA.
- [115] Chiu, W. S., and Lienhard, J. H., 1967, “On Real Fluid Flow Over Yawed Circular Cylinders,” *Journal of Basic Engineering*, **89**(4), pp. 851–857.
- [116] Zdravkovich, M. M., and Stonebanks, K. L., 1990, “Intrinsically Nonuniform and Metastableflow in and behind Tube Arrays,” *Journal of Fluids and Structures*, **4**(3), pp. 305–319.
- [117] Ziada, S., and Oengören, A., 2000, “Flow Periodicity and Acoustic Resonance in Parallel Triangle Tube Bundles,” *Journal of Fluids and Structures*, **14**(2), pp. 197–219.
- [118] Forecast and Performance Analysis Division, 2023, *FAA Aerospace Forecast Fiscal Years 2023–2043*, FAA.
- [119] Han, J.-C., Datta, S., and Ekkad, S., 2013, *Gas Turbine Heat Transfer and Cooling Technology*, CRC Press/Taylor & Francis, Boca Raton, FL.
- [120] Han, J.-C., 2018, “Advanced Cooling in Gas Turbines 2016 Max Jakob Memorial Award Paper,” *Journal of Heat Transfer*, **140**(11), p. 113001.
- [121] Bunker, R. S., 2009, “The Effects of Manufacturing Tolerances on Gas Turbine Cooling,” *Journal of Turbomachinery*, **131**(4), p. 041018.
- [122] Taslim, M. E., and Lengkong, A., 1998, “45 Deg Staggered Rib Heat Transfer Coefficient Measurements in a Square Channel,” *Journal of Turbomachinery*, **120**(3), pp. 571–580.
- [123] Han, J. C., Glicksman, L. R., and Rohsenow, W. M., 1978, “An Investigation of Heat Transfer and Friction for Rib-Roughened Surfaces,” *International Journal of Heat and Mass Transfer*, **21**(8), pp. 1143–1156.
- [124] Lockett, J. F., and Collins, M. W., 1990, “Holographic Interferometry Applied to Rib-Roughness Heat Transfer in Turbulent Flow,” *International Journal of Heat and Mass Transfer*, **33**(11), pp. 2439–2449.
- [125] Taslim, M. E., and Spring, S. D., 1994, “Effects of Turbulator Profile and Spacing on Heat Transfer and Friction in a Channel,” *Journal of Thermophysics and Heat Transfer*, **8**(3), pp. 555–562.
- [126] Korotky, G. J., and Taslim, M. E., 1998, “Rib Heat Transfer Coefficient Measurements in a Rib-Roughened Square Passage,” *Journal of Turbomachinery*, **120**(2), pp. 376–385.

- [127] Rallabandi, A. P., Alkhamis, N., and Han, J.-C., 2011, “Heat Transfer and Pressure Drop Measurements for a Square Channel With 45 Deg Round-Edged Ribs at High Reynolds Numbers,” *Journal of Turbomachinery*, **133**(3), p. 031019.
- [128] Han, J. C., Zhang, Y. M., and Lee, C. P., 1991, “Augmented Heat Transfer in Square Channels With Parallel, Crossed, and V-Shaped Angled Ribs,” *Journal of Heat Transfer*, **113**(3), pp. 590–596.
- [129] Wright, L. M., Fu, W.-L., and Han, J.-C., 2004, “Thermal Performance of Angled, V-Shaped, and W-Shaped Rib Turbulators in Rotating Rectangular Cooling Channels (AR = 4:1),” p. 10.
- [130] Han, J.-C., Huang, J. J., and Lee, C.-P., 1993, “Augmented Heat Transfer in Square Channels with Wedge-Shaped and Delta-Shaped Turbulence Promoters,” *J Enh Heat Transf*, **1**(1), pp. 37–52.
- [131] Han, J. C., and Zhang, Y. M., 1992, “High Performance Heat Transfer Ducts with Parallel Broken and V-Shaped Broken Ribs,” *International Journal of Heat and Mass Transfer*, **35**(2), pp. 513–523.
- [132] Tanda, G., 2004, “Heat Transfer in Rectangular Channels with Transverse and V-Shaped Broken Ribs,” *International Journal of Heat and Mass Transfer*, **47**(2), pp. 229–243.
- [133] Wolff, J., 2023, “Development of Experimental Methodology to Determine the Heat Transfer of Additively Manufactured Airfoil Channels in a High-Speed Linear Cascade Rig,” The Pennsylvania State University.
- [134] Wang, L., Wang, S., Wen, F., Zhou, X., and Wang, Z., 2018, “Effects of Continuous Wavy Ribs on Heat Transfer and Cooling Air Flow in a Square Single-Pass Channel of Turbine Blade,” *International Journal of Heat and Mass Transfer*, **121**, pp. 514–533.
- [135] Wang, L., Wang, S., Liu, W., Wen, F., Zhou, X., and Wang, Z., 2018, “Numerical Predictions on Heat Transfer and Flow Characteristics in a Straight Channel with Different Geometric Parameters Wavy Ribs,” *Applied Thermal Engineering*, **140**, pp. 245–265.
- [136] Wang, L., Wang, S., Wen, F., Zhou, X., and Wang, Z., 2018, “Heat Transfer and Flow Characteristics of U-Shaped Cooling Channels with Novel Wavy Ribs under Stationary and Rotating Conditions,” *International Journal of Heat and Mass Transfer*, **126**, pp. 312–333.
- [137] Chang, S. W., Liou, T. M., Yu, K.-C., and Huang, S.-S., 2018, “Thermal-Hydraulic Performance of Longitudinal Wavy Rib along Wavy Two-Pass Channel,” *Applied Thermal Engineering*, **133**, pp. 224–236.

- [138] Kilpatrick, E., and Sung, K., 2018, “Roughness Effects on Flow and Heat Transfer in a Ribbed Duct Considering Additive Manufacturing,” *Proceedings of GPPS Forum*, pp. 10–12.
- [139] Corbett, T., Thole, K. A., Ryan, D., Bollapragada, S., Kirka, M. M., and Ledford, C., 2023, “Impacts of Superalloys on the Surface Quality of Additively Manufactured Channels,” p. 13.
- [140] Wildgoose, A. J., Thole, K. A., Tuneskog, E., and Wang, L., 2023, “Roughness Related to Cooling Performance of Channels Made Through Additive Manufacturing,” *ASME Turbo Expo 2023: Turbomachinery Technical Conference and Exposition*, American Society of Mechanical Engineers, p. 14.
- [141] Park, J. S., Han, J. C., Huang, Y., Ou, S., and Boyle, R. J., 1992, “Heat Transfer Performance Comparisons of Five Different Rectangular Channels with Parallel Angled Ribs,” *International Journal of Heat and Mass Transfer*, **35**(11), pp. 2891–2903.
- [142] U.S. Energy Information Administration, 2023, *Electric Power Monthly - May 2023*.
- [143] Martinuzzi, R., and Tropea, C., 1993, “The Flow Around Surface-Mounted, Prismatic Obstacles Placed in a Fully Developed Channel Flow (Data Bank Contribution),” *Journal of Fluids Engineering*, **115**(1), pp. 85–92.
- [144] Schofield, W. H., and Logan, E., 1990, “Turbulent Shear Flow Over Surface Mounted Obstacles,” *Journal of Fluids Engineering*, **112**(4), pp. 376–385.
- [145] Castro, I., Vosper, S., Paisley, M., and Hayden, P., 2001, “Vortex Shedding behind Tapered Obstacles in Neutral & Stratified Flow,” *Dynamics of Atmospheres and Oceans*, **34**(2–4), pp. 145–163.
- [146] Martinuzzi, R. J., and AbuOmar, M., 2003, “Study of the Flow around Surface-Mounted Pyramids,” *Exp Fluids*, **34**(3), pp. 379–389.
- [147] Martinuzzi, R., AbuOmar, M., and Savory, E., 2007, “Scaling of the Wall Pressure Field Around Surface-Mounted Pyramids and Other Bluff Bodies,” *Journal of Fluids Engineering*, **129**(9), pp. 1147–1156.
- [148] Martinuzzi, R. J., 2008, “Dual Vortex Structure Shedding from Low Aspect Ratio, Surface-Mounted Pyramids,” *Journal of Turbulence*, **9**, p. N28.
- [149] Cheng, Y., Sun, J., Chen, P., and Chen, W., 2023, “Experimental Study on near Wake Shedding Structure of Pyramid Roughness Element in Liquid–Solid Two-Phase Turbulent Boundary Layer,” *Experimental Thermal and Fluid Science*, **142**, p. 110814.

- [150] Henze, M., and Von Wolfersdorf, J., 2011, “Influence of Approach Flow Conditions on Heat Transfer behind Vortex Generators,” *International Journal of Heat and Mass Transfer*, **54**(1–3), pp. 279–287.
- [151] Valentino, M., Tran, L., Ricklick, M., and Kapat, J., 2011, “Comparison of Heat Transfer and Friction Augmentation for Symmetric and Non-Symmetric Wedge Turbulators on Two Opposite Walls,” *47th AIAA/ASME/SAE/ASEE Joint Propulsion Conference & Exhibit*, American Institute of Aeronautics and Astronautics, San Diego, California.
- [152] Wildgoose, A. J., A. Thole, K., Subramanian, R., Kersting, L., and Kulkarni, A., 2023, “Impacts of the Additive Manufacturing Process on the Roughness of Engine Scale Vanes and Cooling Channels,” *Journal of Turbomachinery*, **145**(4), p. 041013.
- [153] Wilkins, P. H., Lynch, S. P., and Thole, K. A., 2023, “The Impact of Multi-Scale Ceramic Matrix Composite Roughness on Heat Transfer and Boundary Layer Behavior,” pp. 1–10.
- [154] Sanchez, S., Smith, P., Xu, Z., Gaspard, G., Hyde, C. J., Wits, W. W., Ashcroft, I. A., Chen, H., and Clare, A. T., 2021, “Powder Bed Fusion of Nickel-Based Superalloys: A Review,” *International Journal of Machine Tools and Manufacture*, **165**, p. 103729.
- [155] Gisario, A., Kazarian, M., Martina, F., and Mehrpouya, M., 2019, “Metal Additive Manufacturing in the Commercial Aviation Industry: A Review,” *Journal of Manufacturing Systems*, **53**, pp. 124–149.
- [156] Polonsky, A., Francis, T., Pusch, K., Echlin, M., Botman, A., Randolph, S., Geurts, R., Filevich, J., and Pollock, T., 2020, “3D Characterization of a Novel CoNi-Superalloy for Additive Manufacturing,” *Microsc Microanal*, **26**(S2), pp. 1688–1690.
- [157] Chen, Z., Wu, X., and Davies, C. H. J., 2021, “Process Variation in Laser Powder Bed Fusion of Ti-6Al-4V,” *Additive Manufacturing*, **41**, p. 101987.
- [158] Pakkanen, J., Calignano, F., Trevisan, F., Lorusso, M., Ambrosio, E. P., Manfredi, D., and Fino, P., 2016, “Study of Internal Channel Surface Roughnesses Manufactured by Selective Laser Melting in Aluminum and Titanium Alloys,” *Metall and Mat Trans A*, **47**(8), pp. 3837–3844.
- [159] Wildgoose, A. J., Thole, K. A., Subramanian, R., Kersting, L., and Kulkarni, A., 2022, “Impacts of the Additive Manufacturing Process on the Roughness of Engine Scale Vanes and Cooling Channels,” *Journal of Turbomachinery*, **145**(4), p. 041013.
- [160] Charles, A., Elkaseer, A., Thijs, L., Hagenmeyer, V., and Scholz, S., 2019, “Effect of Process Parameters on the Generated Surface Roughness of Down-Facing Surfaces in Selective Laser Melting,” *Applied Sciences*, **9**(6), p. 1256.

- [161] Calignano, F., Manfredi, D., Ambrosio, E. P., Iuliano, L., and Fino, P., 2013, "Influence of Process Parameters on Surface Roughness of Aluminum Parts Produced by DMLS," *Int J Adv Manuf Technol*, **67**(9–12), pp. 2743–2751.
- [162] Tian, Y., Tomus, D., Rometsch, P., and Wu, X., 2017, "Influences of Processing Parameters on Surface Roughness of Hastelloy X Produced by Selective Laser Melting," *Additive Manufacturing*, **13**, pp. 103–112.
- [163] Snyder, J. C., and Thole, K. A., 2020, "Effect of Additive Manufacturing Process Parameters on Turbine Cooling," *J Turbomach*, **142**(5), p. 051007.
- [164] Malekipour, E., and El-Mounayri, H., 2018, "Common Defects and Contributing Parameters in Powder Bed Fusion AM Process and Their Classification for Online Monitoring and Control: A Review," *Int J Adv Manuf Technol*, **95**(1–4), pp. 527–550.
- [165] Wang, D., Liu, Y., Yang, Y., and Xiao, D., 2016, "Theoretical and Experimental Study on Surface Roughness of 316L Stainless Steel Metal Parts Obtained through Selective Laser Melting," *RPJ*, **22**(4), pp. 706–716.
- [166] Zhang, T., and Yuan, L., 2022, "Understanding Surface Roughness on Vertical Surfaces of 316 L Stainless Steel in Laser Powder Bed Fusion Additive Manufacturing," *Powder Technology*, **411**, p. 117957.
- [167] Charles, A., Elkaseer, A., Paggi, U., Thijs, L., Hagenmeyer, V., and Scholz, S., 2021, "Down-Facing Surfaces in Laser Powder Bed Fusion of Ti6Al4V: Effect of Dross Formation on Dimensional Accuracy and Surface Texture," *Additive Manufacturing*, **46**, p. 102148.
- [168] Zhou, Y. H., Zhang, Z. H., Wang, Y. P., Liu, G., Zhou, S. Y., Li, Y. L., Shen, J., and Yan, M., 2019, "Selective Laser Melting of Typical Metallic Materials: An Effective Process Prediction Model Developed by Energy Absorption and Consumption Analysis," *Additive Manufacturing*, **25**, pp. 204–217.
- [169] Bassoli, E., Sola, A., Celesti, M., Calcagnile, S., and Cavallini, C., 2018, "Development of Laser-Based Powder Bed Fusion Process Parameters and Scanning Strategy for New Metal Alloy Grades: A Holistic Method Formulation," *Materials*, **11**(12), p. 2356.
- [170] Kirsch, K. L., Snyder, J. C., Stimpson, C. K., Thole, K. A., and Mongillo, D., 2017, "Repeatability in Performance of Micro Cooling Geometries Manufactured with Laser Powder Bed Fusion," *53rd AIAA/SAE/ASEE Joint Propulsion Conference*, American Institute of Aeronautics and Astronautics, Atlanta, GA.
- [171] Murray, S. P., Pusch, K. M., Polonsky, A. T., Torbet, C. J., Seward, G. G. E., Zhou, N., Forsik, S. A. J., Nandwana, P., Kirka, M. M., Dehoff, R. R., Slye, W. E., and Pollock, T.

- M., 2020, “A Defect-Resistant Co–Ni Superalloy for 3D Printing,” *Nat Commun*, **11**(1), p. 4975.
- [172] Murray, S. P., Raeker, E. B., Pusch, K. M., Frey, C., Torbet, C. J., Zhou, N., Forsik, S. A. J., Dicus, A. D., Colombo, G. A., Kirka, M. M., and Pollock, T. M., 2022, “Microstructure Evolution and Tensile Properties of a Selectively Laser Melted CoNi-Base Superalloy,” *Metall Mater Trans A*, **53**(8), pp. 2943–2960.
- [173] Zhou, N., Dicus, A. D., Forsik, S. A. J., Wang, T., Colombo, G. A., and Epler, M. E., 2020, “Development of a New Alumina-Forming Crack-Resistant High- Γ' Fraction Ni-Base Superalloy for Additive Manufacturing,” *Superalloys 2020*, Springer International Publishing, Cham, pp. 1046–1054.
- [174] Uriati, F., and Nicoletto, G., 2022, “A Comparison of Inconel 718 Obtained with Three L-PBF Production Systems in Terms of Process Parameters, as-Built Surface Quality, and Fatigue Performance,” *International Journal of Fatigue*, **162**, p. 107004.
- [175] Breuer, H., 2021, “Printing Parts for Gas Turbines Is about to Get Easy,” *Seimens Energy*.
- [176] Dowling, L., Kennedy, J., O’Shaughnessy, S., and Trimble, D., 2020, “A Review of Critical Repeatability and Reproducibility Issues in Powder Bed Fusion,” *Materials & Design*, **186**, p. 108346.
- [177] Yadroitsev, I., and Smurov, I., 2011, “Surface Morphology in Selective Laser Melting of Metal Powders,” *Physics Procedia*, **12**, pp. 264–270.
- [178] Calignano, F., Manfredi, D., Ambrosio, E. P., Iuliano, L., and Fino, P., 2013, “Influence of Process Parameters on Surface Roughness of Aluminum Parts Produced by DMLS,” *Int J Adv Manuf Technol*, **67**(9), pp. 2743–2751.
- [179] Cherry, J. A., Davies, H. M., Mehmood, S., Lavery, N. P., Brown, S. G. R., and Sienz, J., 2015, “Investigation into the Effect of Process Parameters on Microstructural and Physical Properties of 316L Stainless Steel Parts by Selective Laser Melting,” *Int J Adv Manuf Technol*, **76**(5), pp. 869–879.
- [180] Whip, B., Sheridan, L., and Gockel, J., 2019, “The Effect of Primary Processing Parameters on Surface Roughness in Laser Powder Bed Additive Manufacturing,” *International Journal of Advanced Manufacturing Technology*, **103**(9–12), pp. 4411–4422.
- [181] Mumtaz, K., and Hopkinson, N., 2009, “Top Surface and Side Roughness of Inconel 625 Parts Processed Using Selective Laser Melting,” *Rapid Prototyping Journal*, **15**(2), pp. 96–103.
- [182] Sanaei, N., Fatemi, A., and Phan, N., 2019, “Defect Characteristics and Analysis of Their Variability in Metal L-PBF Additive Manufacturing,” *Materials & Design*, **182**, p. 108091.

- [183] Dunbar, A. J., Denlinger, E. R., Gouge, M. F., Simpson, T. W., and Michaleris, P., 2017, “Comparisons of Laser Powder Bed Fusion Additive Manufacturing Builds through Experimental in Situ Distortion and Temperature Measurements,” *Additive Manufacturing*, **15**, pp. 57–65.
- [184] Clark, C. L., Karasz, E. K., Melia, M., Hooks, D. E., Hackenberg, R., Colon-Mercado, H., Ganesan, P., Renner, P., Cho, S., Wu, M., Qiu, S. R., Dwyer, J., Rueger, Z., Gorey, T. J., Koehn, Z., and Stull, J. A., 2023, “Machine-to-Machine Variability of Roughness and Corrosion in Additively Manufactured 316L Stainless Steel,” *Journal of Manufacturing Processes*, **106**, pp. 380–392.
- [185] Yasa, E., Demir, F., Akbulut, G., Cizioglu, N., and Pilatin, S., 2014, “Benchmarking of Different Powder-Bed Metal Fusion Processes for Machine Selection in Additive Manufacturing,” *International Solid Freeform Fabrication Symposium*.
- [186] Spierings, A. B., Herres, N., and Levy, G., 2011, “Influence of the Particle Size Distribution on Surface Quality and Mechanical Properties in AM Steel Parts,” *Rapid Prototyping Journal*, **17**(3), pp. 195–202.
- [187] Lim, J. H., and Khan, N. A., 2019, “Effects of Particle Size Distribution on Surface Finish of Selective Laser Melting Parts,” *University of Texas at Austin*.
- [188] Mussatto, A., Groarke, R., O’Neill, A., Ahmed Obeidi, M., Delaure, Y., and Brabazon, D., 2021, “Influences of Powder Morphology and Spreading Parameters on the Powder Bed Topography Uniformity in Powder Bed Fusion Metal Additive Manufacturing,” *Additive Manufacturing*, **38**, p. 101807.
- [189] Huck-Jones, D., and Langley, C., 2017, “Beyond Particle Size: Exploring the Influence of Particle Shape on Metal Powder Performance,” *Metal Additive Manufacturing*, **3**(4), pp. 99–103.
- [190] Strondl, A., Lyckfeldt, O., Brodin, H., and Ackelid, U., 2015, “Characterization and Control of Powder Properties for Additive Manufacturing,” *JOM*, **67**(3), pp. 549–554.
- [191] Lüddecke, A., Pannitz, O., Zetzener, H., Sehrt, J. T., and Kwade, A., 2021, “Powder Properties and Flowability Measurements of Tailored Nanocomposites for Powder Bed Fusion Applications,” *Materials & Design*, **202**, p. 109536.
- [192] Cordova, L., Campos, M., and Tinga, T., 2019, “Revealing the Effects of Powder Reuse for Selective Laser Melting by Powder Characterization,” *JOM*, **71**(3), pp. 1062–1072.
- [193] Yi, F., Zhou, Q., Wang, C., Yan, Z., and Liu, B., 2021, “Effect of Powder Reuse on Powder Characteristics and Properties of Inconel 718 Parts Produced by Selective Laser Melting,” *Journal of Materials Research and Technology*, **13**, pp. 524–533.

- [194] Coupons Manufactured In Collaboration with Oak Ridge National Laboratories, 2022, .
- [195] Coupons Manufactured In Collaboration with Carpenter Technologies, 2022, .
- [196] Coupons Manufactured In Collaboration with Center for Innovative Materials Processing through Direct Digital Deposition, 2020, .
- [197] Coupons Manufactured In Collaboration with 3D Systems, 2023, .
- [198] Coupons Manufactured In Collaboration with Vertex Manufacturing, 2023, .
- [199] Song, J., Tang, Q., Setchi, R., and Ryan, M., 2023, “A Comparative Study of Pulse Wave and Continuous Wave Laser Patterns During Laser Powder Bed Fusion,” *Sustainable Design and Manufacturing*, S.G. Scholz, R.J. Howlett, and R. Setchi, eds., Springer Nature Singapore, pp. 283–290.
- [200] Stimpson, C. K., Snyder, J. C., Thole, K. A., and Mongillo, D., 2017, “Scaling Roughness Effects on Pressure Loss and Heat Transfer of Additively Manufactured Channels,” *Journal of Turbomachinery*, **139**(2), p. 021003.
- [201] Flack, K. A., and Schultz, M. P., 2010, “Review of Hydraulic Roughness Scales in the Fully Rough Regime,” *Journal of Fluids Engineering*, **132**(4), p. 041203.
- [202] Arie, M. A., Shooshtari, A. H., and Ohadi, M. M., 2018, “Experimental Characterization of an Additively Manufactured Heat Exchanger for Dry Cooling of Power Plants,” *Applied Thermal Engineering*, **129**, pp. 187–198.
- [203] Wildgoose, A. J., and Thole, K. A., 2023, “Heat Transfer and Pressure Loss of Additively Manufactured Internal Cooling Channels With Various Shapes,” *Journal of Turbomachinery*, **145**(7), p. 071011.

Appendices

A. PRELIMINARY LATTICE STRUCTURE SCALING RESULTS

In recent years there has been several groups who have begun to investigate the cooling performance of AM lattice structures. Given the broad definition of what a lattice structure is, there have been many different forms of implementation. Liang et al. [83] implemented several lattice shapes, including a BCC and Kagome lattice, in a staggered arrangement similar to pin fins, in addition to two other lattice types that were integrated into a test coupon in an inline arrangement similar to this study. Aider et al. [95] has also studied the thermal-fluid performance of several types of lattice, but as a three-dimensional grid with unit cells of approximately 10mm. Both studies scaled their results using a channel friction factor definition, which is shown in Equation A-1.

$$f_{channel} = \frac{\Delta P}{0.5 \cdot \rho \cdot u_m^2} \cdot \frac{D_h}{L} \quad (A - 1)$$

For this definition, the mass average inlet velocity is used as the velocity scaling, and the channel hydraulic diameter over the coupon length is used as the length scale.

The author of this dissertation also investigated several lattice structures. In Chapter 4, a detailed CFD study was presented that explored the performance of Body Centered Cubic (BCC) and Kagome lattices. In addition to the two metal additive coupons used for experimental validation in Chapter 4, several other metal additive coupons featuring the same BCC and Kagome lattice geometry were printed which varied the lattice porosity that were not included in the results of that Chapter. The friction factor from these additional coupons, as defined using the Equation A-1, was compared to the results from literature, and are shown in Figure A-1.

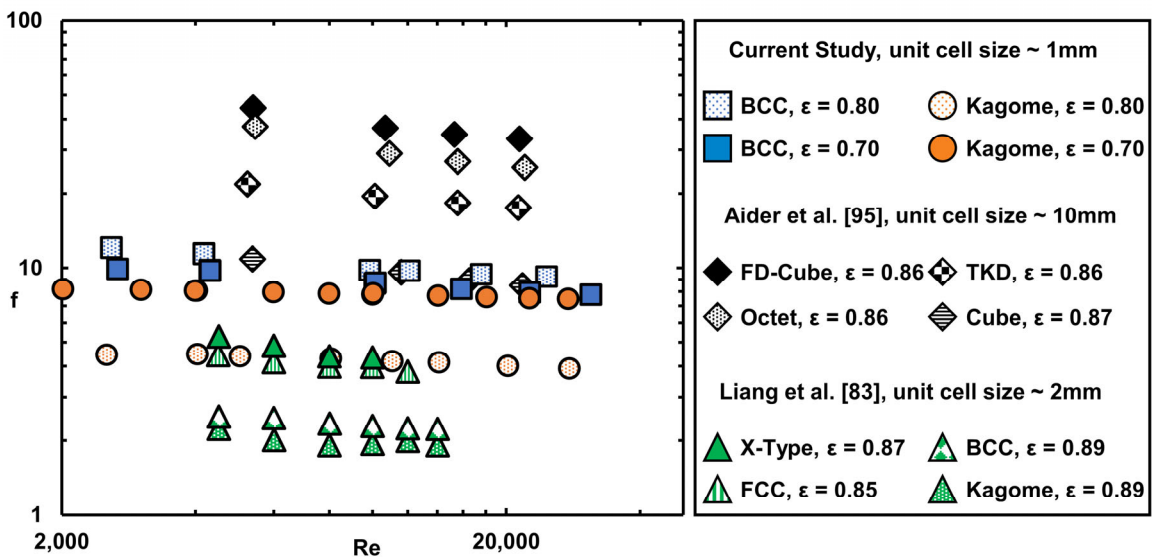


Figure A-1. Friction factor data from the current study compared against literature.

There is an evident difference in performance between the three studies, especially when comparing the results of the large scale designs studied by Aider et al. [95] to those found by the author. It was hypothesized that this order of magnitude difference in results was because this definition of friction factor did not appropriately scale the pressure loss results, rather than a true difference in friction factor as a function of the lattice design and porosity. It was further hypothesized that geometrically similar larger lattice structure designs would result in larger values of friction factor. While the unit cells built by Liang et al. [83] were slightly larger than those studied by the author, the sparse arrangement of lattice was anticipated to significantly reduce the pressure drop and resulting friction factor.

To test this hypothesis, three new test coupons were built on a stereolithography (SLA) printer, whose as-built surfaces were assumed to be hydrodynamically smooth. A diagram of these three coupons can be seen in Figure A-2. The lattice integrated into these test coupons was a Kagome lattice, as was studied in Chapter 4. The 1x scale test coupon matched the same design intent that was used in the Chapter 4, however the upstream and downstream open channel regions were removed from the test coupon design, and the coupon was instead fully dense with 10 rows of lattice structures. The porosity of the Kagome lattice was defined as 0.3 to reduce the error associated with printing the test coupons at the 1x scale, as was found in Chapter 4. All coupons were printed on the same build plate at the same time out of a gray plastic developed by the printer manufacturer.

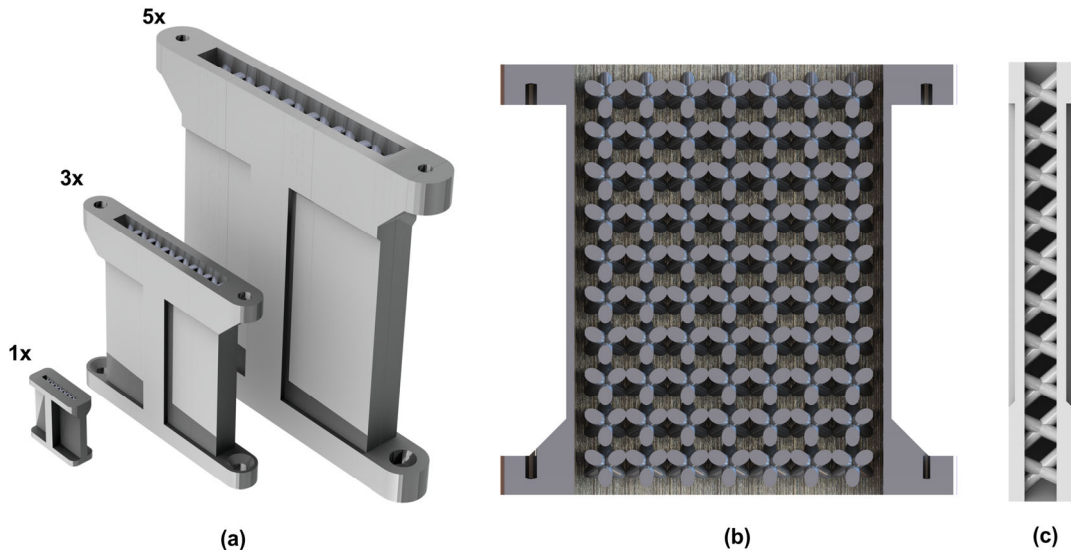


Figure A-2. (a) The three scales of test coupons used for characterizing the performance of the lattice structures, with a view of the internals with the (b) top surface and (c) side wall removed.

The three test coupons were evaluated in the same test rig that was described in prior chapters, using the scaled plenums discussed in Chapter 6. As mentioned in that chapter, the rig

was benchmarked using a coupon featuring straight cylindrical channels which agreed within 5% of the Colebrook correlation. The test coupons were tested over a range of Reynolds numbers to determine pressure drop. The pressure drop for these test coupons were normalized in two ways: first using the definition shown in Equation A-1, and then again using a definition more similar to the definition used to scale pin fin array pressure loss which is presented in Equation A-2.

$$f_{lattice} = \frac{\Delta P}{0.5 \cdot \rho \cdot u_{max}^2} \cdot \frac{1}{N} \quad (A - 2)$$

For this scaling the maximum velocity in the lattice structure is determined using the minimum flow area, which is estimated by subtracting the frontal area of the lattice from the cross-sectional area of the duct. Instead of normalizing using the length of the coupon and duct hydraulic diameter, the results are instead normalized using the number of rows of lattice structures along the flow direction. Equation A-2 is normalized in this way because the disruption from a given row of lattice was anticipated to be the primary contributor to pressure loss. In addition to the friction factor, the Reynolds number for the lattice structures was also redefined to be more consistent with the pin fin definition, as shown in Equation A-3.

$$Re_{lattice} = \frac{u_{max} \cdot \rho \cdot D_{pore}}{\mu} \quad (A - 3)$$

D_{pore} in Equation A-3 was defined as the maximum pore diameter, which was shown by Aider et al. [95] to better scale the Nusselt number results in their study. For the Kagome lattice, this maximum pore diameter is the duct height. The results normalized using the channel and lattice definitions are shown in Figure A-3 for the coupons built at three different scales.

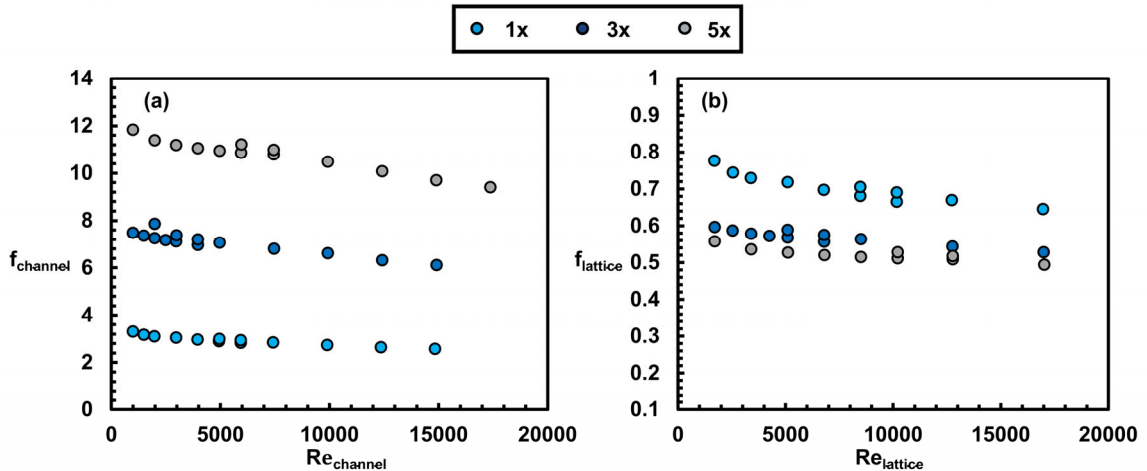


Figure A-3. Scaling the friction factor of the lattice designs using (a) channel definitions and (b) proposed lattice definitions.

Starting with the channel definitions shown in Figure A-3(a), the scale of the test coupon had a clear impact on the friction factor. If the performance was scaled appropriately, the friction

factor should be uniform for a given Reynolds number, regardless of geometric scale. This increase in friction factor as a function of scale is an important determination for the thermos-fluids community, as it makes comparisons between studies reliant on the compared studies sharing not only the same definition of friction factor, but also the same scale.

Leveraging the pin fin definitions shown in Equation A-2 and A-3 shows much better agreement between the coupons of different scales, particularly between the 3x and 5x scale test coupons. The 1x test coupon has an approximately 15% greater friction factor than the 3x coupons for the entire range of Reynolds numbers tested. It is suspected that this discrepancy is the result of the as-printed coupon deviating from the design intent, as the strut diameters and sizes for the 1x coupon approached the limitations of what could reliably be printed. A similar discrepancy between the as-built and as-design test coupon was previously found in the local pressure drop coupons discussed in Chapter 4.

Moving forward, additional work is required to validate the use of these lattice structure definitions for a broader range of lattice structures. Future work should particularly focus on not only comparisons of strut-based lattice, but also include triply periodic minimal surface (TPMS) lattice structures. Additionally, this same style of scaling should be applied to the heat transfer performance of lattice geometry at different scales, to ensure the scaling as proposed by Aider et al. [95] holds for different geometric scales.

B. COMPARISONS TO PRIOR LITERATURE

There are a multitude of different studies who have investigated the performance of both additive and traditional cooling technologies previously in literature. The goal of this appendix is to offer a point of comparison for the data collected in this body of work against that of prior researchers. This was accomplished by using a series of augmentation plots, similar to what was used in the final chapter of this dissertation. The geometries in this section are split into four parts, pin fin arrays (Figure B-1), surface features (Figure B-2), lattice structures (Figure B-3), and channels, including both wavy and non-wavy channels (Figure B-4).

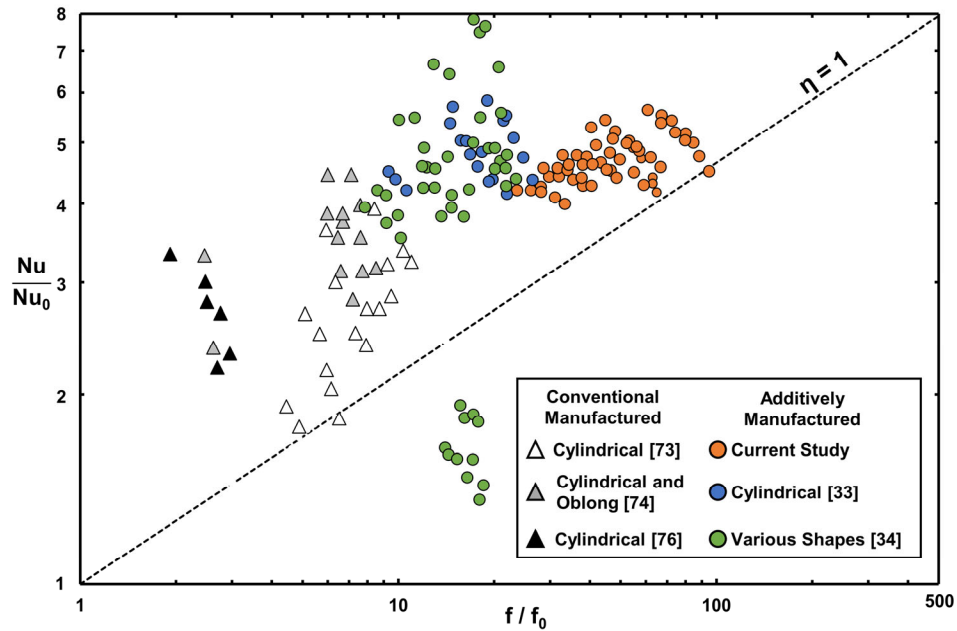


Figure B-1. Augmentation plot of pin fin data from the current study compared against data from literature.

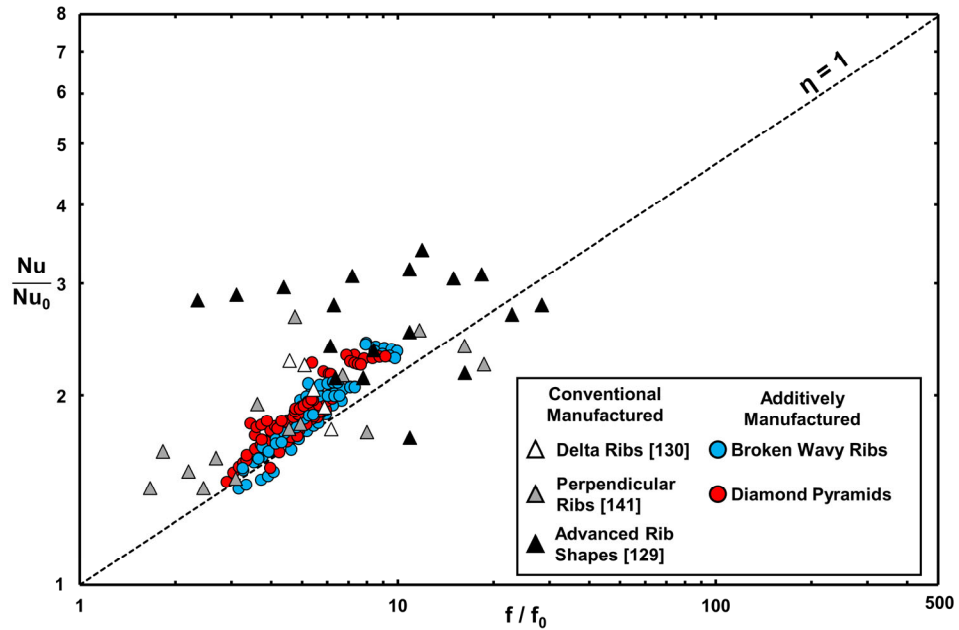


Figure B-2. Augmentation plot of surface feature data from the current study compared against data from literature.

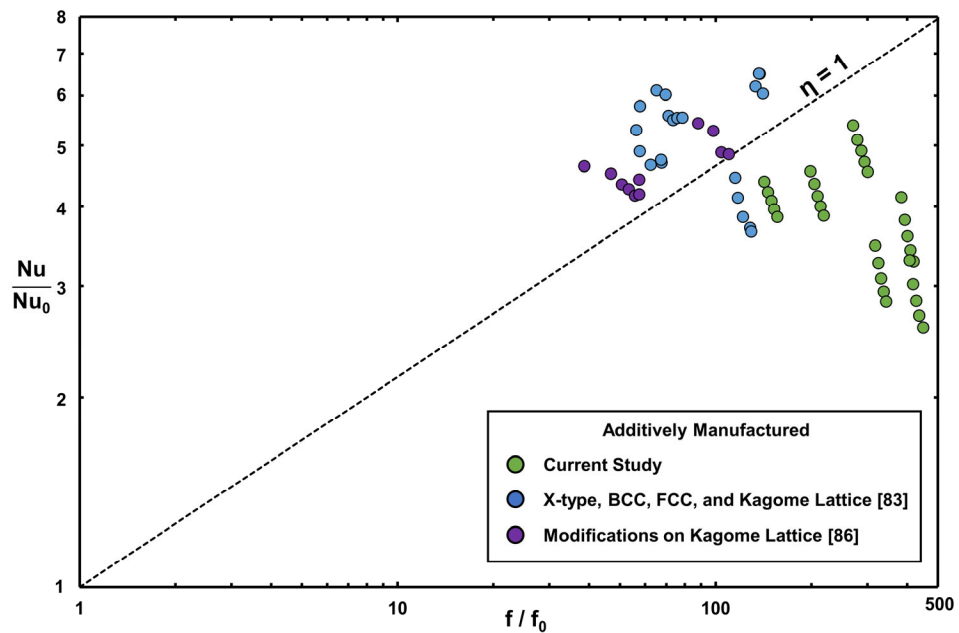


Figure B-3. Augmentation plot of lattice structure data from the current study compared against data from literature.

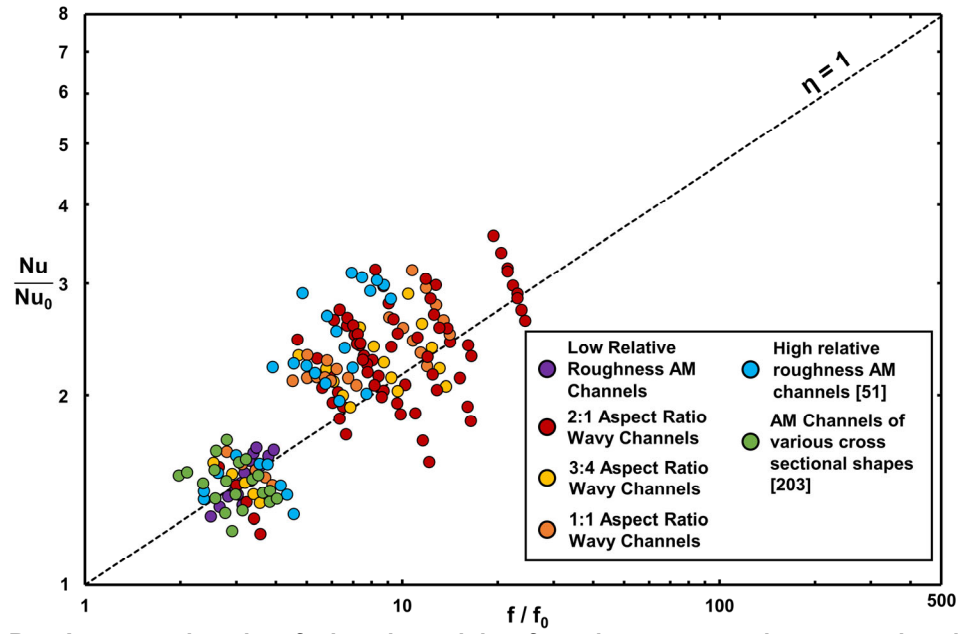


Figure B-4. Augmentation plot of microchannel data from the current study compared against data from literature.

C. UNCERTAINTY CALCULATIONS

Uncertainty Nomenclature

A_c	cross sectional area
D_h	hydraulic diameter
h	convection coefficient
H	channel Height
I	electrical current
k	thermal conductivity
L	channel Length
\dot{m}	mass flow rate
N	number of channels
P	perimeter
P_{atm}	atmospheric pressure
P_{gauge}	gauge pressure
ΔP	pressure drop across the test coupon
Q	heat
Q_{loss}	loss heat to the test rig
R	resistance
R_{cond}	conduction resistance
t	thickness
T	temperature
ΔT_{LMTD}	log mean temperature difference
u	mass averaged velocity
V	voltage
W	Channel Width
Greek	
μ	dynamic viscosity
ρ	density
Subscripts	
cu	copper
coupon	test coupon
far	thermocouple farthest from the test coupon
foam ₁	located in the first foam block
foam ₂	located in the second foam block

in	at the inlet of the test coupon
near	thermocouple nearest to the test coupon
out	at the outlet of the test coupon
plenum ₁	located in the first plenum
plenum ₂	located in the second plenum
s	surface
tp	thermal paste

Uncertainty Calculations

For each data point that was calculated for every paper discussed in this dissertation, an uncertainty analysis was conducted, using the propagation of uncertainty as described by Dunn[57]. This uncertainty analysis was integrated into the core data processing code that was used for analyzing all experimental data, facilitating calculation of uncertainty for each data set. Generally speaking, there were three properties of interest in the prior studies: Reynolds number, the friction factor, and the Nusselt number. These three numbers are defined below in Equations B-1, B-2, and B-3.

$$Re = \frac{\rho u D_h}{\mu} \quad (B - 1)$$

$$f = \frac{\Delta P}{0.5 \cdot \rho \cdot u^2} \cdot \frac{D_h}{L} \quad (B - 2)$$

$$Nu = \frac{h D_h}{k} \quad (B - 3)$$

However, almost all of the properties shown in these equations are functions of other variables themselves, and as such the equations need to be expanded to be defined in terms of the measured quantities. These expanded forms for the Reynolds number and friction factor can be found in Equations B-4, and B-5.

$$Re = \frac{2\dot{m}}{\mu(W + H)} \quad (B - 4)$$

$$f = \frac{4 \cdot \Delta P \cdot (H \cdot W)^3}{(H + W) \cdot L \cdot \dot{m}} \cdot \left[(P_{gauge} + P_{atm}) \cdot \left(\frac{1}{T_{in}} + \frac{1}{T_{out}} \right) - \frac{\Delta P}{T_{out}} \right] \quad (B - 5)$$

While equation A-3 may appear to be the simplest of the three key parameters, it is in fact the most complex to calculate, as it depends on many variables. As such the equation has been broken into several parts for clarity, as shown in Equations B-6 through B-14.

$$h = \frac{Q - Q_{loss}}{(L \cdot (2N \cdot (W + H))) \cdot \Delta T_{LMTD}} \quad (B - 6)$$

$$Q = I_1 \cdot V_{power,1} + I_2 \cdot V_{power,2} = \frac{V_{resistor,1} \cdot V_{power,1}}{R_{resistor,1}} + \frac{V_{resistor,2} \cdot V_{power,2}}{R_{resistor,2}} \quad (B - 7)$$

$$Q_{loss} = Q_{loss,plenum_1} + Q_{loss,plenum_2} + Q_{loss,foam_1} + Q_{loss,foam_2} \quad (B - 8)$$

$$Q_{loss,plenum_1} = \frac{A_{c,Plenum_1}}{k_{nylon} \cdot (T_{near,plenum_1} - T_{far,plenum_1})} \quad (B - 9)$$

$$Q_{loss,plenum_2} = \frac{A_{c,Plenum_2}}{k_{nylon} \cdot (T_{near,plenum_2} - T_{far,plenum_2})} \quad (B - 10)$$

$$Q_{loss,foam_1} = \frac{A_{c,foam,1}}{k_{foam} \cdot (T_{near,foam,1} - T_{far,foam,1})} \quad (B - 11)$$

$$Q_{loss,foam_2} = \frac{A_{c,foam,2}}{k_{foam} \cdot (T_{near,foam,2} - T_{far,foam,2})} \quad (B - 12)$$

$$\Delta T_{LMTD} = \frac{T_{in} - T_{out}}{\ln \left[\frac{\bar{T}_s - T_{out}}{\bar{T}_s - T_{in}} \right]} \quad (B - 11)$$

$$\bar{T}_s = \frac{T_{s,1} + T_{s,2}}{2} \quad (B - 12)$$

$$T_{s,1} = T_{cu,1} - R_{cond} \cdot \left(Q_{loss,foam_1} + \frac{Q_{loss,plenum_1} + Q_{loss,plenum_2}}{2} \right) \quad (B - 13)$$

$$T_{s,2} = T_{cu,2} - R_{cond} \cdot \left(Q_{loss,foam_2} + \frac{Q_{loss,plenum_1} + Q_{loss,plenum_2}}{2} \right) \quad (B - 13)$$

$$R_{cond} = \frac{t_{cu}}{k_{cu} \cdot A_{c,cu}} + \frac{t_{tp}}{k_{tp} \cdot A_{c,tp}} + \frac{t_{coupon}}{k_{coupon} \cdot A_{c,coupon}} \quad (B - 14)$$

In order to calculate the uncertainty for these equations, the root sum square of the first derivative of each parameter multiplied by the uncertainty in that parameter is taken. An example of this method is shown in equation B-15 for the Reynolds number.

$$U_{Re} = \sqrt{\left(\frac{\partial Re}{\partial \dot{m}} \cdot U_{\dot{m}} \right)^2 + \left(\frac{\partial Re}{\partial W} \cdot U_W \right)^2 + \left(\frac{\partial Re}{\partial H} \cdot U_H \right)^2 + \left(\frac{\partial Re}{\partial \mu} \cdot U_{\mu} \right)^2} \quad (B - 15)$$

As an example, the uncertainties and partial derivatives for a Reynolds numbers of 5,000 and 15,000 for a wavy channel geometry are shown in Table C-1 and Table C-2.

Table C-1. Uncertainty Contributions For Reynolds Number at a Reynolds Number of 5,000

Variable	Value of Partial Differential [1/units]	Uncertainty	Contribution
\dot{m} [kg/s]	4.252E+06	2.91E-05	77.9%
W [m]	-1.746E+06	1.75E-05	4.8%
H [m]	-1.746E+06	1.75E-05	4.8%
Mu [m·s/kg]	-2.691E+08	1.84E-07	12.5%
Total Uncertainty	2.80%		

Table C-2. Uncertainty Contributions For Reynolds Number at a Reynolds Number of 15,000

Variable	Value of Partial Differential [1/units]	Uncertainty	Contribution
\dot{m} [kg/s]	4.26E+06	2.91E-05	51.5%
W [m]	-5.24E+06	1.75E-05	10.5%
H [m]	-5.24E+06	1.75E-05	10.5%
Mu [m·s/kg]	-8.09E+08	1.84E-07	27.6%
Total Uncertainty	1.9%		

The contribution to total uncertainty was determined by taking the sum of each of the elements under the square root, and normalizing each partial derivative-uncertainty value pair by the total sum.

Equation B-16 was used to determine the uncertainty in the friction factor.

$$U_f = \sqrt{\left(\frac{\partial f}{\partial \dot{m}} \cdot U_{\dot{m}}\right)^2 + \left(\frac{\partial f}{\partial W} \cdot U_W\right)^2 + \left(\frac{\partial f}{\partial H} \cdot U_H\right)^2 + \left(\frac{\partial f}{\partial \Delta P} \cdot U_{\Delta P}\right)^2 + \dots} \quad (B - 16)$$

$$\left(\frac{\partial f}{\partial L} \cdot U_L\right)^2 + \left(\frac{\partial f}{\partial P_g} \cdot U_{P_g}\right)^2 + \left(\frac{\partial f}{\partial P_{atm}} \cdot U_{P_{atm}}\right)^2 + \dots$$

$$\left(\frac{\partial f}{\partial T_{in}} \cdot U_{T_{in}}\right)^2 + \left(\frac{\partial f}{\partial T_{out}} \cdot U_{T_{out}}\right)^2$$

As an example for determining the uncertainty in friction factor, the uncertainties associated with friction factor for a wavy channel at a Reynolds number of 5,000 and 15,000 are shown in Table C-3 and Table C-4.

Table C-3. Uncertainty Contributions For Friction Factor at a Reynolds Number of 5,000

Variable	Value of Partial Differential [1/units]	Uncertainty	Contribution
P_a [Pa]	1.26E-06	5515.808	24.9%
P_g [Pa]	1.26E-06	2585.535	5.5%
ΔP [Pa]	1.07E-05	172.3689	1.8%
W [m]	182.6042	1.75E-05	5.3%
H [m]	452.7293	1.75E-05	32.5%
\dot{m} [kg/s]	-261.64	2.91E-05	30.0%
R [J/kg/mol]	-0.00053	0.01	0.0%
Coupon Outlet Temperature [K]	-0.00024	1.00	0.0%
Coupon Inlet Temperature [K]	-0.00027	1.00	0.0%
Channel Length [m]	-2.68291	2.54E-05	0.0%
Total			9.2%

Table C-4. Uncertainty Contributions For Friction Factor at a Reynolds Number of 15,000

Variable	Value of Partial Differential [1/units]	Uncertainty	Contribution
P_a [Pa]	4.75E-07	5.52E+03	6.0%
P_g [Pa]	4.75E-07	2.59E+03	1.3%
ΔP [Pa]	3.37E-06	4.31E+02	1.8%
W [m]	1.96E+02	1.75E-05	10.3%
H [m]	4.87E+02	1.75E-05	63.0%
\dot{m} [kg/s]	-9.40E+01	4.76E-05	17.4%
R [J/kg/mol]	-5.71E-04	1.00E-02	0.0%
Coupon Outlet Temperature [K]	-2.61E-04	1.00E+00	0.1%
Coupon Inlet Temperature [K]	-2.98E-04	1.00E+00	0.1%
Channel Length [m]	-2.88E+00	2.54E-05	0.0%
Total			6.6%

Given the significant number of variables that lead to uncertainty in the Nusselt number definition, the uncertainty calculations are broken into two parts, first uncertainty in the coupon surface temperature, and then uncertainty in the Nusselt number. Given the number of variables included in the equation for uncertainty in the surface temperature of the test coupon, an abbreviated form of the equation is shown in Equation B-17.

$$U_{T_{coupon}} = \sqrt{\left(\frac{\partial T_{coupon}}{\partial W} \cdot U_W\right)^2 + \left(\frac{\partial T_{coupon}}{\partial H} \cdot U_H\right)^2 + \dots \left(\frac{\partial T_{coupon}}{\partial Variable} \cdot U_{Variable}\right)^2 + \dots + \left(\frac{\partial T_{coupon}}{\partial T_{cu,1}} \cdot U_{T_{cu,1}}\right)^2 + \left(\frac{\partial T_{coupon}}{\partial T_{cu,2}} \cdot U_{T_{cu,2}}\right)^2} \quad (B - 17)$$

An example of the calculated uncertainty of the coupon surface temperature at a Reynolds number of 10,000 and 30,000 for a wavy channel geometry are shown in Table C-5 and Table C-6.

Table C-5. Uncertainty Contributions For Coupon Surface Temperature at a Reynolds Number of 10,000

Variable	Value of Partial Differential [K/units]	Uncertainty	Contribution
Heater 1 Voltage [V]	-3.36E-02	5.00E-04	0.0%
Heater 2 Voltage [V]	-3.33E-02	5.00E-04	0.0%
Heater 1 Resistor Voltage [V]	-1.38E+01	1.00E-04	0.0%
Heater 2 Resistor Voltage [V]	-1.33E+01	1.00E-04	0.0%
Heater Resistor Resistance [Ohm]	3.19E+01	1.00E-04	0.0%
Plenum Loss Area [m ²]	-9.73E+01	5.40E-07	0.0%
Inlet Plenum, Loss TC 1 [K]	1.42E-03	1.00E+00	0.0%
Inlet Plenum, Loss TC 2 [K]	-1.42E-03	1.00E+00	0.0%
Plenum Thickness [m ²]	6.95E+00	2.54E-05	0.0%
Plenum Thermal Conductivity [W/mK]	-3.15E-02	7.00E-03	0.0%
Outlet Plenum, Loss TC 1 [K]	-1.42E-03	1.00E+00	0.0%
Outlet Plenum, Loss TC 2 [K]	1.42E-03	1.00E+00	0.0%
Foam Cross Section [m ²]	1.42E+00	1.50E-06	0.0%
Foam Thermal Conductivity [W/mK]	3.33E-02	5.40E-04	0.0%
Foam 1, Loss TC 1 [K]	3.06E-04	1.00E+00	0.0%
Foam 1, Loss TC 2 [K]	-3.06E-04	1.00E+00	0.0%
Foam 2, Loss TC 1 [K]	3.06E-04	1.00E+00	0.0%
Foam 2, Loss TC 2 [K]	-3.06E-04	1.00E+00	0.0%
Foam Thermocouple Distance [m]	-2.83E-01	2.54E-05	0.0%
Copper Thickness[m]	-5.78E+01	2.54E-05	0.0%
Copper Thermal Conductivity [W/mK]	9.54E-04	3.85E+00	0.0%
Copper Cross Sectional Area [m ²]	2.53E+03	1.50E-06	0.0%
Thermal Paste Thickness [m]	-1.93E+04	2.54E-05	32.1%
Thermal Paste Conductivity [W/mK]	2.12E-01	2.31E-02	0.0%
Coupon Thickness [m]	-4.45E+03	1.75E-05	0.8%
Coupon Thermal Conductivity [W/mK]	2.35E-01	1.00E-01	0.1%
Fore Copper Temperatures [K]	5.00E-01	1.00E+00	33.5%
Aft Copper Temperatures [K]	5.00E-01	1.00E+00	33.5%
Total			1.1%

Table C-6. Uncertainty Contributions For Coupon Surface Temperature at a Reynolds Number of 30,000

Variable	Value of Partial Differential [K/units]	Uncertainty	Contribution
Heater 1 Voltage [V]	-4.10E-02	5.00E-04	0.0%
Heater 2 Voltage [V]	-4.13E-02	5.00E-04	0.0%
Heater 1 Resistor Voltage [V]	-1.60E+01	1.00E-04	0.0%
Heater 2 Resistor Voltage [V]	-1.58E+01	1.00E-04	0.0%
Heater Resistor Resistance [Ohm]	4.61E+01	1.00E-04	0.0%
Plenum Loss Area [m ²]	-5.63E+01	5.40E-07	0.0%
Inlet Plenum, Loss TC 1 [K]	1.42E-03	1.00E+00	0.0%
Inlet Plenum, Loss TC 2 [K]	-1.42E-03	1.00E+00	0.0%
Plenum Thickness [m ²]	4.03E+00	2.54E-05	0.0%
Plenum Thermal Conductivity [W/mK]	-1.82E-02	7.00E-03	0.0%
Outlet Plenum, Loss TC 1 [K]	-1.42E-03	1.00E+00	0.0%
Outlet Plenum, Loss TC 2 [K]	1.42E-03	1.00E+00	0.0%
Foam Cross Section [m ²]	1.00E+00	1.50E-06	0.0%
Foam Thermal Conductivity [W/mK]	2.35E-02	5.40E-04	0.0%
Foam 1, Loss TC 1 [K]	3.06E-04	1.00E+00	0.0%
Foam 1, Loss TC 2 [K]	-3.06E-04	1.00E+00	0.0%
Foam 2, Loss TC 1 [K]	3.06E-04	1.00E+00	0.0%
Foam 2, Loss TC 2 [K]	-3.06E-04	1.00E+00	0.0%
Foam Thermocouple Distance [m]	-2.00E-01	2.54E-05	0.0%
Copper Thickness[m]	-8.33E+01	2.54E-05	0.0%
Copper Thermal Conductivity [W/mK]	1.37E-03	3.85E+00	0.0%
Copper Cross Sectional Area [m ²]	3.65E+03	1.50E-06	0.0%
Thermal Paste Thickness [m]	-2.78E+04	2.54E-05	49.2%
Thermal Paste Conductivity [W/mK]	3.05E-01	2.31E-02	0.0%
Coupon Thickness [m]	-6.41E+03	1.75E-05	1.2%
Coupon Thermal Conductivity [W/mK]	3.38E-01	1.00E-01	0.1%
Fore Copper Temperatures [K]	5.00E-01	1.00E+00	24.7%
Aft Copper Temperatures [K]	5.00E-01	1.00E+00	24.7%
Total	1.8%		

Using the uncertainty in coupon surface temperature, the uncertainty in Nusselt number can be calculated using equation B-18.

$$U_{Nu} = \sqrt{\left(\frac{\partial Nu}{\partial W} \cdot U_W\right)^2 + \left(\frac{\partial Nu}{\partial H} \cdot U_H\right)^2 + \left(\frac{\partial Nu}{\partial L} \cdot U_L\right)^2 + \left(\frac{\partial Nu}{\partial T_{coupon}} \cdot U_{T_{coupon}}\right)^2 + \left(\frac{\partial Nu}{\partial HP} \cdot U_{HP}\right)^2 + \left(\frac{\partial Nu}{\partial k_{air}} \cdot U_{k_{air}}\right)^2 + \left(\frac{\partial Nu}{\partial T_{out}} \cdot U_{T_{in}}\right)^2} \quad (B - 18)$$

As with the other parameters, an example for the uncertainty calculations for a wavy channel at two Reynolds numbers is shown in Table C-7 and Table C-8.

Table C-7. Uncertainty Contributions for Nusselt Number at a Reynolds Number of 10,000

Variable	Value of Partial Differential [1/units]	Uncertainty	Contribution
Width [m]	-1.14E+04	1.75E-05	0.4%
Height [m]	2.44E+04	1.75E-05	1.9%
Channel Length [m]	-1.06E+03	2.54E-05	0.0%
Coupon Wall Temperature [m]	-2.57E+00	8.64E-01	51.6%
Heater Power [m]	5.47E-01	1.67E-01	0.1%
Conductivity of Air [m]	-2.22E+03	2.73E-04	3.8%
Plenum Inlet Temperature [m]	6.79E-01	1.00E+00	4.8%
Plenum Outlet Temperature [m]	1.89E+00	1.00E+00	37.4%
Total	5.1%		

Table C-8. Uncertainty Contributions for Nusselt Number at a Reynolds Number of 30,000

Variable	Value of Partial Differential [1/units]	Uncertainty	Contribution
Width [m]	-2.31E+04	1.75E-05	0.2%
Height [m]	4.95E+04	1.75E-05	1.1%
Channel Length [m]	-2.16E+03	2.54E-05	0.0%
Coupon Wall Temperature [m]	-6.36E+00	1.01E+00	62.2%
Heater Power [m]	7.63E-01	2.08E-01	0.0%
Conductivity of Air [m]	-4.66E+03	2.64E-04	2.3%
Plenum Inlet Temperature [m]	2.13E+00	1.00E+00	6.9%
Plenum Outlet Temperature [m]	4.22E+00	1.00E+00	27.2%
Total	6.6%		

VITA

Thomas M. Corbett

Thomas Corbett was born and raised in Genoa, Illinois, graduating from Genoa-Kingston Highschool in 2016. Thomas then enrolled at Northern Illinois University (NIU) seeking a BS in mechanical engineering. While at NIU Thomas first conducted research with Dr. Sachit Butail investigating neural responses to a variety of external stimuli. He soon transitioned to working with Dr. Federico Sciammarella in the Advanced Research of Materials and Manufacturing (ARMM) lab investigating the Direct Energy Deposition (DED) metal additive process. While at NIU Thomas completed several internships in industry, including at 3Degrees Company and John Deere. Thomas' senior design project as part of his undergraduate program used CFD to predict the best placement for fans to circulate air in the Fermilab Muon-G2 experimental facility. In May of 2019 Thomas completed his BS earning Suma Cum Laude with full university honors.

In June of 2019 Thomas moved to State College, PA to pursue a PhD in Mechanical Engineering under the direction of Dr. Karen Thole in the Steady Thermal Aero Research Turbine (START) Laboratory at The Pennsylvania State University. While at START Thomas' research was sponsored by Solar Turbines and the US Department of Energy, where he investigated advanced internal cooling schemes that leveraged additive manufacturing. Thomas received his MS in Mechanical Engineering from The Pennsylvania State University in December 2022.

During his time at START Thomas authored or co-authored seven academic papers which were published in the International Journal of Heat and Mass Transfer, ASME Journal of Turbomachinery, and/or presented at ASME Turbo Expo. Thomas also served as a reviewer for both ASME Turbo Expo as well as Additive Manufacturing. Additionally, he served as the student review initiative chair for ASME Turbo Expo 2023, coordinating students with papers that required additional reviewers. In 2023 Thomas and several co-authors were awarded a patent for an internally cooled additive turbine ring segment.

Thomas has been a recipient of the Gabron Graduate Fellowship award, and the 2022 Student Advisory Committee Travel award. In 2020, Thomas was a recipient of the University Turbine System Research (UTSR) Gas Turbine Industrial Fellowship (GTIF), which gave him the opportunity to apply his research to commercial engines through a research appointment at Solar Turbines Inc. Following graduation, Thomas will join Pratt and Whitney as a Senior Engineer in the Secondary Flows group working on effectively allocating cooling air to various sections of an engine.